The behaviour of metals during differentiation of subduction-related lavas: A case study of active submarine volcanoes on the Hunter Ridge, SW Pacific

by

Gisela Rossana Cobeñas Benites
M.Sc. Université Blaise Pascal

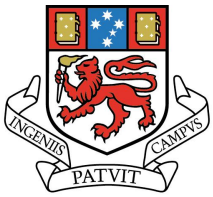

UNIVERSITY OF TASMANIA

Submitted in fulfilment of the requirements for the degree of
Doctor of Philosophy

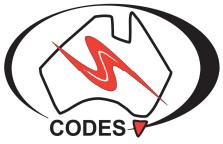

July, 2013

Declaration

This thesis contains no material which has been accepted for the award of any other degree or diploma in any tertiary institution and to the best of my knowledge and belief, contains no material previously published or written by another person, except where due acknowledgement is made in the text of the thesis.

_____Gisela Rossana Cobeñas Benites

15th July 2013

Access Authority

This thesis may be made available for loan and limited copying in accordance with the Copyright Act, 1968.

_____Gisela Rossana Cobeñas Benites

15th July 2013

Abstract

In subduction zone environments, the behaviour of metals and other associated elements during magmatic differentiation has a profound impact on the potential to form magmatic-hydrothermal ore deposits. Understanding the partitioning of ore metals between the melt, crystal and volatile phases is of key importance in their removal from, or concentration in, evolving magmas, and hence, the potential to form economically important mineral deposits.

This study focuses on the partitioning of Cu, Zn, Pb, V, Co and Sc between melts and crystallising mineral phases in subduction-related magmas from the Hunter Ridge. This locality offers a unique opportunity to compare calc-alkaline and adakite rock suites. In addition, effects of contamination by continental material can be excluded due to the intra-oceanic setting of this region.

The main aim of this work is to determine how magma ascent, crystallisation and degassing can lead either to the enrichment or depletion of ore-forming metals. Furthermore, the common association between porphyry copper deposits and high Sr/Y (i.e. "adakitic signature") magmatic rocks is examined, which may be useful for mineral exploration.

Rocks from the Hunter Ridge calc-alkaline series record a protracted history of magma evolution from the very earliest stages of fractionation (i.e. before volatile loss) to their subsequent eruption. Groundmass and glass compositions (rather than whole-rock geochemistry data) together with a detailed trace-element study, have been used to reproduce the liquid line of descent (LLD) for the evolution of the calc-alkaline magmas. Subsequently, it has been demonstrated that in the case of the Hunter Ridge calc-alkaline series, the minerals and melts are genetically related and that fractional crystallisation of olivine + clinopyroxene + plagioclase + magnetite ± amphibole is the primary process recorded in these rocks. Following the same approach for the adakite magma series, it was established that the minerals and melts are genetically related and that fractionation of olivine + clinopyroxene occurred in the more primitive rocks. However, no examples with an MgO wt% lower than 5.2 are represented in our collection.

Metal partitioning behaviour in the principal magma components (of both adakitic and calc-alkaline rocks) was examined (i.e. for olivine, clinopyroxene, plagioclase, magnetite, and melt). Mineral/melt partition coefficients (Ds) for Cu, Zn, V, Pb, Co and Sc used in the modelling were calculated directly from LA-ICP-MS analyses for phenocryst-groundmass/glass equilibrium pairs. For comparison purposes, modelling was also conducted using Ds values obtained from the literature (where available).

Although basaltic rocks from the Hunter Ridge calc-alkaline samples have initial metal abundances similar to those in mid-ocean ridge basalts (MORB), the contents of chalcophile elements such as Cu increase early during magma evolution beyond the range found in typical MORB (from 8.3 to 6.5 MgO wt% while Cu contents in the melt increase from ~89 ppm to ~128 ppm). This behaviour can be linked to the presence of higher water contents and higher oxidation states of arc magmas compared to MORB, which suppresses the formation of sulphide liquids that might otherwise

scavenge Cu from a silicate magma. Plagioclase saturation occurs at a melt MgO wt% of 6.5, which is accompanied by a rapid decrease in Cu contents in the magma. This most likely marks the onset of degassing.

Zinc and V increase during magma evolution (from ~50 ppm and 230 ppm respectively at 8.3 MgO wt% to a maximum of ~66 ppm and 275 ppm respectively at 5 wt% MgO). Similar behaviour is observed in FeO and TiO_2 during magmatic fractionation. Once magnetite enters the liquidus at ~5 wt% MgO, Zn and V both decrease within decreasing MgO (falling to ~50 ppm and 20 ppm respectively at MgO <0.5 wt%). Given that, both $D_{Zn}^{mt/mel}$ and $D_{V}^{mt/melt}$ are high at 5.7 and 9.8 respectively (at ~ 5 wt% MgO), this behaviour can be explained by the partitioning of Zn and V into magnetite.

Lead contents increase from ~1 ppm at 8.3 wt% MgO to 4.5 ppm at 0.3 wt% MgO. Modelling shows that partitioning of Pb into olivine, clinopyroxene and plagioclase is negligible. In addition, it would appear that Pb does not enter a volatile phase (as with Cu).

In contrast to the above elements, Co and Sc concentrations decrease with decreasing MgO wt% of the melt (from ~37 ppm at 8.3 wt% MgO to ~2 ppm and ~8 ppm respectively at 0.3 wt% MgO). This can be explained by the partitioning of Co into olivine and to lesser extent clinopyroxene, and Sc into clinopyroxene (only), during the early stages of magmatic fractionation (as indicated by the high $D_{Co}^{ol/melt}$ of 5.6 - 22.2, $D_{Co}^{cpx/melt}$ of 1.1, $D_{Sc}^{cpx/melt}$ of 2 – 14, measured $D_{Sc}^{ol/melt}$ of 0.1-0.4). Co and Sc also partition into magnetite once it enters the liquidus, as indicated by $D_{Co}^{mt/melt}$ from 6 to 18 and $D_{Sc}^{mt/melt}$ from 0.9 to 2.2 (over a MgO range of 5.3 to 2.3 wt%).

These results provide evidence that: i) Cu partitions into a fluid phase at crustal levels before sulphide saturation occurs; ii) Zn and V are greatly affected by magnetite saturation; iii) Pb behaves as an incompatible element during magmatic fractionation and does not enter a fluid phase; iv) Co behaves as compatible element and partitions into olivine and clinopyroxene (and to lesser extent magnetite); v) Sc also behaves as compatible element and partitions into clinopyroxene (and to lesser extent magnetite).

There are notable differences in the crystallisation sequence between the calc-alkaline and adakitic magmas from the Hunter Ridge. Basalts from both magma series contain olivine and clinopyroxene as early liquidus phases. In the calc-alkaline series, plagioclase enters the liquidus at ~6.5 MgO wt%, whereas in the adakite series plagioclase saturation is suppressed below 5.2 MgO wt%. The adakite magmas are, therefore, consistent with differentiation under higher water and/or volatile contents and at deeper crustal levels than the calc-alkaline magmas. This has an important effect on the partitioning of metals that have affinity for a volatile phase.

The results show that, at least for the Hunter Ridge adakites, there is no a direct contribution of slab-derived melts to the metal budget of these magmas. This is evidenced from the Cu, Zn, Pb, Co and V contents, which in the most primitive adakite samples are comparable (if not lower) than those from the most primitive calc-alkaline samples (i.e. demonstrating that slab melts were not enriched in these elements). Even so, adakitic magmas have more potential to generate economically important ore deposits because they are more likely to exsolve a single-phase fluid at deep crustal levels, which is considered favourable to the formation of large porphyry deposits.

Acknowledgements

I would like to thank my supervisors Leonid Danyushevsky and Trevor Falloon for initiating the research project. I'd like to extend my foremost, hearty and sincere thanks to Leonid for providing unlimited support, inspiration, guidance and encouragement.

The field part of this research was carried out during a four-week voyage aboard the CSIRO research vessel, the 'Southern Surveyor', and I would like to thank all those who provided technical and logistic support and who made life during long overnight shifts enjoyable.

I am especially grateful to the technical staff at CODES and the Central Science Laboratories (CLS) at the University of Tasmania who provided exceptional support during this project. I would like to extend my special thanks to Karsten Goemann for the tremendous help with the microprobe analyses, for always being there to help me with any difficulties I was having, and for great talks during the countless hours I expend in the lab. Special thanks also to Marcel Guillong and Sarah Gilbert for their help with the LA-ICP-MS, for showing me the most efficient ways to reduce my huge datasets and for the discussions about isotopes and interferences. A large number of other people have assisted and supported me, including Phillip Robinson and Katie McGoldrick for their help with XRF analyses, Ian Little for ICP-MS analyses, Simon Stephens and Al Cuison for preparation of thin sections, Prof. Ron Berry for help with the GEM microscope, Karen Mollross for her logistic support, and June Pongratz for her assistance editing my thesis.

I would also like to thank those have read parts of this thesis or provided feedback or comments, not least of which include Professors Ross Large, Andrew McNeill, Dave Cook and Tony Crawford.

I also wish to thank Prof. Jon Blundy for help with the calculation of the lattice strain model and Dr. Jean Bédard for providing me with unpublished equations to calculate partition coefficients for Cu and Zn.

Thanks to all my colleagues, PhD students and post-docs past and present, who always provided good laughs, good discussions and good times. Doing this PhD would have not been the same without the friendship and camaraderie with all of you. Special thanks are deserved for my office mates Roisin, Francisco, Vic and Fiona who had to bear with my loud and terrible singing and to my good friends Dan, Selina and Nina, who I shared many trips, work and non-work related conversations. You contributed to make these years unforgettable.

To my dear friends Sofia, Romy, Rob and Phil, thanks for being such a great friends, for always being there, for listening to my constant nonstop PhD talk (without complaining too much), for feeding me and always making me feel welcome in your homes.

I am very grateful to Dave Hutchinson, for being supportive and critical with my work. Dave, I'd like to thank you for the countless hours of geological discussions and editing support and for being an excellent friend.

Finally, I wish to thank my family, without your unwavering support and love none of this would have happened. Mama, papa, Pedrin y tio Juan, las palabras no alcanzan para expresar mi gratitud por todo el amor y apoyo que me han dado durante todo el tiempo, por siempre confiar en mi sin importar que tan lejos o que tan cerca estoy. Muchas gracias.

Table of Contents

Chapter 4: Petrography and mineral chemistry of the Hunter Ridge magma series

Chapter 5: Identification of the calc-alkaline fractionation series

Chapter 6: Metal behaviour during differentiation of the Hunter Ridge calc-alkaline magma series

List of Figures

List of Tables

List of Appendices

Chapter 1

Introduction

This project investigates the behaviour of metals and other associated elements during magmatic differentiation of intra-oceanic island-arc lavas. Modern and ancient arc settings are linked with large porphyry and epithermal ore deposits that are a major resource for copper, lead, zinc, gold and silver. A better understanding of element behaviour during magmatic fractionation will help constrain whether mineralising ore fluids acquire their metal content directly from a parent magma, or as a consequence of later processes (i.e. seafloor leaching, presence of pre-existing sulphides, etc).

In order to examine metal enrichment/depletion at different stages of fractionation it is necessary to know element partitioning behaviour in the major magma components (i.e. olivine, clinopyroxene, plagioclase, magnetite, melt). Published information on this is scarce and varies between sources. Thus, another aim of this study is to provide further constraints, on mineral/melt partitioning that can be used to model igneous processes for arc-related systems.

Recent studies have indicated an association between porphyry copper deposits and high Sr/Y (i.e. "adakitic signature") magmatic rocks but the nature of this association remains speculative. An additional aim of this study is to examine the links between adakitic rocks and porphyry-type deposits, which may also be useful for mineral exploration.

The Hunter Ridge, (North Fiji Basin, SW Pacific; Fig. 1.1) offers an ideal location to examine the effects of magma evolution by fractional crystallisation. This region hosts a range of primitive to evolved subduction-related lava suites (e.g. calc-alkaline, tholeiite, adakite, boninites and back-arc basin basalts), which are both spatially and temporally associated (all were erupted within approximately 3 Ma). Furthermore, we can exclude the effects of contamination by continental material due to the intra-oceanic setting of the region.

Dredge samples collected from the Hunter Ridge include suites of geochemically primitive to evolved calc-alkaline and adakitic rocks with broad ranges in MgO contents (1–14 and 5–13 wt%. respectively). Both magma suites contain petrologically primitive members, as represented by the olivine ± clinopyroxene phorphyritic basalts with olivine phenocrysts in the range of Fo 89–95 and clinopyroxene Mg# 86–92. Such samples most likely record the early, pre-eruptive, stages of magma fractionation. Phenocryst compositions across all the samples analysed range from olivine Fo 79–95, clinopyroxene Mg# 70–92, and plagioclase An 22–92. Similarly, by comparing element and volatile contents from the two different magmatic series it will be possible to investigate the primary controlling factors that affect the concentration of metals in primary melts; these could include: 1) timing of degassing, 2) depth of crystallisation, 3) partial melts derived from adiabatically upwelling asthenospheric mantle, 4) magma mixing, 5) oxidation state, 6) partial melting of the mantle wedge, 7) components derived from melting of a subducting slab, and 8) element contributions from subducting sediments.

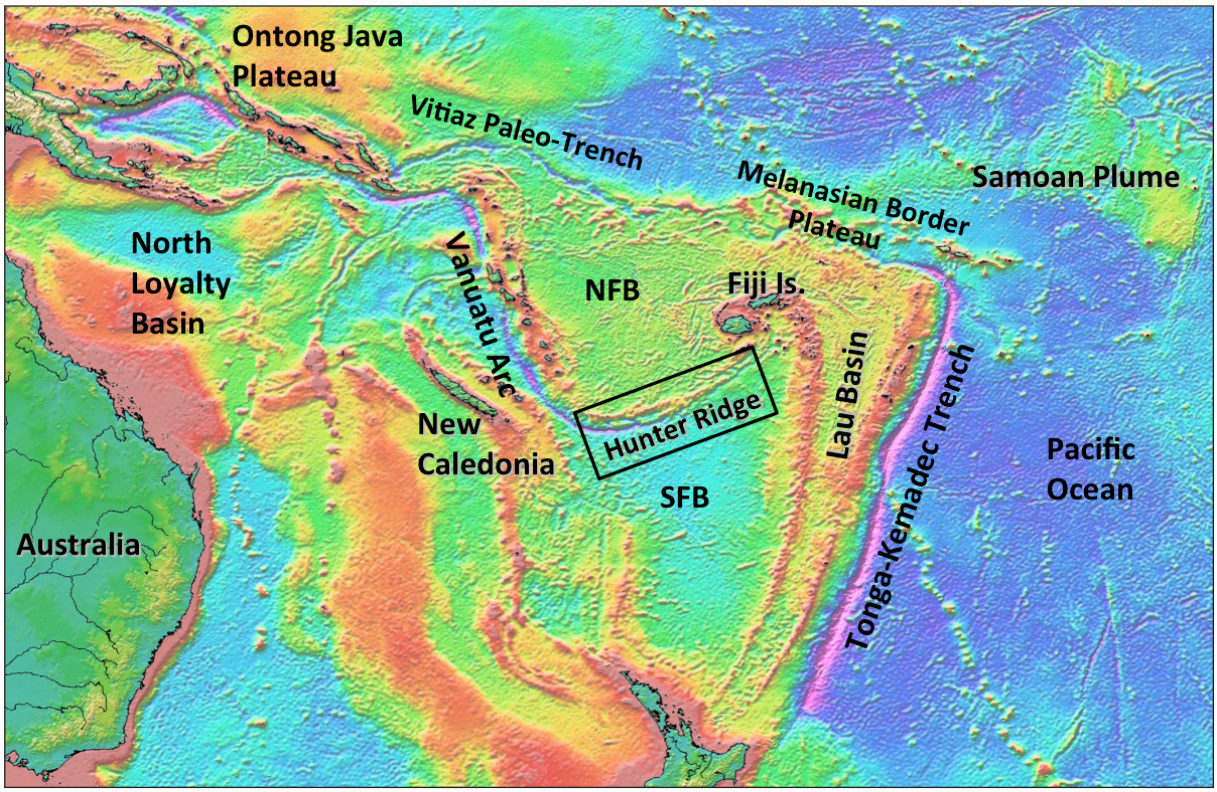

Fig. 1.1. Map of the southwest Pacific, modified after Crawford et al. (2003). Inset showing location of the Hunter Ridge. NFB – North Fiji Basin; SFB – South Fiji Basin.

1.1 Thesis layout

This thesis is divided into eight main sections:

Chapter 1 – Includes the Introduction and provides a brief summary of the terminology used. Also, provides general background information on the study location and details of the sampling sites.

Chapter 2 – Literature review: A summary of findings from previous workers relating to metal behaviour during magmatic differentiation of arc-related lavas. Particular attention is focused on the effects of fractional crystallization and the selection of partition coefficients for petrological modelling.

Chapter 3 – Outlines the techniques used for this study and data processing.

Chapter 4 – Presents detailed petrographic and mineralogical observations made using optical and SEM microscopy and microprobe.

Chapter 5 – Focuses on the identification of the Hunter Ridge calc-alkaline magma series based on the results of major and trace element modelling.

Chapter 6 – Investigates the ore metal behaviour during differentiation of the Hunter Ridge calc-alkaline magma series. This section presents new geochemical data including mineral chemistry and mineral/melt partition coefficients.

Chapter 7 – Focuses on the Hunter Ridge adakitic suite and ore metal behaviour during the differentiation of this magma type.

Chapter 8 – The final section of this thesis summarises the main points and results from each of the preceding sections into a general discussion on metal behaviour during differentiation of both calc-alkaline and adakitic magmas. Ideas regarding the main differences in metal enrichment and concentration between these two magma types, specifically regarding physical and chemical vectors that may be critical in the formation of porphyry-type ore deposits.

1.2 Main terminology specific to this study

The following terms are used extensively throughout the text.

- Arc Tholeiites. Characterised by high Fe_2O_3/FeO ratios (Gill, 1981) and enriched in large ion lithophile elements (LILE) such as Pb, Ba, Cs, K, Rb and Sr compared to MORB with a distinctive Nb anomaly (Macdonald et al., 2000).
- Adakite. A general use of the term 'adakite' is given for igneous rocks with extreme light rare earth element (LREE) enrichment (e.g. La/Yb > 15) and very high Sr/Y ratios (e.g. Sr/Y > 40). Martin et al. (2005) divide adakites in 2 sub-groups: 1) high silica adakites (LSA), when the SiO_2 percentage is higher than 60 wt%, and 2) low silica adakites (LSA), when SiO_2 is lower than 60 wt%.
- Back-arc basin basalts (BABB). BABB are transitional between MORB and arc basalt and are enriched in volatiles and incompatible elements (Hawkins, 1995). Basalts of this series are derived from partial melting of asthenospheric mantle with element enrichments derived from subducting oceanic lithosphere and a mantle wedge component (Taylor et al., 2003).
- Boninite. Boninites are volcanic rocks characterized by relatively high SiO_2 and H_2O but low TiO_2 contents compared to tholeiitic suites. Typically, plagioclase is absent in rocks more mafic than andesite (Taylor et al., 1994), and they often contain very magnesian olivine phenocrysts. Two broad types of boninite magmas are recognized, the high-Ca and low-Ca boninite series (Crawford et al., 1989).
- Calc-alkaline. Currently there is little agreement in the definition and use of the term calc-alkaline. For the purposes of this research, the term is adopted from Kelemen et al. (2003) and refers to magmas with medium K, enriched in large ion lithophile elements (LILE) such as Pb, Ba, Cs, K, Rb and Sr compared to MORB with a distinctive Nb anomaly (Macdonald et al., 2000).
- Cr#. Molar $[Cr_2O_3/(Cr_2O_3+Al_2O_3)]*100$
- "D" or Nernst partition coefficient. Ratio of the concentrations of a trace element in a solid phase and in the equilibrium liquid.
- Hot subduction. The term "hot subduction" in this work refers to a region where subducting oceanic lithosphere (i.e. the southern Vanuatu slab) intersects upwelling asthenospheric mantle beneath a spreading ridge axis (e.g. the North Fiji Basin spreading centre).
- Mg#. Molar [MgO/(MgO+FeO*)] * 100. FeO*=total iron

- Evolved. Lavas and melts with Mg# < 50
- Primitive. Lavas and melts with Mg# > 60
- High Mg#. Lavas and melts with Mg# from 50 to 60.
- MORB: Mid-ocean ridge basalt

1.3 Geological Setting of the Hunter Ridge and the North Fiji Basin

The geology of the North Fiji Basin, and the Hunter Ridge in particular, has received particular attention since the late 80's due to its unique tectonic setting (i.e. spreading-ridge/transform-fault/subduction interactions). Some researchers have focussed on the tectonic evolution of the NFB (e.g. Malahoff et al., 1982a; Auzende et al., 1988, 1994, 1996; Crawford et al. 2003, etc.) while others have turned their attention on the magmatic development of the region, including, among others, those of Verbeteen et al. (1995), Danyushevsky et al. (2002) and Danyushevsky et al. (2006).

The volcanically active junction between the Vanuatu Trench in the west and the Hunter Ridge in the southern portion of the North Fiji Basin is thought to be the product of continuous roll-back of the Vanuatu trench. This unusual tectonic setting has resulted in a unique interaction of upwelling asthenospheric mantle and subducting oceanic lithosphere below a 'back-arc' spreading centre (Danyushevsky et al., 2006). As a consequence, this region of the North Fiji basin produces a wide range of lava types whose geochemical signatures include island arc tholeiites, calc-alkaline, adakites and boninites, all erupted within ~ 3 My and in close proximity to each other.

1.3.1 Location and tectonic evolution of the North Fiji Basin (NFB)

The North Fiji Basin is a mature (~12 Ma), triangular shaped, intra-oceanic, back-arc basin located at a convergent boundary between the Pacific and Australian Plates (Auzende et al., 1995) (Figs 1.1, 1.2). The basin is bordered to the east by the Fiji Islands-Fiji Platform and the Lau Ridge, to the west by the Vanuatu arc, to the north by the Vitiaz paleo-trench and to the south by the Hunter Ridge. Active and fast spreading occurs along several ridges within the basin. South of the Hunter Ridge lies the currently inactive 31–25 Ma South Fiji Basin (Weissel, 1981; Davey, 1982; Malahoff et al., 1982, etc) (Fig. 1.2).

Different models for the opening of the NFB have been proposed. However, most authors agree that this initiated after subduction had ceased along the Vitiaz arc in response to the collision of the Melanesian Border Plateau (Falvey, 1975; Gill and Whelan, 1989a) and /or the Ontong Java Plateau (OJP) with the proto Vitiaz trench (Packham, 1973; Falvey, 1975; Kroenke, 1984). Several authors (i.e. Kroenke, 1984; Yan & Kroenke, 1993; Petterson et al., 1997) report the initial collision of the OJP with the Vitiaz Arc as early as 25–20 Ma, with collision of the Melanesian Border Plateau east of Fiji occurring as late as 7.5 Ma (Gill & Whelan, 1989a; Hathway, 1993).

The cessation of SW-directed subduction along the Vitiaz trench led to a reversal of arc polarity northwest of Fiji along the Vanuatu-New Hebrides segment. This may have occurred between 12 and 8 Ma (e.g. Auzende et al., 1996; Pelletier et al., 1993; Hamburger & Isacks, 1987; Gill & Whelan,

1989a) (Fig. 1.2). The opening of the NFB is believed to have commenced at around 7 Ma as a result of the clockwise rotation of the Vanuatu arc (Auzende et al., 1996) and counter-clockwise rotation of the Fiji Platform (Falvey, 1975, 1978). This anticlockwise rotation of Fiji Platform resulted in subduction of the South Fiji Basin (SFB) crust along the southern limit of the NFB (i.e. Hunter Ridge) (Auzende et al., 1996; Taylor et al., 2000; Crawford et al., 2003). The recent evolution of the NFB (i.e. < 3 Ma to present day) is characterised by an east–west opening direction since 3 to 3.5 Ma and along a north–south spreading ridge centred on 173º 30' E (Fig. 1.2) (Auzende et al., 1996).

1.3.2 Hunter Ridge

The Hunter Ridge (HR) is a largely submarine ridge composed of arc crust that extends from the southern termination of the Vanuatu Trench (Launay, 1982) to the Koro Sea close to Fiji (Leslie, 2004) and strikes approximately NE–SW. The Hunter Ridge was considered by Auzende et al. (1996) to represent a short-lived intra-oceanic arc that occurred in response to a short period (7–3 Ma) of NNW-directed subduction of the South Fiji Basin crust under the North Fiji Basin.

A number of research voyages to the region were aimed at mapping the seafloor between 173–178º E, 20.5–22º S (i.e. "Southern Surveyor" SS10/2004, SS10/2006 & SS03/2009). This mapping revealed the highly deformed nature of the HR crust. Furthermore, the discovery of active submarine volcanic centres along the southern margin of the NFB suggests that this region is currently undergoing extension.

The high-resolution swath mapping (Danyushevsky et al., 2006) (Figs 1.3, 1.4) revealed a number of features including:

- The western end of the HR has been split into two roughly parallel north and south segments aligned in a NE–SW direction. Both segments have approximately the same length (~150 km).
- The northern segment is around 20–30 km wide and the southern segment is narrower ~10 km wide. In this region the mapping discovered a young, volcanically active, rift zone that separates the two segments (Figs 1.3, 1.4). To the southwest both segments seem to join the southern end of the Vanuatu arc.
- The Hunter Ridge crust within the rift is cut by multiple generations of cross-cutting faults. Some of the faults indicate counter-clockwise rotation of the rifted northern segment of the Hunter Ridge.
- Mapping revealed no clear structural boundary between the northern termination of the submarine HR and the western end of the Kadavu Island. The southern edge is sharply defined by a steeply dipping rifted ridge wall.
- There exist a large number of small young volcanic cones on the slopes of the Kadavu Island, on the Hunter Ridge, and on the seafloor of the North Fiji back-arc basin west of Kadavu.

The field part of the current work was carried out during a four-week voyage aboard the CSIRO operated research vessel, the 'Southern Surveyor', to the Hunter Ridge, southern margin of the North Fiji basin (SS03/09). The aims of the voyage were to map the seafloor using multibeam swath bathymetry (hull-mounted Simrad EM300 30 kHz Multibeam system) and to sample volcanic rocks and glasses by dredging and the deployment of a wax-corer. Fifty-six successful dredges

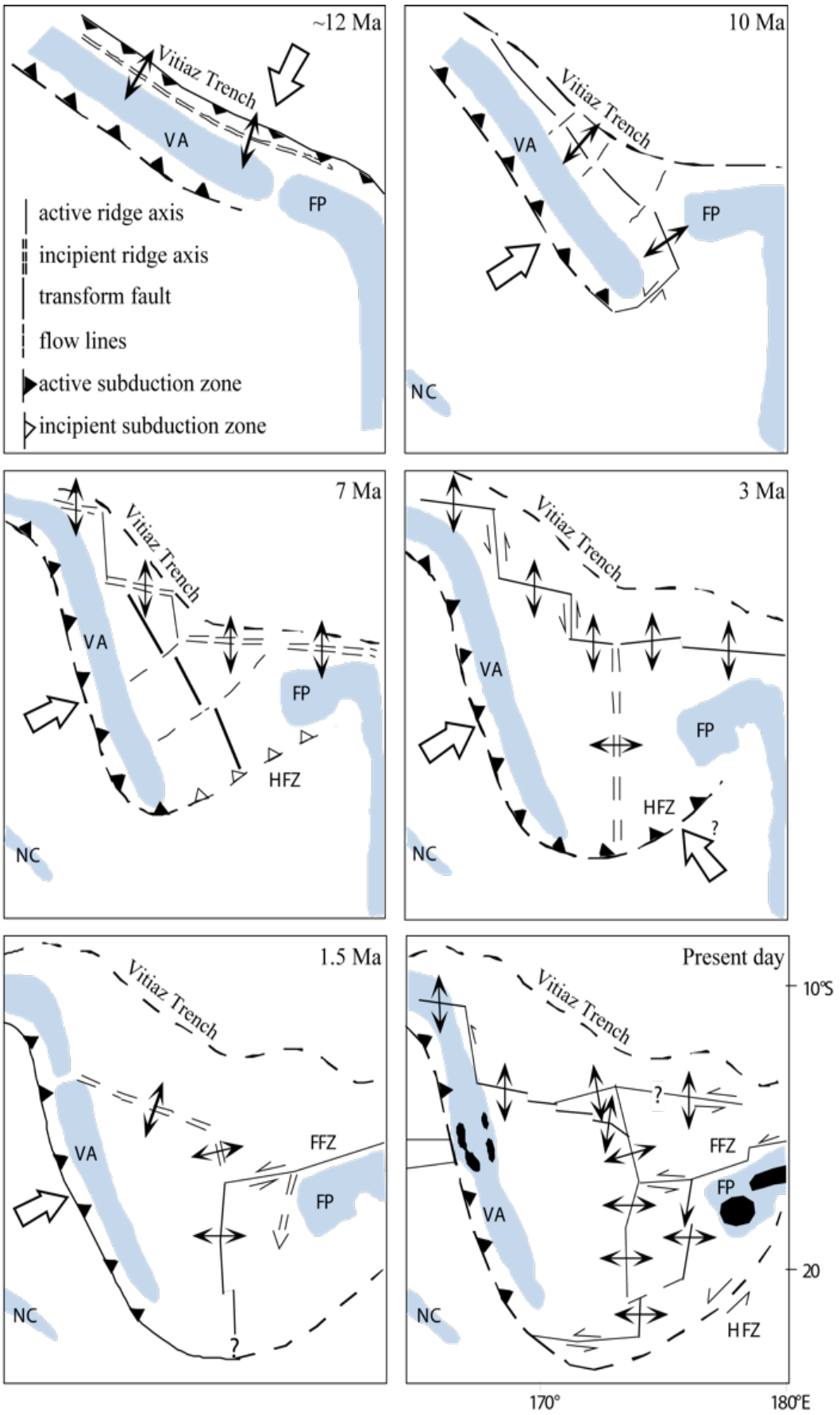

Fig. 1.2. Geodynamic evolution of the North Fiji Basin, after Azunde et al., (1995). VA - Vanuatu Arc; FP - Fiji Platform; NC - New Caledonia; HFZ - Hunter Fracture Zone; FFZ - Fiji Fracture Zone or Hunter Ridge.

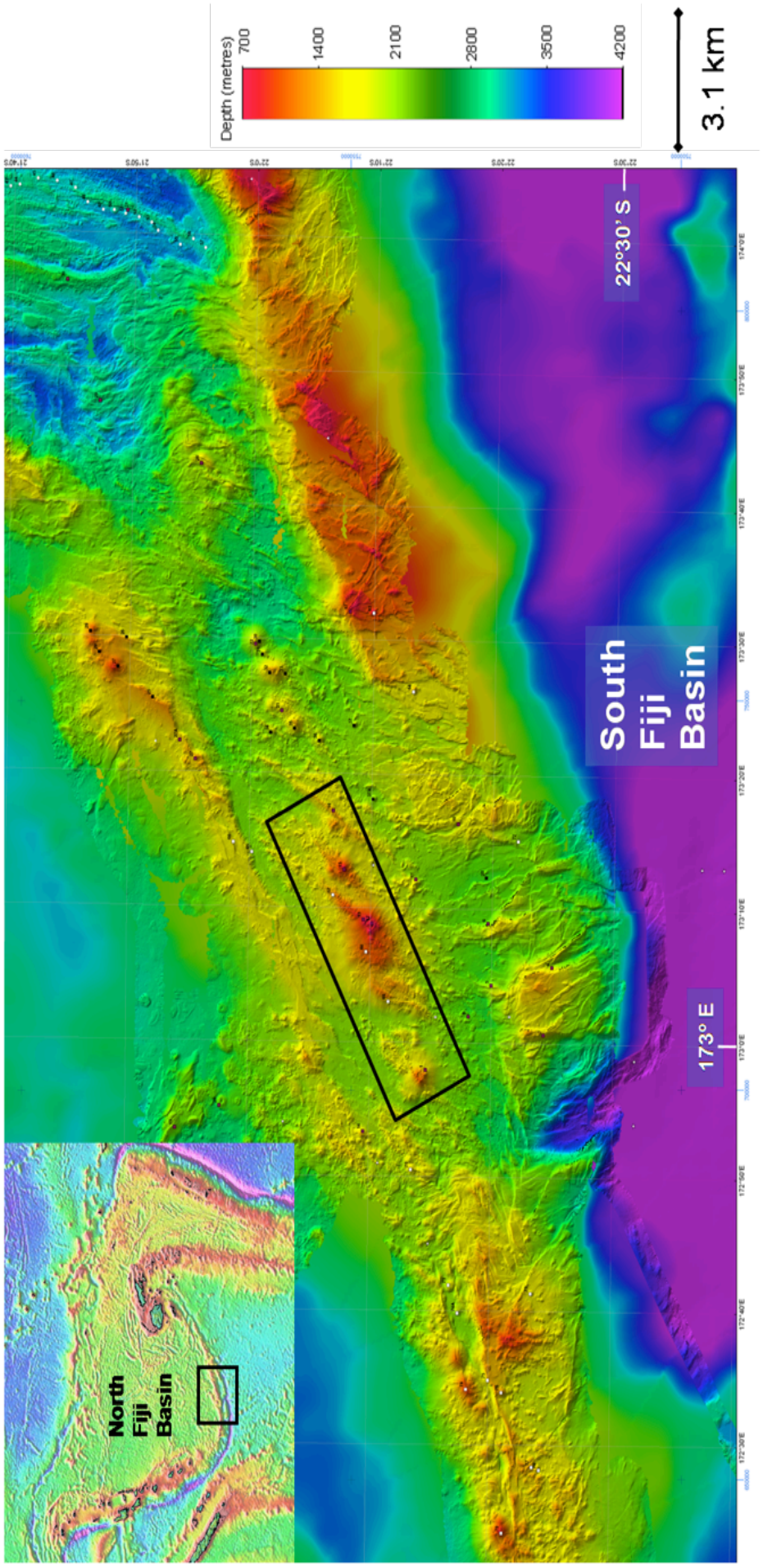

Fig. 1.3. SW Hunter Ridge. Swath bathymetry data overlain on low resolution satellite bathymetry, modified after Danyushevsky et al. (2009). The map shows the north and south rifted segments of the Hunter Ridge and the black rectangle the approximate location of the dredges carried out for this study.

were conducted, three of which were carried out specifically to collect samples for this study (23 samples). Sixty-five additional samples for this project were collected during voyages to the same region conducted in 2004 and 2006 (SS10/04 and SS08/06) led by Leonid Danyushevsky and Trevor Falloon. The locations of the dredges specific to this study are shown in Figures 1.3-1.4 and Table 1.1.

1.3.3 Magmatism at the southern end of the North Fiji Basin

Magmatism along the southern end of the NFB has produced a wide range of subduction-related lava types (Danyushevsky et al., 2006). Five different magma series from three different tectonic settings/environments of formation are recognized in the area (back-arc basins 'BAB', arcs and 'hot subduction'). These magmatic suites include: i) back-arc basin basalts (BABB), ii) calc-alkaline (arc), iii) arc tholeiites (arc), iv) boninites (arc), and v) adakites ('hot subduction'). The adakites are distinctive in this group, and have been shown to be spatially related to the subduction of the southern portion of the Vanuatu slab into an anomalous hot mantle above it. The mantle above the Vanuatu slab has an unusually high temperature due to the proximity of the NFB spreading centre to the arc (Danyushevsky et al., 2006).

Primitive mantle-normalised trace element diagrams for selected rocks from each magma type are shown in Figure 1.5. BABB from the Hunter Ridge produce trace element patterns typical for these rock types which are similar to MORB (i.e. relatively flat patterns; Fig. 1.5). The patterns for the calc-alkaline, arc tholeiite, boninite, and adakite suites display the distinctive characteristics of arc lavas, such as enrichment in large ion lithophile elements (LILE; K, Rb, Sr, Ba and Pb) and a Nb-Ta negative anomaly.

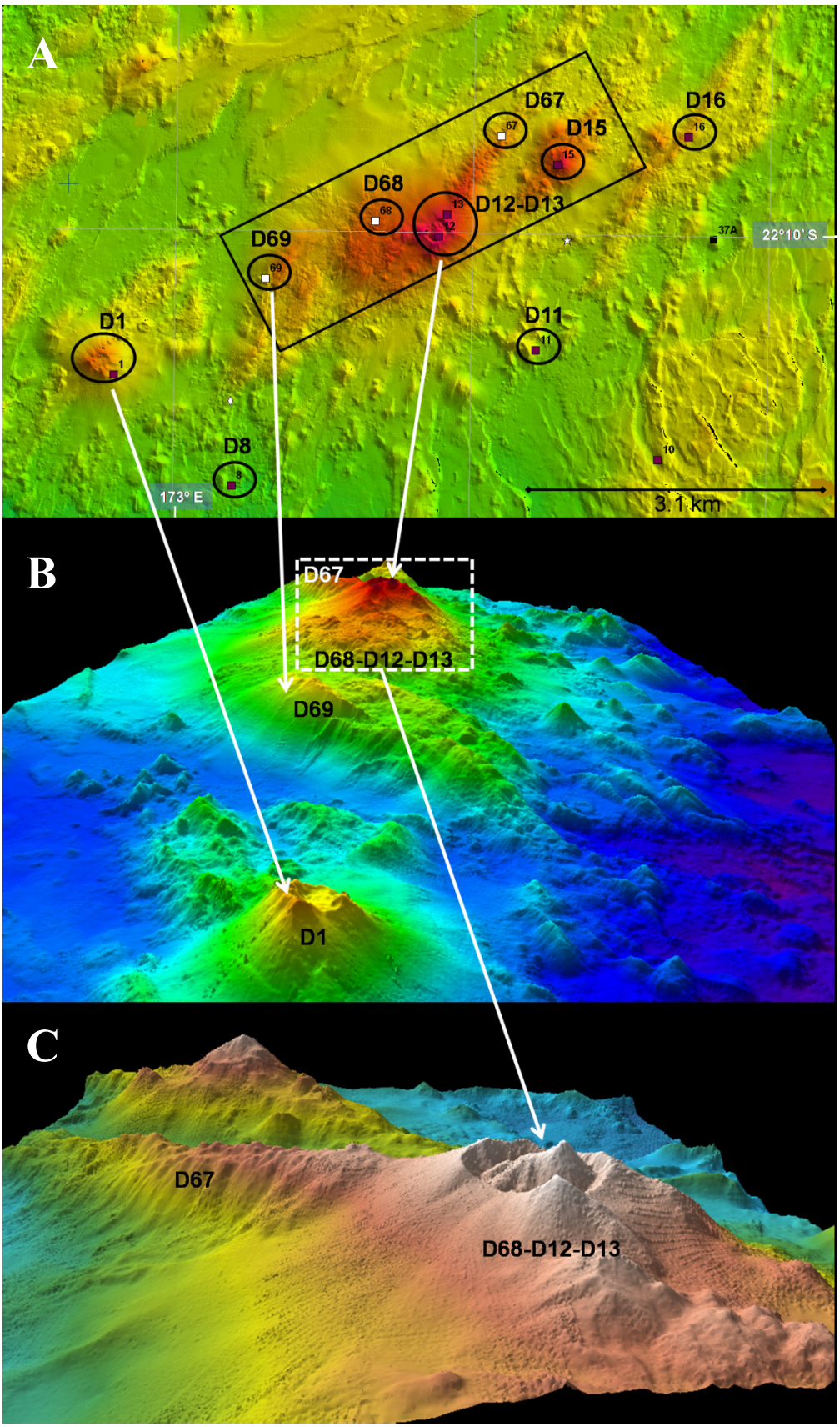

Fig. 1.4. A) SW Hunter Ridge (black inset of Fig. 1.2) showing the approximate location of the dredges carried out for this study. B) 3D image of the Hunter Ridge central rift volcanoes, showing the approximate location of the dredges and the spatial relationship between samples. C) White inset of figure B.

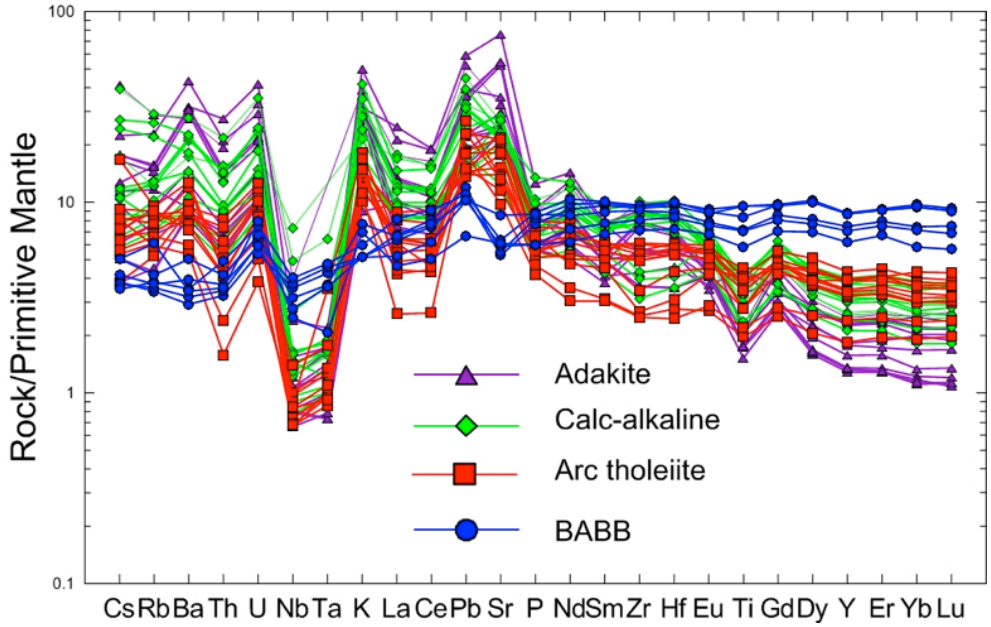

Fig. 1.5. Primitive mantle-normalised multi-element diagram for the Hunter Ridge magmatic suites.

Table 1.1. Location of the Hunter Ridge dredges used during this study.

Voyage	Dredge	Latitude	Longitude	Recovered magma type	Recovered rock type
SS10/2004	D1	-22.245	172.966	calc-alkaline	basaltic andesite
SS10/2004	D8	-22.303	173.033	calc-alkaline	basalt
SS10/2004	D11	-22.229	173.203	calc-alkaline	basalt
SS10/2004	D12	-22.169	173.148	calc-alkaline	dacite
SS10/2004	D13	-22.141	173.152	calc-alkaline	dacite, rhyolite
SS10/2004	D15	-22.130	173.214	calc-alkaline, adakite	basaltic andesite
SS03/2009	D67	-22.116	173.182	calc-alkaline	basaltic andesite
SS03/2009	D68	-22.161	173.112	calc-alkaline	dacite, rhyolite
SS03/2009	D69	-22.193	173.051	calc-alkaline	dacite, rhyolite

Chapter 2

Literature review

2.1 Aims

This section has three aims:

- To provide a thorough yet concise review of the characteristics of subduction-related magmas. To do this, we focus on an intra-oceanic island arc environment, where the effects of crustal contamination by continental material are minimal.
- To compare our data in this and subsequent chapters to data from other well-constrained primitive island arc settings and to MORB glasses.
- To summarise the current understanding of metal behaviour during magmatic differentiation of arc-related lavas. To this aim, a review on the partitioning of trace elements between crystal and melts is presented.

2.2 Petrogenesis of arc magmas

Magmatism generated within intra-oceanic island arcs is the result of multiple processes with magmas originating from multiple sources (Hawkesworth & Powell, 1980; Kay, 1984; Arculus & Powell, 1986; Kelemen et al., 2003; Arculus, 1994, 2004; etc.). As a result, most authors typically consider three principle source components: i) Peridotite represented by the depleted mantle wedge located above a subducting slab, ii) Slab fluids derived from hydrated oceanic crust (e.g. metabasalts) and/or from dehydration of partially serpentinised mantle peridotite and iii) Partial melts derived from subducted sediments and or basaltic layer of the subducted oceanic crust.

Volatile-rich slab-derived fluids typically contain significant amounts of Cl and S, mobile large ion lithophile elements (LILE: e.g. K, Rb, Cs, Ca, Sr, Ba and U), and Pb, B and Sb (Tatsumi et al., 1986; Kogiso et al., 1997; Breeding et al., 2004). Since arc magmas are also found to be enriched in these components, this is taken as evidence for aqueous fluid metasomatism of the mantle wedge (Pearce, 1982). Such mantle metasomatism leads to lowering of the peridotite solidus that can promote partial melting (Arculus, 1994). The depths at which the subducting slab dehydrates extend down to ~100 km, as demonstrated by several experimental studies (Ringwood, 1997, Davies & Stevenson, 1992; Rapp & Watson, 1995; Peacock, 1996; Schmidt & Poli, 1998; Poli & Schmidt, 2002; Forneris & Holloway, 2003, Gaetani & Grove, 2003).

Subducted sediments are also a potential source of metasomatism of the mantle wedge. Some authors have argued that water-rich pelitic subducted sediments would undergo partial melting at a lower temperature than basaltic oceanic crust (Hermann & Spandler, 2008). Other authors have suggested that sediment dehydration occurs at depths of ~100 km and that melting will occur at greater depths (Duggen et al., 2007, Dreyer et al., 2010). Nevertheless, Kessel et al., (2005) argue that at greater depths (>6 GPa) the distinction between aqueous fluids and hydrous silicate melts is imprecise, and the fluid may more strictly be defined as a supercritical fluid. Evidence of sediment

contribution to arc magmas comes from i) enrichments in immobile elements (e.g. Th) relative to light rear earth elements (e.g. Th/La) and ii) enrichments of light/middle REE (Johnson & Plank, 1999; Kelement et al., 2003; Plank, 2005). Further evidence for a contribution of sediments comes from the observation that some arc basalts have (high) Th/La indistinguishable to the subducting sediment column, as demonstrated by Plank (2005).

Partial melts derived from melting of the oceanic slab (i.e. basaltic crust) in the presence of garnet (i.e. under eclogite- or amphibolite-facies conditions) will result in arc magmas with characteristic trace element signatures [i.e. high Sr/Y and high La/Yb, low heavy rare earth element (HREE) and Y concentrations, and unradiogenic Sr isotope ratios ($^{87}Sr/^{86}Sr$ <0.7040) (see reviews by Deffant & Drummond, 1990; Rapp et al., 1991, Rapp & Watson, 1995; Kelemen et al., 2003b, etc)]. The high Sr concentrations reflect the absence of plagioclase at the depth of melting. However, according to most thermodynamic models, melting of the oceanic slab within a subduction zone environment is restricted to young hot crust < 5 m.y. (Peacock et al., 1994). Nevertheless several authors have proposed alternative scenarios that might result in slab melting of older, colder crust, including: i) shallow subduction angle (Gutscher et al., 2000), ii) slab melting at plate margins or slab tears (Yogodzinski et al., 2001; Thorkelson et al., 2005), and iii) where subduction occurs into hot mantle associated with a nearby spreading axis (i.e. "hot subduction", Danyushevsky et al., 2006).

Another characteristic of arc magmas is that Ta and Nb are depleted relative to REE. Given that both high field strength elements (HFSE; including Ta and Nb) and REE are considered to be immobile in aqueous fluids under subduction zone conditions, the most plausible explanation for this fractionation is melt generation in the presence of residual rutile or sphene. This has been suggested to occur under eclogite facies (basalt or sediment; i.e. Elliot et al., 1997; Kelemen et al., 2003a; Audétat & Keppler, 2005).

Arc magmas are also characterised by higher oxidation states than MORB. Oxygen fugacities range within 2 log units of the Ni-NiO buffer, or up to 2 log units above the fayalite-magnetite-quartz buffer (ΔFMQ + 2; Ballhaus, 1993; Brandon & Draper, 1996; Blatter & Carmichael, 1998; Parkinson & Arculus, 1999; Rowe et al., 2009). The means by which arc magmas acquire their relatively high oxidation states are debated. Some authors propose that this is the result of metasomatism of the mantle wedge by fluids derived from altered oceanic crust (Brandon & Drapper, 1996; Mungall, 2002; Kelley & Cottrell, 2009). Alternatively Lee et al. (2005, 2010) proposed that the high oxidation states associated with arc magmas could be the result of shallow level magmatic differentiation processes, and that changes in the redox state of the mantle wedge due to metasomatism (i.e. by oxidized crustal material) is not necessary.

2.3 Metal behaviour during magmatic differentiation of arc-related lavas

Arc and back-arc settings are believed to be the principal environments associated with VMS deposits, porphyry systems and associated epithermal deposits (e.g. Sillitoe, 1973, 2010; Skinner, 1983; Hedenquist & Lowenstern, 1994). However, to date there have been few studies that document the behaviour of economically important metals in arc lavas or in volcanic rocks in general. It is generally

accepted that ore metals in porphyry and related epithermal environments are partitioned from the associated magmas into an exsolving volatile phase upon emplacement in the crust. However there is no broad agreement regarding the importance of the initial metal content of the melt in forming an economically important ore deposit. Some authors argue that in the case of economic porphyry copper mineralisation, neither elevated copper contents nor large volumes of magma are required (Cline and Bodnar, 1991). These authors suggest that a Cl-bearing fluid phase exsolved from magma towards the end of crystallisation can extract enough Cu to form an economic deposit, even when the initial Cu contents are below 100 ppm. Alternatively, Stanton (1994) proposes that some metal-enriched provinces, such as the Iberian Pyrite Belt and the Northern Appalachians, contain vastly more ore than other similar provinces, such as the Lachlan Belt (south-eastern Australia), due to variations of the initial metal content of the parent magmas. Halter et al. (2005) argue that even though metal distribution is controlled by processes at a site of deposition, ore compositions appear to be inherited characteristics from the parent magmas (i.e. Cu/Au ratios).

Of special consideration is the case of giant porphyry copper deposits (i.e. El Teniente, Chile; Bingham Canyon, USA, etc). It is difficult to explain the formation of these deposits by post-magmatic leaching processes alone (i.e. they require leaching of a geologically unreasonable volume of magma). Most of the available isotopic, fluid and melt inclusion evidence points toward the predominance of magma-derived fluids (e.g. Harris et al., 2003; Davidson et al., 2005). Some deposits, however, cannot readily be explained purely by orthomagmatic models of ore formation and require the input of external fluids during the mineralisation processes (e.g. Frikken et al., 2005).

Keith et al. (1997) studied partially decomposed sulphide globules from the Bingham mining district (USA). Their conclusion was that sulphide minerals were re-dissolved into a magmatic hydrothermal phase, which produced the ore fluids responsible for the mineralisation. Similarly, at the Bajo de la Alumbrera Cu-Au porphyry deposit, Argentina, Cu/Au ratios were found to be similar in sulphide melt inclusions, fluid inclusions and bulk ore samples (Ulrich et al., 1999, 2001). More recently, Keller (2008) concluded that the highly oxidized character of arc magmas results in the resorption of pre-existing sulphides and, hence, an increase in the concentration of chalcophile elements in the melt. Similarly, Nadeau et al (2010) proposed that the magmatic hydrothermal fluids responsible for the formation of porphyry and epithermal deposits acquire their metal content due to interactions with sulphide melts.

Jenner et al. (2010) studied lavas from the Pual Ridge (Eastern Manus region of the Manus back-arc basin) that range in composition from basalt to rhyolite, which they believe evolved by fractional crystallisation. Their study suggests that bornite accompanies the appearance of magnetite on the liquidus (at ~60 wt % SiO_2). The amount of magnetite fractionation involved is believed to be sufficient to convert most of the S, originally as sulphate (SO_4^{2-}), to sulphide (S^{2-}) thereby triggering the saturation of a Cu-rich sulphide phase the authors tentatively identified as bornite. The authors further state that this is the critical first step in the enrichment of Cu, Ag and Au in subduction-related settings.

From the above it is clear that understanding the behaviour of ore minerals (i.e. Cu, Zn, Pb, V and Co) during different geological processes (i.e. magmatic differentiation leading to the selective

concentration of metals) is not straightforward. Several factors need to be considered: i) a metal-bearing source region, ii) a mechanism for scavenging metals from the melt phase and partitioning them in another phase (melt/volatile/mineral). Of special importance is the role/composition of the volatile phase (e.g. Cl^-, sulphide phases and CO_2), the crystal/melt & melt/fluid partition coefficients, sulphur saturation and the oxidation state of arc magmas, iii) a mechanism for concentrating and retaining the metal-enriched phase within a given area. The latter is mostly controlled by late-stage magmatic and shallow crustal processes.

2.3.1 The significance of sulphide saturation for chalcophile element behaviour

It is generally understood that chalcophile and siderophile elements are highly compatible in immiscible sulphide liquids, and that these liquids form at some point in response to fractional crystallisation of silicate melts (Campbell & Naldrett, 1979; Peach et al., 1990; Jugo et al., 1999). In normal arc settings, it is therefore essential that, in order to form magmatic hydrothermal ore deposits, sulphide saturation does not occur prior to exsolution of a volatile phase (Candela, 1989b; Richards & Kerrich, 1993; Candela & Piccoli, 1995, 2005; etc). In the case of reduced basaltic melts (i.e. MORB), extensive formation of magmatic sulphides occurs during differentiation, which leads to a rapid decrease in chalcophile and siderophile elements in residual silicate melt (Czamanske & Moore, 1977; Doe, 1994, 1995, etc). As outlined in Section 2.2, arc magmas are more oxidized relative to average MORB, hence sulphur is predominantly present in the melt as sulphate (SO_4^{-2}) rather than sulphide (S^{2-}) (Carroll & Rutherford, 1985; Metrich & Clocchiatti, 1996). In these magmas, Cu and other chalcophile elements will be retained in the melt due to the lack of sulphide formation, which will lead to their progressive enrichment in the silicate melt during differentiation. However, the presence of sparse sulphide inclusions in silicate phenocrysts in arc volcanic rocks and lower crustal arc cumulates suggests that sulphide saturation does occur at some point during evolution of arc magmas (e.g. Hattori, 1997; Stavast et al., 2006; Jenner et al., 2010; Li & Audédat 2012; etc.). Oxygen fugacities in arc magmas range within 2 log units of Ni-NiO buffer, or up to 2 log units above the fayalite-magnetite-quartz buffer (ΔFMQ + 2; Ballhaus, 1993; Brandon & Draper, 1996; Blatter & Carmichael, 1998; Parkinson & Arculus, 1999; Rowe et al., 2009).Li & Audédat (2012) carried out a series of high pressure experiments in order to determine which sulphide phase can be expected to separate from arc magmas, and to calculate partition coefficients between monosulphide solid solution (MSS), sulphide liquid (SL) and silicates melts. These authors have suggested that MSS is likely to be the dominant sulphide phase to precipitate from arc magmas. Conversely, Tomkins & Mavrogenes (2003) proposed that small sulphide droplets or crystals may be entrained in the magmas during their ascent through the crust (i.e. xenocrysts and or xenomelts).

To date, there is no consensus regarding the exact role of magmatic sulphides. Some authors argue that pre-concentration of ore metals in magmatic sulphides is an important first step in porphyry metallogenesis (e.g. Richards et al., 2009; Jenner et al., 2010). Other authors have proposed that direct partitioning from the silicate melt to an exsolving hydrothermal fluid is the critical mechanism for metal concentration in magmatic-hydrothermal systems (e.g. Cline & Bodnar, 1991; Cline, 1995, Candela & Piccoli, 2005; Sun et al., 2004b; etc.).

2.3.2 The significance of partitioning of metals into exsolving hydrothermal fluids

Subduction-related magmas are commonly rich in water and other volatile elements (Johnson et al., 1994; Arculus, 2004). Since water solubility is proportional to pressure, on ascent, decreasing pressure will lead the exsolution of a H_2O-rich magmatic fluid. This is corroborated by several melt and fluid inclusion studies (e.g. Stix & Layne, 1996; Wallace et al., 1999, Webster & De Vivo, 2002; Webster et al., 2003, 2005; Webster, 2004). The onset of exsolution is believed to start relatively early during evolution of arc magmas, where the quantity of fluid increases, progressively as crystallization occurs and/or during magma ascent and cooling (Blundy et al., 2001; Wallace et al, 2005). The composition of the exsolved magmatic fluid depends largely on depth and the magma composition (i.e. alkali content and initial magmatic Cl/H_2O ratio; Cline & Bodnar, 1991; Webster, 1992; Candela & Piccoli, 2005, Webster, 2004). If the fluid is exsolved at depth (~5–10 km) this is likely to be a single-phase supercritical fluid (Burham, 1997; Norton & Dutrow, 2001; Coumou et al., 2008). This will be an aqueous-dominated fluid containing additional CO_2, NaCl, KCl, HCl, sulphur species and metal chlorides (Arculus, 2004; Richards, 2011). Conversely, if the exsolution of a volatile phase occurs at shallow level, this is likely to be in the form of a two-phase vapour-liquid (i.e. a low salinity vapour and high salinity brine). Some authors have proposed that the vapour phase will transport certain ore metals more efficiently than the denser and more viscous saline brine (e.g. Henley & McNabb, 1978; Lewis & Lowell, 2009).

The partitioning behaviour of Cl and sulphur species is of particular importance as these are key ligands for metals in fluid phases (e.g. Candela, 1989a; Candela & Holland, 1986; Candela & Piccoli, 2005; Audédat et al., 2008, Zajacz et al., 2008; Simon & Ripley, 2011). A number of factors are thought to control the solubility of sulphur and chlorine in a silicate melt including, melt composition, temperature and pressure. For chlorine, the largest influence is melt composition (e.g. Cl/H_2O ratios; Webster, 2004), though Na and Fe contents also affect its solubility. Increasing Fe and Na increases Cl solubility in a melt (Webster & De Vivo, 2002). Similarly, Zajacz et al. (2010) found that decreasing the $FeO/(K_2O+Na_2O)$ and increasing K_2O/Na_2O ratios leads to increases in both D_{Cl} and D_S fluid/melt. Melt composition (i.e. FeO and SiO_2 contents) also exerts a marked influence in S solubility in silicate melts and its partitioning between melt and fluids. It is broadly accepted that sulphur solubility is higher in mafic and intermediate melts than in granitic ones (e.g. Carroll & Rutherford, 1985; Botcharnikov et al., 2004, Liu et al., 2007; etc.). More recently, Webster et al. (2009) found that D_{Cl} and D_S fluid/melt increase with increasing Cl and S in the system and that Cl more readily partitions into the fluid phase in presence of S. Decreasing temperature decreases S, and to lesser extent, Cl solubility (Carroll & Webster, 1994). Pressure is thought to have a strong effect on solubility of Cl and S in a silicate melt; both decrease with decreasing pressure (Scaillet & Pichavant, 2003; Webster et al., 2009). Traditionally, it has been suggested that the solubility of chalcophile elements in an exsolved fluid phase is due mainly to the formation of chloride complexes. More recently however, Simon et al. (2006), Seo et al. (2009) and Zajacz et al. (2008, 2011) propose that the solubilities of Au and Cu in magmatic volatiles are enhanced by the presence of sulphide species and not by chloride

complexes alone. Ultimately, the presence of chloride and sulphur species will exert a greater control on the formation of metal complexes than whether the fluid is a single-phase supercritical fluid or a two-phase vapour-liquid fluid (Klemm et al., 2007; William-Jones & Heinrich, 2005).

2.4 Review of trace element partitioning between crystals and melts

In order to constrain metal enrichment/depletion processes it is necessary to understand element partitioning behaviour between crystals and silicate melts. One way to achieve this is to investigate the changes in mineral-melt partition coefficient values (D, the ratio of the concentration of an element in the solid phase divided by its concentration in the equilibrium melt) during different stages of evolution of arc-lava suites.

2.4.1 Selection of partition coefficients for petrological modelling

Although more data have become available in the last 20 years with the development of spatially resolved, in-situ micro-analytical techniques based on mass spectrometry, which allow better precision and better detection limits, there is not a comprehensive understanding of trace element partitioning and how the intensive parameters affect this partitioning. Some authors attribute the variations of Ds predominantly to variations in crystal compositions (e.g. Blundy & Wood, 1994 and 2003b; Wood & Blundy, 1997, 2001, 2002, 2003) while others state that D variations are due mainly to changes in temperature and melt composition (e.g. Nielsen, 1985; Nielsen & Drake, 1979).

In order to select appropriate D values for the element used for modelling, it is necessary to be aware of how D values change with parameters such as pressure, temperature, fO_2 and mineral and melt composition. In general, there are two parallel options to get the correct partition coefficients to model a certain geochemical processes: i) to choose a set of D values from experimental determination done at the same physical conditions (i.e. pressure and temperature, etc) and/or on the basis of the melt of composition being “similar” to the magmatic suite being investigated; ii) To use one of the available theoretical models that predict trace element partitioning (e.g. the lattice strain model, Blundy and Wood; 1994) to calculate D values. In reality, the first approach is problematic because it is unlikely to find a set of partition coefficients for all elements of interest from an experiment that would match the exact conditions of pressure, temperature and composition presented by a natural sample set. Additionally, few bulk compositions have been studied in enough detail, so the variation of Ds with changing pressure, temperature and composition would still not be accounted for. These effects are to some extent interdependent, which results in most approaches being partly empirical or ultimately only accurate for processes that are isobaric and isothermal. Furthermore, geochemical modelling of fractional crystallisation requires knowledge of partitioning at different stages of fractionation. Therefore it is not appropriate to assume that a certain D is constant because significant compositional effects during fractional crystallisation will be ignored. This in turn will lead to misinterpretations about the roles played by the different phases crystallising or in equilibrium with the silicate melt (Blundy & Wood, 1991).

Given that the final goal of this study is to model the behaviour of metals during fractional crystallisation, it is essential to choose appropriate D values for the different stages of magma

evolution. Although several experimental and natural studies can be found in the literature, which report trace element contents in plagioclase, clinopyroxene, olivine, magnetite and amphibole determined by micro-analytical techniques, it was not possible to use a set of Ds that would allow us to model crystallisation processes in our rock suites. In order to compare the measured D values obtained during this thesis using LA-ICP-MS, two different approaches to determine D were chosen based on theoretical studies/models that predict trace element partitioning: i) The lattice strain models after Brice (1975) and Blundy & Wood (1994) and ii) the parameterisation method of Bédard (2005 and 2007). The results of these calculations are compared to measured values and are presented in Table 5.5 of Chapter 5.

It is worth noting that, due to the LA-ICP-MS capability to determine extremely low abundance elements in different materials, this technique has been used successfully in the determination of trace element concentrations in silicate minerals and natural glasses during the last two decades. This has been shown by several natural experimental studies (e.g. Jeffries et al., 1995; Foley et al., 1996; Gregoire et al., 1999; Sattari and Brenan, 2002; Brenan et al., 2003, 2005; Bea et al., 2006; Jochum et al., 2006; Guillong et al., 2007; Bouhifd et al., 2013; etc).

2.4.2 The lattice strain model (LSM)

The lattice strain model of Blundy & Wood (1994) is based in the Brice model (1975) that postulates that the principal factor controlling the incorporation of a cation that is too large to fit into a lattice site is the elastic strain energy required to displace the surrounding atoms. The Blundy & Wood (1994) expression is:

$$Di = D_{0*} \exp\left(-4\pi E N_A\left((r_0/2)(r_i - r_0)^2 + 1/3\,(r_i - r_0)^3\right)/RT\right)$$

Where D_0 is the strain compensated partition coefficient, r_0 is the ionic radius of the cation of interest, r_i is the radius of the substituent cation, E is the Young's modulus of the host site, N_A is the Avogadro's number; R is the gas constant and T is temperature in Kelvin degrees.

The elastic strain energy is inversely correlated with the logarithm of the partition coefficient (log D), which for a specific lattice site follows a semi-parabola distribution as a function of the ionic radius (Onuma et al., 1968). The optimum radius, (i.e. that for which D is largest), is close to the ionic radius of the host cation.

The LSM suggests that because crystals are characterised by a regular arrangement of ions in relatively rigid lattices, they are less tolerant to accommodating misfit cations than silicate melts which have disordered and flexible structures. Thus no melt composition-related term appears in their equation.

Blundy & Wood (1994) and Wood & Blundy (2001) found that, in the case of homovalent substitution (i.e. where trace ion and host ion have the same charge) E_M^{2+} and E_M^{1+} in plagioclase lie close to the bulk crystal Young's moduli for anorthite and albite respectively, while E_{M2}^{2+} in clinopyroxene was similar to the bulk crystal Young's modulus of diopside. Blundy & Dalton (2000) found that for plagioclase and clinopyroxene the partitioning parabola becomes tighter (E_M^{n+} increases) and is displaced to lower $r_{0(M)}^{n+}$ as charge increases.

Blundy & Wood (1994) and Wood & Blundy (1997) also found that values for the optimum site radius, $r_{0(M)}^{n+}$, are not the same as the radius of the cation normally resident at the site of interest. For example, for clinopyroxene $r_{0(M2)}^{2+}$ is slightly smaller than the radius of Ca^{2+}, the ion which normally occupies that site. They proposed that $r_{0(M)}^{n+}$ is closely related to the known metal-oxygen bond lengths (dM-O) in the host minerals, taken to be 1.38Å (Shannon, 1976), i.e. dM-O = $r_{0(M)}^{n+}$ + 1.38 Å. Additionally, Blundy and Wood (2002) observed a decrease in $r0^{n+}_{(M)}$ with charge and suggested that a highly charged cation (i.e. net positive charge at the site of interest) draws in the oxygen anions reducing the optimum radius, with $r0^{n+}_{(M)}$ being nearly constant at high charge of the site. Contrarily, a low-charged cation (with net negative charge) repels the oxygens, thus increasing the optimum radius of the site.

Blundy et al. (1996) concluded that D_0 (the strain-compensated partition coefficient) depends on activity-composition relationships in both crystal and melt phases, and might be sensitive to melt composition as well as to pressure and temperature. Similarly, Hill et al. (2011) found that partition coefficients for cations with charge greater than 2^+ decrease as a result of increasing P and T. These findings further corroborate a dependence of clinopyroxene-melt partitioning on pressure and temperature.

Blundy & Wood (1994, 2003a, b) and Wood & Blundy (1997, 2001, 2003) used the LSM to rationalise a large data set of lanthanide, yttrium and other elements partition coefficients for a range of minerals. They obtained values of D_0, $r_0$and E for several hundred experiments and then parameterised them as a function of chemical composition (of the melt and crystals), P and T. Their approach has been used to calculate Ds for REE, Y and when applicable for the metals of interest for this study.

For elements partitioning into clinopyroxene, the majority of the elements that we studied are 3^+ ions (i.e. REE, Y, V and Sc) or 2^+ ions (Sr, Ba, Cu, Zn, Co and Pb), with the exception of copper which could also be 1^+. These elements are thought to partition mostly into the M2 clinopyroxene site (Blundy & Wood 1994, 2003a, b; Wood & Blundy 1997, 2001, 2004; Hill et al., 2011). The equations used for D clinopyroxene/melt calculations can be found in Wood & Blundy (2003) and Hill et al., (2011).

Plagioclase has only one single large cation site (M) into which all the elements that we studied partition. This site is normally occupied by Ca and Na. Equations used for the calculation of D_{Ba} and D_{Sr} can be found in Blundy & Wood (1991). Equations to calculate Ds for REE and metals of interest can be found in Wood & Blundy (2003). However, because the parameters for 3^+ cations (e.g. REE) are difficult to derive due to $r_0^{3+}{}_{(M)}$ values being larger than La^{3+} (Wood & Blundy 2003 and references therein) we have not used the obtained values for our geochemical modelling. These authors also do not recommend using their equations for cations with lone pair of electrons (i.e. Pb).

Olivine has two octahedral sites (M1 and M2) but because they have a similar size and geometry, most authors refer to it simply as M site. The equations used to calculate Ds for 1^+, 2^+ and 3^+ cations can be found in Wood & Blundy (2004). While using the equations to calculate Ds for 1^+ and 3^+ D_{Li} values in the range of 0.3–0.5 and D_{Sc} values of 0.1–0.2 have been assumed, as recommended by the authors. Currently there are no LSM formulations to predict element partitioning into magnetite.

2.4.3 Parameterisation method of Bédard

The parameterisation method is a semi-empirical approach that provides mathematical expressions for changes in the D values for a range of elements (e.g. REE and HFSE)that partition into olivine (Bédard, 2005) and orthopyroxene (Bédard, 2007). The author compiled a large amount of published natural and experimental D values for olivine and orthopyroxene with the aim of examining covariations of D with pressure, temperature, and changes in melt and mineral compositions. An advantage of this method would be that it provides a large compilation of natural and experimental mineral/melt partitioning studies, which allows a wide range of intensive parameters to be taken into account. Nevertheless, it would also provide several sources of error and uncertainties.

Given that modelling for orthopyroxene is not necessary for this study, the following section will only review the work of Bédard (2005) which studies element partitioning between olivine and silicate melt.

Bédard (2005) found that titanium was the element with most reported D values and used this advantage to constrain the different effects that changes in temperature, pressure, H_2O, olivine Fo, MgO and SiO_2 content of the melt have on element partitioning. After calculating regressions for all the parameters mentioned above, Bédard (2005) found that regressions against both MgO content of the melt and temperature yielded reasonable trends. However, he suggested that MgO would provide more practical correlations as MgO contents can be calculated from microprobe mineral analyses whereas temperature is difficult to deduce in natural systems. Consequently, the MgO content of the melt was used to parameterise Ds for all trace elements.

Bédard (2005) also compares his $D^{olivine/liquid}$ regressions to calculations using the lattice strain model of Blundy and Wood (1994). He found that using a constant r_0 value of 0.807Å, MgO shows good correlation with D_0 and $E_M{}^{3+}$. This suggests that it is possible to use the parameterisation equations in conjunction with the LSM to calculate D for most 3^+ cations (e.g. Sc and REE).

The equations listed in Table 2 of Bédard (2005) have been used to calculate Ds for all the elements of interest for this study. Additionally, Jean Bédard provided us with a number of regression equations to calculate Ds for Cu and Zn partitioning into clinopyroxene, plagioclase and magnetite. The results of these calculations are presented in Table 2.1 along with the results obtained by using the lattice strain model of Blundy & Wood (1994).

2.4.4 Metal partitioning behaviour between magnetite and silicate melts.

Magnetite is an important crystallising phase during differentiation of island arc rocks, therefore understanding metal partitioning into magnetite is important to constrain the behaviour of metals during fractional crystallisation of these magma types. Unfortunately, very little magnetite/melt partitioning data have been published to date and it was also not possible to calculate Ds (for most elements partitioning into magnetite) using either of the above described theoretical models. Two studies have been found that report partitioning data between magnetite and silicate melts relevant for this study.

Nielsen et al. (1994) reports experimental D values for HFSE, Sc, and V, amongst other elements, between magnetite-rich spinels and a range of mafic to intermediate composition silicate melts. The

authors found a mildly positive correlation between D_{Sc} and increasing Ti content of magnetite, and a negative correlation of D_V with D_{Ti}. Reported values of D_{Sc} varies between 0.67–5.76 and D_V between 0.02–6.85. However, these authors further state that their experiments did not provide sufficient details about V partitioning and their results are most likely to be applicable in low fO_2 systems. Hanger (2009) analysed two magnetite-bearing samples containing 67 and 68 wt% SiO_2, and reported strong partitioning of Mn and Zn into the oxide phase with D values up to 30 for Mn and up to 100 for Zn.

Though magnetite/melt partitioning data are sparse, element partitioning into this oxide phase cannot be ignored when modelling fractional crystallisation processes. In order to accurately model the partitioning behaviour of metals, we use $D^{magnetite/melt}$ values measured during this study. Partition coefficients for Cu, Zn, V, Pb, Co and Sc between magnetite and host magma were calculated from LA-ICP-MS and microprobe analyses (magnetite grains and glass) in samples with an MgO range from 0.4 wt% to 2.3 wt%. From this, the D values were extrapolated for magmas up to 5.0 wt% MgO. For comparison purposes (where available), modelling was also conducted using D values obtained by the parameterisation method of Bédard (i.e. for Cu and Zn).

2.5 Summary

Table 2.1 summarises the D values obtained by using the lattice strain model after Blundy & Wood (1994) and the parameterisation of Bédard (2005). Selected D values are compared in Figures 2.1-2.3 with the measured values obtained from LA-ICP-MS measurements (see Chapters 5 and 6 for details about the methodology).

Table 2.1. Olivine-clinopyroxene-plagioclase-magnetite/melt partition coefficients for a range of trace elements calculated using the LSM model of Blundy & Wood (1994), and for selected elements (where equations are available) using the parameterisation method of Bédard (2005).

Olivine		**Ds using LSM**				**Ds using Parameterisation**		
Fo #	88	84	81	79	88	84	81	78
MgO melt	8.35	6.12	5.21	2.41	8.35	6.12	5.21	2.41
D Cu	0.40	0.40	0.40	0.39	0.06	0.06	0.07	0.08
D Zn	5.12	6.35	6.72	8.31	1.33	1.65	1.84	3.06
D V	0.15	0.15	0.15	0.15	-	-	-	-
D Co	5.08	6.30	6.67	8.25	3.89	5.15	5.96	11.79
D Sc		0.1-0.2			0.01	0.02	0.04	0.19
Clinopyroxene		**Ds using LSM**				**Ds using Parameterisation**		
Cpx Mg#	90	85	83	75	90	85	83	75
MgO melt	8.35	6.12	5.21	2.41	8.35	6.12	5.21	2.41
D La	0.12	0.14	0.13	0.14	-	-	-	-
D Ce	0.18	0.21	0.21	0.23	-	-	-	-
D Nd	0.35	0.42	0.42	0.47	-	-	-	-
D Sm	0.51	0.63	0.63	0.71	-	-	-	-
D Eu	0.56	0.71	0.70	0.80	-	-	-	-
D Gd	0.61	0.77	0.76	0.87	-	-	-	-
D Dy	0.64	0.81	0.81	0.93	-	-	-	-
D Er	0.60	0.77	0.77	0.88	-	-	-	-
D Yb	0.54	0.69	0.68	0.78	-	-	-	-
D Lu	0.50	0.64	0.64	0.72	-	-	-	-
D Y	0.63	0.81	0.80	0.92	-	-	-	-
D Cu	0.00	0.00	0.00	0.00	0.03	0.04	0.05	0.02
D Zn	-	-	-	-	0.71	0.77	0.83	1.35
D Zr	0.23	0.25	0.27	0.20	-	-	-	-
D Hf	0.40	0.46	0.49	0.34	-	-	-	-
D Ti	0.50	0.53	0.54	0.47	-	-	-	-
Plagioclase		**Ds using LSM**				**Ds using Parameterisation**		
An #	87	85	70	31	87	85	70	31
MgO melt	8.35	6.12	5.21	2.41	8.35	6.12	5.21	2.41
D La	0.14	0.14	0.16	0.22	-	-	-	-
D Ce	0.13	0.13	0.15	0.20	-	-	-	-
D Nd	0.10	0.10	0.11	0.15	-	-	-	-
D Sm	0.07	0.07	0.07	0.10	-	-	-	-
D Eu	0.06	0.06	0.06	0.08	-	-	-	-
D Gd	0.04	0.04	0.04	0.06	-	-	-	-
D Dy	0.03	0.03	0.03	0.04	-	-	-	-
D Er	0.01	0.01	0.01	0.02	-	-	-	-
D Yb	0.01	0.01	0.01	0.01	-	-	-	-
D Lu	0.01	0.01	0.01	0.01	-	-	-	-
D Y	0.02	0.02	0.02	0.03	-	-	-	-
D Cu	0.57	0.58	0.65	0.90	0.01	0.03	0.01	0.80
D Zn	-	-	-	-	0.05	0.06	0.07	0.19
D V	0.00	0.00	0.00	0.00	-	-	-	-
D Pb	0.08	0.09	0.21	1.84	-	-	-	-
D Co	-	-	-	-	-	-	-	-
D Sc	0.00	0.00	0.00	0.00	-	-	-	-
D Sr	1.38	1.44	2.12	5.86	-	-	-	-
D Ba	0.13	0.13	0.22	0.84	-	-	-	-
Magnetite	**Ds using Parameterisation**							
MgO melt	2.71	0.30	0.27					
D Cu		1.4						
D Zn	15.6 - 16.0	26.5 - 32.7	26.7 - 31.2					

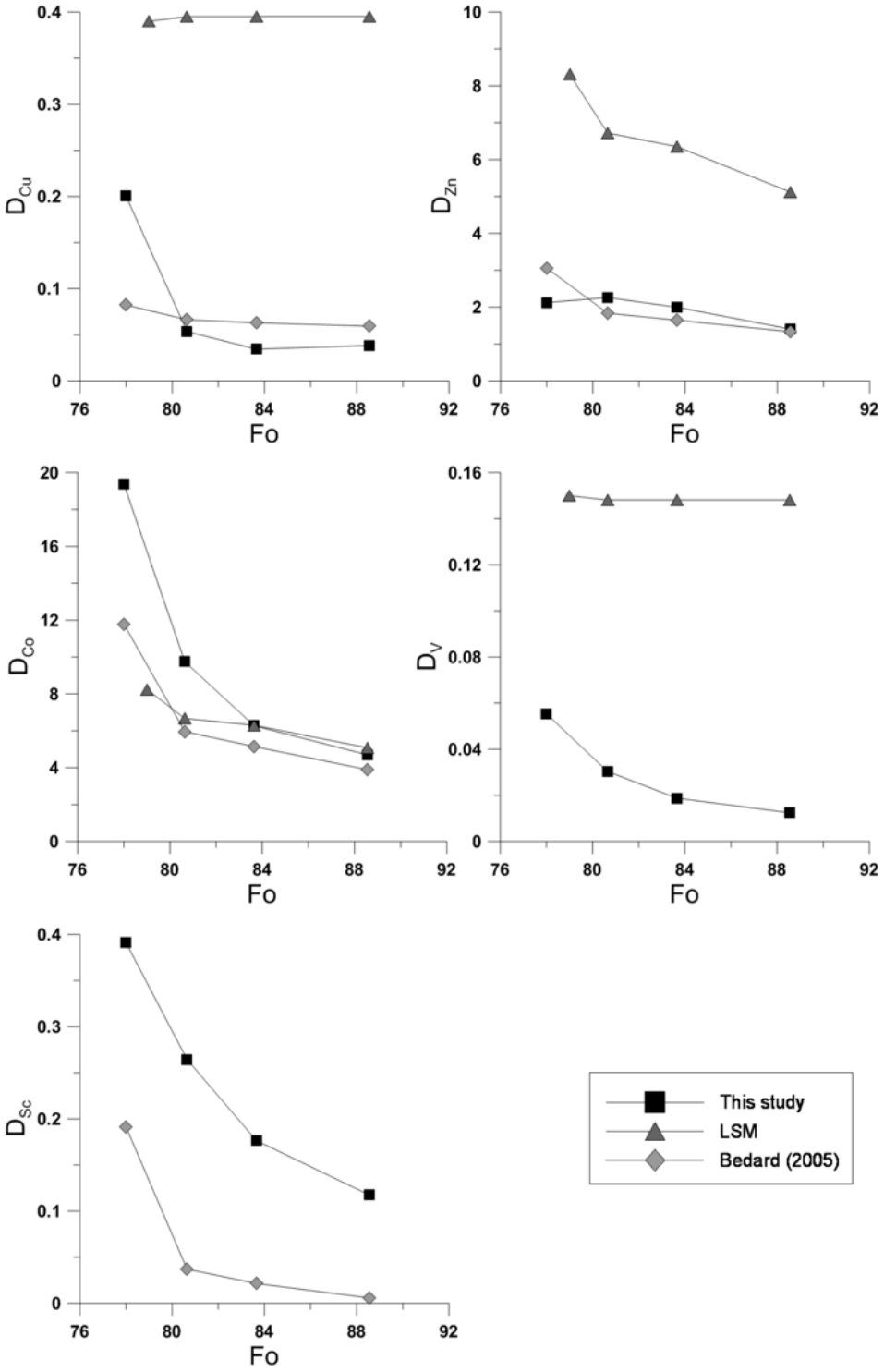

Fig. 2.1. Partition coefficients for Cu, Zn, Co, V and Sc as a function of Fo. LSM is the method of Blundy & Wood (1994).

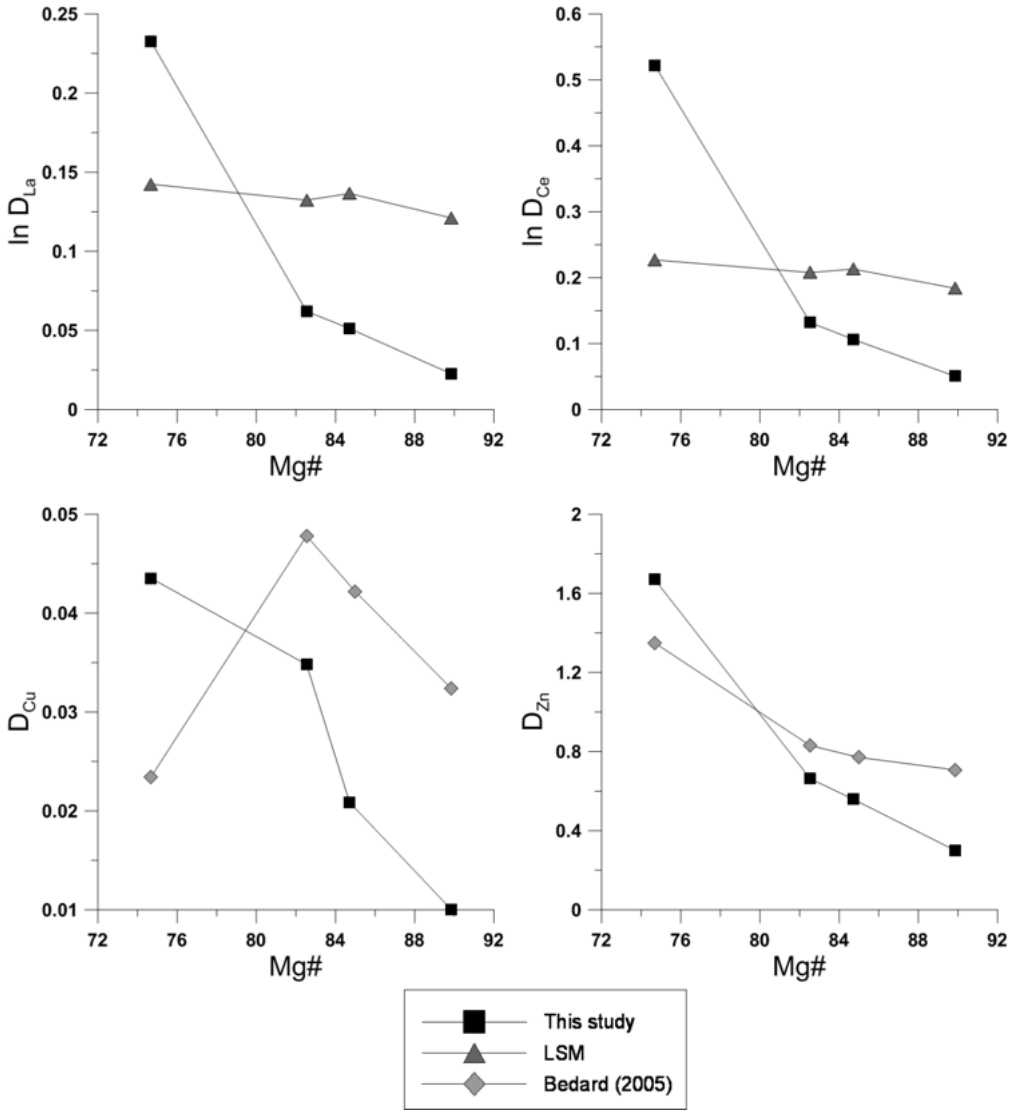

Fig. 2.2. Partition coefficients for La, Ce, Cu, and Zn in clinopyroxene as a function of Mg#. LSM is the method of Blundy & Wood (1994).

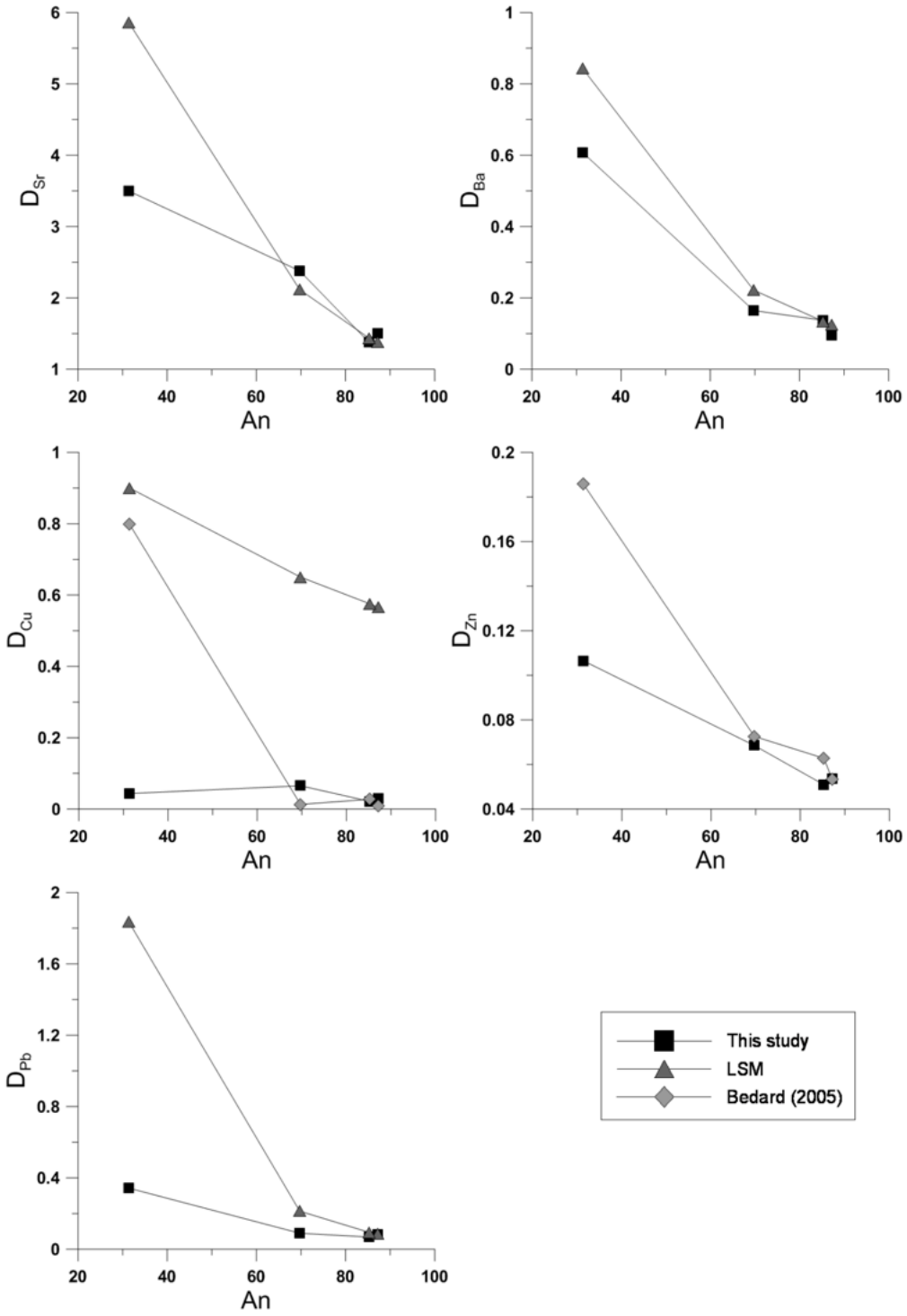

Fig. 2.3. Partition coefficients for Sr, Ba, Cu, Zn and Pb in plagioclase as a function of An. LSM is the method of Blundy & Wood (1994).

Chapter 3

Sample preparation, analytical methods and data processing

3.1 Sample preparation

Laboratory work described in the following section relates to 60 volcanic rocks recovered from 10 dredges (see Figs 1.3, 1.4). These comprise vesicular, mostly phyric, rocks (including pillows) many with glassy rims of variable thickness. The majority of the samples are fresh, although a small number are slightly to moderately altered.

Polished thin sections were prepared from all the rocks to allow detailed petrographic observations.

Whole-rock analyses were carried out using X-ray fluorescence (XRF). Low-level element analyses on thirty-three representative samples were obtained by inductively coupled plasma mass spectrometry (ICP-MS). Mineral, phenocryst and groundmass analyses on thirty nine representative samples were acquired from polished thin sections by electron microprobe. From these samples, polished grain mounts of mineral separates (phenocrysts), together with their co-existing groundmass and glass, on eighteen samples, were prepared and analysed by laser ablation-inductively coupled plasma mass spectrometry (LA-ICP-MS). Mineral separates were prepared by crushing and sieving before careful hand picking under a binocular microscope. Where fresh glassy rims were present, these were carefully chiselled off and mounted in epoxy. Table 3.1 summarises all the studied rocks and analyses performed on them during this work.

Details on each individual technique, including operating parameters and standardisation are given below.

3.2 Analytical methods and data processing

3.2.1 Electron microprobe (EMP).

A Cameca SX100 electron microprobe based at the Central Science Laboratory (CSL), University of Tasmania, was used to analyse major elements (Na, Mg, Al, Si, Ca, K, Fe, Ti, Cr and P) and volatiles (S and Cl) in glasses, groundmass and phenocrysts (olivine, pyroxenes, plagioclase, amphibole, and oxides) on polished thin sections and grain mounts.

International standards from Jarosewich et al. (1980) were run at the beginning and at the end of each analytical session (a total of 6 spots per mineral). These include: USNM 111240/2 (Juan de Fuca basaltic glass ‘VG2’), USNM 122142 (Kakannui – augite), USNM 115900 (Lake County – plagioclase), USNM 111312/444 (San Carlos – olivine), USNM 143965 (Kakannui – hornblende), USNM 104021 (Durango – apatite) and USNM 117075 (Tiebaghi mine – chromite).

The following conditions were used:

- Silicates were analysed at 15kV, 20nA with beam sizes of 5 or 10μm depending on the phenocrysts size. An average of 15 grains was analysed for each mineral type present in a sample,

with measurements taken on both core and rims on each grain.

- Glasses were analysed at 15 kV, 20 nA and a beam size of 5 μm with an average of 10 points per sample.
- Groundmasses analyses were carried out at 15 kV, 20 nA with a defocused beam of 20 μm. On average, 10 points per sample were measured.

Analytical standard deviations for major and minor elements are in the order of 0.34–0.02% and 0.36–0.01 % respectively.

Analyses of chlorine and sulphur in glasses and groundmass were performed at 15 kV, 40 nA with a beam size of 10 μm using counting times of 60 and 30 seconds for Cl and S, respectively. Tugtupite was used as the standard for chlorine and Marcasite for sulphur. Detection limits for Cl and S are 24 ppm and 285 ppm respectively with a standard deviation in the order of 0.02–0.04%. Analyses of zinc in magnetite were performed at 20 kV, 40nA with a beam size of 5 μm using a counting time of 60 seconds to assure high precision. The detection limit for Zn is 50 ppm at 1 sigma precision. Gahnite was used as the standard for Zn.

3.2.2. X-Ray Fluorescence (XRF)

Whole-rock major and trace element analyses on glasses were performed at CODES, the University of Tasmania using a Philips PW1480 X-Ray Spectrometer.

Major elements concentrations are determined on glass discs made by fusing a small amount (~1 g) of powdered rock at 1100 C° diluted with lithium metaborate and tetraborate fluxes. Trace element concentrations were obtained by analyses of pressed pellets composed of 10 grams rock powder mixed with a binder (see Robinson, 2003 for details regarding the method and Watson et al., 1996 for more information regarding sample preparation).

3.2.3 Solution Inductively Coupled Plasma Mass Spectrometry (ICP-MS)

Whole-rock trace element analyses were obtained by solution ICP-MS at CODES, the University of Tasmania on an Agilent 7700 X Series quadrupole mass spectrometer.

Samples were dissolved by a high pressure acid digestion on a PicoTrace unit using a combination of sulphuric, hydrofluoric ($HF–H_2SO_4$) and perchloric ($HClO_4$) acids. This dissolves all resistant (accessory) minerals such as zircon in silica rocks. After evaporation, samples are dissolved in 2% nitric acid (HNO_3). International standards AGV-1 and GSD-12 were run and also “in-house” standard TASBAS (basalt) and TASGRAN (granite). See Yu et al. (2001) for details regarding this method.

3.2.4 Laser Ablation Inductively Coupled Plasma Mass Spectrometry (LA-ICPMS)

A Resolution 193nm excimer laser ablation system coupled to an Agilent7500cs Series quadrupole mass-spectrometer at CODES, University of Tasmania, was used to measure trace element abundances in glasses, groundmass and phenocrysts (olivine, pyroxenes, plagioclase, amphibole, and magnetite).

The following elements were measured: ^{7}Li, ^{23}Na, ^{25}Mg, ^{27}Al, ^{29}Si, ^{39}K, ^{43}Ca, ^{45}Sc, ^{47}Ti, ^{51}V, ^{53}Cr, ^{55}Mn, ^{57}Fe, ^{59}Co, ^{62}Ni, ^{63}Cu, ^{65}Cu, ^{66}Zn, ^{69}Ga, ^{71}Ga, ^{88}Sr, ^{89}Y, ^{90}Zr, ^{91}Zr, ^{95}Mo, ^{97}Mo, ^{98}Mo, ^{102}Ru, ^{107}Ag, ^{111}Cd, ^{118}Sn, ^{137}Ba, ^{139}La, ^{140}Ce, ^{146}Nd, ^{147}Sm, ^{153}Eu, ^{157}Gd, ^{163}Dy, ^{166}Er, ^{172}Yb, ^{175}Lu, ^{178}Hf, ^{197}Au, ^{202}Hg, ^{208}Pb,^{209}Bi, ^{232}Th and ^{238}U.

Zircon and tantalite were used to monitor for isotopic interferences for TaO on ^{197}Au and HfOH on ^{197}Au. No corrections were found to be necessary.

Data acquisition for elements other than Au, Ag, Bi in phenocrysts, were performed using a 30 second background with 60 seconds of acquisition. Spot sizes of 120–80 µm-diameter and 10 Hz laser pulsing rate were used. A separate method was developed for key, extremely low abundance elements, Au, Ag and Bi, employing longer counting times and larger spot sizes of 150–120 µm. Glasses and groundmass were analysed using spot sizes of 80 and 110 µm-diameter respectively and 10 Hz.

NIST SRM 612 glass was used as the primary calibration standar and GSD-1G glass as the secondary standard (Table 3.2). Both primary and secondary standards were analysed at the beginning and end of each batch to correct for instrument drift. Data from each session were normalized to GSD-1G to compensate for instrument variability. Values for NIST SRM 612 and GSD-1G are from the GeoReM website (Jochum and Stoll, 2008) and listed in Table 3.2.

MgO wt% concentrations derived by EMP were used as the internal calibration for olivine and orthopyroxene, FeO for magnetite and CaO wt% was used for plagioclase, clinopyroxene, amphibole, glasses and groundmass. Data quantification was performed with the SILLS program. SILLS is a MATLAB based program for the reduction of LA-ICP-MS data of homogeneous samples and inclusions (Guillong et al., 2008).

3.2.5 Fourier transform infrared (FTIR) spectroscopy

The water content of selected glasses was measured using a Bruker Opus/IFS 66 spectrometer with an attached optical microscope. Samples were mounted in epoxy and doubly polished. A complete description of the method can be found in Ihinger et al. (1994), and details on the calibration and procedures used in Danyushevsky et al. (1992) and in Dayushevsky et al. (2000).

3.2.6 Data Comparison: EMP vs LA-ICP-MS

Minor element analyses from olivine, clinopyroxene and plagioclase obtained using the electron microprobe are compared to those obtained using LA-ICP-MS. The results are shown in:

- Figure 3.1 for olivine (CaO, MnO and NiO vs Fo).
- Figure 3.2 for clinopyroxene (TiO_2, MnO, Na_2O, and Cr_2O_3 vs Mg#).
- Figure 3.3 for plagioclase (FeO, MgO and K_2O vs An).

The results for both analytical techniques are in close agreement (taking analytical errors into consideration) even though it was not possible to collect data on the exact same position within the minerals being investigated. Minor element data presented in the mineralogy chapter (Chapter 4) were acquired using LA-ICP-MS, since this technique offers higher precision and lower detection limits.

Table 3.1. List of all samples analysed during this study and analyses performed on them.

Voyage	Dredge	Sample	TS*	WR (XRF)	ICP-MS	EMP	LA-ICP-MS	FTIR	Isotopes
SS10/2004	D1	D1-1	X	X	X	X	X	X	
SS10/2004	D1	D1-2	X	X					
SS10/2004	D1	D1-3	X	X		X			
SS10/2004	D8	D8-1	X	X		X	X		
SS10/2004	D8	D8-2	X	X	X				X
SS10/2004	D8	D8-3				X	X	X	
SS10/2004	D11	D11-1	X	X		X			
SS10/2004	D11	D11-2	X	X	X	X	X		X
SS10/2004	D11	D11-6	X	X				X	
SS10/2004	D11	D11-8	X	X	X				
SS10/2004	D12	D12-1	X			X			
SS10/2004	D12	D12-2	X	X					
SS10/2004	D12	D12-3	X	X		X			
SS10/2004	D12	D12-4	X	X		X			
SS10/2004	D12	D12-5	X			X			
SS10/2004	D12	D12-6	X	X					
SS10/2004	D13	D13-2	X	X					
SS10/2004	D13	D13-3	X	X		X			
SS10/2004	D13	D13-4	X	X		X			
SS10/2004	D13	D13-5	X	X		X			
SS10/2004	D13	D13-6	X	X					
SS10/2004	D13	D13-7	X	X					
SS10/2004	D13	D13-8	X	X	X	X	X		
SS10/2004	D13	D13-9	X	X		X			
SS10/2004	D13	D13-11	X	X					
SS10/2004	D13	D13-12	X	X		X			
SS10/2004	D13	D13-13	X	X					
SS10/2004	D15	D15-1	X	X	X	X	X		
SS10/2004	D15	D15-2	X	X	X	X			
SS10/2004	D15	D15-3	X	X	X				
SS10/2004	D15	D15-4	X	X	X	X	X	X	X
SS10/2004	D15	D15-5	X	X	X	X			
SS10/2004	D15	D15-6	X	X	X				
SS10/2004	D15	D15-7	X	X				X	
SS10/2004	D15	D15-7a	X	X	X	X	X	X	X
SS10/2004	D15	D15-8	X	X					
SS03/2009	D67	D67-2	X	X					
SS03/2009	D67	D67-3	X	X		X	X		
SS03/2009	D67	D67-4	X	X	X				
SS03/2009	D67	D67-5	X	X		X	X		

Table 3.1. cont.

Voyage	Dredge	Sample	TS*	WR (XRF)	ICP-MS	EMP	LA-ICP-MS	FTIR	Isotopes
SS03/2009	D67	D67-6	X	X					
SS03/2009	D68	D68-2	X	X	X	X			
SS03/2009	D68	D68-3	X	X					
SS03/2009	D68	D68-4	X	X					
SS03/2009	D68	D68-5	X	X					
SS03/2009	D68	D68-6	X	X	X	X	X		
SS03/2009	D68	D68-7	X	X		X			
SS03/2009	D68	D68-8	X	X	X	X	X		
SS03/2009	D68	D68-9	X	X	X				
SS03/2009	D68	D68-10	X	X		X			
SS03/2009	D68	D68-11	X	X	X				
SS03/2009	D69	D69-2	X	X		X			
SS03/2009	D69	D69-3	X	X	X	X	X		
SS03/2009	D69	D69-4	X	X					
SS03/2009	D69	D69-5	X	X					
SS03/2009	D69	D69-6	X	X	X				
SS03/2009	D69	D69-7	X	X					
SS03/2009	D69	D69-8	X	X					
SS03/2009	D69	D69-9	X	X		X			
SS03/2009	D69	D69-10	X	X	X	X			

* TS - thin section

Table 3.2. List of values for NIST SRM 612 and GSD-1G used for calibration of LA-ICP-MS data after Jochum & Stoll (2008).

Element	NIST SRM 612	GSD-1G	Element	NIST SRM 612	GSD-1G
Li	42.0	43.0	Ag	21.4	23.0
Be	38.0	46.0	Cd	28.3	18.0
B	33.0	50.0	In	37.0	38.0
Na	103704.0	26706.8	Sn	35.6	29.0
Mg	64.0	21709.3	Sb	31.4	43.0
Al	11166.9	73300.8	Cs	42.0	32.0
Si	336114.4	248675.4	Ba	39.7	67.0
P	51.0	860.0	La	35.8	39.1
S	350.0		Ce	38.7	41.4
K	66.3	25300.0	Pr	37.2	45.0
Ca	85263.8	51456.6	Nd	35.9	44.7
Sc	41.0	52.0	Sm	38.1	47.8
Ti	44.0	7431.9	Eu	35.0	41.0
V	39.0	44.0	Gd	36.7	50.7
Cr	36.0	42.0	Tb	36.0	47.0
Mn	38.0	220.0	Dy	36.0	51.2
Fe	51.0	103381.5	Ho	38.0	49.0
Co	35.0	40.0	Er	38.0	40.1
Ni	38.8	58.0	Tm	38.0	49.0
Cu	37.0	42.0	Yb	39.2	50.9
Zn	38.0	54.0	Lu	37.2	51.5
Ga	36.0	54.0	Hf	37.9	39.0
Ge	38.0	32.0	Ta	35.9	40.0
As	32.6	27.0	W	38.1	43.0
Se	15.0	2.0	Re	6.6	-
Rb	31.4	37.3	Ir	0.0	12.0
Sr	78.4	69.4	Pt	2.5	6.0
Y	38.0	42.0	Au	4.5	4.0
Zr	37.7	42.0	Tl	14.8	0.9
Nb	40.0	42.0	Pb	38.6	50.0
Mo	33.0	39.0	Bi	30.0	35.0
Rh	0.9	-	Th	37.8	41.0
Pd	1.1	-	U	37.4	41.0

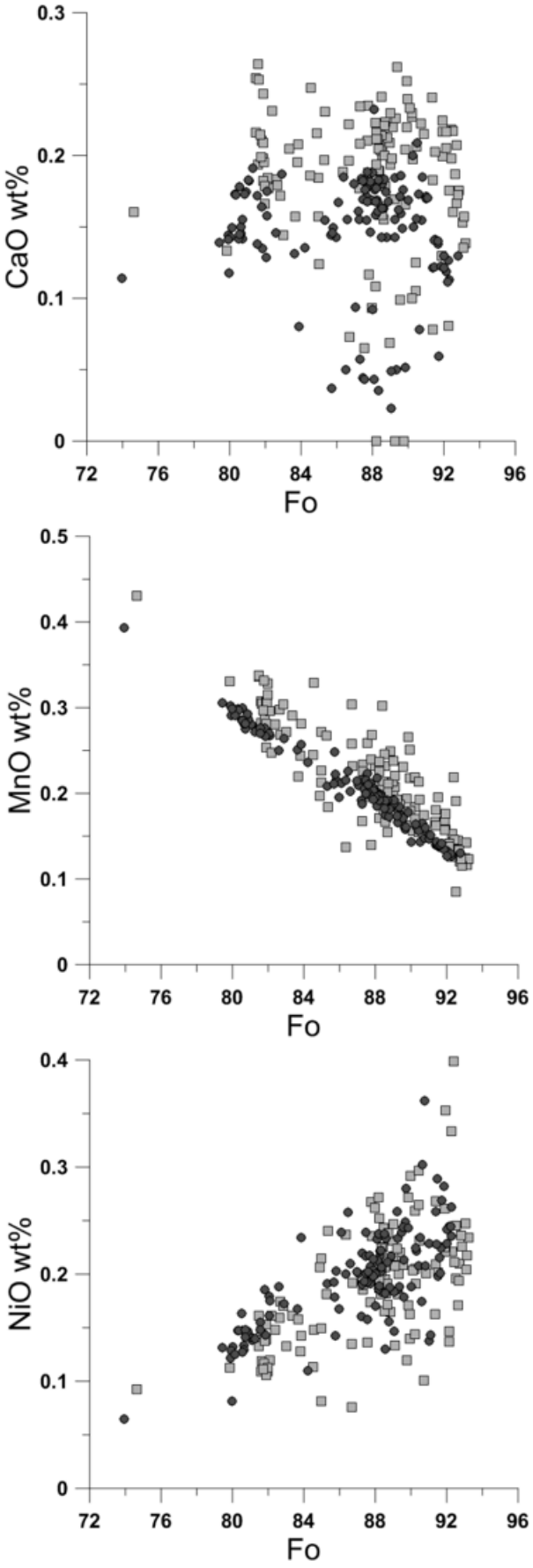

Fig. 3.1. Data comparison for minor element analyses from olivine: EMP (squares) vs LA-ICP-MS (circles).

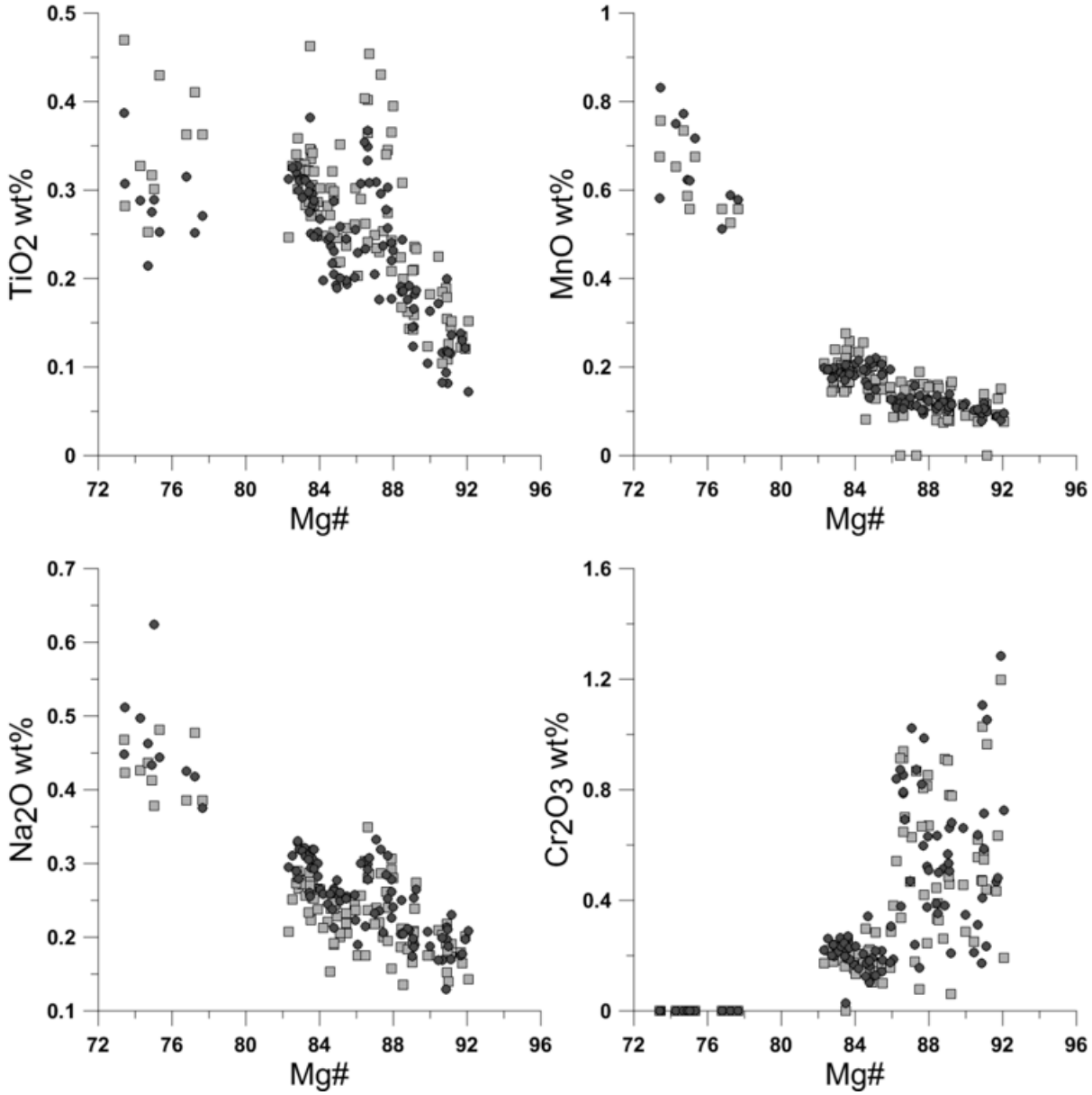

Fig. 3.2. Data comparison for minor element analyses from clinopyroxene: EMP (squares) vs LA-ICP-MS (circles).

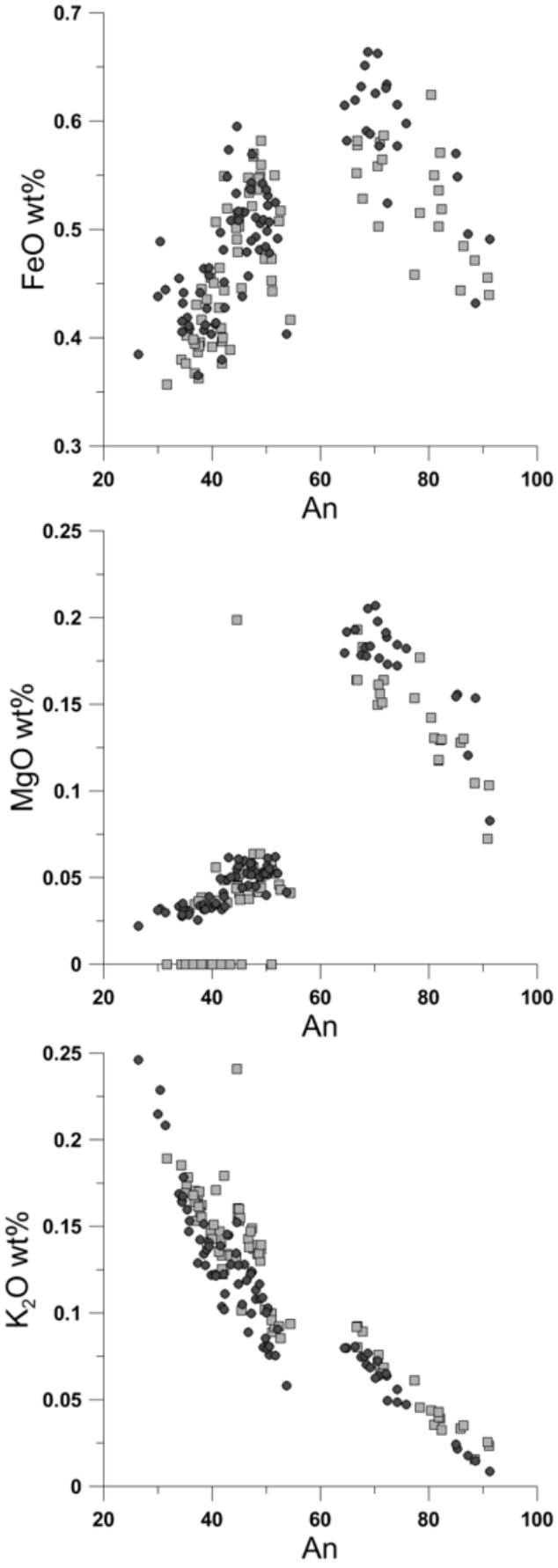

Fig. 3.3. Data comparison for minor element analyses from plagioclase: EMP (squares) vs LA-ICP-MS (circles).

Chapter 4

Petrography and mineral chemistry of the Hunter Ridge magma series

4.1 Introduction

As discussed in Chapter 1, the active magmatism and the particular tectonic setting of the southern tip of the North Fiji Basin results in a wide range of arc-related magma types within the Hunter Ridge area. Samples from the Hunter Ridge selected for this study include rocks from the calc-alkaline and adakite magma series. This chapter focuses on the petrographical and mineralogical characteristics of both calc-alkaline and adakitic rocks. Detailed petrographic analyses were carried out in all samples recovered from the different dredges. EMP and LA-ICP-MS analyses were performed in selected representative samples from each dredge. Details of the sample locations can be found in Chapter 1.

4.2 Petrography of the Hunter Ridge calc-alkaline rocks

Calc-alkaline rocks from the Hunter Ridge range in composition from basalt to rhyolite. All samples are typically porphyritic rocks, containing three to seven mineral phases (plagiolclase + clinopyroxene ± olivine ± Fe-Ti oxides ± orthopyroxene ± amphibole ± apatite). Crystal abundances were determined by point counting across petrographic thin sections.

4.2.1 Basalts

Basaltic rocks are poorly to highly vesicular (up to 30 volume %) pillow lavas with glassy rims. Vesicles range in size from ~1 to 6 mm, small vesicles are sub-spherical and/or irregular and become highly irregular with increasing size, showing at times coalescence. (Fig. 4.1).

The groundmasses are generally glassy or consist of partially devitrified glass displaying hyalopilitic texture, and sometimes spherulitic texture. These groundmasses contain numerous small (< 0.02 mm) lath-shaped plagioclase crystallites and less abundant, very small (<0.025 mm) pyroxene and olivine grains. Oxides are very rare and occur as individual grains of up to 0.15 mm. Groundmass makes up to 65% by volume of the samples.

Phenocrysts represent on average ~20% by volume of the samples. Olivine (~15 volume %) and clinopyroxene (4% volume) are the dominant phenocryst phases and occur throughout the groundmass as large clusters of small to large phenocrysts or as single small to large grains that are typically subhedral or euhedral. The clusters range in size from 1 mm to 7 mm and the individual olivine and pyroxene phenocrysts range from 0.5 to 5 mm. Olivine and clinopyroxene commonly have melt and mineral inclusions (i.e., inclusions of pyroxene in olivine and vice versa, and oxide inclusions). Some of the olivine phenocrysts have resorbed rims. Plagioclase phenocrysts and microphenocrysts (0.1–1 mm) occur in some samples; when present these are rare and represent less than 1% on average. Photomicrographs in Figure 4.1 show the petrographic features described here.

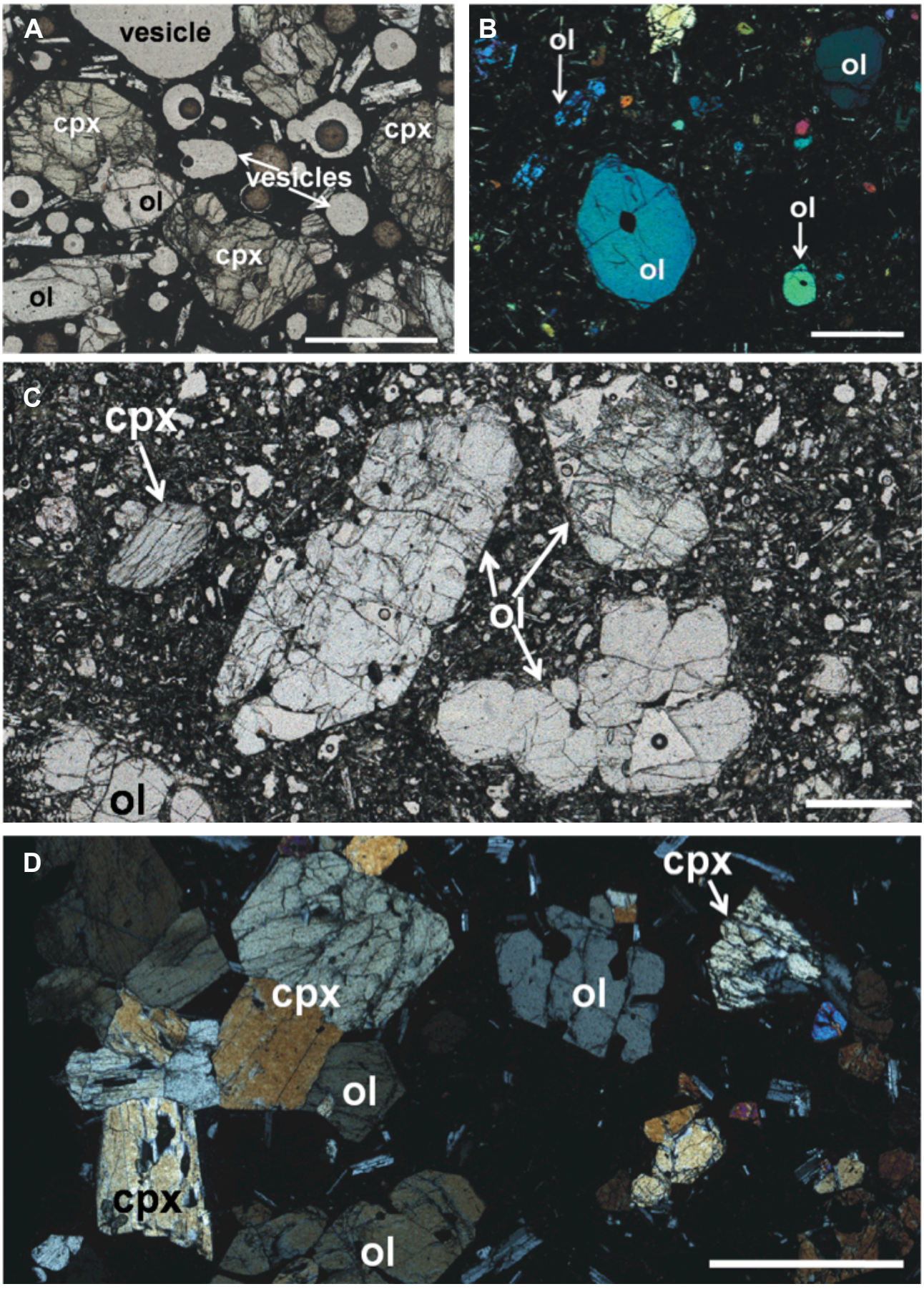
A
vesicle
cpx
cpx
vesicles
ol
cpx
ol
B
ol
ol
ol
ol
C
cpx
ol
ol
D
cpx
cpx
ol
ol
cpx
ol

4.2.2 Basaltic andesites

All basaltic andesite rocks from the Hunter Ridge calc-alkaline series are petrographically similar, although the modal proportion of minerals can vary. Most rocks are moderately to highly vesicular (up to 25 volume%) pillow lavas with glassy rims. Vesicles range in size from ~0.1 to 6 mm; with the smaller ones being subspherical with irregular borders. Larger vesicles display a range of different shapes (e.g., irregular, subspherical, elongated, etc) and some show coalescence (Fig. 4.2).

The groundmasses generally consist of partially devitrified glass, which often has hyalopilitic textures. Similar to basalts, these groundmasses contains numerous small (< 0.02 mm) lath-shaped, randomly arranged plagioclase crystallites, and rare very small (<0.025 mm) pyroxene and olivine grains. Oxides are very rare and occur as individual grains of up to 0.2 mm. Groundmasses represent up to 80% by volume of the sample.

Phenocrysts represent approximately 15% by volume of the samples. Plagioclase (~13 volume %) is the dominant phenocryst phase and occurs as discrete, 0.5 to 3.5 mm long, generally euhedral, grains, and as clusters comprising small to large grains. Clusters range in size from 1 to < 8 mm. Melt inclusions are common in most plagioclase grains and in addition to zoning textures, some phenocrysts display corroded rims. In some of the samples, plagioclase phenocrysts containing numerous melt inclusions are extremely common, though others in the same sample contain few if any. Clinopyroxene and olivine phenocrysts (~2 volume %) are also present and occur mostly as euhedral to subhedral single grains, or as resorbed and skeletal crystals. In some of the samples, clusters containing clinopyroxene+olivine±plagioclase are present. The clusters range in size from 1 to 5 mm and the individual olivine and pyroxene phenocrysts range from 0.5 to 4 mm. Olivines commonly contain melt inclusions, whereas clinopyroxene have both melt and mineral inclusions (i.e., of olivine, oxides and plagioclase). Photomicrographs in Fig. 4.2 show the petrographic features described above.

4.2.3 Dacites

Dacite samples are moderately vesicular (up to 20 volume %) and moderately porphyritic rocks. Vesicles range in size from ~0.1 to 5 mm and, in some samples the smaller vesicles are spherical and become elongated with increasing size. In other samples, the smaller ones are mostly subspherical with irregular borders and the larger ones display a range of different shapes (e.g., irregular, subspherical, elongated, etc.) (Fig. 4.3).

The groundmasses generally consist of fresh to partially devitrified glass, which sometimes have a trachytic texture. These groundmasses can contain numerous (up to 40 %) small (< 0.02 mm) lath-shaped plagioclase crystallites and rare (up to 1%) very small (<0.025 mm) ferromagnesian

Fig. 4.1 (opposite). Petrographic features of basalts from the Hunter Ridge cal-alkaline series. A) Subhedral-euhedral olivine (ol) and clinopyroxene (cpx) phenocrysts in a glassy groundmass of a highly vesicular rock (Sample No. D11-1). B) Olivine phenocrysts displaying various sizes and shapes (i.e., subhedral, euhedral and skeletal) in a glassy groundmass containing plagioclase crystallites (Sample No. D8-1). C) Large olivine and clinopyroxene phenocrysts in a partially devitrified groundmass containing numerous plagioclase crystallites (Sample No. D8-2). D) Crystal cluster containing clinopyroxene and olivine and large olivine grains displaying skeletal texture in a fresh glassy groundmass (Sample No. D11-1).

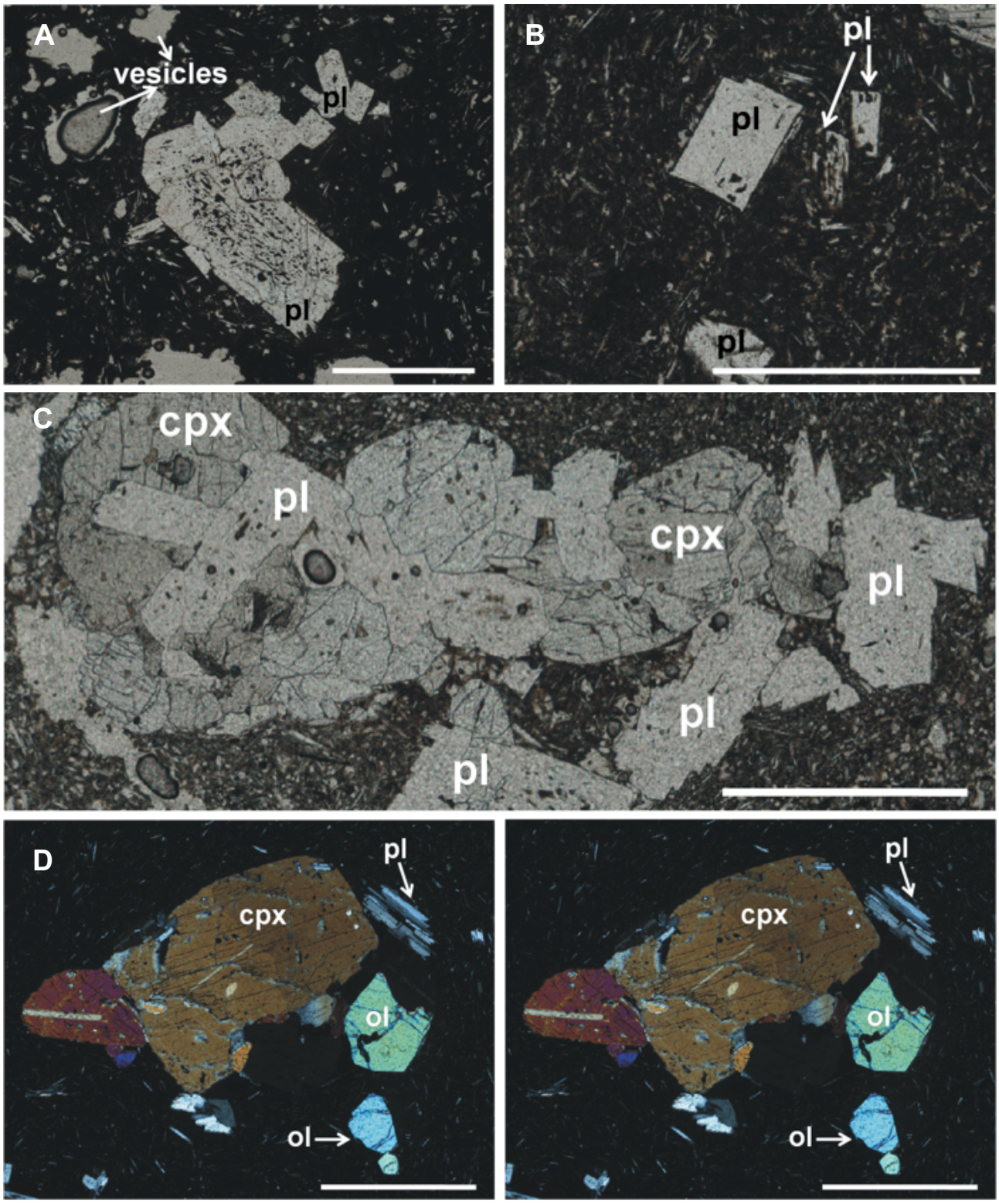

Fig. 4.2. Petrographic features of basaltic andesites from the Hunter Ridge cal-alkaline series. A) Crystal clot containing plagioclase phenocrysts (pl) that display numerous melt inclusions in a glassy groundmass with plagioclase crystallites (Sample No. D1-1). B) Euhedral-subhedral plagioclase phenocrysts in a glassy partially devitrified groundmass containing numerous plagioclase crystallites (Sample No. D15-7A). C) Crystal cluster containing large plagioclase and clinopyroxene (cpx) phenocrysts (Sample No. D15-7A). D) Plagioclase, clinopyroxene and olivine (ol) grains in a glassy groundmass containing small plagioclase crystallites (Sample No. D15-7A). E) Olivine phenocryst showing resorption features in a glassy groundmass containing numerous plagioclase crystallites displaying trachytic textures (Sample No. D67-3). Scale bars represent 1 mm.

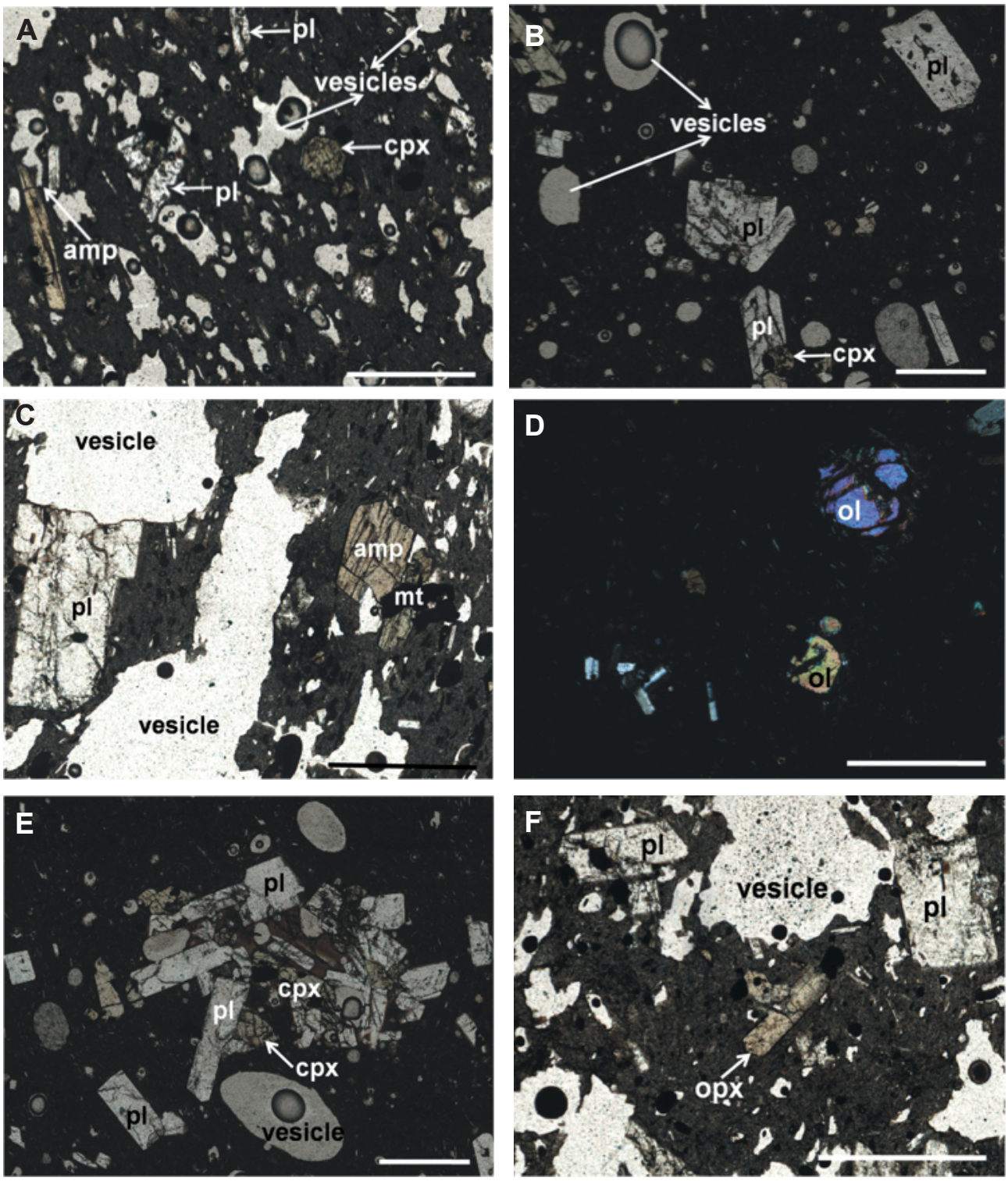

Fig. 4.3. Petrographic features of dacites from the Hunter Ridge cal-alkaline series. A) plagioclase (pl), clinopyroxene (cpx) and amphibole (amp) phenocrysts in a glassy groundmass of a highly vesicular dacite (Sample No. D12-1). B) Euhedral-subhedral plagioclase phenocrysts in a glassy groundmass of a moderately vesicular dacite (Sample No. D13-8). C) Amphibole phenocryst being replaced by magnetite (mt) (Sample No. D12-2). D) Olivine (ol) grains displaying disequilibrium textures in a glassy groundmass (Sample No. D13-8). E) Crystal clot containing clinopyroxene and plagioclase (Sample No. D13-8). F) Orthopyroxene (opx) phenocryst with Fe–Ti oxides along its rims (Sample No. D12-2). Scale bars represent 1 mm.

minerals. Oxides occur as individual grains (of up to 0.2 mm) sparsely disseminated throughout the groundmass. Groundmasses represent around 90 % by volume of the sample.

Phenocrysts represent approximately 10 % by volume of the samples. Plagioclase (~9 volume %) is the dominant phenocryst phase and occurs as single small to large grains and in lesser amounts in large clusters of small to large phenocrysts. The clusters range in size from 1 to 4 mm and the individual phenocrysts from 0.5 to 3 mm and are typically euhedral to subhedral. Two textural groups of plagioclase can be recognised, and both can occur in a single thin section. The first group forms euhedral, blocky crystals up to 2.5 mm in size with little or no visible zoning and few inclusions (mineral and melt inclusions). The second group occurs as subhedral to anhedral (sometimes spongy) grains up to 3 mm in size that typically contain numerous inclusions and exhibit oscillatory zoning. This group also displays disequilibrium textures with embayments and other evidence for resorption.

Clinopyroxene, orthopyroxene and amphibole (~1 volume %) are also present and occur mostly as single grains that range in size from 0.5 to 2 mm and are mostly subhedral. Many clinopyroxene grains are embayed and exhibit resorption features. Amphibole grains display strong cleavage and birefringence and are rimmed by oxides. Dacites mark the first occurrence of amphibole. Oxides minerals (less than 0.5 volume %) occur either as individual grains (< 0.15 mm) or associated with pyroxene and amphibole, either partially replacing these minerals or aligning along their edges. Oxides range in size from 0.5 to 0.2 mm. Apatite inclusions are present in some plagioclase and pyroxene phenocrysts. These occur as very thin needles that range in size from 0.005 to 0.02 mm in length. Although extremely rare, small (< 0.008 mm) sulphide inclusions occur in some oxide grains.

One of the dacite samples contains rare phenocrysts and clots of olivine within a glassy matrix containing oriented microlites of plagioclase (i.e. trachytic texture). The olivines have a grain size of ~1–2 mm and commonly show a reaction halo, which suggests that these are not in equilibrium and therefore may have crystallised from a more primitive melt and were subsequently entrained during magma ascent. Photomicrographs in Fig. 4.3 show the petrographic features described here.

4.2.4 Rhyolites

Rhyolite samples are moderately vesicular (up to 15 volume %) and phenocrysts-poor lavas (maximum phenocrysts content ~ 10%). The vesicles range in size from ~0.1 to 5 mm, the smaller ones are subspherical with irregular borders and become highly irregular in shape with increasing size (Fig. 4.4).

The groundmasses generally consist of very fresh to partially devitrified glass, having sometimes trachytic or vitrophyric textures. When the groundmasses show trachytic texture, these contain numerous (up to 40 %) small (< 0.02 mm) lath-shaped plagioclase crystallites. Oxides occur as individual grains (of up to 0.3 mm) throughout the groundmass. Groundmasses represent up to ~90 % by volume of the sample.

Phenocrysts represent approximately 10 % by volume of the samples. Similar to dacites, the main phenocryst phase in these rocks is plagioclase (~8 % volume) and occurs as single small to large grains and sometimes in large clusters of small to large phenocrysts. The clusters range in size from 1 to 3 mm and the individual phenocrysts from 0.5 to 2.5 mm and are typically subhedral to euhedral.

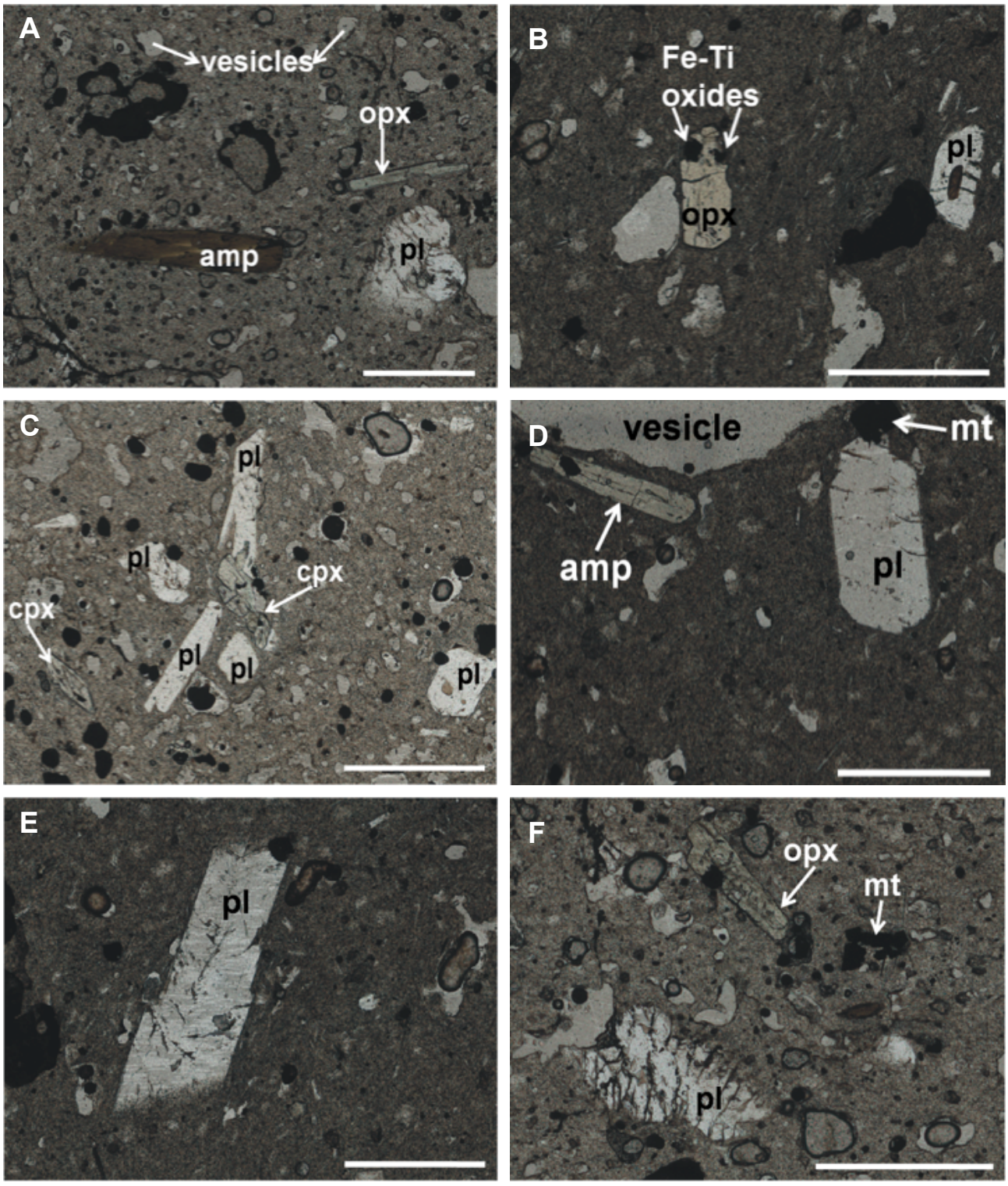

Fig. 4.4. Petrographic features of rhyolites from the Hunter Ridge cal-alkaline series. A) plagioclase (pl), orthopyroxene (opx) and amphibole (amp) phenocrysts in a glassy groundmass (Sample No. 68-8). B) Orthopyroxene phenocryst showing Fe-Ti oxides along its edges and resorbed plagioclase phenocrysts in a groundmass containing abundant plagioclase crystallites (Sample No. D69-3). C) Subhedral-anhedral plagioclase phenocrysts and clinopyroxene (cpx) being replaced by Fe-Ti oxides in a glassy groundmass of a moderately vesicular rhyolite (Sample No. D68-10). D) Subhedral amphibole and plagioclase phenocrysts in a groundmass containing plagioclase crystallites (Sample No. D69-3). E) Plagioclase grain displaying disequilibrium border in a groundmass with abundant plagioclase crystallites (Sample No. D69-3). F) Orthopyroxene (opx) phenocryst with a Fe–Ti oxides grain along its left rim and a plagioclase grain displaying disequilibrium features (Sample No. D68-8). Scale bars represent 1 mm.

Plagioclase phenocrysts can exhibit a wide variety of optical zoning characteristics, from mostly unzoned, to grains showing oscillatory and rare sieved textures. Melt and mineral inclusions typically occur in most plagioclase phenocrysts. The amounts and distribution of clinopyroxene, orthopyroxene and amphibole (~1.5 volume %) are also similar to those in dacites. These minerals occur mostly as single grains that range in size from 0.5 to 2 mm. Clinopyroxene and orthopyroxene are mostly subhedral to euhedral, and many clinopyroxene grains are embayed and exhibit resorption features whereas orthopyroxene mostly presents faceted forms. Amphibole grains show strong cleavage and birefringence and are rimmed by oxides. Oxides minerals, although slightly more abundant than in dacites represent less than ~1 volume % of phenocrysts. These can occur as individual grains (> 0.15 mm) or associated with pyroxene and amphibole, either partially replacing these minerals or aligning along their edges. Oxides range in size from 0.5 to 0.2 mm. Apatite inclusions are present in some plagioclase and pyroxene phenocrysts. These occur as very thin needles that range in size from 0.005 to 0.02 mm in length.

4.3 Mineral Chemistry of the Hunter Ridge calc-alkaline rocks

This section documents the variation of mineral chemistry with magma fractionation (i.e.,decreasing MgO and increasing SiO_2 contents) of the Hunter Ridge calc-alkaline samples. To this aim, mineral analyses are presented as both a series of histograms of Fo contents of olivine, Mg# 100*Mg/(Mg+Fe) for clino- and ortho-pyroxene and An for plagioclase, and a series of variation diagrams of minor elements. All mineral analyses presented as histograms in this section were obtined using a Cameca SX-100 electron microprobe (EMP). Analyses of minor elements for olivine, clinopyroxene and plagioclase were obtained using LA-ICP-MS and analyses of orthopyroxene, amphibole, oxides and apatite were obtained using EMP (see Chapter 3 for details on the analytical methods)

4.3.1 Olivine

Olivine (Table 4.1; Figs 4.5, 4.6) occurs in basalt, basaltic andesites and occasionally in some dacite samples. Cores of 183 and rims of 60 grains (from 8 samples) were analysed to characterise the compositional range of olivine in the Hunter Ridge calc-alkaline lavas. Cores exhibit a wide range of composition from Fo 75–94, with a mode of Fo 82 (Fig. 4.5). Rim compositions range from Fo 82–93, which is within the range measured for the cores (Fig. 4.5). The more restricted range in composition of the rims is likely due to the lack of rim analyses of the more evolved olivine grains. Most olivine crystals present none or normal zoning (i.e., within two forsterite units).

Olivine core compositions range from Fo 80–94 in basalts, Fo 79–91 in basaltic andesites and from Fo 75–89 in dacites. Rim compositions vary between Fo# 82–93 in basalts and Fo 82–91 in basaltic andesites. No olivine rims were analysed in dacites (Fig. 4.6).

Minor elements in olivine

Plots of MnO, CaO and NiO wt% versus Fo content for olivine cores from the calc-alkaline rocks are shown on Figure 4.7. MnO ranges from 0.1 to 0.4 wt% and shows a strong negative correlation with Fo. CaO concentrations vary from 0.02 to 0.24 wt% and do not display a coherent trend with changing

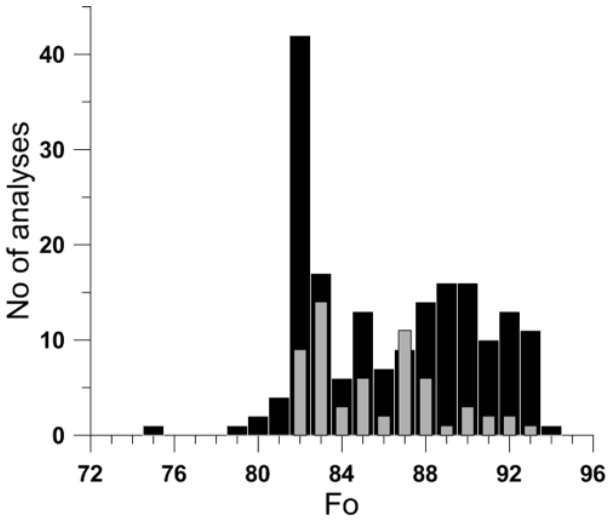

Fig. 4.5. Histogram showing the total distribution of olivine forsterite content for the Hunter Ridge calc-alkaline rocks. Black coloured bars indicate core compositions and gray coloured bars indicate rim compositions.

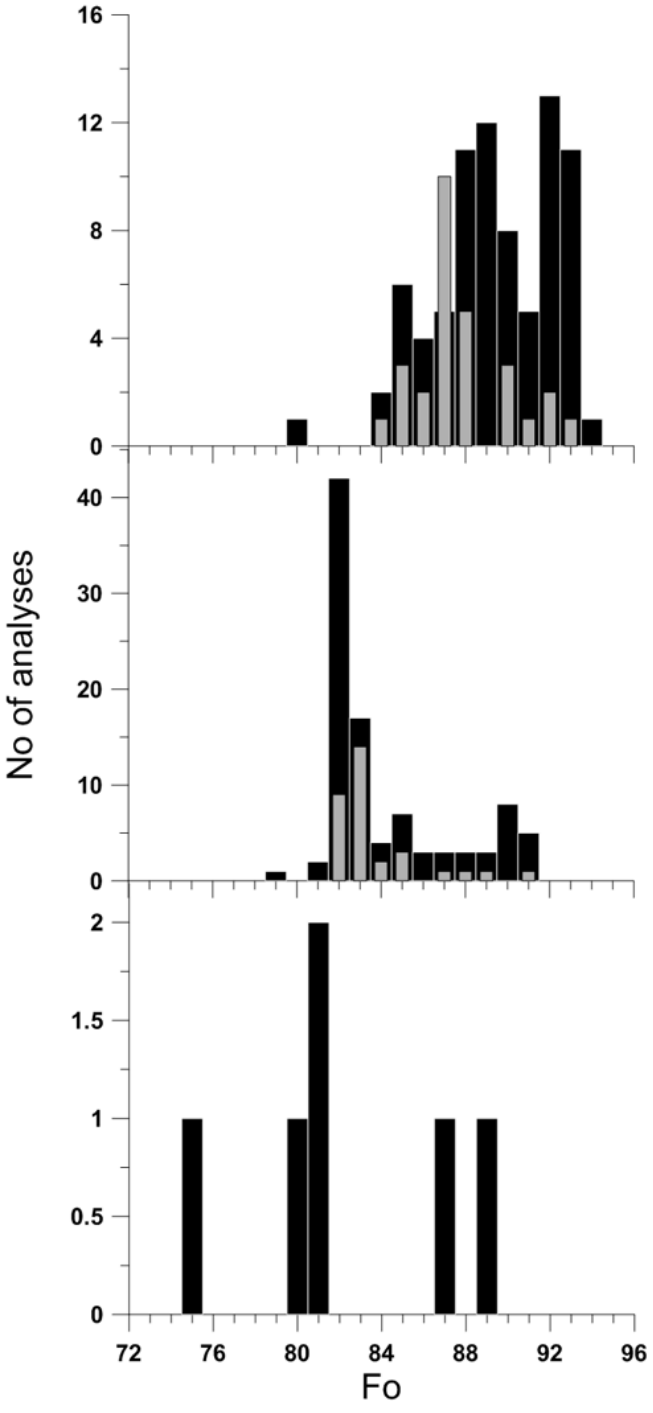

Fig. 4.6. Histograms showing the total distribution of olivine forsterite content in a) basalts, b) basaltic andesites and c) dacites. Black coloured bars indicate core compositions and gray coloured bars indicate rim compositions.

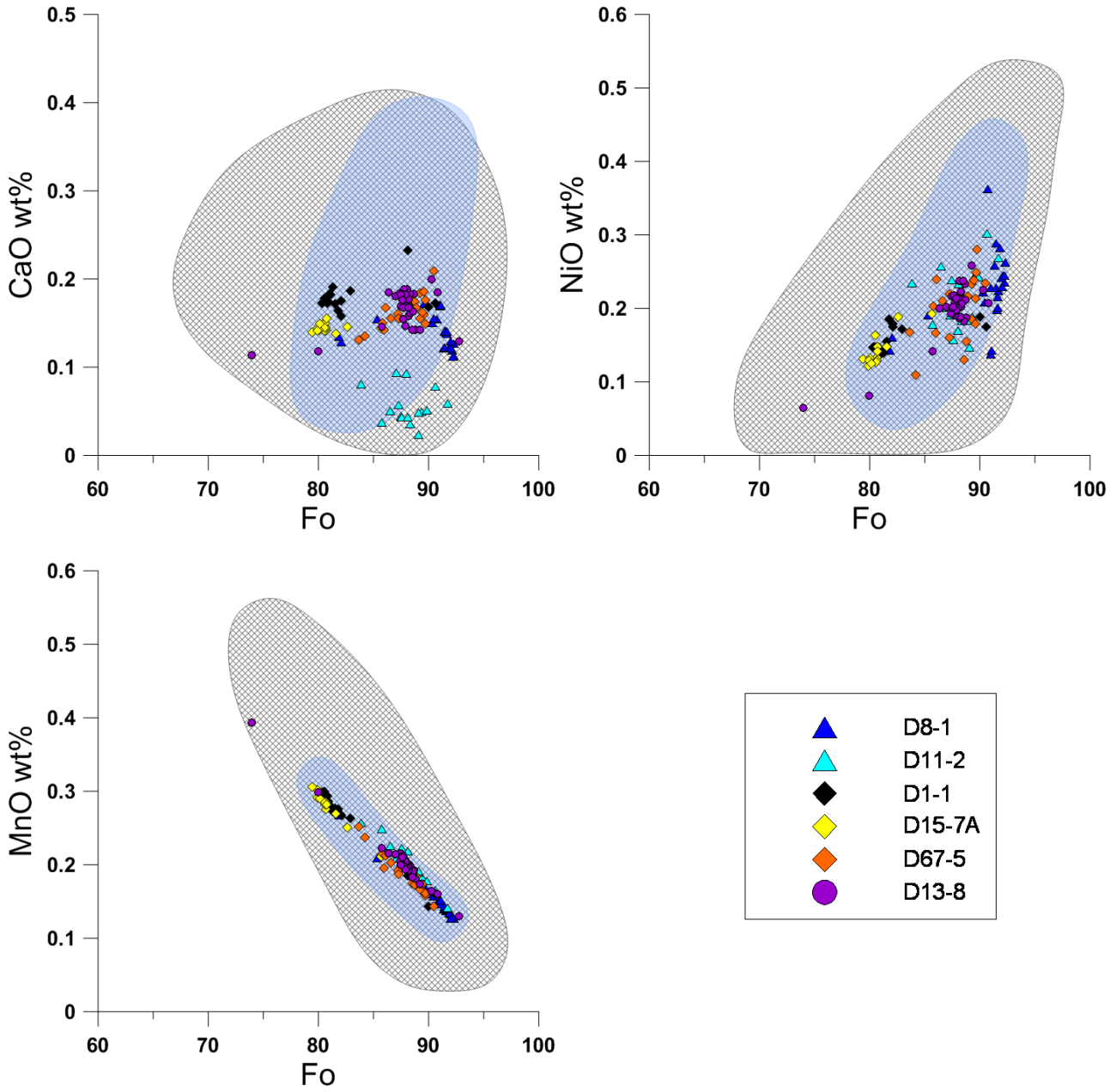

Fig. 4.7. Minor element contents plotted against Fo# for olivine phenocrysts from the Hunter Ridge calc-alkaline rocks compared to olivine from MORB (blue shaded field) and to olivine from calc-alkaline rocks from the Vanuatu arc (grey hatched field). Triangle symbols represent basalts, diamonds represent basaltic andesites, circles represent dacites and square symbols represent rhyolites. Data for MORB and data for the Vanuatu arc are from Danyushevsky (umpublished).

Fo content. Furthermore, olivine grains from basalt samples D11 contain lower CaO contents (> 0.1 wt%) than grains from other samples at a similar Fo. NiO shows a weak positive correlation with Fo. Overall NiO values range from 0.06 to 0.37 wt%. However, at Fo 90–92, NiO varies from 0.12 to 0.37 wt%, which is almost the entire range displayed by these phenocrysts.

4.3.2 Clinopyroxene

Clinopyroxene phenocrysts are present in all calc-alkaline rocks, but decrease in abundance from basalt to rhyolites. (Table 4.1, Figs 4.8, 4.9). Analyses of 264 cores and 93 rims (from 15 samples) were carried out to document the large compositional range of clinopyroxene in the Hunter Ridge calc-

alkaline lavas. Clinopyroxene phenocrysts in these samples display an overall range in compositions between Mg# 72–92 (Fig. 4.8). Core compositions cover the entire range and display a bimodal distribution with the two main populations of crystals having Mg# 76 and Mg# 84 (Fig. 4.8). Rim compositions range from Mg# 72–91, which is within the range measured for the cores (Fig. 4.8). Most phenocrysts are augites, although diopside sometimes occurs as phenocrysts in basalts and dacites. In all rock types, clinopyroxene is largely unzoned, however, grains displaying minor normal and reverse zoning patterns (up to 2–3 units of Mg#) are also present and commonly observed in a single sample.

In basalts, clinopyroxene core compositions vary between Mg# 83–92 and rims between Mg# 84–89 (Fig. 4.9). Most phenocrysts (73%) are augites in the range of $En_{47–52}Fs_{5–12}Wo_{39–45}$ and in lesser amount diopside (27%) in the range of $En_{45–49}Fs_{6–9}Wo_{45–47}$.

In basaltic andesites, clinopyroxene core compositions vary from Mg# 81–92 and rims from Mg# 81–91 (Fig. 4.9). The phenocrysts are augites in the range of $En_{48–52}Fs_{5–12}Wo_{37–44}$.

In dacites, clinopyroxene core compositions range between Mg# 72–91 and rims from Mg# 72–88 (Fig. 4.15). The majority of the dacite samples studied contain two groups of clinopyroxene phenocrysts: i) relatively low-Mg clinopyroxene (Mg#< 78) which generally represents ~ 65% of the total clinopyroxene, and ii) high-Mg phenocrysts (Mg# >80) which represents ~ 35% of the total clinopyroxene content. The clinopyroxenes are augites ($En_{42–51}$ $Fs_{5–17}$ $Wo_{38–45}$) and diopside ($En_{45–50}$ $Fs_{5–8}Wo_{45–48}$). Modally these account for 83 and 17% respectively.

In rhyolites, clinopyroxene core compositions vary from Mg# 74–78 and rims from Mg# 74–77 (Fig. 4.9). These phenocrysts are mostly augites in the range $En_{41–45}Fs_{13–16}Wo_{39–44}$.

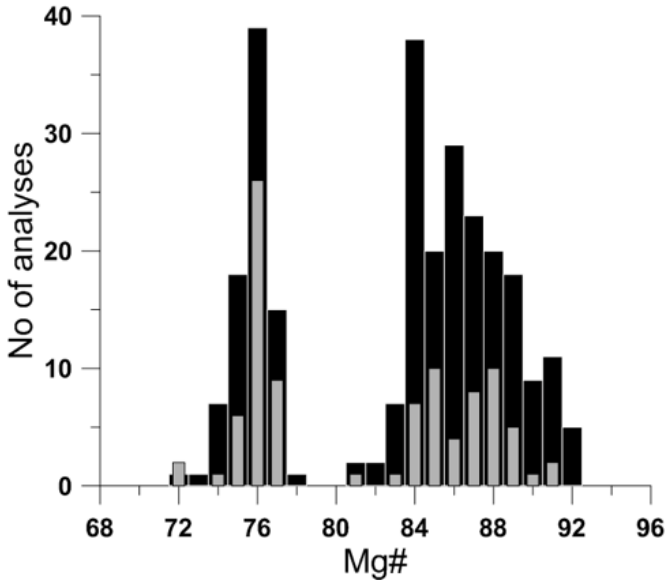

Fig. 4.8 Histogram showing the total distribution of clinopyroxene Mg# for the Hunter Ridge calc-alkaline rocks. Black coloured bars indicate core compositions and grey coloured bars indicate rim compositions.

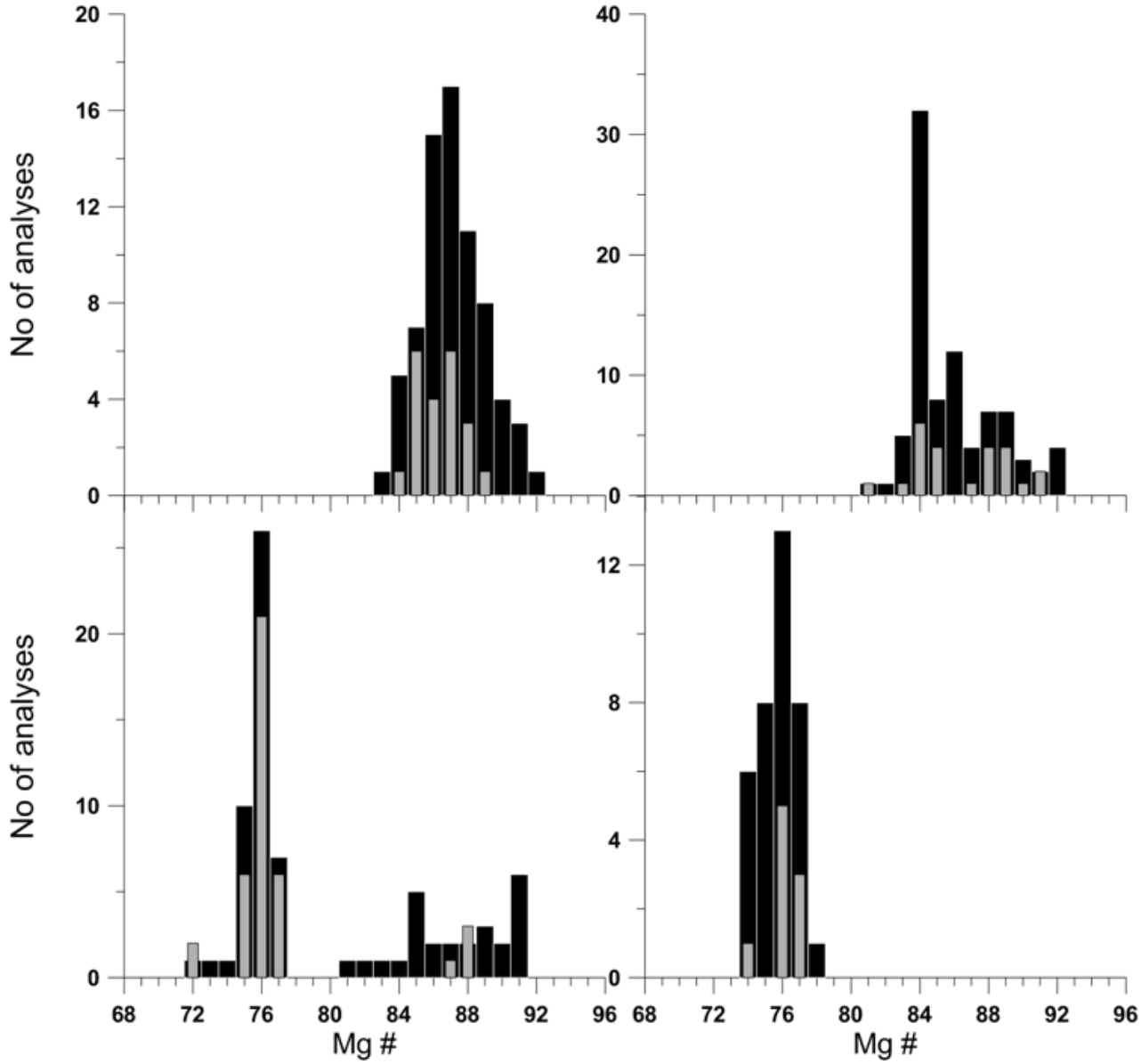

Fig. 4.9 Histograms showing the total distribution of clinopyroxene Mg# in a) basalts, b) basaltic andesites c) dacites and d) rhyolites. Black coloured bars indicate core compositions and grey coloured bars indicate rim compositions.

Minor elements in clinopyrexene

TiO_2, MnO, Na_2O and Cr_2O_3 contents of the clinopyroxene phenocryst cores are shown on Figure 4.16. TiO_2 contents in phenocrysts with high Mg# (i.e. >81) display a negative correlation with Mg#. TiO_2 in these phenocrysts range from 0.07 to 0.38 wt%. TiO_2 contents in phenocrysts with Mg# <81) do not display a coherent trend. MnO ranges from 0.08–0.83 and shows an exponential increase with decreasing Mg#. Na_2O contents vary from 0.13 to 0.62 wt% and show negative correlation with Mg#. Overall, Cr_2O_3 varies from 0.03 to 1.28 wt%, with phenocrysts with Mg# < 81 having contents below detection limits. However Cr_2O_3 values scatter and display considerable variations between samples. In samples D67-5, D8-1 and D13-8, Cr_2O_3 values decrease with decreasing Mg#, whereas in samples D1-1, D15-7a and D11-2, Cr_2O_3 does not show any correlation with Mg#. It is also worth noting that

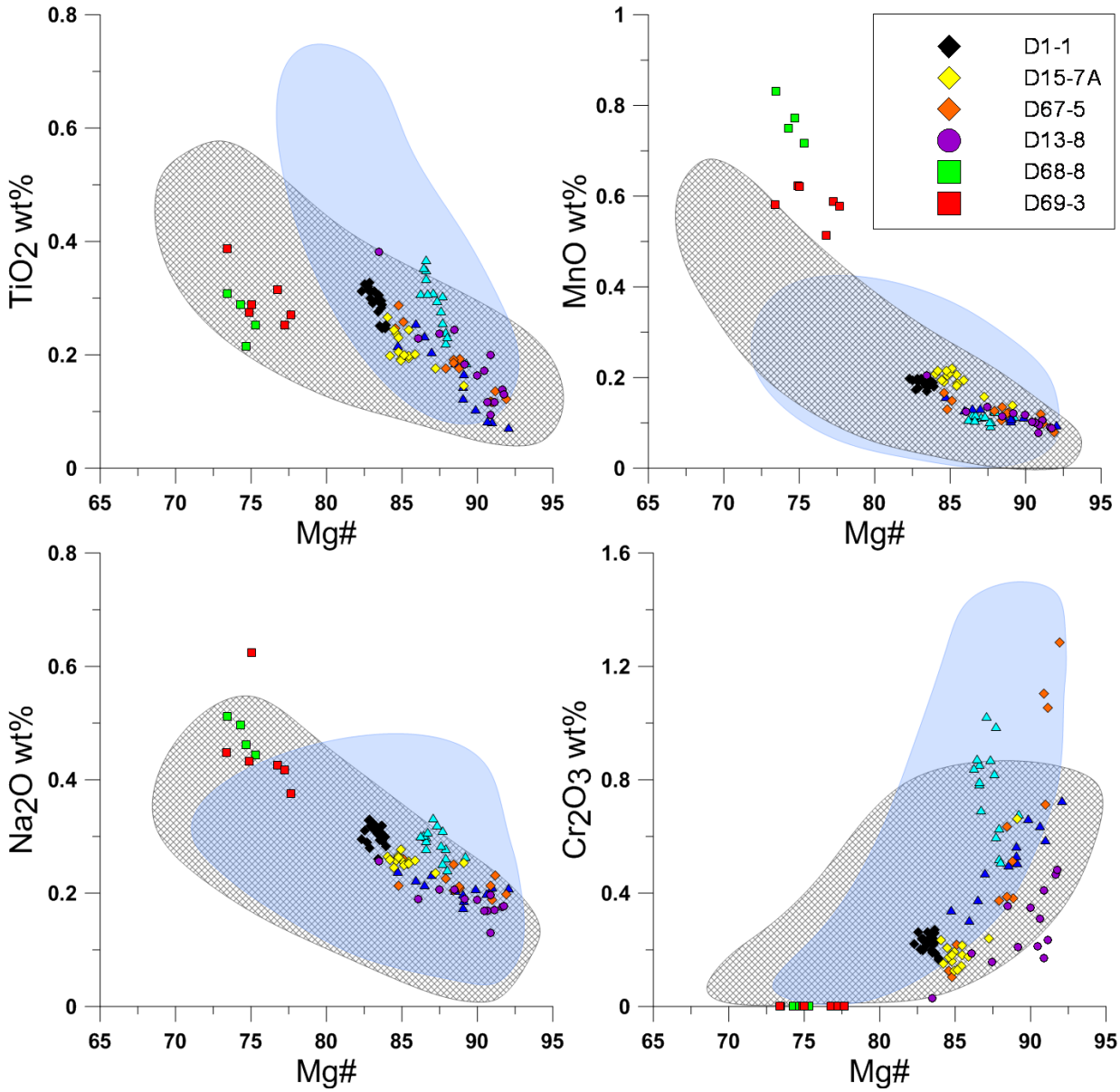

Fig. 4.10. Minor element contents plotted against Mg# for clinopyroxene phenocrysts from the Hunter Ridge calc-alkaline rocks compared to clinopyroxenes from MORB (blue shaded field) and to clinopyroxenes from calc-alkaline rocks from the Vanuatu arc (grey hatched field). Triangle symbols represent basalts, diamonds represent basaltic andesites, circles represent dacites and square symbols represent rhyolites. Data for MORB and data for the Vanuatu arc are from Danyushevsky (unpublished)

sample D11-2 generally contains phenocrysts with higher TiO_2 and Na_2O than grains from other samples at similar Mg#.

4.3.3. Orthopyroxene

Orthopyroxene (Table 4.1, Figs 4.11, 4.12) is only present in dacites and rhyolites. Cores of 108 and rims of 53 grains (from 10 samples) were analysed to illustrate the compositional range of orthopyroxene in the Hunter Ridge calc-alkaline lavas. Core compositions range from Mg# 68–74 and show a uni-modal distribution, with the majority of cores having Mg# 71 (Fig. 4.11). Rim

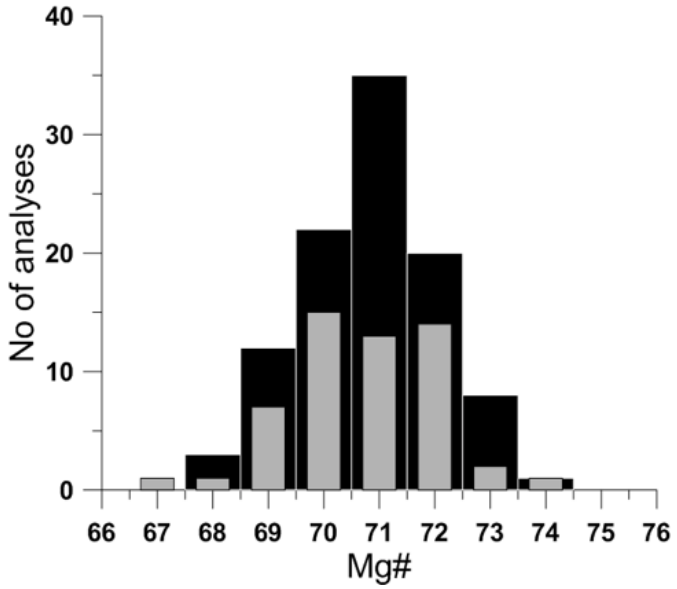

Fig. 4.11. Histogram showing the total distribution of orthopyroxene Mg# for the Hunter Ridge calc-alkaline rocks. Black coloured bars indicate core compositions and grey coloured bars indicate rim compositions.

compositions range from Fo# 67–74, with a mode of 70 (Fig. 4.11). The orthopyroxenes are mostly unzoned (up to 2–3 units of Mg#) clino-enstatite in the range of $En_{65–72}$ $Fs_{25–37}$ $Wo_{1–4}$, although weakly normally or reversely zoned grains could be found within a single rock.

Dacites and rhyolites show a similar range in orthopyroxene compositions. In dacites, orthopyroxene core compositions range between Mg# 70–73 and rims between Mg# 70–74. In rhyolites, core compositions vary from Mg# 68–74 and rims from Mg# 67–72 (Fig. 4.12).

Minor elements in orthopyrexene

Plots of TiO_2 wt%, Al_2O_3wt%, MnO wt%, and CaO wt% versus Mg# for orthopyroxene cores are shown on Figure 4.13. Orthopyroxenes from dacites and rhyolites from the calc-alkaline series display an overall range in TiO_2 from 0.13 to 0.36 wt%, Al_2O_3 from 0.3 to 1.81 wt%, MnO from 0.56 to 1.42 wt%, and CaO from 0.97 to 1.7 wt%. TiO_2, Al_2O_3 and CaO contents are scattered and do not show any correlation with Mg# whereas MnO displays an overall negative correlation with Mg#.

4.3.4. Plagioclase

Plagioclase (Table 4.1; Figs 4.14, 4.15) is the most abundant phenocryst phase in basaltic andesites, dacites and rhyolites. Plagioclase phenocrysts do not occur in basaltic samples, in basalts plagioclase typically occurs as microlites. Cores of 337 and rims of 164 grains (from 17 samples) were analysed to characterise the wide compositional range of plagioclase in the Hunter Ridge calc-alkaline lavas. Cores exhibit a wide range of composition from An 27–92, and display a bimodal distribution with two peaks at An 48 and An 76–80 (Fig. 4.14). Rim compositions range from An 22–91 (Fig. 4.14). Within a single thin section, some plagioclase crystals display complex compositional zoning patterns (e.g. normal, reverse, and patchy), whereas others display little or no zoning.

In basalts, microlite plagioclase compositions vary from An 66–79 (Fig. 4.15). In basaltic

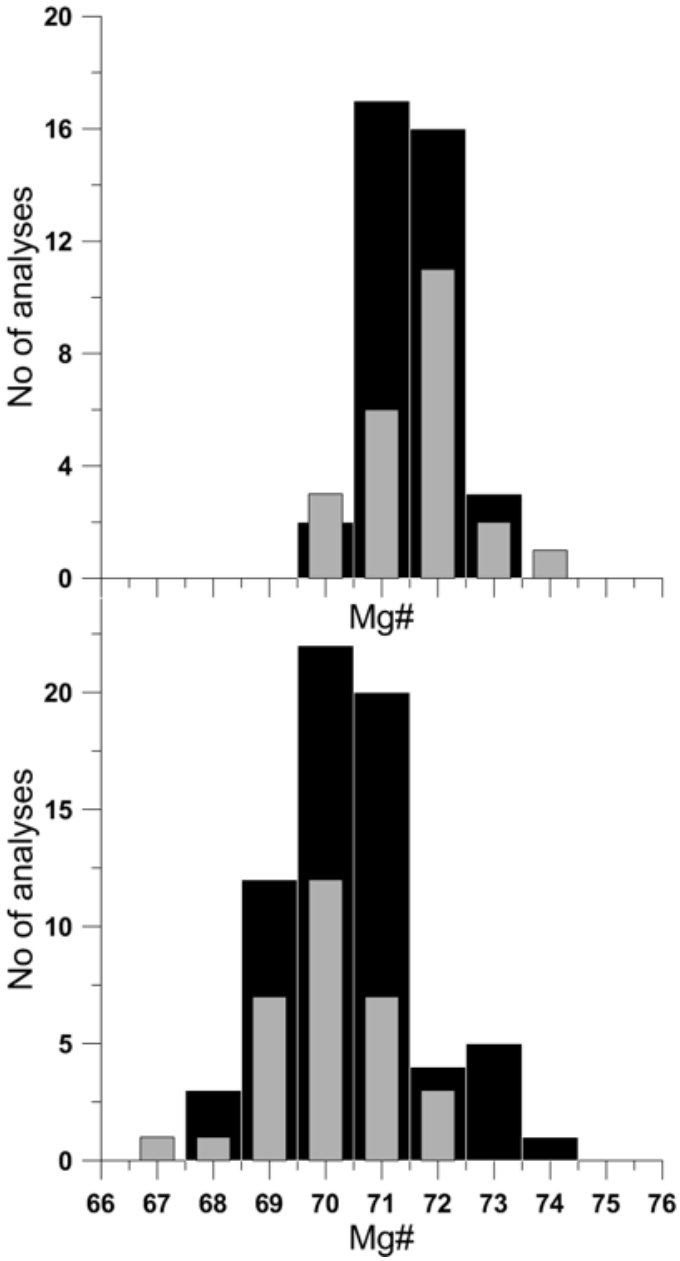

Fig. 4.12. Histograms showing the total distribution of orthopyroxeneMg# in a) dacites and b) rhyolites. Black coloured bars indicate core compositions and grey coloured bars indicate rim compositions.

andesites, plagioclase core compositions range between An 64–92 and rims from An 64 to 91 (Fig. 4.16).

In dacites, core compositions vary from An 37–91 and rims from 37 to 87 (Fig. 4.15). Dacite samples contain two populations of plagioclase phenocrysts: i) relatively low-An phenocrysts (An <64), which typically represent ~90% of the total of plagioclase phenocrysts, and ii) more calcic phenocrysts (An >68), which represent ~10% of the total plagioclase (Fig. 4.15). This latter group often display disequilibrium textures (i.e., resorption and embayments).

In rhyolites, core compositions vary from An 27–58 and rims from 22–53 (Fig. 4.15).

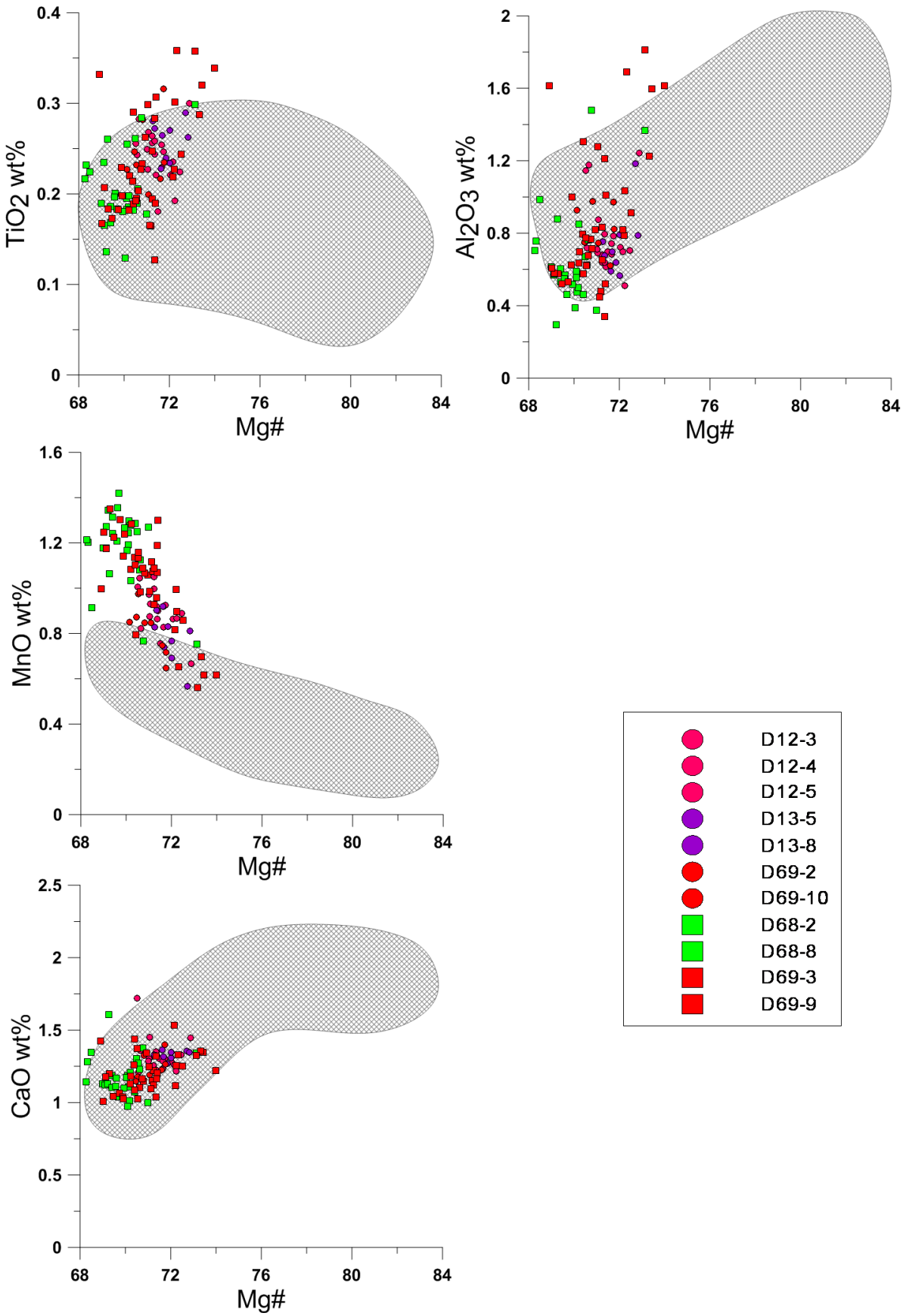

Fig. 4.13. Minor element contents plotted against Mg# for orthopyroxene phenocrysts from the Hunter Ridge calc-alkaline rocks compared to orthopyroxenes from calc-alkaline rocks from the Vanuatu arc (grey hatched field). Circle symbols represent dacites and square symbols represent rhyolites. Data for the Vanuatu arc are from Danyushevsky (unpublished).

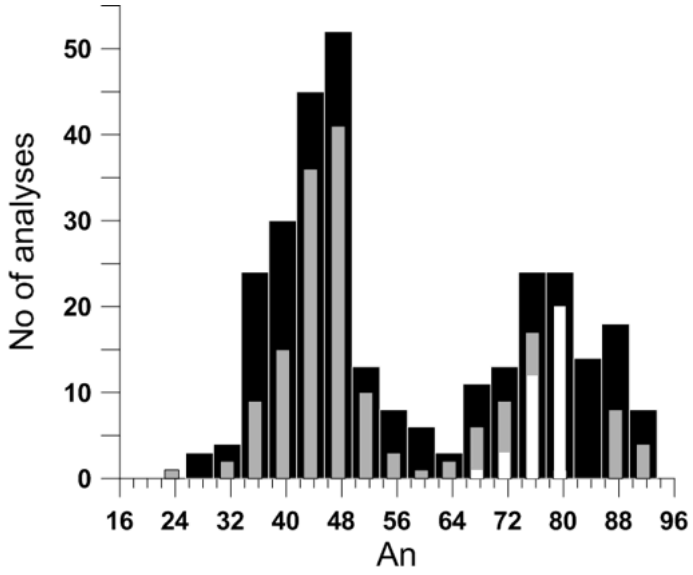

Fig. 4.14. Histogram showing the total distribution of plagioclase An for the Hunter Ridge calc-alkaline rocks. Black coloured bars indicate core compositions, grey bars indicate rim compositions and white coloured bars indicate microlite compositions.

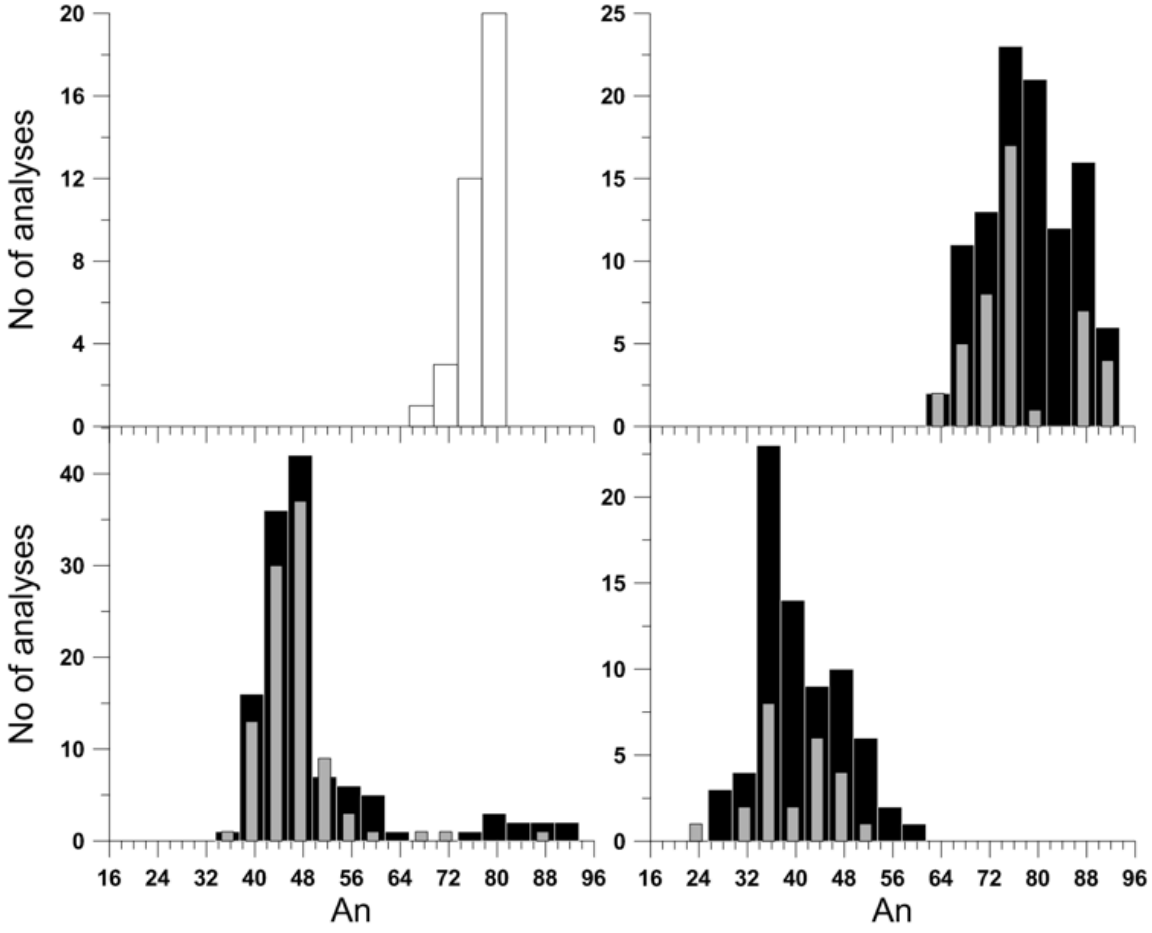

Fig. 4.15. Histograms showing the total distribution of plagioclase An in a) basalts (microlites), b) basaltic andesites c) dacites and d) rhyolites. Black coloured bars indicate core compositions and grey coloured bars indicate rim compositions.

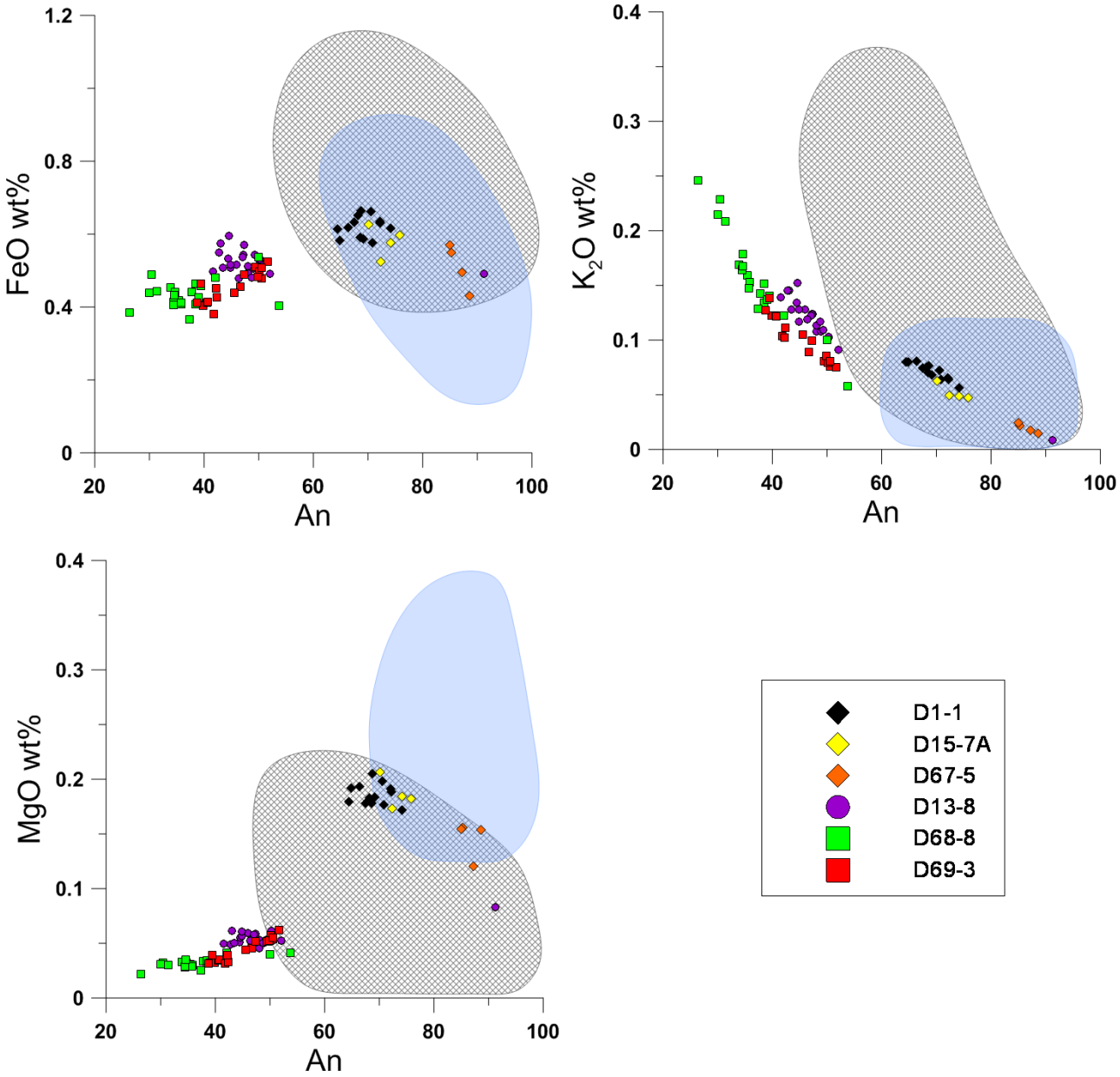

Fig. 4.16.Minor element contents plotted against An for plagioclase phenocrysts from the Hunter Ridge calc-alkaline rocks compared to plagioclases from MORB (blue shaded field) and to plagioclases from calc-alkaline rocks from the Vanuatu arc (grey hatched field). Diamond symbols represent basaltic andesites, circles represent dacites and square symbols represent rhyolites. Data for MORB are from McNeill (1997) and data for the Vanuatu arc are from Danyushevsky (unpublished).

Table 4.1 Average mineral compositions (wt%) for the Hunter Ridge calc-alkaline samples.

Sample	SiO_2	TiO_2	Al_2O_3	FeO	MnO	MgO	CaO	Na_2O	K_2O	P_2O_5	Cr_2O_3	NiO	Total	
Olivine														**Fo**
D8-1	40.38	0.00	0.01	10.20	0.19	48.50	0.20	0.00	0.00	0.00	0.00	0.26	99.76	89
D11-1	40.23	0.00	0.00	12.70	0.25	46.59	0.20	0.00	0.00	0.01	0.00	0.25	100.21	87
D11-2	40.26	0.00	0.00	11.86	0.21	47.18	0.16	0.00	0.00	0.00	0.01	0.28	99.96	88
D67-3	39.89	0.00	0.01	13.26	0.17	46.57	0.18	0.00	0.00	0.00	0.00	0.13	100.22	86
D67-5	40.90	0.00	0.02	10.22	0.18	48.96	0.21	0.00	0.00	0.01	0.02	0.21	100.73	90
D1-1	39.53	0.00	0.00	16.49	0.28	43.51	0.22	0.00	0.00	0.01	0.00	0.12	100.17	82
D1-3	39.48	0.00	0.00	16.50	0.29	43.71	0.21	0.00	0.00	0.00	0.00	0.13	100.34	83
D15-7a	39.45	0.00	0.00	17.03	0.28	42.98	0.19	0.01	0.00	0.00	0.00	0.12	100.06	82
Clinopyroxene														**Mg#**
D8-1	52.38	0.30	3.33	4.63	0.14	16.87	22.03	0.20	0.00	0.00	0.55	0.01	100.44	87
D11-1	52.02	0.37	3.69	4.91	0.14	16.57	21.82	0.28	0.00	0.00	0.64	0.01	100.45	86
D11-2	52.74	0.32	3.00	4.53	0.14	16.93	22.06	0.25	0.00	0.00	0.63	0.00	100.61	87
D67-3	53.05	0.25	2.62	4.22	0.06	17.71	22.47	0.22	0.00	0.00	0.40	0.00	100.99	88
D67-5	53.00	0.28	2.65	5.03	0.18	17.57	21.15	0.21	0.00	0.00	0.26	0.00	100.33	86
D1-1	53.41	0.35	2.74	6.09	0.23	17.91	20.06	0.27	0.00	0.00	0.26	0.00	101.32	84
D1-3	53.32	0.34	2.64	6.19	0.20	18.00	19.77	0.28	0.00	0.01	0.23	0.00	100.98	84
D15-7a	53.66	0.29	2.09	6.08	0.22	18.43	19.37	0.23	0.01	0.00	0.14	0.00	100.51	84
D12-1	51.56	0.49	1.62	8.84	0.50	15.40	20.82	0.38	0.00	0.00	0.00	0.00	99.62	76
D12-3	52.79	0.45	1.51	8.76	0.51	15.50	20.37	0.37	0.00	0.00	0.00	0.00	100.26	76
D12-5	52.73	0.48	1.61	9.08	0.52	15.60	19.86	0.37	0.00	0.00	0.00	0.00	100.25	75
D13-3	52.78	0.53	1.61	8.98	0.50	15.53	20.33	0.41	0.00	0.00	0.00	0.00	100.69	76
D13-4	53.54	0.41	1.42	8.41	0.40	15.28	21.60	0.35	0.00	0.00	0.00	0.00	101.41	76
D13-5	53.39	0.47	1.38	8.81	0.49	15.75	20.22	0.37	0.00	0.00	0.00	0.00	100.87	76
D13-8	52.84	0.44	2.25	6.99	0.30	16.43	20.93	0.31	0.00	0.00	0.15	0.00	100.63	81
D69-2	53.01	0.49	1.64	8.54	0.38	15.24	21.31	0.36	0.00	0.01	0.00	0.00	100.98	76
D69-3	52.93	0.42	1.53	8.47	0.55	15.13	21.36	0.43	0.00	0.00	0.00	0.00	100.82	76
D68-8	52.19	0.32	1.18	8.96	0.58	15.30	20.89	0.37	0.00	0.00	0.00	0.00	99.80	75
D69-9	53.14	0.45	1.67	8.66	0.50	15.78	20.28	0.40	0.00	0.00	0.00	0.00	100.87	76
D69-10	53.07	0.43	1.46	8.91	0.47	15.56	20.40	0.37	0.00	0.00	0.00	0.00	100.68	76
Orthopyroxene														**Mg#**
D12-1	53.18	0.24	0.61	17.98	0.84	25.58	1.36	0.00	0.00	0.00	0.00	0.00	99.77	72
D12-3	54.37	0.26	0.80	18.22	0.92	25.66	1.31	0.01	0.00	0.00	0.00	0.00	101.54	72
D12-5	54.03	0.25	0.88	18.02	0.88	25.61	1.34	0.01	0.00	0.00	0.00	0.00	101.03	72
D13-3	54.55	0.27	0.80	17.90	0.87	25.82	1.36	0.01	0.00	0.00	0.00	0.00	101.57	72
D13-5	54.56	0.27	0.76	17.95	0.75	25.89	1.33	0.01	0.00	0.00	0.00	0.00	101.51	72
D13-8	54.88	0.25	0.68	17.92	0.88	25.76	1.35	0.00	0.00	0.00	0.00	0.00	101.72	72
D69-2	54.19	0.26	0.90	17.74	0.69	25.30	1.37	0.00	0.00	0.00	0.00	0.00	100.45	72
D69-10	54.45	0.23	0.79	18.83	0.85	25.52	1.19	0.01	0.00	0.00	0.00	0.00	101.86	71
D68-2	53.04	0.63	2.01	17.70	1.03	23.25	3.03	0.42	0.04	0.00	0.00	0.00	101.15	70
D69-3	54.45	0.21	0.71	18.28	1.09	25.04	1.16	0.00	0.00	0.00	0.00	0.00	100.94	71
D68-8	53.25	0.21	0.75	19.05	1.07	24.42	1.29	0.00	0.00	0.00	0.00	0.00	100.04	70
D69-9	54.50	0.22	0.72	18.66	1.29	25.41	1.09	0.02	0.00	0.00	0.00	0.00	101.90	71
Amphibole														
D13-4	45.37	2.98	9.78	11.81	0.31	15.20	11.14	2.41	0.24	0.03	0.00	0.00	99.26	
D68-2	45.29	2.40	7.71	12.55	0.47	14.94	10.90	2.18	0.20	0.01	0.00	0.00	96.65	
D68-8	45.09	2.80	9.02	12.36	0.35	15.33	11.01	2.38	0.21	0.02	0.00	0.00	98.56	
D69-3	44.47	2.88	9.63	13.18	0.34	14.65	11.05	2.42	0.18	0.06	0.00	0.00	98.85	
D69-9	43.67	2.56	10.35	13.97	0.26	14.08	10.96	2.42	0.18	0.10	0.00	0.00	98.56	

Table 4.1 cont.

Sample	SiO_2	TiO_2	Al_2O_3	FeO	Fe_2O_3	MnO	MgO	CaO	Na_2O	K_2O	P_2O_5	Cr_2O_3	NiO	Total	
Plagioclase															**An#**
D8-1*	49.48	0.00	31.98	0.73	0.00	0.00	0.27	15.36	2.68	0.06	0.00	0.00	0.00	100.56	76
D11-1*	49.01	0.01	32.15	0.63	0.00	0.00	0.15	15.29	2.76	0.06	0.00	0.00	0.00	100.05	75
D11-2*	49.60	0.02	31.76	0.62	0.00	0.00	0.17	14.99	2.97	0.06	0.00	0.00	0.00	100.18	74
D67-3	45.58	0.00	34.47	0.46	0.00	0.00	0.12	18.05	1.26	0.02	0.00	0.00	0.00	99.97	89
D67-5	45.97	0.00	34.27	0.49	0.00	0.00	0.14	17.76	1.40	0.02	0.00	0.00	0.00	100.06	88
D1-1	49.85	0.01	31.67	0.58	0.00	0.00	0.17	14.88	2.85	0.07	0.00	0.00	0.00	100.09	74
D1-3	50.08	0.02	31.52	0.59	0.00	0.00	0.17	14.69	2.98	0.07	0.00	0.00	0.00	100.11	73
D15-7a	49.18	0.01	32.08	0.52	0.00	0.00	0.16	15.33	2.62	0.06	0.00	0.00	0.00	99.95	76
D12-1	57.11	0.04	27.08	0.53	0.00	0.00	0.05	9.27	6.09	0.16	0.01	0.00	0.00	100.34	46
D12-3	55.98	0.03	27.77	0.54	0.00	0.00	0.05	9.88	5.54	0.15	0.01	0.00	0.00	99.95	50
D12-5	57.18	0.04	27.02	0.52	0.00	0.00	0.05	8.96	6.04	0.16	0.00	0.00	0.00	99.98	45
D13-3	57.57	0.04	26.51	0.55	0.00	0.00	0.04	8.78	6.05	0.16	0.00	0.00	0.00	99.70	45
D13-4	55.21	0.03	28.45	0.52	0.00	0.00	0.05	10.70	5.17	0.12	0.00	0.00	0.00	100.24	53
D13-5	57.49	0.03	26.71	0.55	0.00	0.00	0.04	8.84	6.22	0.15	0.00	0.00	0.00	100.04	44
D13-8	56.52	0.04	27.47	0.57	0.00	0.00	0.06	9.76	5.65	0.14	0.00	0.00	0.00	100.19	49
D13-12	57.43	0.04	26.86	0.55	0.00	0.00	0.05	9.03	6.02	0.15	0.00	0.00	0.00	100.13	45
D69-2	56.20	0.03	27.27	0.49	0.00	0.00	0.05	9.53	5.81	0.14	0.00	0.00	0.00	99.53	48
D68-2	59.48	0.01	25.48	0.38	0.00	0.00	0.00	7.23	7.29	0.18	0.00	0.00	0.00	100.05	35
D68-8	58.77	0.01	26.77	0.42	0.00	0.00	0.03	8.40	6.61	0.14	0.00	0.00	0.00	101.17	41
D69-3	57.69	0.03	26.44	0.46	0.00	0.00	0.02	8.39	6.48	0.14	0.02	0.00	0.00	99.67	42
D69-9	57.17	0.02	26.87	0.45	0.00	0.00	0.03	9.00	6.16	0.12	0.01	0.00	0.00	99.83	45
D69-10	57.21	0.02	26.84	0.48	0.00	0.00	0.03	9.07	6.07	0.14	0.00	0.00	0.00	99.86	45
Ilmenite															
D12-3	0.00	38.79	0.34	55.11	0.00	0.53	2.55	0.00	0.00	0.00	0.00	0.00	0.00	97.31	
D12-5	0.08	40.03	0.30	54.40	0.00	0.69	2.16	0.00	0.00	0.00	0.00	0.00	0.00	97.67	
D13-8	0.00	39.37	0.36	54.37	0.00	0.49	2.61	0.00	0.00	0.00	0.00	0.00	0.00	97.21	
D69-2	0.00	39.90	0.33	53.93	0.00	0.46	2.46	0.00	0.00	0.00	0.00	0.00	0.00	97.08	
D69-10	0.00	40.43	0.31	53.82	0.00	0.57	2.35	0.02	0.00	0.00	0.00	0.00	0.00	97.50	
D68-2	0.00	41.03	0.24	53.62	0.00	0.82	2.32	0.00	0.00	0.00	0.00	0.00	0.00	98.04	
D69-3	0.00	39.85	0.24	54.20	0.00	0.81	2.20	0.00	0.00	0.00	0.00	0.00	0.00	97.30	
D69-9	0.00	39.46	0.29	54.77	0.00	0.66	2.32	0.00	0.00	0.00	0.00	0.02	0.00	97.52	
Magnetite															
D12-1	0.10	10.72	2.06	38.38	46.59	0.72	1.60	0.00	0.00	0.00	0.00	0.03	0.00	100.19	
D12-3	0.11	9.91	2.11	48.29	36.63	0.63	2.28	0.00	0.00	0.00	0.00	0.03	0.00	99.98	
D12-5	0.10	9.95	2.17	48.34	36.63	0.61	2.29	0.00	0.02	0.00	0.00	0.04	0.00	100.14	
D13-8	0.08	10.54	2.35	46.80	37.14	0.55	2.35	0.00	0.00	0.00	0.00	0.02	0.00	99.84	
D69-2	0.07	10.17	2.35	47.34	37.01	0.55	2.18	0.00	0.00	0.00	0.00	0.03	0.00	99.71	
D69-10	0.05	9.97	2.06	47.92	37.07	0.57	1.93	0.00	0.00	0.00	0.00	0.02	0.00	99.60	
D68-2	0.04	9.08	1.84	50.78	36.60	0.72	1.82	0.01	0.00	0.00	0.00	0.00	0.00	100.89	
D69-3	0.09	9.01	1.75	49.91	36.73	0.78	1.45	0.00	0.00	0.00	0.00	0.02	0.00	99.74	
D69-9	0.00	9.24	2.07	49.95	35.89	0.73	2.20	0.00	0.00	0.00	0.00	0.00	0.00	100.08	
Spinel															**Cr#**
D8-1	0.08	0.31	13.85	7.19	16.09	0.54	11.62	0.01	0.00	0.00	0.00	50.21	0.12	100.02	71
D11-2	0.04	0.39	13.26	8.36	15.80	0.57	11.42	0.04	0.00	0.00	0.00	48.66	0.12	98.67	71
D67-5	0.05	0.29	14.60	6.65	12.42	0.50	14.02	0.00	0.00	0.00	0.00	51.04	0.12	99.68	70
Apatite															
D69-2	0.24	0.00	0.00	0.43	0.00	0.12	0.26	53.81	0.17	0.02	40.03	0.00	0.00	95.08	
D69-3	0.23	0.00	0.00	0.38	0.00	0.16	0.24	54.10	0.17	0.00	40.61	0.00	0.00	95.89	

* Plagioclase microlites

Minor elements in plagioclase

Covariations of FeO wt%, MgO wt% and K_2O wt% versus An for plagioclase cores (from phenocrysts only) are shown on Figure 4.16. Plots of FeO and MgO depict two groups of plagioclase phenocrysts, whereas K_2O seems to record a wide compositional continuum from 0.25 wt% at An 27 to 0.01 at An 92.

In calcic plagioclase (An >65), FeO do not display a coherent trend with changing An and ranges from 0.43 to 0.66 wt%. MgO shows a weak negative correlation with An and its contents vary from 0.08 to 0.21 wt%. In less calcic plagioclase phenocrysts (An <64), FeO does not display any correlation with An and its contents vary from 0.37 to 0.60 wt%. MgO wt% shows a weak positive correlation and varies from 0.02 to 0.06 wt%.

4.3.5 Amphibole

Amphibole (Table 4.1) is the less abundant of all phenocryst phases (less than 0.5% of the total phenocrysts content) and is only present in dacites and rhyolites. Folowing the nomenclature of Leake (1978), compositions are tschermakite hornblende and magnesio-hornblende in dacites and ferri-titanian-magnesio-hornblende and ferri-titanian-tschermakitic hornblende in rhyolites.

4.3.6 Oxides

Where present, oxide minerals include Cr-spinel, titanomagnetite and ilmenite (Table 4.1). Cr-spinel typically occurs in basalts and basaltic andesites as i) inclusions in phenocrysts (e.g., olivine), ii) as individual grains (>0.15 mm) sparsely disseminated throughout the groundmass, and iii) in rare cases also associated with pyroxene and olivine often along their margins. Spinel compositions range from Cr# 53 to Cr# 85 (Table 4.1). Titanomagnetite and ilmenite commonly occur together in dacites and rhyolites. Typically they occur as i) individual grains (>0.15 mm) sparsely disseminated throughout the groundmass, and ii) relatively large grains (0.2–0.5 mm) associated with pyroxene and amphibole, either along their edges or partially replacing them. In dacites, the TiO_2 content of magnetite varies between 9.7–10.7 wt%, and in ilmenite between 38.8–40.6 wt%. In rhyolites, the TiO_2 content of magnetite varies between 8.8–9.2 wt%, and ilmenite from 39.3–41.2 wt%.

4.3.7 Apatite

Apatite is only present in dacite and rhyolite samples. These occur as 0.005–0.02 mm long needle-shape inclusions in phenocrysts of low-calcic plagioclase and low-magnesian pyroxene, and occasionally as small <5 micron-sized crystals in magnetite (Table 4.1).

4.4 Summary of the petrography and mineralogy of the Hunter Ridge calc-alkaline rocks

The petrographic and mineralogical study suggests that the Hunter Ridge calc-alkaline series formed largely as a result of fractional crystallisation and crystal accumulation processes, coupled with some degree of magma mixing. This is not surprising as magma mixing processes are widely recognised in subduction-related rocks.

Samples with high MgO wt% contents (>9 wt%) contain abundant high-Fo olivine and high-Mg# clinopyroxene phenocrysts that are not in equilibrium with their groundmasses (see Chapter 5 for more detail). The groundmasses are commonly relatively evolved containing less than 6.5 wt% MgO. Therefore, the high overall MgO wt% contents of these samples is most likely due to accumulation of high-Fo olivine and high-Mg# pyroxene phenocrysts rather than representing true primitive magma compositions.

Additional evidence for entrainment of pre-existing material (e.g. either phenocrysts phases, or crystals derived from disruption of pre-existing rocks (i.e. wall-rock of the plumbing system) includes i) the presence of glomerocrysts (olivine and pyroxene) and ii) the phenocrysts with primitive compositions that display varying degrees of disequilibrium. Interaction between new batches of magma and pre-existing cumulate material within the plumbing system is a typical feature of subduction-related volcanic systems (e.g. Danyushevsky et al., 2002, 2004; Dungan & Davidson, 2004; Davidson et al., 2005; Reubi & Blundy, 2008).

For the more evolved rocks with low MgO (<3.5 wt%; e.g. dacites), the plagioclase and clinopyroxene phenocrysts span a wider range in composition than those in basalts, basaltic andesites and rhyolites. In addition, the dacites contain bimodal populations of plagioclase and clinopyroxene (Figs 4.9, 4.15). These samples also contain olivine with a wide range in compositions (Fo# 74–89) that commonly display disequilibrium textures (i.e. resorption features, embayments). Although some of the textural features displayed by the high calcic- plagioclase (i.e. hollows inside the crystals) could be explained through rapid crystallisation of evolved hydrous magmas, the calculated partition coefficients for Sr and Ba are not (see Chapter 5). As we show later, trace elements in plagioclase indicate that they were not formed from the melt corresponding to groundmass in composition.

Thus, the mineral chemistry, along with textural observations for the dacites point to some form of mixing combined with dissolution-reaction–mixing processes (DRM; Danyushevsky et al., 2004), in which crystals of different provenance are found in the same rock. DRM processes occur within the plumbing system, at the margin of primitive magma bodies, where the magma is in contact with cooler rocks (i.e. wall rocks or mush zones). This interaction of a hot magma body with cooler material leads to partial dissolution of mineral phases than are not in equilibrium with the ascending hotter magma, and mixing will inevitably occur. If this pre-existing material comes from within a mush zone, the crystals and melts are likely to be comagmatic. Mush columns are recognised to contain phenocrysts and residues formed during fractionation of earlier magmas of the same magma type (e.g. Davidson & Tepley, 1997; Danyushevsky et al., 2004; Smith et al., 2009).

In summary, the broad range in compositions of the main mineral phases in these samples

record prolonged histories of magma evolution from the very earliest stages of fractionation to their subsequent eruption. This is an important concept, which will be used to reconstruct the crystallization history of these rocks in the next chapter.

4.5 Petrography of the Hunter Ridge adakitic rocks

Adakite samples from the Hunter Ridge are moderately vesicular (~20–30 volume %) pillow lavas with glassy rims. All samples used for this study are porphyritic basaltic andesites where phenocrysts represent approximately 15% by volume of the sample. Olivine (~8 volume %) and clinopyroxene (7% volume) are the dominant phenocrysts phases and occur throughout the groundmass as large clusters of small to large phenocrysts or as single small to large grains. The clusters range in size from 1 mm to 5 mm and the individual olivine and clinopyroxene phenocrysts from 0.5 to 3.5 mm. Some clinopyroxene and olivine crystals display melt and mineral inclusions (e. g., spinel inclusions and/or olivine inclusions in clinopyroxene and vice versa). Oxides are very rare and occur as individual grains of up to 0.1 mm or as small inclusions (<0.05 mm) in phenocrysts.

Groundmasses represent up to 65% by volume of the sample and are generally glassy or consist of partially devitrified glass displaying hyalopilitic texture. In the latter, these can contain numerous small (<0.025 mm) pyroxene and olivine grains, representing up to 5% of the groundmass. Photomicrographs in Fig. 4.17 show the petrographic features described here.

4.6 Mineral Chemistry of the Hunter Ridge adakitic rocks

4.6.1 Olivine

Cores and rims of olivine phenocrysts (74 and 23 respectively) were analysed to document the compositional range of olivine in the Hunter Ridge adakitic lavas. Core compositions range from Fo 86–92 and display a unimodal distribution with the majority of cores having Fo 88–89 (Fig. 4.18). Rim compositions range from Fo 86–90, which is within the range measured for the cores (Fig. 4.18). Most olivine grains are unzoned.

Trace elements in olivine

Minor and trace elements such as MnO, CaO and NiO show some variations among the analysed olivine phenocrysts from adakite magma suites. Plots of MnO wt%, CaO wt% and NiO wt% versus Fo content for olivine cores from these rocks are shown on Figure 4.19. CaO and NiO concentrations are scattered and do not show any coherent trend with changing forsterite content. %. CaO concentrations in these olivines range from 0.13 to 0.20 wt% and NiO from 0.18 to 0.41 wt%. . MnO shows a negative correlation with Fo# and varies between 0.13 and 0.22 wt%.

4.6.2 Clinopyroxene

Cores and rims of clinopyroxene grains (72 and 18 respectively) were analysed to characterise their compositional range in the Hunter Ridge adakites. Core compositions range from Mg# 81–92 with a

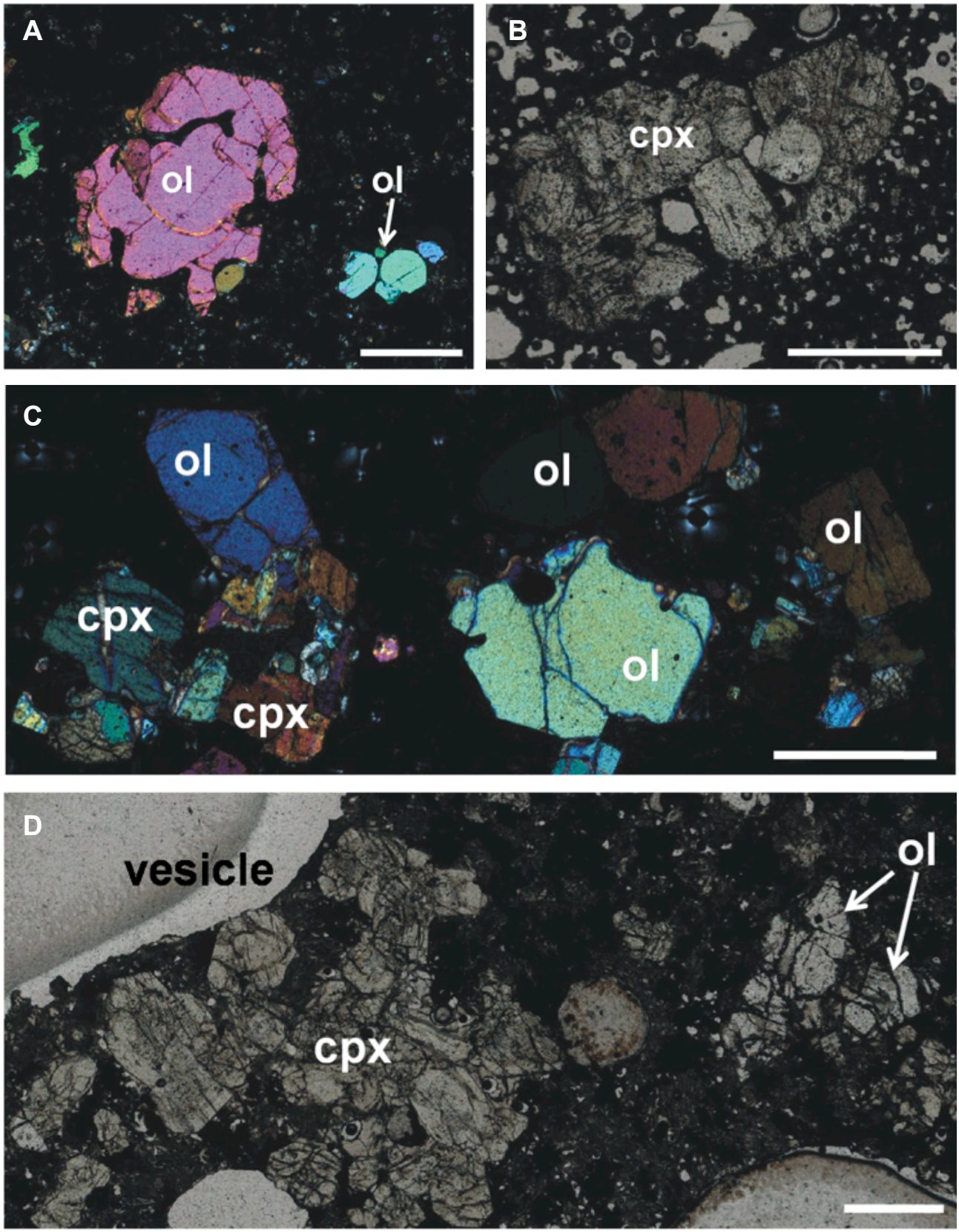

Fig. 4.17. Petrographic features of basaltic andesites from the Hunter Ridge adakite series. A) Large olivine (ol) phenocryst showing resorption features and smaller subhedral olivine grains in a glassy groundmass containing very small olivine±clinopyroxene grains (Sample No. D15-1). B) Crystal cluster containing euhedral-subhedral clinopyroxene (cpx) phenocrysts in a glassy groundmass containing of a moderately vesicular sample (Sample No. D15-2). C) Crystal cluster containing large olivine and clinopyroxene phenocrysts and subhedral-anhedral olivine grains in a glassy groundmass (Sample No. D15-2). D) Crystal cluster containing subhedral clinopyroxene grains and two olivine phenocrysts showing resorption features in a glassy groundmass of a highly vesicular rock (Sample No. D15-4).

near uni-modal distribution with a mode of 89 (Fig. 4.20). Rim compositions range from Mg# 85–91 with a mode lower than that of the cores at 87 (Fig. 4.20). Clinopyroxene is augite with a range from $En_{50–56}$ $Fs_{5–9}$ $Wo_{38–43}$. Most phenocrysts are unzoned, however, grains displaying minor normal and reverse zoning patterns (up to 2–3 units of Mg#) are also present and are commonly observed within a single sample.

Minor elements in clinopyroxene

TiO_2, MnO, Na_2O and Cr_2O_3 contents of the clinopyroxene phenocryst cores are shown on Figure 4.21. TiO_2 shows a weak negative correlation with Mg# and varies from 0.08 to 0.21 wt%. MnO and Na_2O do not display a large range in values and do not show any coherent trend with Mg# (MnO ranges from 0.12 to 0.17 wt% and Na_2O from 0.22 to 0.29 wt%). Cr_2O_3 contents are scattered and vary from 0.04 to 1.04 wt%.

4.6.3 Oxides

Oxide minerals are Cr-spinel, typically occurring as inclusions in phenocrysts (e.g., olivine), in rare cases also associated with pyroxene and olivine often along their margins. Spinel compositions range from Cr# 70 to Cr# 85 (Table 4.2).

4.7 Comparison to the Hunter Ridge calc-alkaline rocks

Table 4.3 shows a generalised comparison for the calc-alkaline and adakitic basaltic andesite lavas from the Hunter Ridge. The primary difference is the presence of significant plagioclase phenocrysts in the calc-alkaline lavas. Basaltic andesites in both magma series contain olivine and clinopyroxene, although these minerals are universally more abundant in the latter. Fo contents in olivine phenocrysts from adakite samples display a narrower range than in the calc-alkaline samples, with the former having more primitive compositions (Fo 86–92 vs 79–91). Overall, clinopyroxene phenocrysts display the same range in Mg# in both magmatic suites (Figs 4.18, 4.20). However, in the adakite samples, the clinopyroxene phenocrysts tend to have more primitive compositions. Minor element compositions in both olivines and clinopyroxenes overlap with those of the calc-alkaline minerals (Figs 4.19, 4.21).

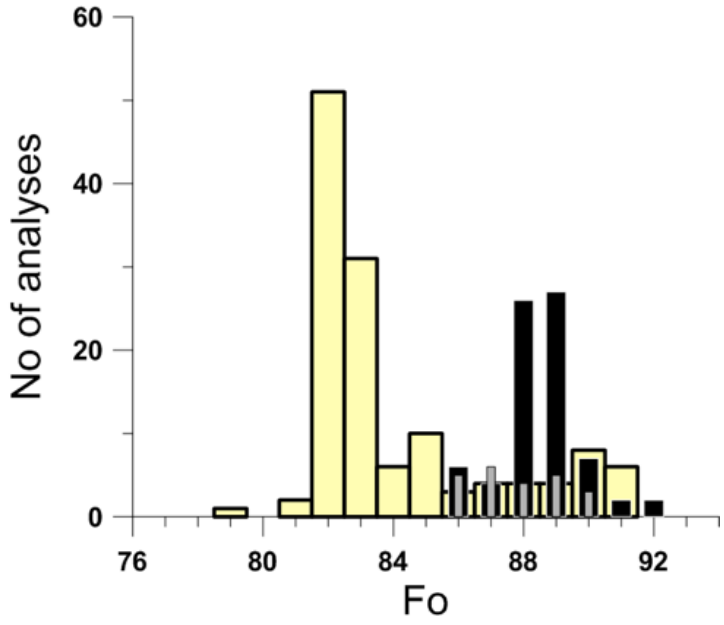

Fig. 4.18. Histogram showing the total distribution of olivine forsterite content for the Hunter Ridge adakites. Black coloured bars indicate core compositions and grey coloured bars indicate rim compositions. Yellow coloured bars show the total distribution of olivine Fo for the basaltic andesite rocks from the calc-alkaline series.

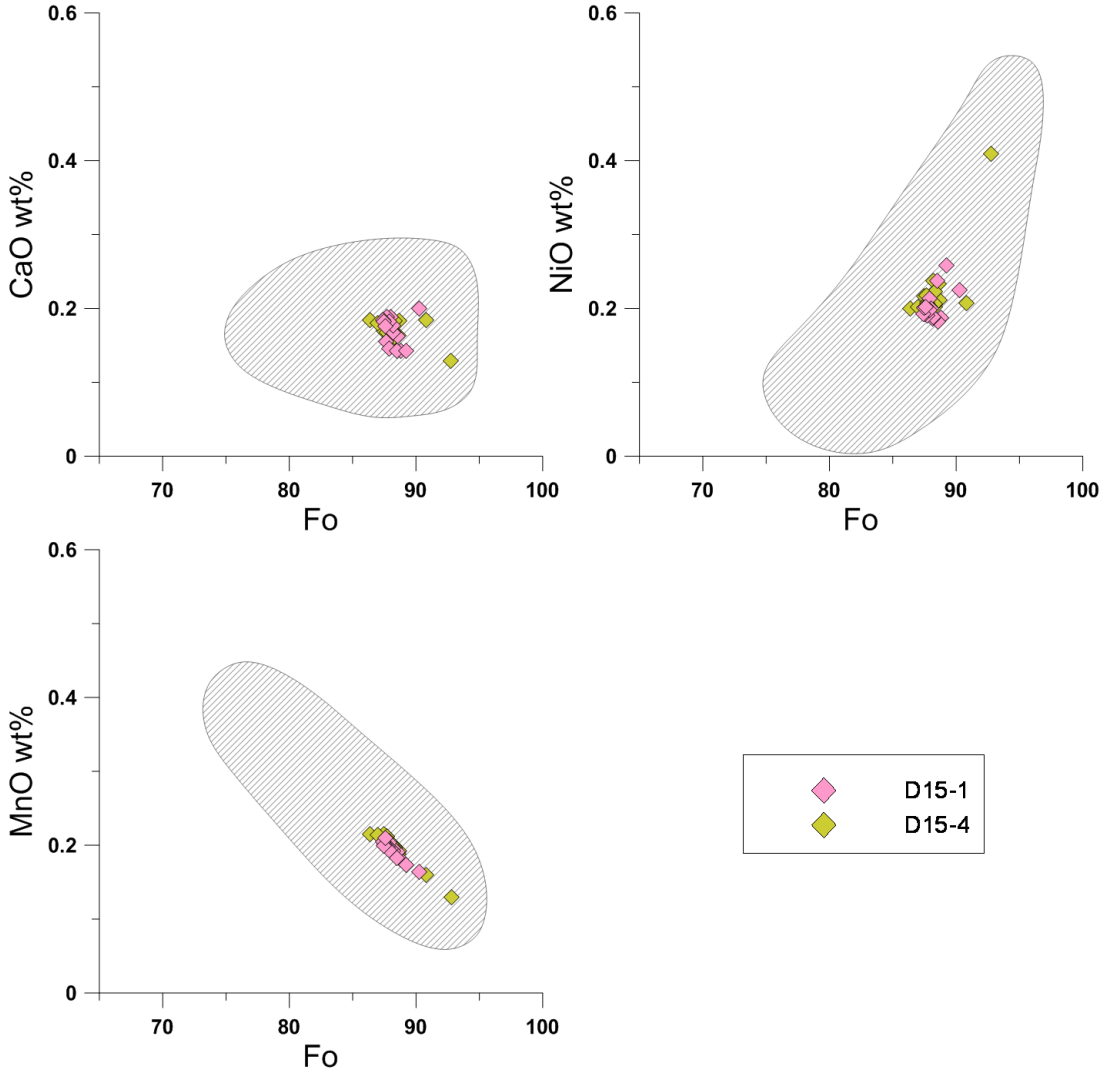

Fig. 4.19. Minor element contents plotted against Fo for olivine phenocrysts from the Hunter Ridge adakites compared to olivines from the Hunter Ridge calc-alkaline series (grey shaded field).

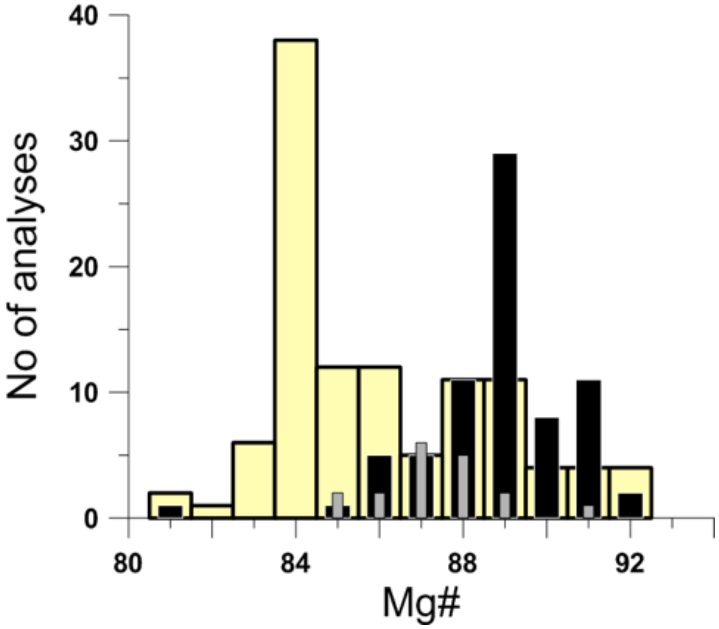

Fig. 4.20. Histogram showing the total distribution of clinopyroxene Mg# for the Hunter Ridge adakites. Black coloured bars indicate core compositions and grey coloured bars indicate rim compositions. Shaded bars show the total distribution of olivine Fo for the basaltic-andesite rocks from the calc-alkaline series.

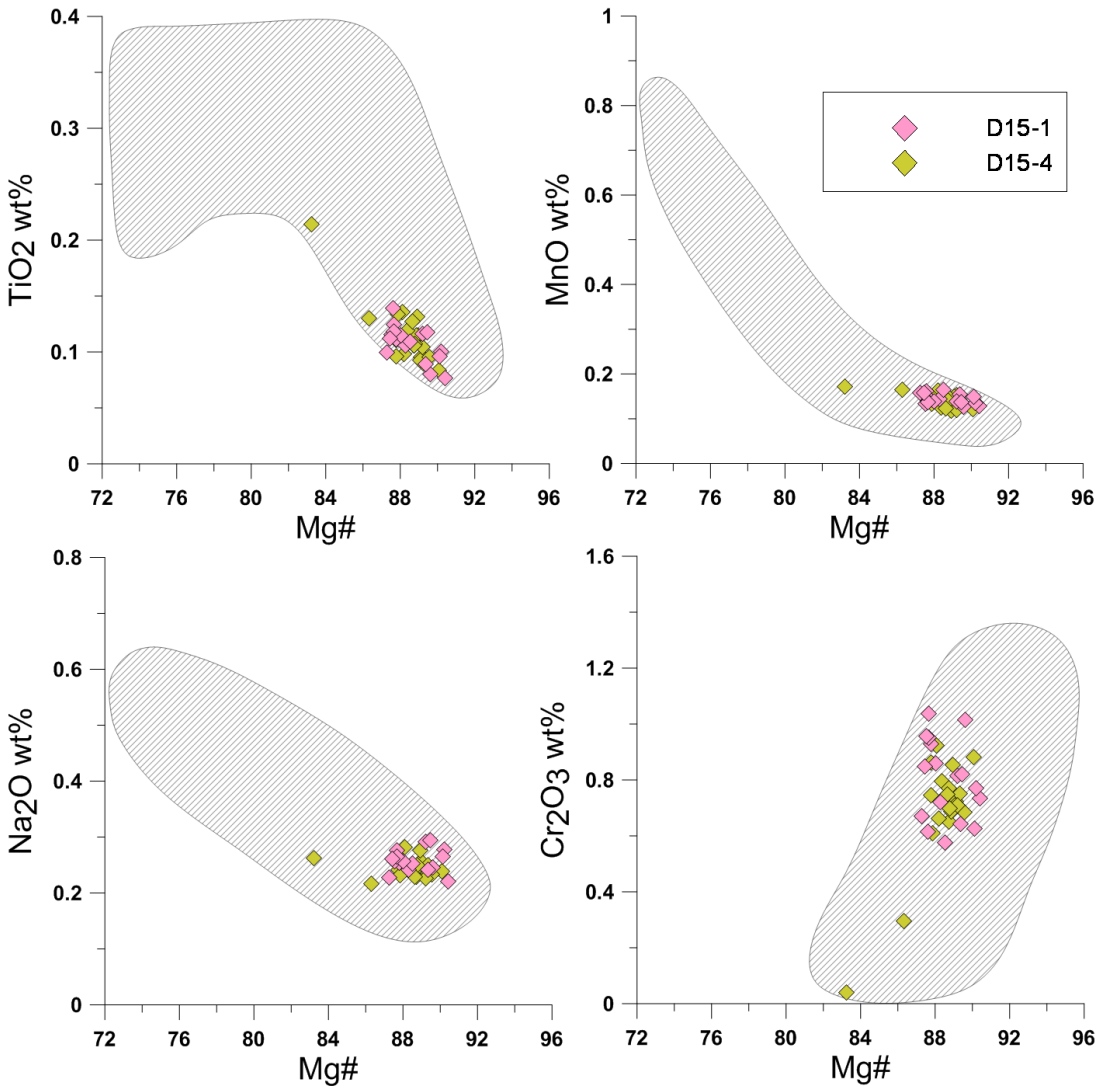

Fig. 4.21. Minor element contents plotted against Mg# for clinopyroxene phenocrysts from the Hunter Ridge adakites compared to clinopyroxenes from the Hunter Ridge calc-alkaline series (grey shaded field).

Table 4.2. Average mineral compositions (wt%) for the Hunter Rudge adakites.

Sample	SiO_2	TiO_2	Al_2O_3	FeO	Fe_2O_3	MnO	MgO	CaO	Na_2O	K_2O	P_2O_5	Cr_2O_3	NiO	Total	
Olivine															**Fo**
D15-1	40.17	0.00	0.00	10.95	0.00	0.21	48.44	0.18	0.00	0.00	0.00	0.01	0.00	99.96	89
D15-2	40.40	0.00	0.00	12.91	0.00	0.24	46.32	0.19	0.01	0.00	0.00	0.00	0.16	100.25	86
D15-4	40.24	0.00	0.00	10.92	0.00	0.22	47.73	0.20	0.00	0.00	0.00	0.00	0.21	99.52	89
D15-5	40.22	0.00	0.00	12.95	0.00	0.25	46.54	0.19	0.00	0.00	0.00	0.01	0.17	100.33	87
Clinopyroxene															**Mg#**
D15-1	53.88	0.15	1.73	4.05	0.00	0.15	19.27	20.26	0.24	0.00	0.00	0.76	0.00	99.74	89
D15-2	53.88	0.18	2.03	5.04	0.00	0.19	18.39	20.34	0.21	0.00	0.00	0.52	0.00	100.80	87
D15-4	53.87	0.20	2.22	4.68	0.00	0.17	18.09	20.19	0.31	0.04	0.01	0.48	0.01	100.28	87
D15-5	53.73	0.19	2.16	5.17	0.00	0.19	18.72	19.72	0.21	0.00	0.00	0.63	0.00	100.72	87
Spinel															**Cr#**
D15-2	0.00	0.46	9.17	13.12	16.98	0.56	10.44	0.00	0.00	0.00	0.00	48.76	0.09	99.58	78
D15-4	0.07	0.41	9.74	10.76	15.90	0.52	11.18	0.03	0.00	0.00	0.00	50.58	0.10	99.29	78
D15-5	0.02	0.43	9.00	13.11	17.47	0.55	10.14	0.03	0.00	0.00	0.00	48.98	0.07	99.80	78

Table 4.3. Comparison between the Hunter Ridge calc-alkaline and adakitic basaltic andesites.

Rock Series	Phyric (Y/N)	Phenocryst phases	Approximate abundance
Calc-Alkaline	Y	Plagioclase	85%
(basaltic andesite)		Olivine	5%
		Cpx	10%
Adakite	Y	Olivine	60%
(basaltic andesite)		Cpx	40%

Chapter 5

Identification of the calc-alkaline fractionation series

5.1 Introduction

Calc-alkaline rocks from the Hunter Ridge display a wide compositional range from picritic basalts (SiO_2 ~50 wt%, MgO ~13 wt %) to rhyolites (SiO_2 ~73 wt%, MgO ~0.3 wt %) reflecting an example of magmatic evolution by fractional crystallisation.

The main aim of this chapter is to reconstruct the crystallisation history of these rocks. This relies on the rocks being genetically related and, therefore, belonging to a single magma fractionation series.

In the first part of this chapter, major element data are used to model the fractional crystallisation processes. As magmas crystallise, their major and trace element compositions evolve along lines determined by their phase equilibria (i.e. liquid lines of descent 'LLD'). Identifying a single liquid line of descent establishes a common genetic relationship between the rocks, and that they therefore belong to a single magma series (or are closely related). As with most arc magmas, rocks from the Hunter Ridge are affected to some extent by magma mixing and crystal accumulation.

In the second part of this chapter, trace element data are presented that allow the effects of magma mixing and crystal accumulation to be recognised and accounted for during subsequent modelling.

5.2 Modelling of fractional crystallisation: Major elements

Before attempting to explain the crystallisation history of the Hunter Ridge calc-alkaline rocks, it is necessary to ascertain which samples or what portions of these samples (e.g. quenched glass, groundmass) represent melts and what minerals are in equilibrium with these melts.

As outlined in the previous chapter, most of the primitive samples from the Hunter Ridge are phyric lavas with a large proportion of high-Fo olivine phenocrysts, high Mg# clinopyroxene and high-An plagioclase. The large range of compositions of unzoned phenocrysts in these rocks (see Chapter 4) implies that most of the phenocryst population is not in equilibrium with the groundmass of the samples, which is interpreted as being a record of the composition of the melt phase in the erupted magma. These compositional features suggest that the rocks have undergone crystal accumulation, and therefore their bulk compositions are not representative of the compositions of melts which existed in the plumbing system. Where quenched glass rinds were present, their compositions were considered representative of the composition of the melt phase of the erupted magmas. Where possible, groundmasses were analysed by electron microprobe and LA-ICP-MS for samples which did not have quenched glass rinds. Where this was not possible, groundmass compositions were calculated using a mass-balance method. Whole-rock data for the Hunter Ridge calc-alkaline samples are presented in Table 5.1., major element compositions of glasses and groundmass are presented in Table 5.2 and shown in Figure 5.1.

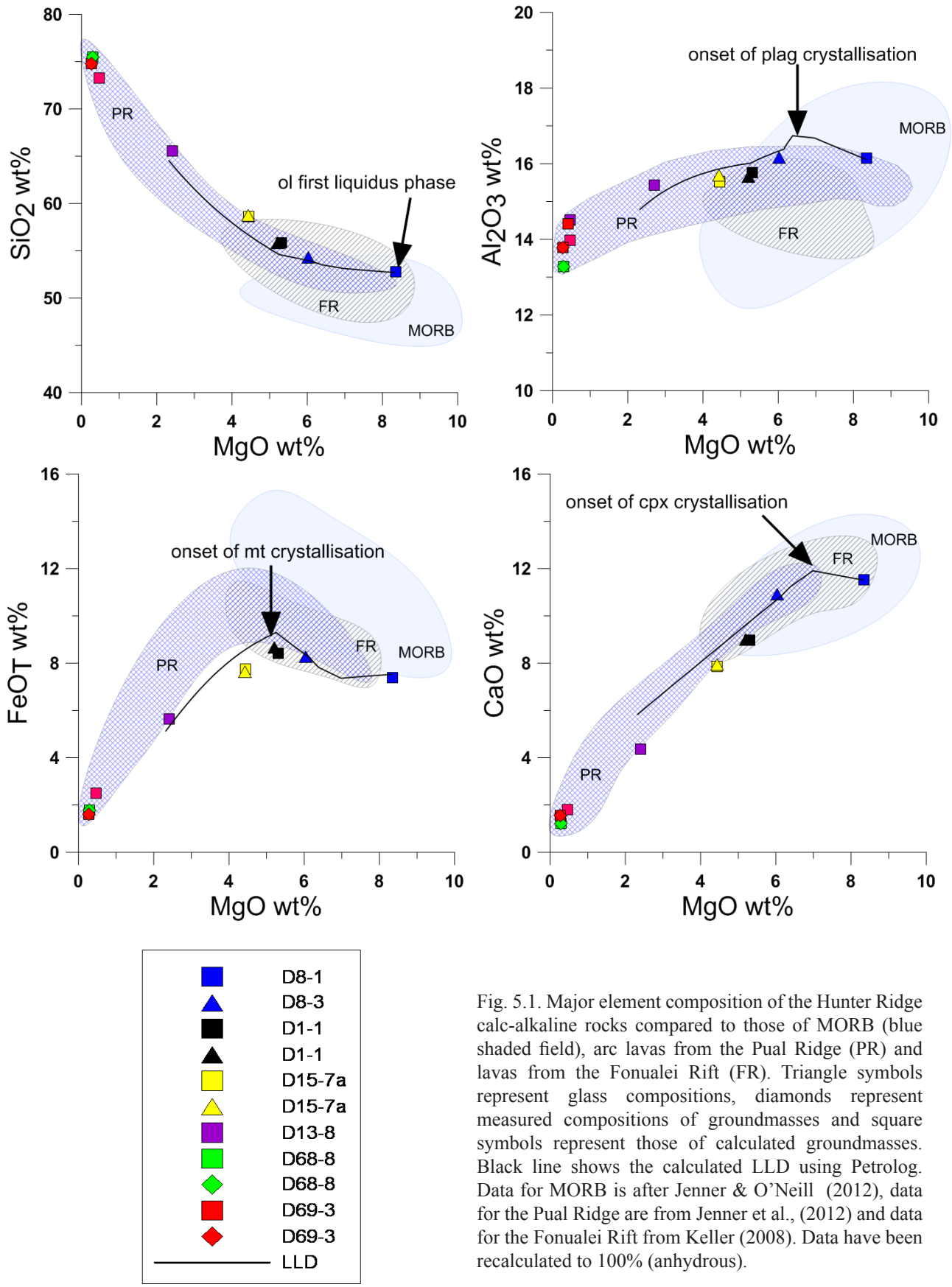

Fig. 5.1. Major element composition of the Hunter Ridge calc-alkaline rocks compared to those of MORB (blue shaded field), arc lavas from the Pual Ridge (PR) and lavas from the Fonualei Rift (FR). Triangle symbols represent glass compositions, diamonds represent measured compositions of groundmasses and square symbols represent those of calculated groundmasses. Black line shows the calculated LLD using Petrolog. Data for MORB is after Jenner & O'Neill (2012), data for the Pual Ridge are from Jenner et al., (2012) and data for the Fonualei Rift from Keller (2008). Data have been recalculated to 100% (anhydrous).

5.2.1 Estimation of groundmass composition by mass-balance calculations

Where direct measurements of the groundmass were not possible, these were calculated from the whole-rock data using a mass-balance approach. This method uses the average composition of the mineral phases, which are then subtracted from the whole-rock data in accordance with their modal proportions (Tables 5.2, 5.6). For the calculations, all compositions were recalculated to 100 wt% (anhydrous). To account for the differences in density between the groundmass (2.4–2.8 g/cm^3) and the ferromagnesian minerals (i.e. clinopyroxene: 3.19–3.56 g/cm^3; olivine: 3.22–3.37 g/cm^3; amphibole: 3.02–3.59 g/cm^3; Deer, Howie and Zussman, 1966) the volume proportions of the minerals were adjusted to mass proportions. This is not required for plagioclase since its density is similar to that of the groundmass. The results of the calculations are shown in Tables 5.2, 5.3 and 5.6 and in Figure 5.1.

In order to assess the accuracy of this approach, groundmass compositions calculated using a mass-balance method are compared, where possible, to direct measurements from the microprobe (results shown in Table 5.3). This was possible for samples D1-1, D15-7a, D69-3, and D69-10 and the results show good agreement between the calculated and measured compositions for all major oxides (Table 5.3).

Groundmass compositions define an evolutionary trend from basalt (represented by sample D8-1-groundmass; SiO_2 52.8 wt%, MgO 8.4 wt%) to rhyolite (represented by samples D68-8-groundmass and D69-3-groundmass; SiO_2 ~75 wt%, MgO ~0.3 wt%). Major element trends displayed for these samples are shown in Figure 5.1. These are shown together with fields for i) MORB, ii) a suite of arc-related rocks from the Pual Ridge, Eastern Manus Basin (from Jenner et al., 2010), and iii) a suite of back-arc basin rocks with arc signature from the Fonualei Rift, Lau Basin (from Keller, 2009). samples from the Vanuatu arc, the Pual Ridge and the Fonulaei Rift because rocks from these locations represent arc lavas or have a typical arc signature. Analyses reported for these locations show a similar range in composition to the Hunter Ridge calc-alkaline samples and provide good comparison examples. Our data show that the calc-alkaline rocks from the Hunter Ridge display major element behaviour similar to those of the arc-related suites from Pual Ridge and Fonualei Rift. All the arc-related rock suites show coherent trends of increasing SiO_2, K_2O and Na_2O with decreasing melt MgO contents. SiO_2 and K_2O contents in arc rocks are higher than those in MORB at similar melt MgO contents. In contrast, Na_2O contents overlap with the field for MORB. For the Hunter Ridge samples, FeO and TiO_2 increase to their maximum values at ~5 wt% MgO content of the melt and thereafter markedly decrease. The abundances of these two major oxides in all arc rocks are lower than those in MORB at similar melt MgO contents. Similarly, CaO contents initially rise with decreasing MgO from 8.3–7 wt%, then rapidly fall. CaO contents in all arc rocks overlap those in MORB at a similar MgO content. Al_2O_3 content in samples from the Hunter Ridge and the Pual Ridge show initial behaviour similar to CaO and decreases with decreasing MgO. Conversely, samples from the Fonualei Rifts do not show a coherent trend. MORB samples show a more pronounced decrease in Al_2O_3 with decreasing melt MgO content compared to the arc-related samples.

5.2.2 Establishing mineral/melt correspondence

The compositions of minerals in equilibrium with the groundmass (calculated or measured) were derived using Petrolog v3 (Danyushevsky & Plechov, 2011), which uses published models of mineral-melt equilibrium. For olivine, models by Ford et al. (1983) are used, for clinopyroxene and plagioclase those by Ariskin et al. (1993), and for magnetite, Ariskin and Barmina (1999). These estimate pseudo-liquidus temperatures and liquidus mineral compositions. The mineral(s) present on the liquidus for a given melt composition is that with the highest calculated pseudo-liquidus temperature. Minerals are considered to be on the liquidus simultaneously (i.e. cotectic crystallisation) when the difference in their calculated pseudo-liquidus temperatures is $<\pm 20^{O}C$ (Danyushevsky & Plechov, 2011). It is worth noting that the errors in the calculated mineral compositions using the models listed above are within ±1–3 mol% for clinopyroxene, plagioclase and magnetite, and ±1 mol% for olivine. The results of the calculations are shown in Table 5.4. All calculations were done for water-saturated conditions with an oxygen fugacity Ni–NiO+2 log units, which is typical for arc magmas (Blatter and Carmichael, 1998; Brandon and Draper, 1996; Gill, 1981; Arculus, 1985; Parkinson and Arculus, 1999; Kelemen et al., 2003).

Sample D8-1-groundmass (the most primitive melt composition) has both olivine (Fo ~88) and clinopyroxene (Mg# ~90) as liquidus phases (Table 5.4). These are in good agreement with the mineral compositions obtained by microprobe from sample D8-1, in which olivine compositions range from Fo 83–93 and clinopyroxene from Mg# 84–92.

Melt-liquidus calculations for samples D1-1-glass and D1-1-groundmass result in extremely similar liquidus compositions for olivine (Fo ~81), clinopyroxene (Mg# ~82) and plagioclase (An ~59) (Table 5.4). For olivine and clinopyroxene, the modelled compositions closely match measurements made on phenocrysts from sample D1-1 (olivine Fo 82–84 and clinopyroxene Mg# 81–91). For plagioclase, the difference in the calculated An (~59) and the lower end of the measured An (63–83) is close when the errors are taken into consideration (i.e. ±1–3 mol%).

Melt liquidus calculations for samples D15-7a-glass and D15-7a-groundmass produce slightly different liquidus compositions for olivine (Fo 80 and 83 respectively), clinopyroxene (Mg# 80 and 84 respectively) and plagioclase (An 57 and 55, respectively) (Table 5.4). Similar to sample D1-1, only the compositions for olivine and clinopyroxene are similar between the calculated and measured values in sample D15-7a, where olivine varies between Fo 82–85 and clinopyroxene between Mg# 75–89. Measured compositions for plagioclase are significantly more calcic and range from An 65–84.

Melt liquidus calculations for sample D13-8-groundmass, produce olivine (Fo ~78), clino-pyroxene (Mg# ~75), orthopyroxene (Mg# ~79) and plagioclase An 22 (Table 5.4). The calculated compositions for olivine and clinopyroxene are a close match to those measured in sample D13-8, though both minerals display a wide range of compositions (olivine Fo 75–89 and clinopyroxene Mg# 71–88). Conversely, calculated orthopyroxene and plagioclase compositions do not match those measured in this sample. The most magnesian orthopyroxene has an Mg# of 74, and even the least calcic plagioclase has an An of 40.

Sample D68-8-groundmass (the most evolved melt) has calculated compositions for clinopyroxene (Mg# ~44), orthopyroxene (Mg# ~61) and plagioclase (An ~3) (Table 5.4). These

calculated compositions are not consistent with those measured from clinopyroxene, orthopyroxene and plagioclase phenocrysts in this sample. The least magnesian clinopyroxene and orthopyroxene both have Mg# of 70, whereas even the least calcic plagioclase has An 27 (i.e. significantly higher than predicted from the modelling).

It is worth noting that, currently, there are no models available in Petrolog for amphibole and there is a recognised issue for plagioclase. The software in its current version does not accurately model plagioclase within hydrous (e.g. arc) magmas, with errors thought to be around 10 mol% An (see end of Section 5.3.3).

5.2.3 Modelling fractional crystallisation using a least-squared regression method

Major element concentrations were modelled using the 'MIXING' application in IgPet (Carr, 2001). The approach uses a least square regression to calculate the proportions of crystallising phases between any two given melt compositions.

The parental melt composition (P) represents the most primitive melt of the calc-alkaline magma series present in our rocks (sample D8-1-Groundmass; Table 5.3). The chosen daughter (D) composition is the most differentiated melt, which in our samples is represented by sample 'D68-8-Groundmass' (Table 5.3).

The goal of the modelling is to explain the major element changes between points P and D assuming this is due to fractional crystallisation, and modelling of the differentiation trends were divided in four stages/steps. The crystallising phenocryst phases (i.e. olivine, clinopyroxene, plagioclase, magnetite and amphibole) are considered to be in equilibrium with their melts at a given stage of fractionation. For each step of the modelling, the mineral compositions used for the calculations reflect an intermediate (equilibrium) value between the start and end of the run. This approach produced a better fit with lower errors than using mineral compositions in equilibrium with either the initial or final melt compositions. The major element trends displayed by the Hunter Ridge calc-alkaline magmas are shown in Figure 5.1.

During the first step of modelling (8.4–6.12 wt% MgO), we assume that olivine, clinopyroxene and plagioclase crystallise during the initial 20% of fractionation (modal proportions: 26, 33, and 41 % respectively). In the second step (6.12–5.2 wt% MgO), olivine, clinopyroxene and plagioclase continue to crystallise but their modal proportions change substantially (modal proportions: 5, 43, and 52 % respectively). During the third step (5.2–2.4 wt% MgO), magnetite joins the liquidus assemblage together with olivine, clinopyroxene and plagioclase (modal proportions: 8, 5, 31, 56 % respectively). During the fourth and last step of the modelling, the crystallising assemblage becomes magnetite, clinopyroxene, plagioclase and amphibole (modal proportions: 9, 16, 56 and 19% respectively). The fourth step of fractionation has also been modelled including orthopyroxene (Mg# 70–74) as part of the crystallising assemblage. According to IgPet, orthopyroxene will not precipitate from the chosen start composition for this step. Mineral compositions, as well as results for each stage, are listed in Table 5.5 and shown in Figure 5.2.

The model explains the steady increase in SiO_2 from 52.8 to 75.4 wt%, Na_2O from 2.5 to 5.5 wt%, and K_2O from 0.5 to 2 wt% (Fig. 5.1). CaO contents generally fall, though there is a slight rise

from 8.3–7 wt% MgO, due to a small amount of olivine-only crystallisation before clinopyroxene appears on the liquidus. The modelling also explains the trends displayed by TiO_2, Al_2O_3 and FeO. Early crystallisation of olivine and clinopyroxene leads to an increase in Al_2O_3, FeO, and TiO_2 with decreasing MgO wt%. This initially incompatible behaviour results in their enrichment in the melt. The concentration of Al_2O_3 rises at first (composition range 8.3–6 MgO wt%; Fig. 5.1), after which it falls due to the onset of plagioclase crystallisation (Fig.5.1). Similarly, TiO_2 and FeO contents increase between 8.3–5.5 MgO wt%, and then fall due to onset of magnetite crystallisation (Fig. 5.1).

Modelling calculations in Petrolog were carried out with two main objectives: i) to corroborate whether the mineral proportions obtained using IgPet are consistent with the expected mineral proportions during crystallisation of these lavas, and ii) to identify the LLD for the calc-alkaline magmas. The models used to calculate the compositions of the phases crystallising along the LLD are the same as those described in Section 5.2.2. Some of these models include the effects of pressure and water content on mineral-melt equilibrium. Alternatively, Petrolog offers the option of a user-defined correction to account for the effects of pressure and/or water-content. This does not alter the mineral composition, only the temperature of crystallisation for a given mineral. A customised correction for magnetite was developed as none of the available models are designed for hydrous magmas. The pressure correction was set at 5 ºC /Kbar. The water correction was modified from the equation by Falloon and Danyushevsky (2000) and follows: dT (ºC) = –45*(H_2O wt%)^0.352. The use of –45 as opposed to –76 in their original equation was determined after considering the trends displayed by FeO and TiO_2 (both of which plummet at a melt MgO content of 5 wt%). A higher water correction factor will delay magnetite saturation.

The same parent melt composition (i.e. D8-1-groundmass) was used in both IgPet and Petrolog calculations (results listed in Table 5.5). The degree of fractionation was tracked by changes in melt MgO content. The crystallising assemblage after 20% of fractionation (i.e. from MgO 8.4 to 6.12 wt%, corresponding to the first of modelling using IgPet) is olivine, clinopyroxene and plagioclase (modal proportions: 21, 40, and 39% respectively). From 6.1 to 5.2 wt% MgO (corresponding to the second step of modelling using IgPet) the mineral assemblage consists of olivine, clinopyroxene and plagioclase (modal proportions: 5, 45, and 50% respectively) and the degree of fractionation attained at this point is 35%. From 5.2 to 2.4 wt% MgO (corresponding to the third step of modelling using IgPet) the crystallising assemblage is olivine, clinopyroxene, plagioclase and magnetite (modal proportions: 2, 37, 51, and 11% respectively) and the degree of fractionation is ~ 70%. At this point we have stopped the modelling of crystallisation, as the current version of Petrolog does not consider amphibole. Consequently, comparison of IgPet and Petrolog modelling has been done only for the first 3 steps of the IgPet modelling. Similar to the calculations carried out in IgPet, Petrolog does not indicate orthopyroxene crystallisation from the starting composition P at the conditions established for the modelling.

Unlike IgPet, Petrolog takes into account pressure, temperature, water contents and oxygen fugacity, and calculates the composition of the minerals being removed. Figure 5.1 shows the crystallisation trends (LLD) modelled using Petrolog with a thick black line. This LLD was defined using a polybaric crystal fractionation path with 1.5 wt% H_2O in the parental melt and an oxygen

fugacity of Ni–NiO+2. The value of 1.5 wt% H_2O is a starting value, by setting a polybaric fractionation path, the software allows H_2O to change along the LLD, rising as a result of fractionation and falling as a result of degassing. The initial pressure was set at 0.6 Kbar and the final pressure at 0.05 Kbar. Decompression along the crystallisation path is necessary to reproduce water saturation and the onset of plagioclase crystallisation. The value used of 1.5 wt% H_2O matches water contents measured using FTIR on the most primitive glasses from the calc-alkaline series (dredge D8, Table 5.3). The magma is initially H_2O-undersaturated and reaches saturation after ~ 10 % crystallisation at a pressure of 0.3 Kbar. When the modelling is done at water contents below 1.5 wt% or above 2 wt% the match to the differentiation trend displayed by Al_2O_3 is poor. In the former case, plagioclase appears earlier in the crystallisation sequence and the proportion of plagioclase relative to the Fe-Mg silicates increases. In the latter case, higher water contents cause a delay in plagioclase saturation (i.e. plagioclase appears on the liquidus at MgO contents < 6.5 wt%). Specifically, the more H_2O is in the magma, the more plagioclase saturation will be delayed and the higher the Al_2O_3 contents in the melt will become. Since the observed Al_2O_3 contents start decreasing at ~6.5 wt% MgO, this is supporting evidence for water contents in the parental melt of around 1.5–2 wt%. Water also plays an important role on the onset of magnetite crystallisation; Petrolog modelling predicts that at the same range in oxygen fugacity (fO_2 = Ni–NiO +2) lower water contents (i.e. < 2 wt%) would delay magnetite saturation.

Oxygen fugacity has the most significant effect on magnetite crystallisation, affecting also the Mg# of the melt and minerals. Oxygen fugacities of Ni–NiO +2 are required to trigger magnetite saturation at a MgO content of 5 wt%. This value is typical for magmas of most arcs and many back arcs (Blatter and Carmichael 1998; Brandon and Draper, 1996; Gill, 1981; Arculus, 1985; Parkinson and Arculus, 1999; Kelemen et al., 2003). At higher oxygen fugacities (fO_2 > Ni–NiO +2) magnetite crystallises earlier and this contradicts the FeO trend displayed by the Hunter Ridge calc-alkaline rocks, in which FeO starts decreasing at ~ 5 wt% MgO.

The primary discrepancies between the results of the Petrolog modelling and what is observed occurs with TiO_2 and Na_2O. The models predict higher TiO_2 contents in the more evolved end members than what is observed. This could be due either to the presence of an unaccounted phase containing Ti (e.g. rutile or ilmenite, or ulvospinel/titanomagnetite exsolution from the magnetites), or that the model does not accurately predict Ti in evolved rocks. The amount of ilmenite required to explain quantitatively the discrepancy in TiO_2 contents is around 1.5-2 wt% (calculated using mass balance). However there is also a problem with the magnetite model in Petrolog which underestimate the TiO_2 content of the magnetite from the moment magnetite first appears in the liquidus. Small ulvospinels were observed in many of these samples. Conversely, Na_2O contents are predicted to decrease more rapidly than the melt geochemical data shows for the more evolved rocks. This could be due to the fact that Petrolog in its current version does not accurately model plagioclase in hydrous (e.g. arc) magmas; the associated errors are thought to be around 10–11 mol% An. Evidence to support this comes from modelling using IgPet, which more accurately reproduces the proportions of the crystallising phases for a given melt composition when using plagioclase An values +10 (i.e. $\sum r^2$> 0.2, 0.6 and 1.5 for Steps 1 to 3 respectively using original Petrolog plagioclase An values, vs 0.04, 0.3 and 0.2 respectively using plagioclase An +10; Table 5.5).

Trace element partition coefficients were used to further investigate the discrepancy between the

observed and calculated An content of plagioclase. To this end, the method of Blundy and Wood (1991) was used to calculate Kd's for Sr and Ba which are known to be strongly dependent on plagioclase molar An content. The results for our samples indicate there is a systematic discrepancy of ~10 An units between the expected plagioclase An values and those calculated by Petrolog. For example, using the method of Blundy and Wood (1991), a plagioclase of An~87 (i.e. the most anorthitic composition used in our modelling) is expected to have $D_{Sr}^{plag/melt}$ and $D_{Ba}^{plag/melt}$ of 1.4 and 0.13 respectively. These values are in close agreement with the $D_{Sr}^{plag/melt}$ and $D_{Ba}^{plag/melt}$ obtained from LA-ICP-MS measurements in groundmass/phenocrysts equilibrium pairs (1.5 and 0.10 respectively). Petrolog, however, calculates the plagioclase in these samples to be less calcic by approximately –10 An units.

5.2.4 Summary of the major-element modelling

The crystallisation sequence for the Hunter Ridge calc-alkaline rocks is shown in Figure 5.1 and Table 5.5. The geochemical data measured from groundmasses analyses (recalculated to 100% anhydrous) closely correspond to the model liquid-line-of-descent from Petrolog (black lines on Fig. 5.1). Furthermore, the modal proportions for the main crystallising phases from Petrolog are a close match to the mineral proportions calculated with IgPet (Table 5.5). Modelling in Petrolog provides information on the compositions of the crystallising phases (Fig. 5.2), and these compare closely to those measured from the samples (once the systematic ~10 mol% An offset is taken into consideration).

The trends displayed by the major elements can be summarised in four main steps: i) from 8.4 to 6.5 wt% MgO in melt, crystallisation of olivine is followed closely by clinopyroxene, as shown by the slight increase in CaO from 8.3 to 7.0 wt% MgO. The Fo and Mg# of the first olivine and clinopyroxene to appear on the liquidus are 90 and 88, respectively, ii) at ~6.5 wt% MgO plagioclase starts to crystallise, as evidenced by the decrease in Al_2O_3. The composition of the early plagioclase is An 87, iii) magnetite saturation can be traced back to ~5 wt% MgO as evidenced from the plummet in FeO contents, and iv) below ~2.5 wt% MgO, amphibole + apatite will join the crystallisation sequence (this agrees with our petrographical observations where amphibole and apatite are present only in the more evolved samples). An important point to emerge from the modelling is that both IgPet and Petrolog fail to consider orthopyroxene as a liquidus phase. This does not agree with our petrographic observations where orthopyroxene is present in the dacites and rhyolites. Consequently, either the modelling software does not fully consider the mechanics of orthopyroxene crystallisation, or the orthopyroxene crystals observed are xenocrysts that did not crystallize from these melts. Orthopyroxene present in the dacite samples display more evolved compositions (Mg# ~70–75) than those predicted using the "melt-liquidus association" tool in Petrolog (Mg# ~79). Similarly, the orthopyroxenes present in the rhyolites display more primitive compositions (Mg# ~68–74) than those calculated with Petrolog (Mg# ~61). It is also worth noting that the modal proportion of orthopyroxene phenocrysts in the dacites and rhyolites is less than 0.5 % and, consequently, their influence on the major element compositions is negligible.

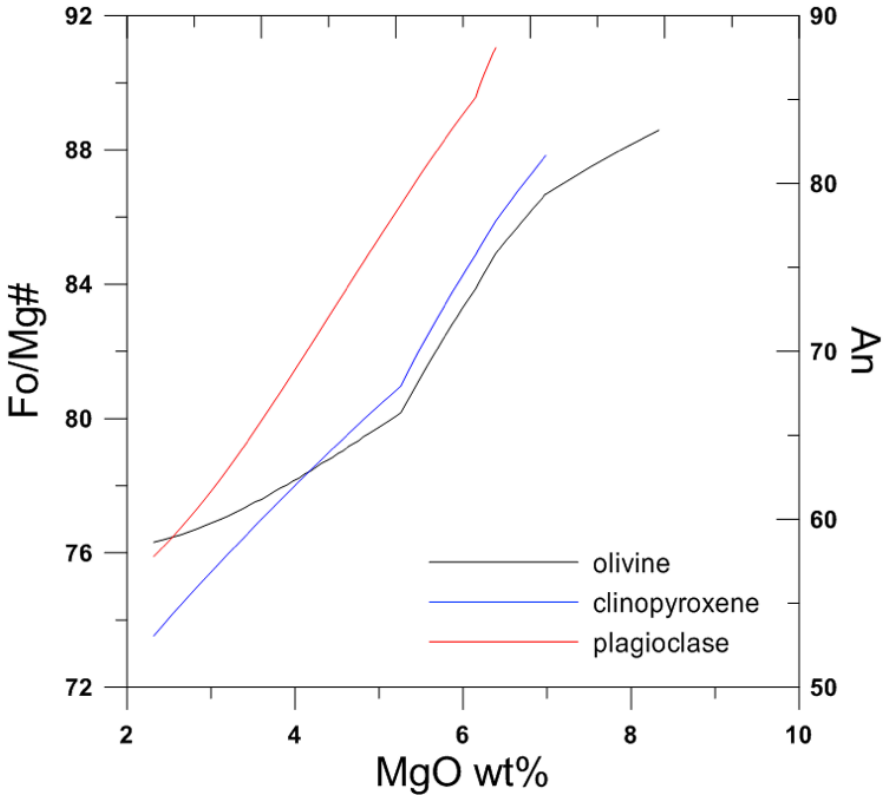

Fig. 5.2. Mineral Fo, Mg# and An versus melt MgO wt%, showing the evolution pathways of the minerals.

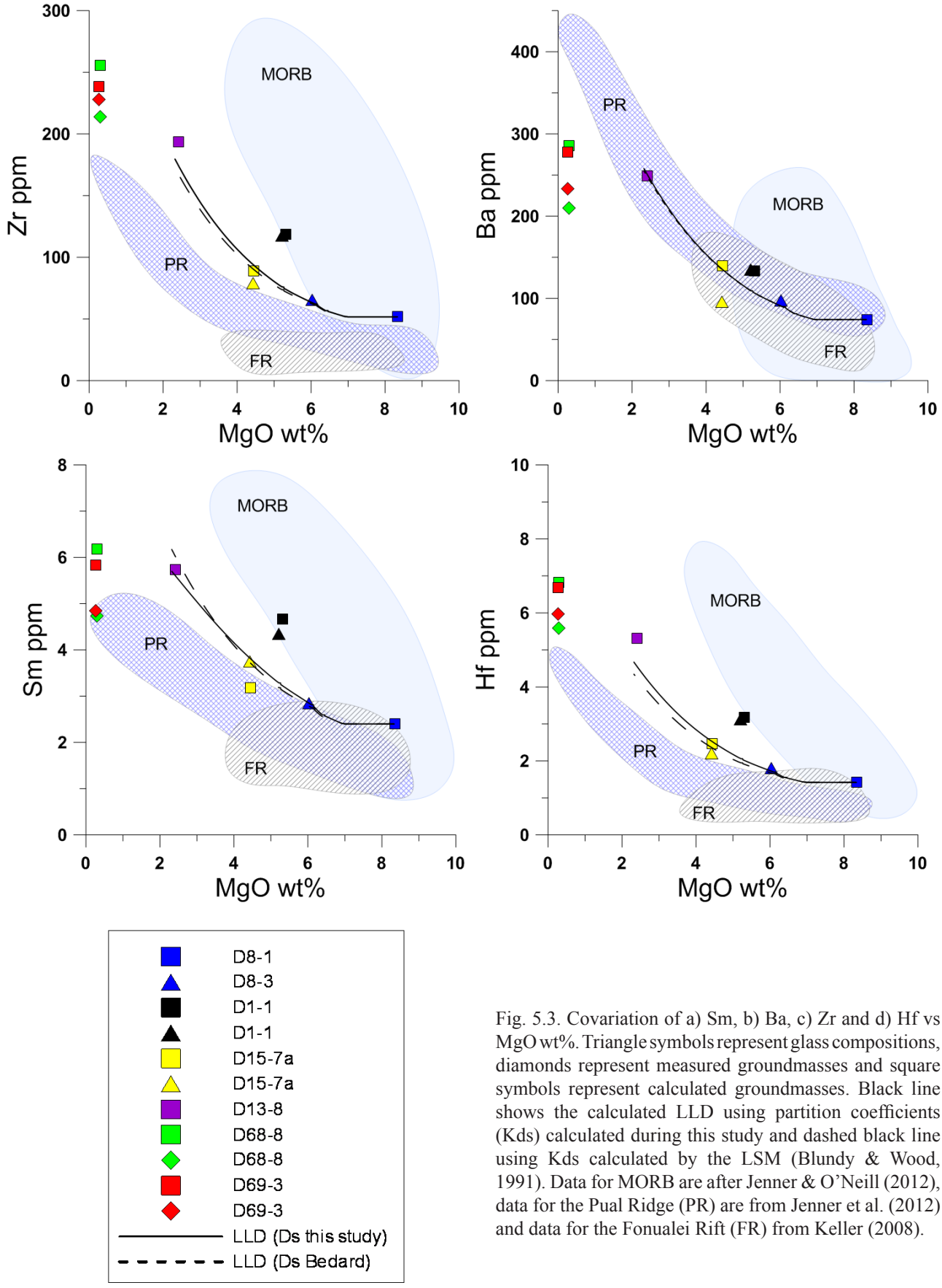

Fig. 5.3. Covariation of a) Sm, b) Ba, c) Zr and d) Hf vs MgO wt%. Triangle symbols represent glass compositions, diamonds represent measured groundmasses and square symbols represent calculated groundmasses. Black line shows the calculated LLD using partition coefficients (Kds) calculated during this study and dashed black line using Kds calculated by the LSM (Blundy & Wood, 1991). Data for MORB are after Jenner & O'Neill (2012), data for the Pual Ridge (PR) are from Jenner et al. (2012) and data for the Fonualei Rift (FR) from Keller (2008).

The broad range in the phenocryst compositions analysed in many of the samples indicates disequilibrium between the crystals and the melt. This could reflect some degree of mixing, either of evolved crystals with a more primitive melt, or of primitive crystals in a more evolved melt, though it does not necessarily mean the samples belong to different magmatic suites (see Chapter 4). Nevertheless, in the next section we present trace element and isotopic data that shows that magma mixing is not the dominant process operating in the magmatic systems.

In summary, as evident from Table 5.5 and Figures 5.1 and 5.2, the models produced in IgPet and Petrolog are in good agreement. Thus, the evolution pathways generated using these software packages are considered to be a reasonable approximation of fractional crystallisation in these magmas.

5.3 Modelling of fractional crystallisation: Trace elements

The aims of the second part of this chapter are: i) to use detailed trace element geochemistry to confirm that fractional crystallisation is the main controlling factor for magma evolution, and ii) to establish mineral/melt correspondence using quantitative modelling of REE, Ba, Zr and Hf using partition coefficients. This will allow us to distinguish samples affected by magma mixing and crystal accumulation.

5.3.1 Trace element composition

Trace element concentrations in phenocrysts, glasses and groundmass are presented in Table 5.6. The concentrations of these elements in phenocrysts and glasses were measured directly using LA-ICP-MS (spot analysis). Where possible, groundmasses were also analysed using LA-ICP-MS, where this was not possible, trace element concentrations in the groundmasses were calculated using a mass-balance method (see 5.2.1 for explanation of the mass balance method).

All glasses and groundmasses display similar negative Nb anomalies and similar ratios of incompatible trace elements regardless of their MgO contents (e.g. Nb/U, La/Sm, Dy/Er, La/Yb, and Ba/La; Fig. 5.5). This indicates that all samples have experienced the same relative enrichment/depletion in subduction-related components and same degree of partial melting.

Trace elements can also be a useful tool to corroborate the order of crystallisation suggested from modelling software such as Petrolog or IgPet. For example, Eu contents in clinopyroxene can help to establish when plagioclase starts crystallising. Olivine and clinopyroxene crystallisation do not fractionate Eu from other REE, whereas plagioclase with its high partition coefficient for Eu will. Hence, once plagioclase begins to crystallise the Eu content in the melt will decrease, which will lead to lower Eu contents in the clinopyroxene that crystallises from the melt. This is shown in a plot of Eu/Eu* [Eu/Eu* = Eu/(Sm x Gd)$^{0.5}$] against clinopyroxene Mg# (where Eu* represents the expected value if thre was no Eu anomaly; Fig. 5.4). Our data suggests that plagioclase saturation occurred at a clinopyroxene Mg# of 87 (at ~6.5 wt% MgO), which is in good agreement with the values obtained from the Petrolog modelling.

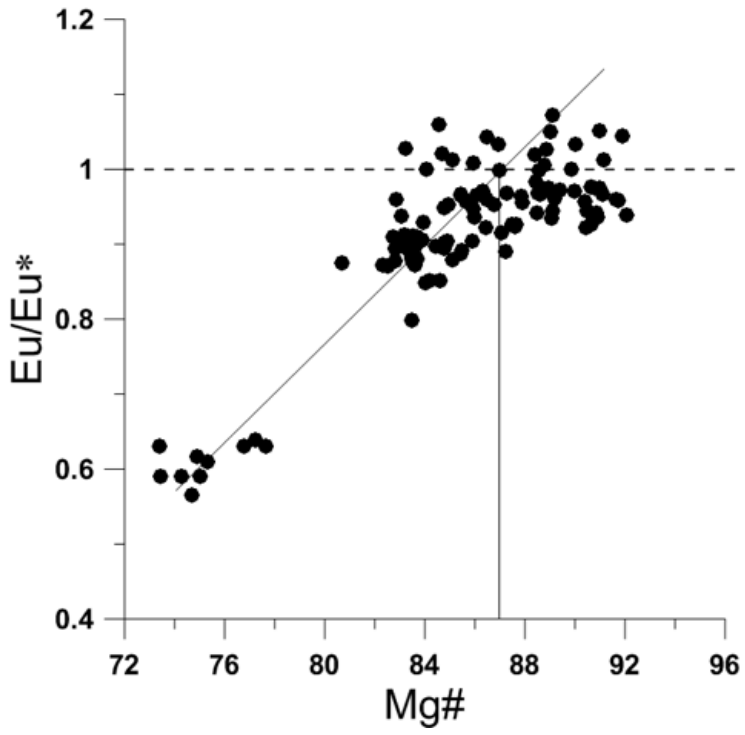

Fig. 5.4. Europium anomaly in clinopyroxene. Note that the appearance of plagioclase is consistent with the crystallisation order established using major element modelling. The cpx Mg# is ~87 when plagioclase appears on the liquidus.

Similarly, trace elements can be used to determine melt-mineral correspondence. To do this, the model of Blundy & Wood (1991) was used to calculate D_{Sr} and D_{Ba} as a function of plagioclase compositions, where the concentrations of Sr and Ba in the groundmass or glass from pillow rims are taken to be the liquid values. According to this, plagioclase crystallising with An of ~90 should have D_{Sr} and D_{Ba} of 1.3 and 0.12 respectively. The D_{Sr} and D_{Ba} calculated from LA-ICP-MS measurements in the plagioclase phenocrysts, with measured compositions of An 90, are 2.7 and 0.05 respectively. Calculations for partition coefficients assume that the plagioclase is in equilibrium with the host (dacite) melts. Clearly this is not the case. On the basis of this, we can say that the plagioclase is not in equilibrium with, and therefore did not crystallise from, the evolved magmas that formed the dacite.

5.3.2 Selection of partition coefficients

In order to model the fractional crystallisation of the Hunter Ridge lavas, bulk distribution coefficients or D values (ratio of the concentration of an element in the solid phase divided by its concentration in the equilibrium melt) were estimated by three methods (see Chapter 2 for a more extensive description and discussion of the methods).

1) The parameterisation method of Bédard (2005) to calculate D values appropriate for most of the trace elements used in this study. This provides mathematical expressions for changes in the D values for the REE and most of the HFSE as a function of changes in melt composition that are consistent with experimental observations and data from natural systems.

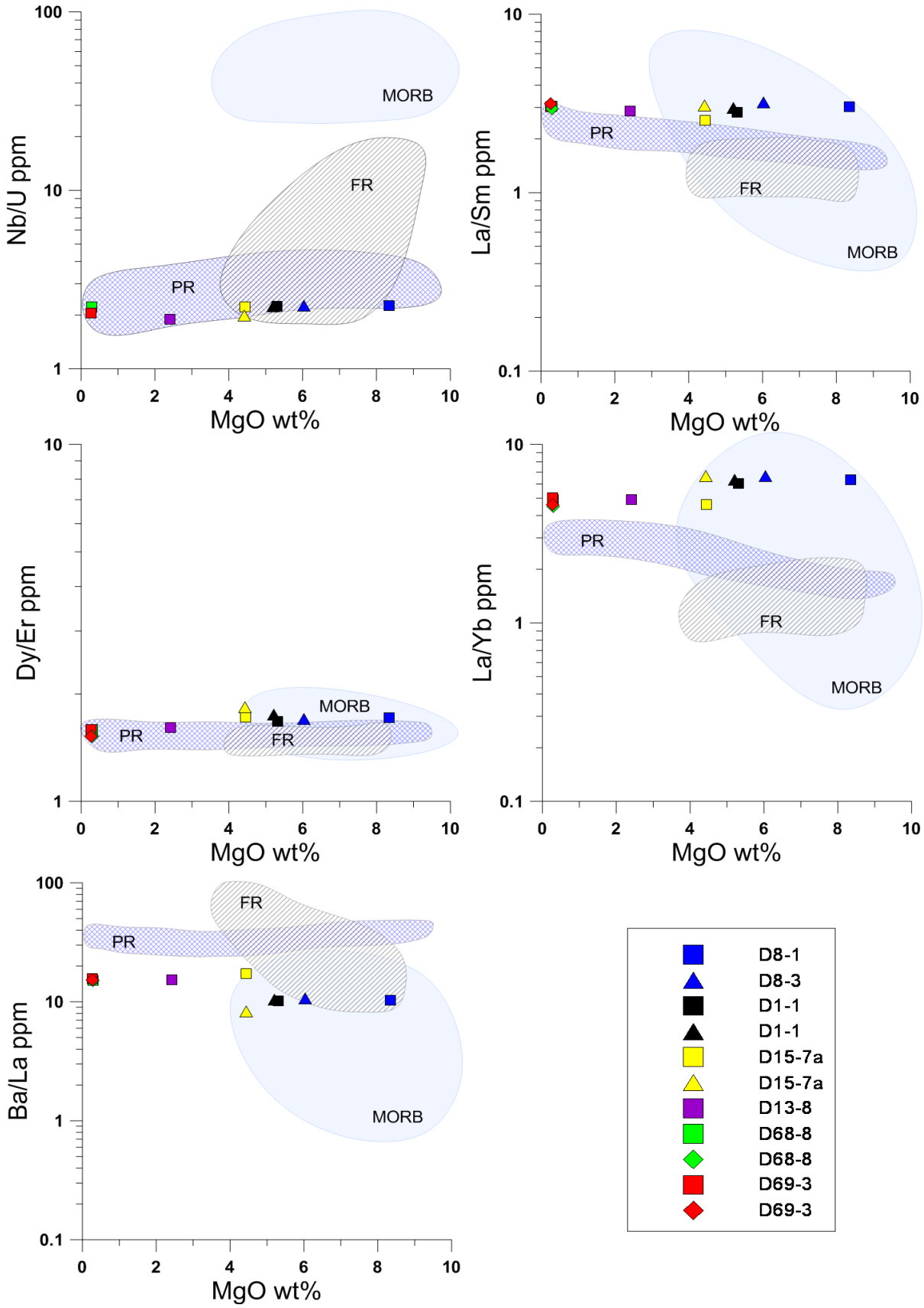

Fig. 5.5. Covariation of a) Nb/U, b) La/Sm, c)Dy/Er and d) La/Yb. All samples show indistinguishable REE ratios, demonstrating that they belong to a single fractionation magma series. Triangle symbols represent glass compositions, diamonds represent measured compositions of groundmasses and square symbols represent those of calculated groundmasses. Data for MORB are after Jenner & O'Neill (2012), data for the Pual Ridge (PR) are from Jenner et al., (2012) and data for the Fonualei Rift (FR) from Keller (2008).

2) The lattice strain model (LSM) of Blundy and Wood (1994). This method is based on the Brice (1975) model and postulates that log D values for a trace element follow a parabolic distribution around the ionic radius and apparent Young's modulus of the crystallographic sites into which they substitute. The Blundy and Wood (1994) expression is:

$$Di = D_0 \exp\left(-4\pi E N_A \left((r_0/2)(ri - r_0)^2 + 1/3\,(r_i - r_0)^3\right)/RT\right)$$

Where D_0 is the strain compensated partition coefficient, r_0 is the ionic radius of the cation of interest, E is the Young's modulus of the host site, N_A is the Avogadro's number; R is the gas constant and T is temperature in degrees Kelvin.

3) The third method is to calculate D values directly from high-precision trace element data for phenocryst-groundmass/glass pairs in equilibrium (i.e. from LA-ICP-MS analyses). This approach is necessary particularly for those elements where the first two methods produce unreliable results. Our preferred method (number 3) is valid as our samples provide an ideal (natural) sample set that cover a range of bulk compositions. Consequently, our empirical approach, combined with establishing phenocrysts and groundmass/glass pair equilibrium, is robust. Table 5.7a–d lists melt-mineral partition coefficients calculated using methods 1, 2, and 3.

5.3.3 Results from trace-element modelling

Results of the trace element modelling are listed in Table 5.6 and selected incompatible elements are shown in Figure 5.3. The modelling approach used in this study considers the effects of changing Ds on the crystallisation path, where D values are independently (LSM) or semi-independently established (calculated). All of these coefficients are within the experimental range for basalts, basaltic andesites, dacites and rhyolites (GeoReM website) and are consistent with phenocrysts-groundmass pairs for the Hunter Ridge lavas calculated for this study. Figure 5.2 shows plots of Zr, Ba, Sm and Hf against melt MgO contents. Modelling of these incompatible elements was done using Ds obtained by the LSM (dashed balck line) and D values calculated for this study (continuous black line) (Table 5.6). These lines show the path of liquid evolution resulting from fractional crystallisation of the initial composition D8-1-groundmass. From these plots, we can observe that both differentiation trends are nearly identical, conveying that the modelling of fractional crystallisation accounts for the trends display by the data using either set of Ds.

Zirconium is found to be moderately incompatible in clinopyroxene as indicated by the measured $D_{Zr}^{cpx/melt}$ of 0.05–0.21 and the calculated $D_{Zr}^{cpx/melt}$ of 0.20–0.27 (using LSM). $D_{Zr}^{cpx/melt}$ increases with decreasing clinopyroxene Mg# within the measured range (Mg# 75–90). Zr values in olivine, plagioclase and magnetite are largely below detection, therefore, we can assume that its partitioning into these minerals is negligible. In the melt, Zr increases from ~52 ppm at 8.3 wt% MgO to a maximum value of ~250 ppm at 0.3 wt% MgO (Fig. 5.3).

Similarly to zirconium, hafnium is found to be moderately compatible in clinopyroxene as indicated by the measured $D_{Hf}^{cpx/melt}$ of 0.1–0.37 and the calculated $D_{Hf}^{cpx/melt}$ of 0.34–0.49 (using LSM). $D_{Hf}^{cpx/melt}$ increases with decreasing clinopyroxene Mg# within the measured range (Mg# 75–90). Hf

values in olivine, plagioclase and magnetite are largely below detection, therefore, we can assume that its partitioning into these minerals is negligible. In the melt, Hf increases from ~1 ppm at 8.3 wt% MgO to a value of ~5 ppm at 0.3 wt% MgO (Fig. 5.3).

Barium is slightly to moderately compatible in plagioclase as indicated by the measured $D_{Ba}^{pl/melt}$ of 0.1–0.61 and the calculated $D_{Ba}^{pl/melt}$ of 0.13–0.84 (using LSM). $D_{Ba}^{pl/melt}$ increases with decreasing plagioclase An within the measured range (An 31–87). Ba values in olivine, clinopyroxene and magnetite are largely below detection, therefore, we can assume that its partitioning into these minerals is insignificant. In the melt, Ba increases from ~74 ppm at 8.3 wt% MgO to a value of ~285 ppm at 0.3 wt% MgO (Fig. 5.3).

Samarium is found to be mildly incompatible to compatible in clinopyroxene as evidenced from measured $D_{Sm}^{cpx/melt}$ of 0.21–1.40 and the calculated $D_{Sm}^{cpx/melt}$ of 0.50–0.70 (using LSM). $D_{Sm}^{cpx/melt}$ increases with decreasing clinopyroxene Mg# within the measured range (Fo 75–90). Samarium is also slightly partitioned into plagioclase as indicated by $D_{Ba}^{pl/melt}$ of 0.02–0.06 and the calculated $D_{Ba}^{pl/melt}$ of 0.07–0.01 (using LSM). Sm values in olivine and magnetite are mostly below detection, therefore, we can assume that its partitioning into these minerals is negligible. In the melt, Sm increases from ~2.4 ppm at 8.3 wt% MgO to a maximum value of ~6.2 ppm at 0.3 wt% MgO (Fig. 5.3).

The results of the trace-element modelling described above suggest that the mineral assemblages and proportions modelled using Petrolog and IgPet can also explain the observed trace-element variations, as well as major-element trends.

5.4 Discussion

Geochemical modelling alone cannot identify all the processes and parameters, such as temperature, pressure and water content, that vary or operate during fractional crystallisation. However, the major and trace element trends displayed by the Hunter Ridge calc-alkaline rocks can be explained as a product of olivine-clinopyroxene-plagioclase-magnetite-amphibole fractionation as shown by the modelling performed using Petrolog and IgPet. Using Petrolog, the temperature of the initial magma is estimated at ~1125 ºC, which was used for the liquidus of our Stage-1 parent melts (Table 5.5). The other parameters used were 1.5 wt% H_2O at 0.6 Kbar and an oxygen fugacity of Ni–NiO+2. Our fractional crystallisation modelling considers pressure and water content variations along the crystallisation path, and allows degassing to occur as would be expected in natural systems. Accordingly, we believe that degassing occurs at ~ 6.5 wt% MgO, which correlates with the maximum Al_2O_3 reached by the calculated LLD (Fig. 5.1). Parman et al., (2011) found that H_2O contents estimated using the Al_2O_3 LLD method corresponds to the maximum H_2O measured in non-degassed, glassy melt, inclusions in lavas from the Mariana Arc. In our case, this value is in good agreement with FTIR water measurements on the most primitive glass samples from the Hunter Ridge calc-alkaline series. However, we are aware that this water content represents the H_2O of the magma under low pressure fractionation, and not the initial water content of the melt. We also cannot be sure of the exact melt composition at which plagioclase enters the liquidus based on our samples. We used the highest Al_2O_3 measured from groundmass compositions, which may be an underestimation of the true value.

Isotopic data (i.e. $^{143}Nd/^{144}Nd$, $^{87}Sr/^{86}Sr$ and $^{206}Pb/^{204}Pb$) for samples D8-2 (basalt) and D15-7a (basaltic andesite) are very similar (Table 5.8). Had considerable isotopic variation been present, this would be an indication for magma mixing processes rather than fractional crystallisation alone. This would invalidate any subsequent LLD modelling, though no such isotopic variations were observed. Consequently, the isotope data suggests that the phenocrysts and their host magmas are genetically related.

Therefore, we conclude that in the case of the Hunter Ridge calc-alkaline series, the minerals and melts are genetically related, the system was largely closed, and the samples represented by composition D1 (most evolved) can be derived from P (most primitive) by fractional crystallisation (Table 5.3).

Our study also suggests that mixing processes do not entirely obscure the differentiation trends that result from fractional crystallisation. Detailed petrographic and geochemical studies can be used to identify samples in which mixing processes have occurred. Once it has been established that the melts, and the minerals that crystallise from them, are from the same magma series, we can trace the evolution of ore metals during differentiation.

Table 5.1. Major-element composition (wt%) of the Hunter Ridge calc-alkaline rocks (XRF whole-rock geochemistry).

Sample	SiO_2	TiO_2	Al_2O_3	FeO	MnO	MgO	CaO	Na2O	K_2O	P_2O_5	Total	LOI
D1-1	54.63	0.79	17.54	7.46	0.13	5.28	9.67	3.63	0.67	0.19	100	0.41
D1-2	54.46	0.78	17.78	7.29	0.13	5.29	9.70	3.75	0.66	0.17	100	0.26
D1-3	54.24	0.81	17.54	7.56	0.20	5.32	9.67	3.82	0.66	0.18	100	0.65
D8-1	52.00	0.49	15.04	7.54	0.13	10.95	10.89	2.34	0.51	0.11	100	0.48
D8-2	51.89	0.49	14.78	7.56	0.13	11.46	10.75	2.31	0.51	0.12	100	0.52
D11-1	50.47	0.60	14.76	8.14	0.15	12.18	9.86	3.20	0.52	0.13	100	0.19
D11-2	50.03	0.57	13.99	8.31	0.15	13.77	9.68	2.96	0.41	0.13	100	-0.08
D11-6	50.30	0.59	14.47	8.18	0.15	12.72	9.83	3.14	0.50	0.13	100	0.16
D11-8	50.67	0.60	14.73	8.28	0.15	11.61	10.22	3.06	0.53	0.14	100	0.31
D12-2	68.16	0.71	15.08	3.89	0.10	1.32	3.34	5.67	1.56	0.17	100	0.72
D12-3	68.16	0.69	14.99	4.31	0.10	1.32	3.38	5.33	1.55	0.17	100	0.11
D12-4	68.26	0.70	14.93	4.28	0.10	1.26	3.34	5.39	1.58	0.16	100	0.86
D12-6	68.24	0.70	15.14	3.86	0.13	1.29	3.29	5.63	1.56	0.17	100	0.69
D13-5	69.95	0.77	15.08	2.95	0.07	0.92	2.87	5.70	1.57	0.12	100	1.34
D13-6	66.39	0.79	15.33	4.47	0.10	1.91	4.28	5.21	1.36	0.16	100	0.92
D13-7	72.73	0.79	15.37	1.29	0.02	0.33	2.37	5.60	1.44	0.07	100	1.49
D13-8	64.41	0.78	15.48	5.20	0.11	2.48	5.09	5.00	1.26	0.20	100	0.59
D15-7	56.15	0.68	17.22	7.32	0.12	5.10	8.98	3.64	0.65	0.13	100	0.41
D15-7a	56.57	0.69	17.46	6.60	0.12	5.03	9.05	3.66	0.68	0.13	100	0.53
D15-8	56.68	0.69	17.40	6.60	0.12	5.00	8.98	3.72	0.68	0.14	100	0.33
D67-2	53.29	0.52	16.93	6.42	0.12	8.05	11.36	2.73	0.51	0.09	100	0.69
D67-3	53.31	0.52	16.78	6.44	0.12	8.19	11.34	2.72	0.49	0.09	100	0.58
D67-4	53.04	0.50	16.90	6.34	0.12	8.38	11.38	2.78	0.48	0.09	100	0.66
D67-5	53.21	0.51	17.38	6.24	0.11	7.73	11.50	2.74	0.47	0.09	100	0.49
D67-6	53.30	0.53	17.15	6.37	0.12	7.85	11.38	2.71	0.51	0.09	100	0.56
D68-2	71.30	0.49	14.73	2.63	0.09	0.78	2.24	6.04	1.61	0.09	100	1.30
D68-3	71.48	0.51	14.62	2.63	0.09	0.77	2.21	5.99	1.60	0.10	100	1.25
D68-4	71.42	0.50	14.66	2.62	0.09	0.80	2.22	5.97	1.62	0.10	100	1.46
D68-5	71.45	0.50	14.61	2.65	0.09	0.80	2.19	6.01	1.60	0.10	100	1.64
D68-8	71.57	0.50	14.56	2.62	0.09	0.78	2.16	6.04	1.58	0.09	100	1.31
D68-9	55.77	0.69	17.92	7.14	0.14	4.57	9.18	3.87	0.60	0.11	100	0.27
D68-10	71.25	0.50	14.62	2.65	0.09	0.82	2.23	6.09	1.65	0.10	100	1.99
D68-11	71.37	0.50	14.67	2.66	0.09	0.78	2.22	6.00	1.62	0.10	100	1.56
D69-2	68.81	0.73	15.24	3.49	0.08	1.09	3.06	5.71	1.62	0.17	100	1.29
D69-3	71.09	0.52	14.91	2.60	0.09	0.79	2.32	6.14	1.44	0.10	100	1.29
D69-4	70.53	0.61	14.82	3.03	0.08	0.87	2.65	5.69	1.58	0.13	100	1.37
D69-5	71.33	0.52	14.80	2.59	0.09	0.77	2.29	6.05	1.44	0.11	100	1.43
D69-6	68.88	0.71	15.32	3.41	0.08	1.07	3.05	5.62	1.68	0.17	100	1.63
D69-7	71.19	0.52	14.85	2.62	0.09	0.78	2.31	6.09	1.44	0.11	100	1.51
D69-8	71.04	0.53	14.88	2.63	0.09	0.80	2.33	6.13	1.46	0.11	100	1.44
D69-9	71.33	0.51	14.83	2.57	0.09	0.77	2.26	6.06	1.48	0.10	100	1.54
D69-10	70.66	0.61	14.73	3.02	0.08	0.86	2.59	5.68	1.64	0.13	100	1.56

Table 5.2. Measured and calculated groundmass and average mineral compositions (wt%) and modal proportions of the Hunter Ridge calc-alkaline rocks.

Sample	SiO_2	TiO_2	Al_2O_3	FeO	MnO	MgO	CaO	Na2O	K_2O	P_2O_5	Total	%
D8-1-calculated	52.77	0.52	16.14	7.38	0.13	8.35	11.53	2.52	0.55	0.12	100	
D8-1-ol	40.59	0.00	0.01	10.25	0.19	48.75	0.21	0.00	0.00	0.00	100	0.06
D8-1-cpx	52.44	0.30	3.34	4.64	0.14	16.89	22.06	0.20	0.00	0.00	100	0.01
D1-1-probe	55.84	0.93	15.77	8.42	0.16	5.31	8.97	3.69	0.73	0.19	100	
D1-1-calculated	55.64	0.93	15.61	8.42	0.15	5.47	8.98	3.82	0.78	0.23	100	
D1-1 pl	49.81	0.01	31.64	0.58	0.00	0.17	14.87	2.85	0.07	0.00	100	0.14
D1-1-ol	39.46	0.00	0.00	16.46	0.28	43.44	0.22	0.00	0.00	0.01	100	0.01
D1-1-cpx	52.71	0.35	2.70	6.01	0.23	17.67	19.80	0.27	0.00	0.00	100	0.00
D15-7A-probe	58.59	0.89	15.53	7.74	0.13	4.44	7.86	3.85	0.81	0.15	100	
D15-7a-calculated	57.89	0.80	15.81	7.30	0.14	5.03	8.23	3.89	0.78	0.15	100	
D15-7a-ol	39.48	0.00	0.00	17.04	0.28	43.00	0.19	0.01	0.00	0.00	100	0.01
D15-7a-cpx	53.46	0.29	2.08	6.06	0.22	18.37	19.30	0.23	0.01	0.00	100	0.01
D15-7a-pl	49.20	0.01	32.10	0.52	0.00	0.16	15.34	2.63	0.06	0.00	100	0.12
D13-8-calground	65.57	0.87	14.37	5.63	0.12	2.41	4.36	5.02	1.41	0.23	100	
D13-8-cpx	52.58	0.43	2.24	6.96	0.30	16.35	20.83	0.30	0.00	0.00	100	0.01
D13-8-opx	53.95	0.25	0.67	17.62	0.86	25.33	1.32	0.00	0.00	0.00	100	0.01
D13-8-pl	56.41	0.04	27.42	0.56	0.00	0.06	9.74	5.63	0.13	0.00	100	0.10
D69-10-probe	73.27	0.46	14.40	2.00	0.00	0.41	1.99	5.29	2.11	0.07	100	
D69-10-calculated	72.22	0.67	13.81	3.08	0.08	0.61	1.84	5.74	1.80	0.14	100	
D69-10-cpx	52.72	0.43	1.46	8.85	0.46	15.46	20.26	0.36	0.00	0.00	100	0.01
D69-10-opx	53.45	0.23	0.77	18.48	0.83	25.05	1.17	0.01	0.00	0.00	100	0.01
D69-10-pl	57.29	0.02	26.88	0.48	0.00	0.03	9.08	6.07	0.14	0.00	100	0.09
D69-3-probe	74.80	0.38	13.79	1.60	0.06	0.27	1.54	5.72	1.78	0.06	100	
D69-3-calculated	73.52	0.59	13.30	2.75	0.09	0.58	1.20	6.18	1.67	0.12	100	
D69-3-cpx	52.50	0.42	1.52	8.41	0.54	15.01	21.18	0.43	0.00	0.00	100	0.01
D69-3-opx	53.94	0.21	0.70	18.11	1.08	24.81	1.15	0.00	0.00	0.00	100	0.01
D69-3-pl	57.88	0.03	26.52	0.46	0.00	0.02	8.42	6.50	0.14	0.02	100	0.14
D69-3-amph	44.99	2.91	9.74	13.34	0.34	14.82	11.18	2.45	0.18	0.06	100	0.00

Table 5.3. Glass and groundmass major element and volatile compositions (wt%) of the Hunter Ridge calc-alkaline rocks used for the geochemical modelling. *=Calculated groundmass using a mass-balance approach.

Sample	SiO_2	TiO_2	Al_2O_3	FeO	MnO	MgO	CaO	Na2O	K_2O	P_2O_5	Total	H_2O	Cl
D1-1-groundmass	55.84	0.93	15.77	8.42	0.16	5.31	8.97	3.69	0.73	0.19	100		
D1-1-glass	55.85	0.92	15.66	8.67	0.15	5.21	9.00	3.58	0.74	0.22	100	0.97	0.15
D8-1-groundmass*(P)	52.77	0.52	16.14	7.38	0.13	8.35	11.53	2.52	0.55	0.12	100		
D8-3-glass	54.27	0.65	16.15	8.28	0.15	6.03	10.92	2.77	0.63	0.14	100	1.50	0.14
D12-3-groundmass	73.28	0.52	13.98	2.50	0.07	0.46	1.79	5.36	1.95	0.08	100		
D13-5-groundmass	72.09	0.60	14.52	2.54	0.04	0.46	2.11	5.21	2.34	0.08	100		
D13-8-groundmass	65.05	0.65	15.43	4.15	0.12	2.71	5.72	4.76	1.19	0.22	100		
D13-8-groundmass*	65.57	0.87	14.37	5.63	0.12	2.41	4.36	5.02	1.41	0.23	100		
D15-7A-groundmass	58.59	0.89	15.53	7.74	0.13	4.44	7.86	3.85	0.81	0.15	100		
D15-7a-groundmass*	57.69	0.78	15.82	7.30	0.14	5.25	8.26	3.85	0.77	0.15	100		
D15-7-glass	58.63	0.91	15.68	7.72	0.13	4.52	7.88	3.51	0.86	0.16	100	0.85	0.17
D15-7A-glass	58.73	0.91	15.69	7.63	0.13	4.43	7.93	3.56	0.83	0.17	100	0.78	0.14
D67-5b-glass	55.40	0.70	16.13	7.70	0.14	5.84	10.44	2.93	0.60	0.12	100		0.14
D68-8-groundmass(D)	75.44	0.40	13.28	1.76	0.05	0.30	1.23	5.49	1.98	0.08	100		
D69-3-groundmass	74.80	0.38	13.79	1.60	0.06	0.27	1.54	5.72	1.78	0.06	100		
D69-10-groundmass	73.27	0.46	14.40	2.00	0.00	0.41	1.99	5.29	2.11	0.07	100		

P = parental melt composition.
D = most differentiated melt.
a H_2O determined by FTIR.

Table 5.4. Calculated melt-liquidus association for groundmass compositions for the Hunter Ridge calc-alkaline rocks.

Sample	Fo	T (°C)	An#	T (°C)	Mg# Cpx	T (°C)	T (°C)	Mg# Opx
D8-1-groundmass	88.37	1099	77.45	990	89.61	1075		
D8-3-glass	83.35	1039	76.62	995	84.85	1044		
D1-1-groundmass	81.50	1040	58.83	948	82.32	1029		
D1-1-glass	80.62	1035	59.47	948	81.59	1027		
D15-7A-groundmass	83.27	1054	55.17	939	83.85	1033		
D15-7A-glass	79.58	1025	57.24	938	80.16	1017		
D13-8-groundmass	78.29	1034	21.85	895	74.68	993	996	79.07
D68-8-groundmass	69.24	1016	3.12	885	44.32	913	873	60.72
D69-3-groundmass	66.45	953	5.04	889	43.21	903	840	61.74

Table 5.5. Four-step modelling of the fractional crystallisation trends display by the Hunter Ridge calc-alkaline rocks.

	SiO_2	TiO_2	Al_2O3	FeO	MnO	MgO	CaO	Na_2O	K_2O	P_2O_5	Ol Fo/%	Cpx Mg#/%	Pl An/%	Mt%	Amph %	Ol Fo/%	Cpx Mg#/%	Pl An/%	Mt%
Step 1											**IgPet**					**Petrolog**			
Start	52.77	0.52	16.14	7.38	0.13	8.35	11.53	2.52	0.55	0.12									
End	54.35	0.64	16.45	7.94	0.14	6.12	10.85	2.72	0.64	0.14									
Calc	52.87	0.53	16.19	7.42	0.13	8.34	11.53	2.33	0.52	0.12	85/26	84/33	86/41	-	-	84/21	85/40	75/39	-
Sum of squares of residuals: 0.04																			
F	0.8																		
Step 2																			
Start	54.35	0.64	16.45	7.94	0.14	6.12	10.85	2.72	0.64	0.14									
End	55.85	0.92	15.66	8.67	0.152	5.209	8.997	3.575	0.744	0.221									
Calc	54.5	0.75	16.19	7.6	0.14	6.2	10.75	3.11	0.58	0.17	81/5	83/43	77/52	-	-	80/5	81/45	68/50	-
Sum of squares of residuals: 0.32																			
F	0.8																		
Step 3																			
Start	55.85	0.92	15.66	8.67	0.152	5.209	8.997	3.575	0.744	0.221									
End	65.58	0.87	14.37	5.63	0.12	2.41	4.36	5.02	1.41	0.23									
Calc	55.78	0.98	15.48	8.67	0.19	5.23	9.03	3.95	0.59	0.09	80/5	77/31	50/56	8		76/2	74/37	48/51	11
Sum of squares of residuals: 0.19																			
F	0.4																		
Step 4																			
Start	65.58	0.87	14.37	5.63	0.12	2.41	4.36	5.02	1.41	0.23									
End	75.43	0.4	13.28	11.8	0.05	0.3	1.23	5.49	1.98	0.08									
Calc	65.78	0.77	14.28	5.68	0.14	2.46	4.37	5.22	1.24	0.05	-	74/16	32/56	9	19	-	-	-	-
Sum of squares of residuals: 0.12																			
F	0.6																		

Table 5.6. Glass, groundmass and mineral trace element compositions (ppm) used for the geochemical modelling. *=Calculated groundmass using mass balance. ~Groundmass measured by LA-ICP-MS. All mineral analyses are averaged.

Sample	Sr	Y	Zr	Ba	La	Ce	Nd	Sm	Eu	Gd	Dy	Er	Yb	Lu	Hf
D13-8	364.00	25.13	170.57	226.93	14.66	35.42	21.89	5.08	1.41	5.22	4.90	3.04	2.96	0.45	4.67
D13-8-cpx	28.37	5.92	4.45	0.00	0.21	1.12	1.81	0.79	0.28	1.09	1.17	0.66	0.52	0.07	0.23
D13-8-opx*	0.09	9.88	1.98	0.00	0.03	0.15	0.32	0.25	0.07	0.57	1.29	1.43	2.10	0.38	0.09
D13-8-pl	1103.70	0.27	0.02	79.05	2.52	4.12	1.72	0.22	1.09	0.14	0.06	0.02	0.01	0.00	0.00
D13-8-ol	0.00	0.08	0.02	0.00	0.00	0.00	0.00	0.00	0.00	0.00	0.00	0.00	0.03	0.00	0.00
D13-8-groundmass*	235.68	24.95	170.50	217.77	14.36	34.93	21.67	5.04	1.28	5.18	4.86	3.02	2.93	0.45	4.67
D1-1	617.00	16.81	100.86	116.37	11.31	27.87	17.65	3.98	1.26	3.79	3.33	1.99	1.85	0.27	2.69
D1-1-cpx	41.95	11.01	10.00	0.00	0.72	3.68	4.99	1.78	0.58	2.18	2.13	1.22	1.02	0.15	0.52
D1-1-pl	976.79	0.13	0.05	21.97	0.68	1.24	0.59	0.09	0.28	0.06	0.03	0.01	0.00	0.00	0.00
D1-1-ol	0.01	0.08	0.02	0.00	0.00	0.00	0.00	0.00	0.00	0.00	0.03	0.01	0.00	0.00	0.00
D1-1-groundmass*	408.91	16.64	100.72	111.70	11.16	27.56	17.47	3.94	1.19	3.74	3.30	1.97	1.84	0.27	2.69
D1-1-glass	577.65	19.73	117.52	134.76	13.00	32.75	19.49	4.35	1.33	4.07	3.61	2.07	2.05	0.30	3.12
D15-7a	512.77	14.63	76.56	122.64	6.99	16.10	10.60	2.75	0.93	2.83	2.78	1.61	1.51	0.22	2.12
D15-7A-cpx	29.27	8.24	5.15	0.00	0.33	1.72	2.49	1.04	0.36	1.47	1.58	0.91	0.76	0.11	0.27
D15-7A-pl	952.49	0.10	0.07	21.30	0.49	0.98	0.43	0.07	0.25	0.04	0.03	0.00	0.00	0.00	0.00
D15-7A-ol	0.00	0.08	0.02	0.00	0.00	0.00	0.00	0.00	0.00	0.00	0.00	0.00	0.03	0.00	0.00
D15-7A-groundmass*	361.29	14.55	76.51	119.26	6.91	15.93	10.52	2.74	0.89	2.81	2.76	1.60	1.50	0.22	2.12
D15-7A-glass	573.74	16.06	78.83	95.66	11.56	27.64	17.76	3.76	1.11	3.28	3.13	1.70	1.73	0.26	2.21
D68-8	224.28	31.43	230.42	267.16	17.28	40.84	24.47	5.67	1.38	5.33	5.44	3.42	3.51	0.54	6.15
D68-8-cpx	25.38	87.36	34.61	0.00	3.76	21.97	33.28	13.15	2.87	16.97	17.61	10.02	8.28	1.22	1.64
D68-8-opx*	0.09	9.88	1.98	0.00	0.03	0.15	0.32	0.25	0.07	0.57	1.29	1.43	2.10	0.38	0.09
D68-8-pl	1004.52	0.26	0.02	115.45	3.34	5.27	1.98	0.25	1.58	0.16	0.06	0.02	0.00	0.00	0.00
D68-8-groundmass*	64.75	30.42	230.04	248.85	16.71	39.78	23.80	5.49	1.10	5.12	5.24	3.30	3.41	0.52	6.13
D68-8-groundmass~	154.07	28.75	213.67	209.81	13.94	34.80	20.53	4.73	1.12	5.31	4.76	3.13	3.11	0.49	5.58
Sample no	Sr	Y	Zr	Ba	La	Ce	Nd	Sm	Eu	Gd	Dy	Er	Yb	Lu	Hf
D69-3	258.30	27.54	203.16	246.10	15.37	36.37	22.05	5.09	1.34	4.87	4.87	3.06	3.07	0.48	5.70
D69-3-cpx	27.65	67.80	35.67	1.78	2.90	15.56	24.37	9.89	2.31	13.17	13.63	7.85	6.46	0.96	1.73

Table 5.6 cont.

Sample	Sr	Y	Zr	Ba	La	Ce	Nd	Sm	Eu	Gd	Dy	Er	Yb	Lu	Hf
D69-3-opx*	0.09	9.88	1.98	0.00	0.03	0.15	0.32	0.25	0.07	0.57	1.29	1.43	2.10	0.38	0.09
D69-3-pl	1175.99	0.25	0.03	70.54	2.34	3.74	1.56	0.21	1.09	0.14	0.06	0.02	0.01	0.00	0.00
D69-3-amph	200.30	72.80	56.16	32.58	3.82	18.82	29.71	11.66	3.55	15.12	14.65	8.06	6.31	0.85	2.53
D69-3-groundmass*	70.88	26.60	202.67	234.82	14.97	35.58	21.49	4.93	1.13	4.68	4.68	2.95	2.98	0.47	5.68
D69-3-groundmass~	138.22	29.91	228.05	233.02	15.23	37.61	21.34	4.85	1.14	5.40	4.93	3.24	3.30	0.51	5.97
D67-5	585.47	10.83	53.77	85.01	5.23	12.87	8.74	2.17	0.77	2.19	2.05	1.23	1.09	0.17	1.52
D67-5-cpx	31.97	4.78	3.77	0.00	0.21	1.18	1.71	0.69	0.26	0.90	0.96	0.54	0.42	0.06	0.21
D67-5-pl	794.13	0.07	0.01	7.94	0.24	0.47	0.25	0.05	0.15	0.03	0.02	0.00	0.00	0.00	0.00
D67-5-ol	0.00	0.04	0.01	0.00	0.00	0.00	0.00	0.00	0.00	0.00	0.00	0.00	0.01	0.00	0.00
D67-5-groundmass*	573.62	10.38	53.41	84.92	5.21	12.75	8.57	2.11	0.75	2.10	1.96	1.18	1.05	0.16	1.50
D67-5b glass	553.10	12.23	58.09	82.26	5.58	13.63	9.61	2.38	0.82	2.42	2.23	1.33	1.20	0.18	1.59
D8-1	506.31	10.29	48.88	70.15	6.83	15.50	9.97	2.27	0.75	2.14	1.99	1.16	1.08	0.16	1.34
D8-1-cpx	31.05	4.41	3.27	0.00	0.23	1.18	1.65	0.66	0.25	0.85	0.87	0.50	0.39	0.06	0.17
D8-1-ol	0.00	0.02	0.01	0.00	0.00	0.00	0.00	0.00	0.00	0.00	0.00	0.00	0.01	0.00	0.00
D8-1-groundmass*	506.08	10.26	48.86	70.15	6.83	15.49	9.96	2.27	0.75	2.14	1.98	1.16	1.08	0.16	1.34
D8-3-glass	598.38	13.17	65.24	97.51	9.13	21.74	12.80	2.85	0.93	2.73	2.44	1.43	1.38	0.20	1.81

Table 5.7a. Melt-mineral partition coefficients for clinopyroxene using three different methods: Calculated Ds (this study by phenocrysts-groundmass equilibrium pairs). LSM (lattice strain model) is the method of Blundy & Wood (1994) and parameterisation is the method of Bédard (2005).

Clinopyroxene	**Measured Ds**				**Ds using LSM**				**Ds using Parameterisation**			
Cpx Mg#	90	85	83	75	90	85	83	75	90	85	83	75
MgO melt	8.35	6.12	5.21	2.41	8.35	6.12	5.21	2.41	8.35	6.12	5.21	2.41
D La	0.02	0.05	0.06	0.23	0.12	0.14	0.13	0.14	-	-	-	-
D Ce	0.05	0.11	0.13	0.52	0.18	0.21	0.21	0.23	-	-	-	-
D Nd	0.11	0.26	0.30	1.23	0.35	0.42	0.42	0.47	-	-	-	-
D Sm	0.21	0.48	0.54	1.40	0.51	0.63	0.63	0.71	-	-	-	-
D Eu	0.24	0.48	0.54	1.83	0.56	0.71	0.70	0.80	-	-	-	-
D Gd	0.30	0.65	0.73	2.42	0.61	0.77	0.76	0.87	-	-	-	-
D Dy	0.33	0.75	0.85	2.62	0.64	0.81	0.81	0.93	-	-	-	-
D Er	0.32	0.73	0.81	2.40	0.60	0.77	0.77	0.88	-	-	-	-
D Yb	0.28	0.62	0.71	2.10	0.54	0.69	0.68	0.78	-	-	-	-
D Lu	0.26	0.60	0.70	2.04	0.50	0.64	0.64	0.72	-	-	-	-
D Y	0.33	0.71	0.86	2.57	0.63	0.81	0.80	0.92	-	-	-	-
D Cu	0.01	0.02	0.03	0.04	0.00	0.00	0.00	0.00	0.03	0.04	0.05	0.02
D Zn	0.30	0.56	0.66	1.67	-	-	-	-	0.71	0.77	0.83	1.35
D V	0.68	0.97	1.45	0.84	-	-	-	-	-	-	-	-
D Pb	0.01	0.01	0.01	0.02	-	-	-	-	-	-	-	-
D Co	0.94	1.43	2.25	1.95	-	-	-	-	-	-	-	-
D Sc	1.93	3.22	4.95	12.55	-	-	-	-	-	-	-	-
D Sr	0.05	0.06	0.10	0.09	-	-	-	-	-	-	-	-
D Zr	0.05	0.10	0.10	0.21	0.23	0.25	0.27	0.20	-	-	-	-
D Hf	0.10	0.19	0.16	0.37	0.40	0.46	0.49	0.34	-	-	-	-
D Ti	0.28	0.39	0.38	0.31	0.50	0.53	0.54	0.47	-	-	-	-

Table 5.7b. Melt-mineral partition coefficients for plagioclase using 3 different methods: Calculated Ds (this study by phenocrysts-groundmass equilibrium pairs). LSM (lattice strain model) is the method of Blundy and Wood (1994) and parameterisation is the method of Bédard (2005).

Plagioclase	**Measured Ds**				**Ds using LSM**				**Ds using Parameterisation**			
An	87	85	70	31	87	85	70	31	87	85	70	31
MgO melt	8.35	6.12	5.21	2.41	8.35	6.12	5.21	2.41	8.35	6.12	5.21	2.41
D La	0.04	0.03	0.06	0.29	0.14	0.14	0.16	0.22	-	-	-	-
D Ce	0.03	0.03	0.04	0.18	0.13	0.13	0.15	0.20	-	-	-	-
D Nd	0.03	0.03	0.03	0.11	0.10	0.10	0.11	0.15	-	-	-	-
D Sm	0.02	0.02	0.02	0.06	0.07	0.07	0.07	0.10	-	-	-	-
D Eu	0.16	0.15	0.25	1.41	0.06	0.06	0.06	0.08	-	-	-	-
D Gd	0.02	0.01	0.02	0.04	0.04	0.04	0.04	0.06	-	-	-	-
D Dy	0.01	0.01	0.01	0.01	0.03	0.03	0.03	0.04	-	-	-	-
D Er	0.01	0.01	0.01	0.01	0.01	0.01	0.01	0.02	-	-	-	-
D Yb			bdl		0.01	0.01	0.01	0.01	-	-	-	-
D Lu			bdl		0.01	0.01	0.01	0.01	-	-	-	-
D Y	0.01	0.01	0.01	0.01	0.02	0.02	0.02	0.03	-	-	-	-
D Cu	0.03	0.02	0.07	0.04	0.57	0.58	0.65	0.90	0.01	0.03	0.01	0.80
D Zn	0.05	0.05	0.07	0.11	-	-	-	-	0.05	0.06	0.07	0.19
D V	0.01	0.01	0.01	0.00	0.00	0.00	0.00	0.00	-	-	-	-
D Pb	0.08	0.07	0.09	0.34	0.08	0.09	0.21	1.84	-	-	-	-
D Co	0.02	0.02	0.04	0.01	-	-	-	-	-	-	-	-
D Sc	0.01	0.01	0.02	0.02	0.00	0.00	0.00	0.00	-	-	-	-
D Sr	1.50	1.38	2.38	3.50	1.38	1.44	2.12	5.86	-	-	-	-
D Ba	0.09	0.14	0.16	0.61	0.13	0.13	0.22	0.84	-	-	-	-

* bdl - below detection limit

Table 5.7c. Melt-mineral partition coefficients for olivine using three different methods: Calculated Ds (this study by phenocrysts-groundmass equilibrium pairs). LSM (lattice strain model) is the method of Blundy & Wood (1994) and parameterisation is the method of Bédard (2005).

Olivine	**Measured Ds**				**Ds using LSM**				**Ds using Parameterisation**			
Fo	88	84	81	78	88	84	81	79	88	84	81	78
MgO melt	8.35	6.12	5.21	2.41	8.35	6.12	5.21	2.41	8.35	6.12	5.21	2.41
D Cu	0.04	0.03	0.05	0.20	0.40	0.40	0.40	0.39	0.06	0.06	0.07	0.08
D Zn	1.40	2.00	2.26	2.12	5.12	6.35	6.72	8.31	1.33	1.65	1.84	3.06
D V	0.01	0.02	0.03	0.06	0.15	0.15	0.15	0.15	-	-	-	-
D Co	4.70	6.27	9.75	19.39	5.08	6.30	6.67	8.25	3.89	5.15	5.96	11.79
D Sc	0.12	0.18	0.26	0.39	0.1-0.2				0.01	0.02	0.04	0.19

Table 5.7d. Melt-mineral partition coefficients for magnetite: Calculated Ds (this study by phenocrysts-groundmass equilibrium pairs) and calculated Ds using the parameterisation method of Bédard (2005).

Magnetite	**Measured Ds**			**Ds using Parameterisation**		
MgO melt	2.41	0.30	0.27	2.71	0.30	0.27
D Cu	0.53	0.63	0.72	1.4		
D Zn	9.07	14.50	13.96	15.6 - 16.0	26.5 - 32.7	26.7 - 31.2
D V	27.21	68.77	76.11	equation not available		
D Co	12.39	32.92	39.63	equation not available		
D Sc	1.57	2.98	3.19	equation not available		

Table 5.8. Isotope data for selected calc-alkaline rocks from the Hunter Ridge.

Sample	**$^{87}Sr/^{86}Sr$**	**$^{143}Nd/^{144}Nd$**	**$^{206}Pb/^{204}Pb$**	**$^{207}Pb/^{204}Pb$**	**$^{208}Pb/^{204}Pb$**
D15-7a	0.703	0.513	18.826	15.535	38.356
D11-2	0.703	0.513	18.803	15.526	38.328
D8-2	0.703	0.513	18.876	15.528	38.360

Chapter 6

Metal behaviour during differentiation of the Hunter Ridge calc-alkaline magma series

6.1 Introduction

Ore formation in porphyry and related epithermal environments is thought to be dependent on the partitioning of metals from the magma into an exsolving magmatic–hydrothermal fluid phase. Thus, understanding the behaviour of ore metals during magmatic differentiation is of prime importance to constrain the efficiency of their separation from evolving magmas and hence the potential to form economically important ore deposits.

This chapter will focus on the partitioning of Cu, Zn, Pb, V, Co and Sc between melts and crystallising mineral phases during the evolution of the Hunter Ridge calc-alkaline magma series. The partitioning of these ore metals between evolving melts and the main crystallising minerals (i.e. olivine, clinopyroxene, plagioclase and magnetite) was modelled in order to determine how magma ascent, crystallisation or degassing can led either to their enrichment or depletion in evolving melt.

Mineral/melt partition coefficients (Ds) for Cu, Zn, V, Pb, Co and Sc used in the modelling were calculated directly from LA-ICP-MS analyses for phenocryst-groundmass/glass equilibrium pairs. Olivine/melt, clinopyroxene/melt and plagioclase/melt partition coefficients for Cu, Zn, V, Pb, Co and Sc were determined for the following range of phenocrysts compositions: olivine Fo 89–79; clinopyroxene Mg# 90–75 and plagioclase An 87–31, and melt MgO content between 2.4 wt% and 8.3 wt%. Partition coefficients for Cu, Zn, V, Pb, Co and Sc between magnetite and host magma were calculated from LA-ICP-MS and microprobe analyses (magnetite grains and glass) in samples with a MgO range from 0.4 wt% to 2.4 wt%. From this, the D values were extrapolated for magmas up to 5.0 wt% MgO. For comparison purposes, where available, modelling was also conducted using D values obtained from the literature or calculated using the LSM and the parameterisation method of Bédard.

A comparison of the calculated metal partition coefficients obtained during this study with published data is listed in Table 6.1, and Figures 6.1–6.3.

6.2 Copper

Copper is found to be incompatible in silicate minerals and in magnetite as indicated by the measured $D_{Cu}^{ol/melt}$ of 0.03–0.20 (Fo 89–79), $D_{Cu}^{cpx/melt}$ of 0.01–0.04 (Mg# 90–75), $D_{Cu}^{plag/melt}$ of 0.02–0.07 (An 87–31) indicating that Cu partitioning into silicates is negligible (Fig. 6.4). $D_{Cu}^{mt/melt}$ was calculated to vary from 0.39 to 0.53, between a MgO range of 5.3 to 2.4 wt%. $D_{Cu}^{mt/melt}$ increases with decreasing MgO wt% (Fig. 6.4).

In the melt, Cu initially behaves incompatibly (i.e increasing with decreasing MgO) between 8.3 and 6.5 wt% MgO. Cu contents increase from ~89 ppm at 8.3 wt% MgO reaching a maximum

Table 6.1. Metal melt-mineral partition coefficients for olivine, clinopyroxene, plagioclase and magnetite using three different methods: Calculated Ds (this study by phenocrysts-groundmass equilibrium pairs). LSM (lattice strain model) is the method of Blundy & Wood (1994a, b) and parameterisation is the method of Bédard (2005).

Olivine		**Measured Ds**				**Ds using LSM**			**Ds using Parameterisation**			
Fo	89	84	81	78	89	84	81	79	89	84	81	78
MgO melt	8.35	6.12	5.21	2.41	8.35	6.12	5.21	2.41	8.35	6.12	5.21	2.41
D Cu	0.04	0.03	0.05	0.20	0.40	0.40	0.40	0.39	0.06	0.06	0.07	0.08
D Zn	1.40	2.00	2.26	2.12	5.12	6.35	6.72	8.31	1.33	1.65	1.84	3.06
D V	0.01	0.02	0.03	0.06	0.15	0.15	0.15	0.15	equation not available			
D Co	4.70	6.27	9.75	19.39	5.08	6.30	6.67	8.25	3.89	5.15	5.96	11.79
D Sc	0.12	0.18	0.26	0.39	0.1-0.2				0.01	0.02	0.04	0.19
Clinopyroxene		**Measured Ds**			**Ds using Parameterisation**							
Cpx Mg#	90	85	83	75	85	90	83	75				
MgO melt	8.35	6.12	5.21	2.41	8.35	6.12	5.21	2.41				
D Cu	0.01	0.02	0.03	0.04	0.03	0.04	0.05	0.02				
D Zn	0.30	0.56	0.66	1.67	0.71	0.77	0.83	1.35				
D V	0.68	0.97	1.45	0.84	equation not available							
D Pb	0.01	0.01	0.01	0.02	equation not available							
D Co	0.94	1.43	2.25	1.95	equation not available							
D Sc	1.93	3.22	4.95	12.55	equation not available							
Plagioclase		**Measured Ds**			**Ds using Parameterisation**							
An	87	85	70	31	87	85	70	31				
MgO melt	8.35	6.12	5.21	2.41	8.35	6.12	5.21	2.41				
D Cu	0.03	0.02	0.07	0.04	0.01	0.03	0.01	0.80				
D Zn	0.05	0.05	0.07	0.11	0.05	0.06	0.07	0.19				
D V	0.01	0.01	0.01	0.00	equation not available							
D Pb	0.08	0.07	0.09	0.34	equation not available							
D Co	0.02	0.02	0.04	0.01	equation not available							
D Sc	0.01	0.01	0.02	0.02	equation not available							
Magnetite		**Measured Ds**			**Ds using Parameterisation**							
MgO melt	2.41	0.30	0.27		2.41	0.30	0.27					
D Cu	0.53	0.63	0.72		1.4							
D Zn	9.07	14.50	13.96		15.6 - 16.0	26.5 - 32.7	26.7 - 31.2					
D V	27.21	68.77	76.11		equation not available							
D Co	12.39	32.92	39.63		equation not available							
D Sc	1.57	2.98	3.19		equation not available							

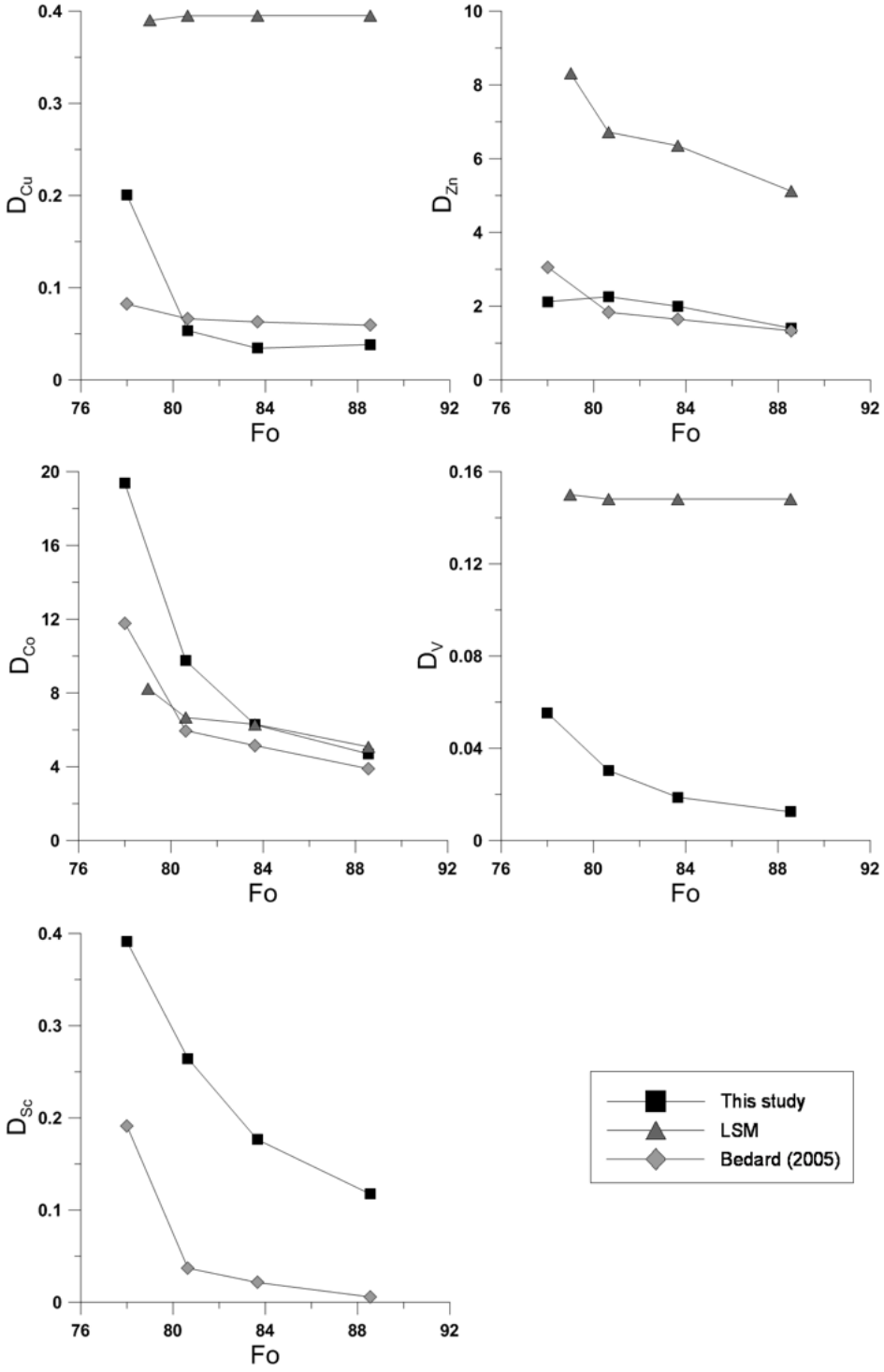

Fig. 6.1. Partition coefficients for Cu, Zn, Co, V and Sc in olivine as a function of Fo. LSM is the method of Blundy & Wood (1994). For the parameterisation method of Bedard R2 (Cu) = 0.26, R2 (Zn) = 0.97, R2 (Co) =0.80 and R2 (Sc) =0.92. For the LSM: R2 (Zn) = 0.74, R2 (Co) = 0.74, and R2 (V) =0.93. For this study: R2 (Cu) = 0.75, R2 (Zn) = 0.85, R2 (Co) =0.86, R2 (V) = 0.88 and R2 (Sc) = 0.93.

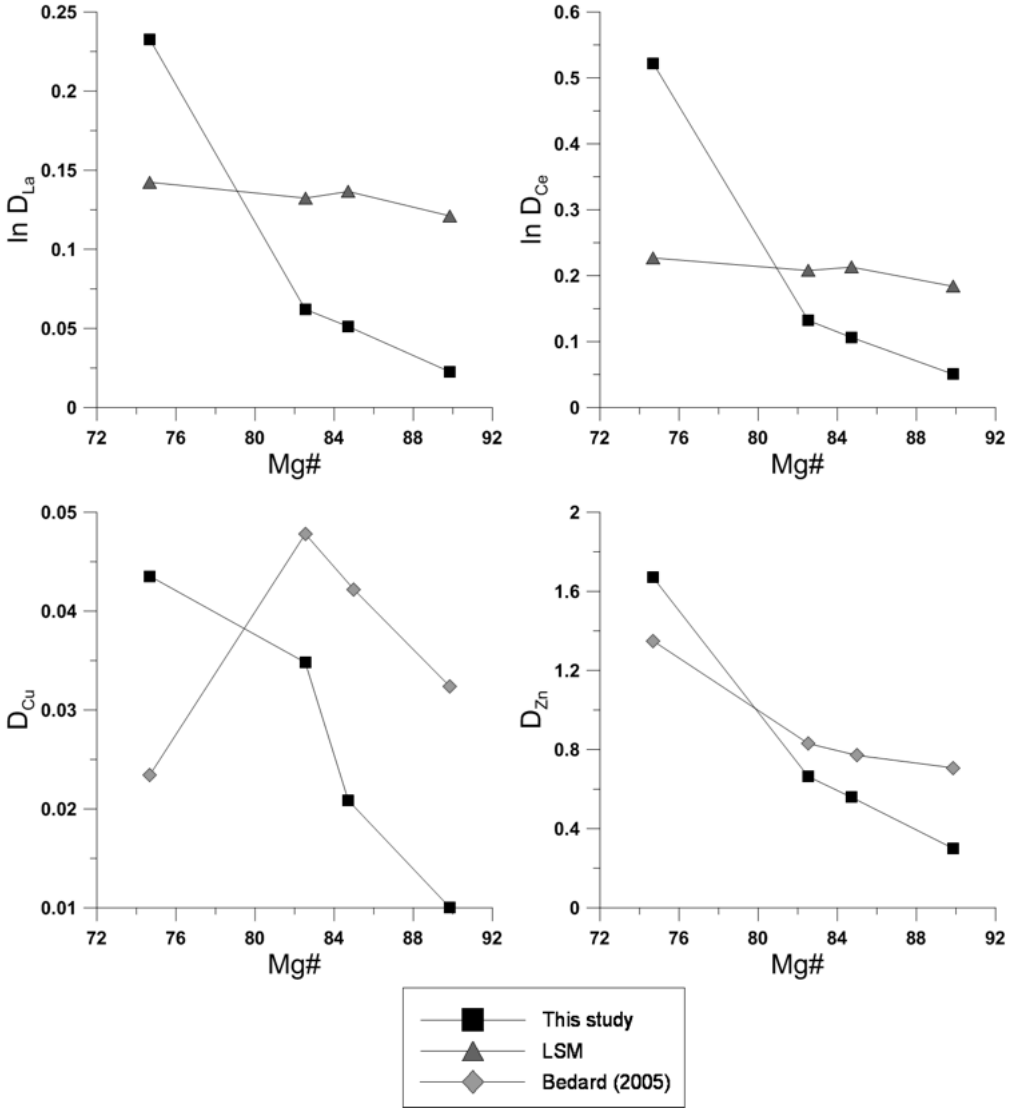

Fig. 6.2. Partition coefficients for La, Ce, Cu, and Zn in clinopyroxene as a function of Mg#. LSM is the method of Blundy & Wood (1994). For the parameterisation method of Bedard R2 (Cu) = 0.70 and R2 (Zn) = 0.28. For the LSM: R2 (La) = 0.84 and R2 (Ce) = 0.89. For this study: R2 (La) = 0.93, R2 (Ce) = 0.93, R2 (Cu) = 0.81 and R2 (Zn) = 0.90.

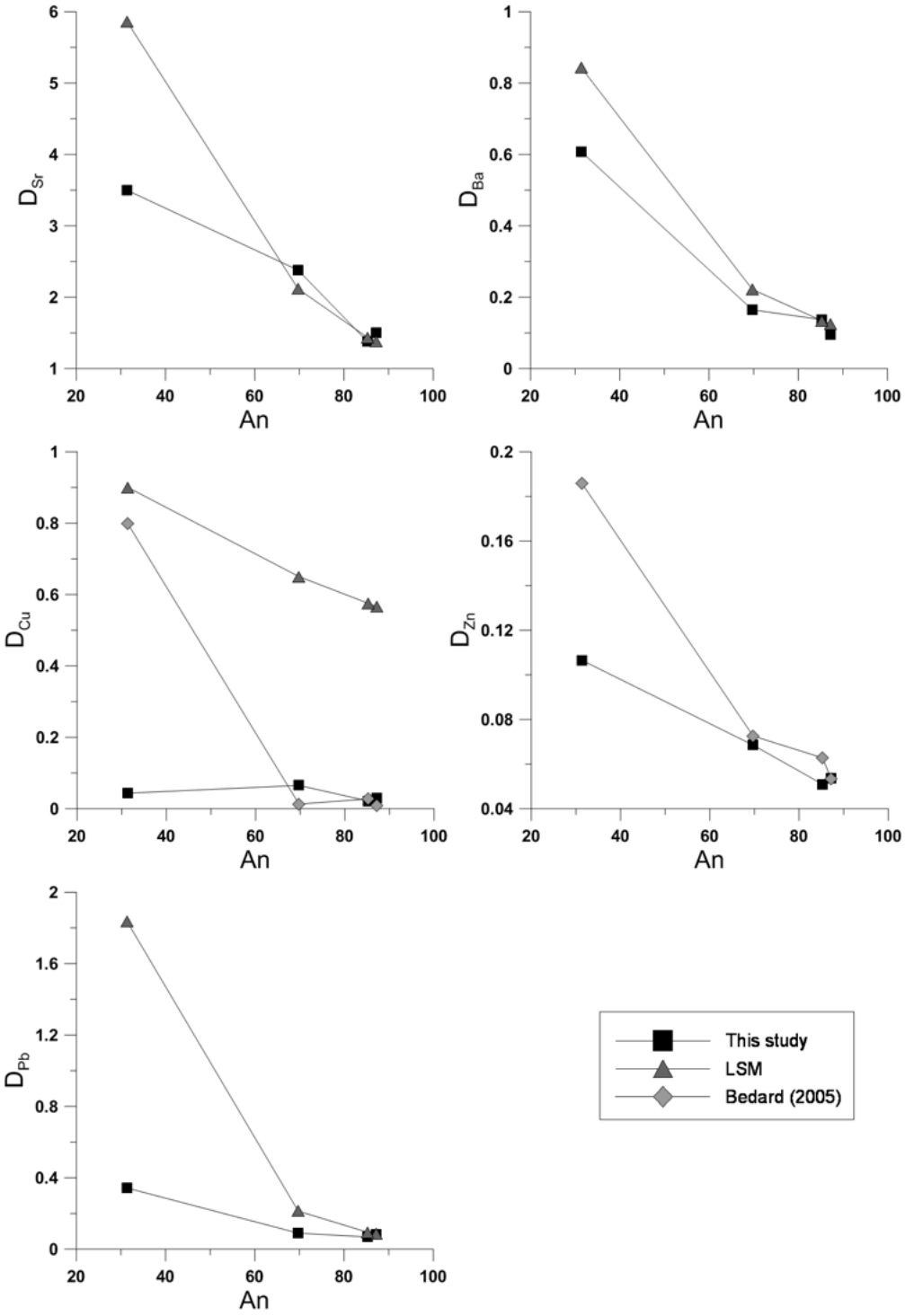

Fig. 6.3. Partition coefficients for Sr, Ba, Cu, Zn and Pb in plagioclase as a function of An. LSM is the method of Blundy & Wood (1994). For the parameterisation method of Bedard: R2 (Cu) = 0.73 and R2 (Zn) = 0.34. For the LSM: R2 (Sr) = 0.97, and R2 (Ba) = 0.96. For this study: R2 (Sr) = 0.96, R2 (Ba) = 0.95, R2 (Cu) = 0.89, R2 (Zn) = 0.93 and R2 (Pb) = 0.95.

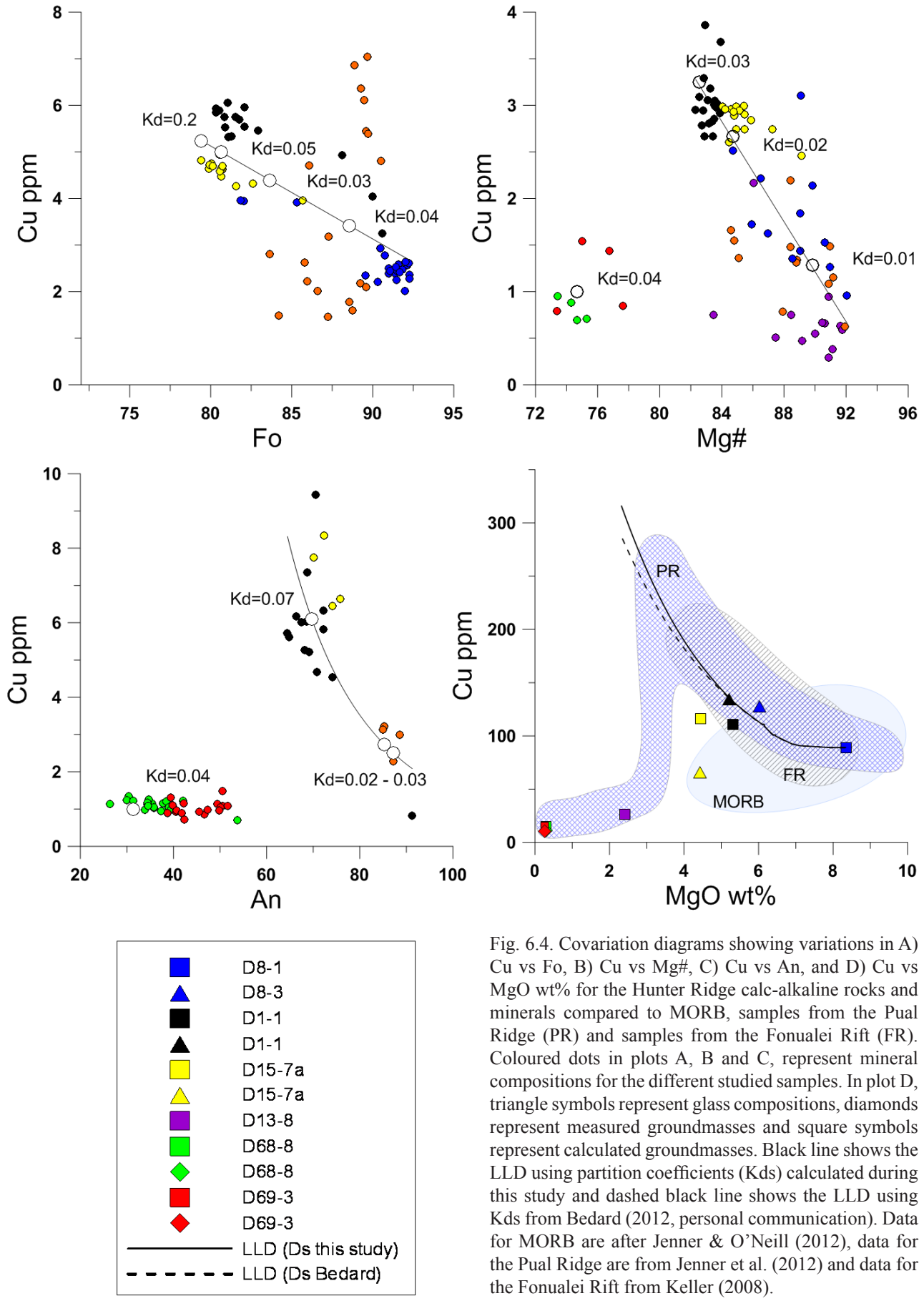

Fig. 6.4. Covariation diagrams showing variations in A) Cu vs Fo, B) Cu vs Mg#, C) Cu vs An, and D) Cu vs MgO wt% for the Hunter Ridge calc-alkaline rocks and minerals compared to MORB, samples from the Pual Ridge (PR) and samples from the Fonualei Rift (FR). Coloured dots in plots A, B and C, represent mineral compositions for the different studied samples. In plot D, triangle symbols represent glass compositions, diamonds represent measured groundmasses and square symbols represent calculated groundmasses. Black line shows the LLD using partition coefficients (Kds) calculated during this study and dashed black line shows the LLD using Kds from Bedard (2012, personal communication). Data for MORB are after Jenner & O'Neill (2012), data for the Pual Ridge are from Jenner et al. (2012) and data for the Fonualei Rift from Keller (2008).

value of ~130 ppm at 6.5 wt% MgO. After this, Cu plummets as MgO decreases further, reaching values of ~10 ppm at MgO values < 0.5 wt% (Fig. 6.4).

6.3 Zinc

Zinc is found to be compatible in olivine as indicated by the measured $D_{Zn}^{ol/melt}$ of 1.40–2.26. $D_{Zn}^{ol/melt}$ range from 1.40 to 2.26 increasing with decreasing Fo content in olivine (Fo 89–79) (Fig. 6.5). At lower Fo contents (i.e., Fo ~78), $D_{Zn}^{ol/melt}$ has been calculated as ~2.12. In clinopyroxene, $D_{Zn}^{cpx/melt}$ also increase from 0.30 to 1.67 with decreasing Mg# (Mg# 90–75) (Fig. 6.5). Zn is compatible in magnetite; $D_{Zn}^{mt/melt}$ was calculated to vary from 5.00 to 10.55, between a MgO range of 5.3 to 2.4 wt%. $D_{Zn}^{mt/melt}$ increases with decreasing MgO wt%. Conversely, Zn is found to be incompatible in plagioclase where $D_{Zn}^{pl/melt}$ range from 0.05 to 0.11, increasing with decreasing An content of the plagioclase (An 87–31) (Fig. 6.5).

In the melt, Zn initially behaves incompatibly (i.e increasing with decreasing MgO) between 8.3 wt% and 5 wt% MgO. Zn contents increase from ~53 ppm at 8.3 wt% MgO to a maximum value of ~75 ppm at 5 wt% MgO. After this, Zn decreases as MgO wt% decreases further, reaching values of ~60 ppm at MgO values of < 0.5 wt% (Fig. 6.5).

6.4 Vanadium

Vanadium is found to be incompatible in olivine as indicated by the measured $D_V^{ol/melt}$ of 0.01–0.06. $D_V^{ol/melt}$ increases with decreasing Fo content in olivine within the measured range (Fo 89–79) (Fig. 6.6). Vanadium concentrations in the melt and clinopyroxene are close, resulting in D values close to 1. $D_V^{cpx/melt}$ increases from 0.68 to 1.45 with decreasing Mg# (Mg# 90–83) (Fig. 6.6). At Mg# =75, $D_V^{cpx/melt}$ has been calculated to be ~1. V is found to be extremely incompatible in plagioclase where $D_V^{pl/melt}$ range from 0.006 to 0.011, increasing with decreasing An content of plagioclase (An 87–70) (Fig. 6.6). At lower An contents of plagioclase (i.e., An ~33), $D_V^{pl/melt}$ has been calculated as ~0.002. Vanadium is compatible in magnetite; $D_V^{mt/melt}$ was calculated to vary from 7.40 to 27.21, between a MgO range of 5.3 to 2.4 wt%. $D_V^{mt/melt}$ increases with decreasing MgO wt%.

In the melt, V initially behaves incompatibly (i.e., increasing with decreasing MgO) between 8.3 wt% and 5 wt% MgO. V contents increase from ~232 ppm at 8.3 wt% MgO to a maximum value of ~295 ppm at 5 wt% MgO. After this, V decreases as MgO wt% decreases further, reaching values of ~20 ppm at MgO values of < 0.5 wt% (Fig. 6.6).

6.5 Lead

Lead is found to be almost perfectly incompatible in clinopyroxene as indicated by the measured $D_{Pb-cpx/melt}$ of 0.01–0.02 indicating that Pb partitioning into clinopyroxene is negligible (Mg# 90–75) (Fig. 6.7). Lead values in olivine and magnetite are largely below detection, therefore, we can assume that

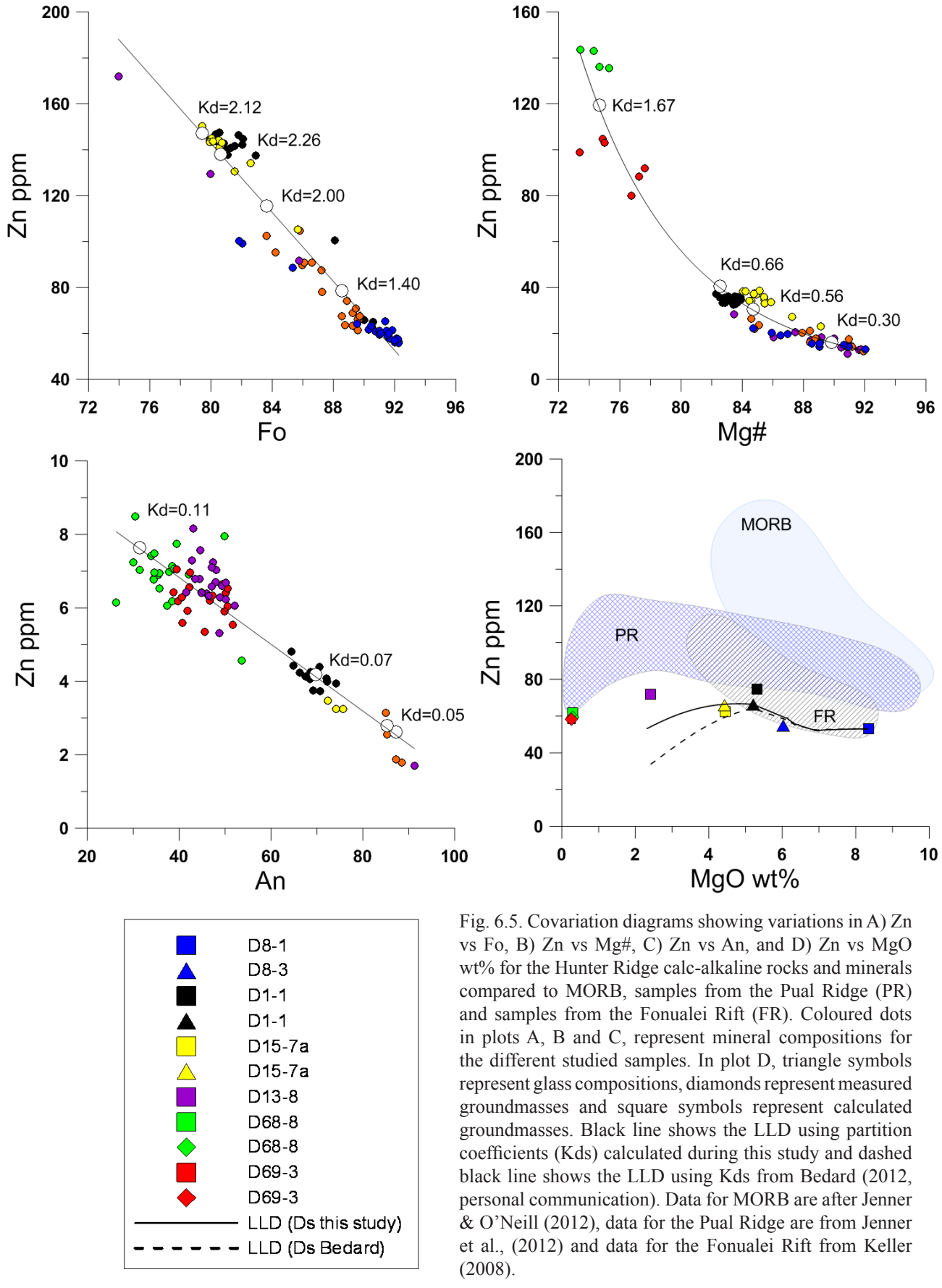

Fig. 6.5. Covariation diagrams showing variations in A) Zn vs Fo, B) Zn vs Mg#, C) Zn vs An, and D) Zn vs MgO wt% for the Hunter Ridge calc-alkaline rocks and minerals compared to MORB, samples from the Pual Ridge (PR) and samples from the Fonualei Rift (FR). Coloured dots in plots A, B and C, represent mineral compositions for the different studied samples. In plot D, triangle symbols represent glass compositions, diamonds represent measured groundmasses and square symbols represent calculated groundmasses. Black line shows the LLD using partition coefficients (Kds) calculated during this study and dashed black line shows the LLD using Kds from Bedard (2012, personal communication). Data for MORB are after Jenner & O'Neill (2012), data for the Pual Ridge are from Jenner et al., (2012) and data for the Fonualei Rift from Keller (2008).

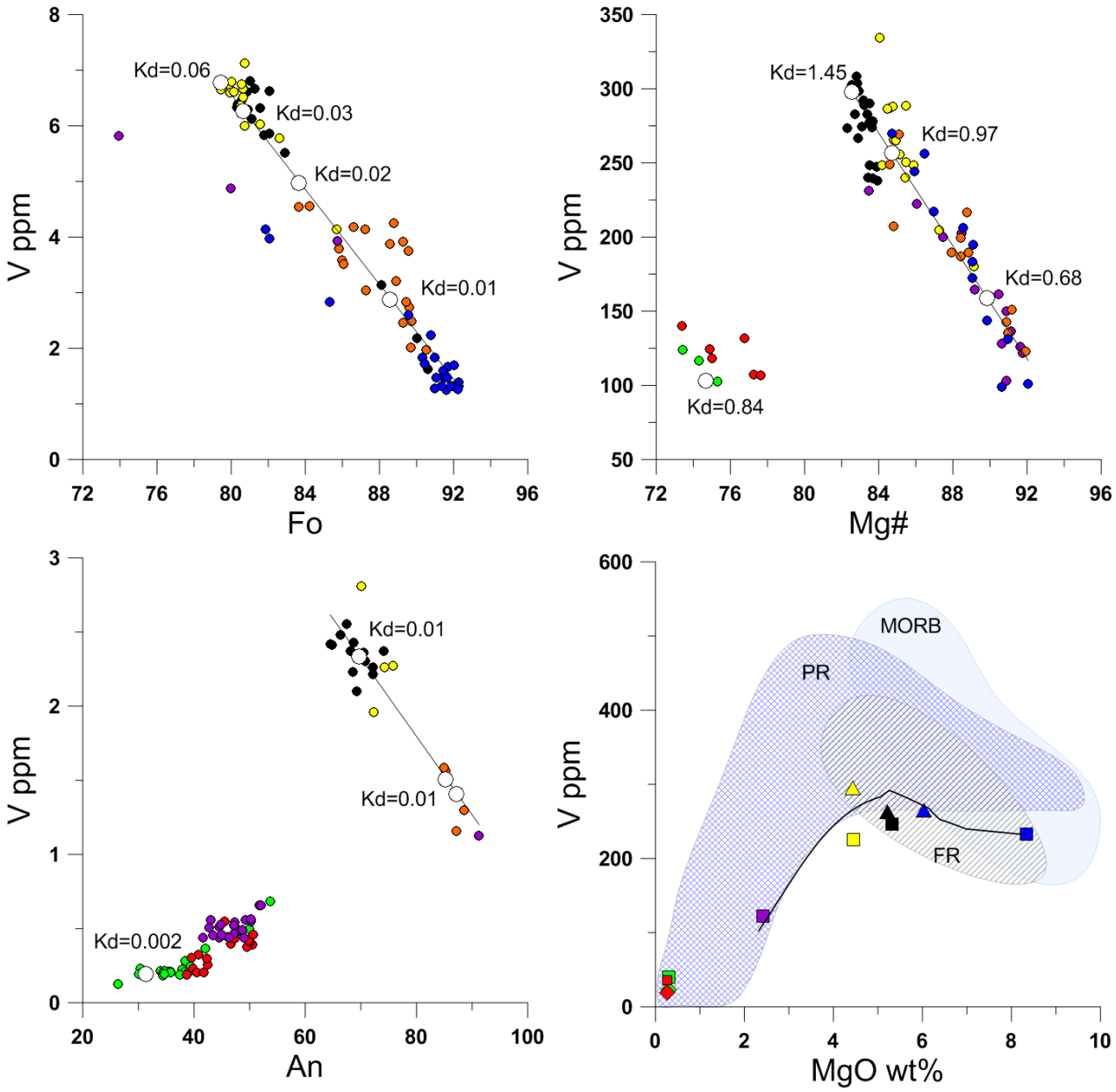

Fig. 6.6. Covariation diagrams showing variations in A) V vs Fo, B) V vs Mg#, C) V vs An, and D) V vs MgO wt% for the Hunter Ridge calc-alkaline rocks and minerals compared to MORB, samples from the Pual Ridge (PR) and samples from the Fonualei Rift (FR). Coloured dots in plots A, B and C, represent mineral compositions for the different studied samples. In plot D, triangle symbols represent glass compositions, diamonds represent measured groundmasses and square symbols represent calculated groundmasses. Black line shows the LLD using partition coefficients (Kds) calculated during this study. Data for MORB are after Jenner & O'Neill (2012), data for the Pual Ridge are from Jenner et al., (2012) and data for the Fonualei Rift from Keller (2008).

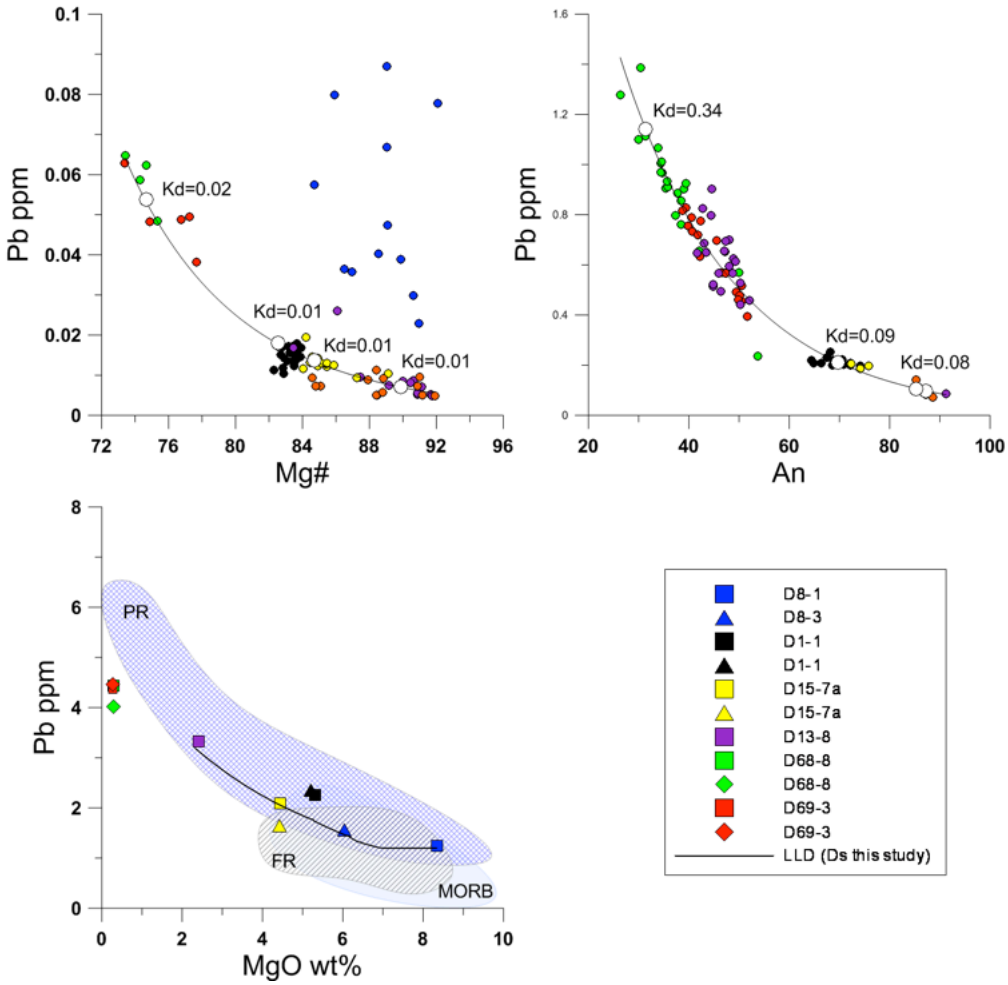

Fig. 6.7. Covariation diagrams showing variations in A) Pb vs Mg#, B) Pb vs An, and C) Pb vs MgO wt% for the Hunter Ridge calc-alkaline rocks and minerals compared to MORB, samples from the Pual Ridge (PR) and samples from the Fonualei Rift (FR). Coloured dots in plots A, B and C, represent mineral compositions for the different studied samples. In plot D, triangle symbols represent glass compositions, diamonds represent measured groundmasses and square symbols represent calculated groundmasses. Black line shows the LLD using partition coefficients (Kds) calculated during this study. Data for MORB are after Jenner & O'Neill (2012), data for the Pual Ridge are from Jenner et al., (2012) and data for the Fonualei Rift from Keller (2008).

its partitioning into these minerals is insignificant. $D_{Pb}^{plag/melt}$ varies between 0.07–0.34 (An 87–31) and increases with decreasing plagioclase An (Fig. 6.4).

In the melt, Pb behaves incompatibly (i.e increasing with decreasing MgO) during the entire studied MgO range. Pb contents increase from ~1.2 ppm at 8.3 wt% MgO to 4.5 ppm at 0.3 wt% MgO (Fig. 6.7).

6.6 Cobalt

Cobalt is found to be compatible in olivine as indicated by the measured $D_{Co}^{ol/melt}$ of 4.70–19.39. $D_{Co}^{ol/melt}$ increases with decreasing Fo content in olivine within the measured range (Fo 89–79) (Fig. 6.8). Cobalt is also compatible in clinopyroxene; $D_{Co}^{cpx/melt}$ increases from 0.94 to 2.25 with decreasing Mg# (Mg# 90–83). At lower Mg contents (i.e., Mg 75), $D_{Co}^{cpx/melt}$ has been calculated as ~1.95 (Fig.

6.8). Cobalt behaves compatibly in magnetite; $D_{Co}^{mt/melt}$ was calculated to vary from 2.97 to 12.39, between a MgO range of 5.3 to 2.4 wt%. $D_{Co}^{mt/melt}$ increases with decreasing MgO wt%. Conversely, Co is found to be incompatible in plagioclase where $D_{Co}^{pl/melt}$ initially increases (from 0.02 to 0.04) with decreasing An content of the plagioclase (An 87–70). At an anorthite content of ~30, $D_{Co}^{pl/melt}$ is ~ 0.01 (Fig. 6.8).

In the melt, Co behaves compatibly (i.e decreasing concentration with decreasing MgO wt%) throughout the entire studied MgO range. Co contents decrease from ~37 ppm at 8.3 wt% MgO to ~2 ppm at 0.3 wt% MgO (Fig. 6.8).

6.7 Scandium

Scandium is found to be incompatible in olivine as indicated by the measured $D_{Sc}^{ol/melt}$ of 0.12–0.39. $D_{Sc}^{ol/melt}$ increases with decreasing Fo content in olivine within the measured range (Fo 89–79) (Fig. 6.9). Scandium is also incompatible in plagioclase where $D_{Sc}^{pl/melt}$ ranges from 0.01 to 0.02; it increases slightly with decreasing An content of the plagioclase (An 87–31) (Fig. 6.9). Contrarily, Sc behaves compatibly in clinopyroxene, $D_{Sc}^{cpx/melt}$ increase from 1.93 to 12.55 with decreasing Mg# (Mg# 90–75) (Fig. 6.6). In magnetite, Sc behaves mildly compatibly, showing increasing compatibility with decreasing MgO wt%. $D_{Sc}^{mt/melt}$ was calculated to vary from 0.64 to 1.57, between a MgO range of 5.3 to 2.4 wt%.

In the melt, Scandium behaves compatibly (i.e decreasing with decreasing MgO) for the entire studied MgO range (8.3–5.0 wt%). Sc contents decrease from ~37 ppm at 8.3 wt% MgO to ~8 ppm at 0.3 wt% MgO (Fig. 6.9).

6.8 Discussion

The most primitive glasses from the Hunter Ridge calc-alkaline magma series (i.e. with the highest MgO wt% content) have Cu, Pb, Zn, Co, V and Sc contents similar to those in primitive mid-ocean ridge basalt (MORB). This rules out the possibility that the mantle wedge above the subducted slab, with which the ascending magmas interact, was enriched in these elements.

Primitive MORB (molar Mg# > 60 wt %) have ~70 ppm Cu (Kelemen et al., 2003). Copper in the Hunter Ridge calc-alkaline samples shows initial incompatible behaviour during magma evolution (i.e. decreasing MgO content of the melt). From 8.3 to 6.5 MgO wt%, Cu contents in the melt increase from ~89 to ~128 ppm, which is beyond the range found in typical MORB (Fig. 6.4).

Cu behaviour depends on the presence of immiscible sulphide (Jugo, 2009), during magmatic differentiation as Cu is highly compatible in sulphide phases. It is noteworthy that the partitioning of Cu during fractional crystallisation of arc-magmas and MORB is different. During differentiation of MORB-type melts, Cu contents decrease with continued fractional crystallisation. This decrease is attributed, by many authors, to the partition of Cu into a Fe-Ni-rich sulphide phase (e.g., Czamanske & Moore, 1977; Doe, 1995, Yi et al., 2003, Barnes et al., 2009, etc). In most arc magmas, Cu initially behaves incompatibly, increasing with decreasing MgO wt% until a maximum value is reached, after

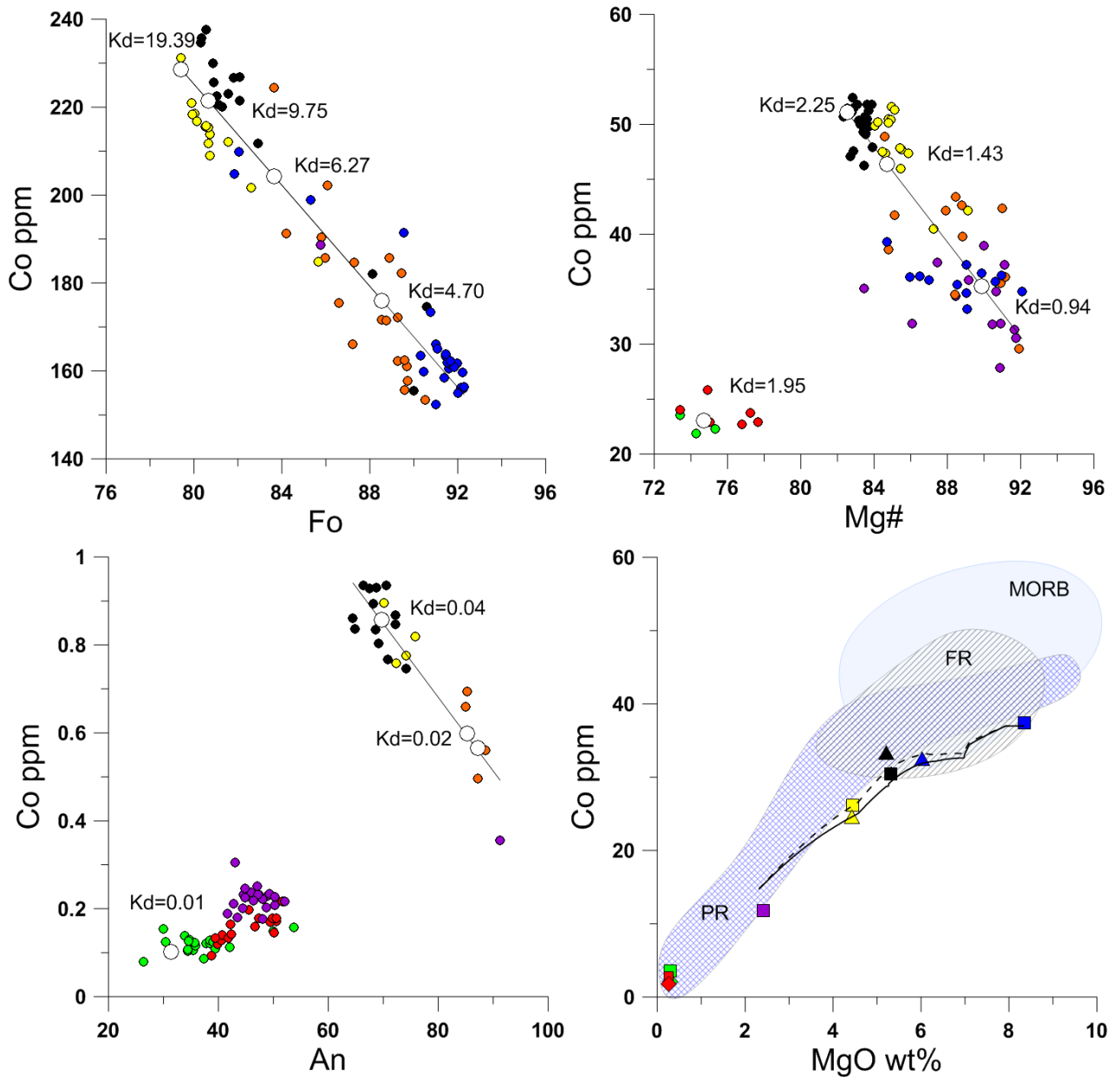

Fig. 6.8. Covariation diagrams showing variations in A) Co vs Fo, B) Co vs Mg#, C) Co vs An, and D) Co vs MgO wt% for the Hunter Ridge calc-alkaline rocks and minerals compared to MORB (blue shaded field), samples from the Pual Ridge (PR) and samples from the Fonualei Rift (FR). Coloured dots in plots A, B and C, represent mineral compositions for the different studied samples. In plot D, triangle symbols represent glass compositions, diamonds represent measured groundmasses and square symbols represent calculated groundmasses. Black line shows the LLD using partition coefficients (Kds) calculated during this study and dashed black line shows the LLD using Kds from Bedard (2012, personal communication). Data for MORB are after Jenner & O'Neill (2012), data for the Pual Ridge are from Jenner et al., (2012) and data for the Fonualei Rift from Keller (2008).

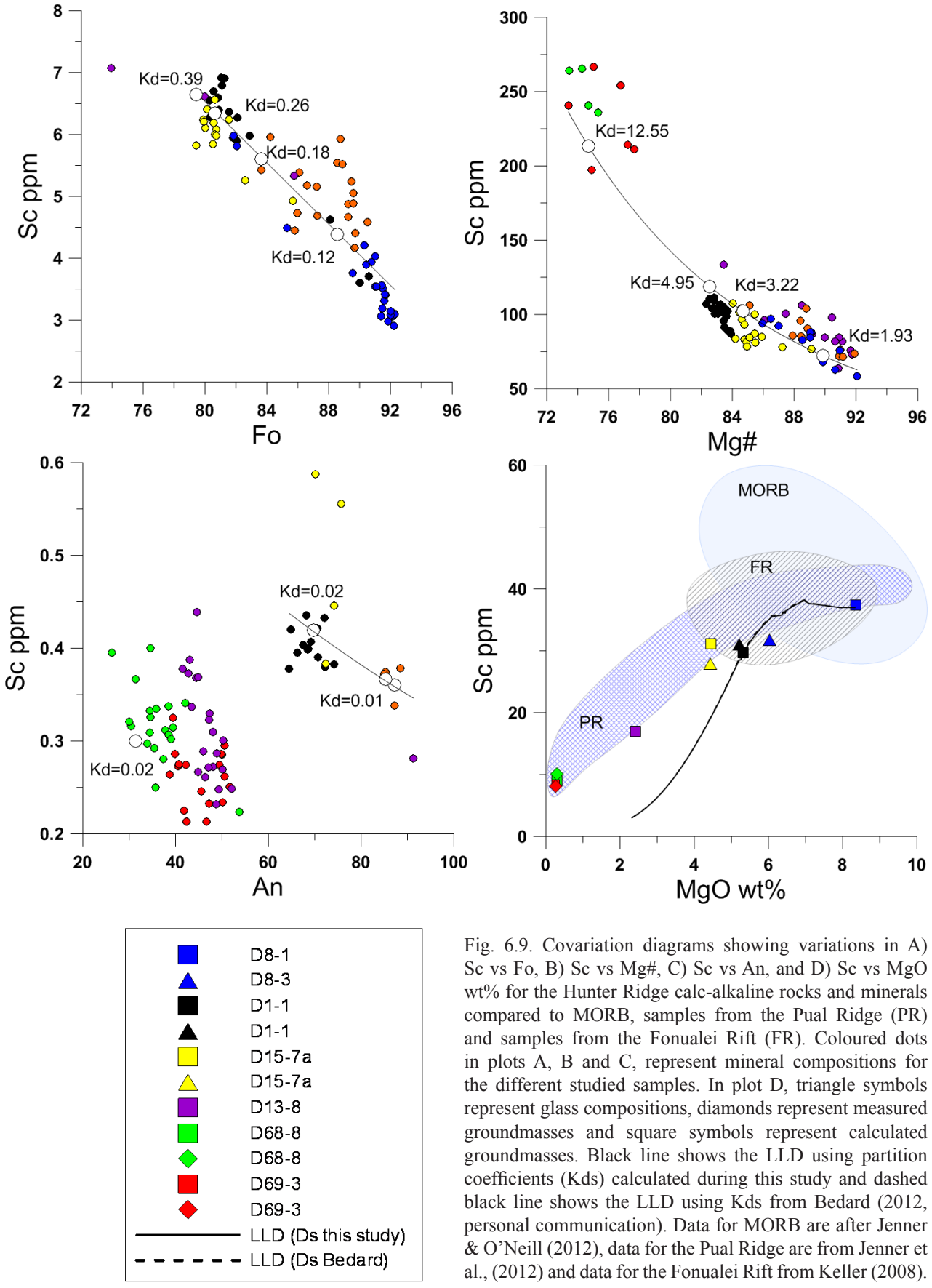

Fig. 6.9. Covariation diagrams showing variations in A) Sc vs Fo, B) Sc vs Mg#, C) Sc vs An, and D) Sc vs MgO wt% for the Hunter Ridge calc-alkaline rocks and minerals compared to MORB, samples from the Pual Ridge (PR) and samples from the Fonualei Rift (FR). Coloured dots in plots A, B and C, represent mineral compositions for the different studied samples. In plot D, triangle symbols represent glass compositions, diamonds represent measured groundmasses and square symbols represent calculated groundmasses. Black line shows the LLD using partition coefficients (Kds) calculated during this study and dashed black line shows the LLD using Kds from Bedard (2012, personal communication). Data for MORB are after Jenner & O'Neill (2012), data for the Pual Ridge are from Jenner et al., (2012) and data for the Fonualei Rift from Keller (2008).

which Cu becomes increasingily compatible and plummets as MgO wt% further decreases. The initial increase in Cu concentration in the melt would, therefore, require suppression of sulphide formation (Lee et al., 2012). This is expected under the high fO_2 conditions typical of arc magmas, where sulphur would be expected to be stable as sulphate (SO_4^{2-}) rather than a sulphide phase. As for the subsequent decrease in Cu in arc magmas, some authors have suggested that the observed decrease is evidence that the melts have ultimately reached sulphide saturation (Jenner et al., 2010; Lee et al., 2012; Li & Audetat, 2012, etc). It is worth noting that sulphur contents in the calc-alkaline samples are below the detection limit, which indicates that S was lost via degassing during eruption.

Our data shows that plagioclase saturation occurs at 6.5 MgO wt% content of the melt, which most likely marks the onset of degassing (water suppresses the plagioclase crystallisation and initiation of degassing expands the plagioclase stability field triggering plagioclase crystallisation). Degassing is the result of a pressure drop and decrease in H_2O solubility as magmas ascent, and is also dependent on the initial H_2O contents of the melt. Following plagioclase saturation, the Cu content of melt rapidly decreases. Given that Cu is not compatible in the mineral phases investigated and that sulphide is unlikely to be present, the implication is that copper is being partitioned into a volatile (i.e. fluid) phase. The most likely explanation for the abrupt decrease in Cu is that this element is being removed from the magma during degassing. This is supported by the steady decrease shown by the ratios of Cu and other elements of similar incompatibility during crystallisation (i.e. Cu/La ratios). Furthermore, there is a notable absence of sulphide globules in the glass and groundmass, though in extremely rare cases sulphides occur as small (< 80 μm) mineral inclusions in magnetite in the most evolved samples (i.e., dacites and rhyolites), other phenocrysts occurring in these samples (e.g., plagioclase, amphibole, clinopyroxene) do not contain suphide inclusions. Several authors have reported that Cu partitions into a volatile phase upon hydrous fluid saturation from a magma ($D_{Cu}^{fluid/melt} > 1$; Candela & Holland, 1984; Williams et al., 1995; Simon et al., 2006). Similarly, Zajacz et al., (2011) proposed that the solubility of Cu in magmatic volatiles increases with decreasing temperature. Furthermore, Cu-chloride complexes are predicted to be the dominant species in most magmatic volatiles (Keller, 2008; Zajacz et al., 2008 and 2009). Consequently, we believe that the most likely explanation for our observations is that Cu is preferentially entering a volatile phase, most likely as a chloride complex.

The initial fractionating crystalline assemblage (olivine-clinopyroxene-plagioclase) causes Zn and V contents to increase in the melt (from ~50 ppm and 230 ppm at 8.3 MgO wt% to a maximum of ~66 ppm and 275 ppm, respectively, at 5 wt% MgO). At this point (5 wt% MgO), magnetite saturation occurs, which results in a decrease in FeO_t, and TiO_2 in residual melt. Following magnetite saturation, Zn and V both decrease as MgO further decreases, reaching values of ~50 ppm and 20 ppm respectively at MgO values of < 0.5 wt% (Figs 6.5, 6.6). The similar behaviour of Zn and V during magmatic fractionation can be explained by our modelling by their partitioning into magnetite (Figs 6.5, 6.6). Both $D_{Zn}^{mt/melt}$ and $D_V^{mt/melt}$ are high (5.0 and 7.4 respectively at ~5 wt% MgO) which indicates that Zn and V are extremely compatible in magnetite. The amount of magnetite required to account for the observed Zn partitioning has been estimated to be approximately 6–8 %. This is similar to the amount of magnetite calculated from modelling using IgPet and Petrolog (8–11%). The discrepancy between the observed and modelled Zn trends could be due to the calculated $D_{Zn}^{mt/}$

^{mel} values used for the modelling being too high. This is difficult to assess due to problems associated with measuring Zn contents within small magnetite grains (i.e. < 40 μm), such as those present in the more primitive samples (MgO from 3 to 5 wt%). Nevertheless, partitioning of Zn into magnetite is the most likely explanation for the marked decrease in Zn within the melt at ~5 wt% MgO. The same mechanism was proposed by Mavrogenes et al. (2008) to explain the behaviour of Zn in a suite of glasses from the Manus Basin, in which Zn initially increases from 50 to 60 wt% SiO_2 then decreases with higher SiO_2 contents.

The abundance of Pb increases with decreasing MgO wt% content of the melt. Lead contents increase from ~1 ppm at 8.3 wt% MgO to 4.5 ppm at 0.3 wt% MgO. Our modelling shows that Pb partitioning into olivine, clinopyroxene, magnetite and plagioclase is negligible, which causes Pb to remain in the melt during magmatic differentiation (Fig. 6.7). In addition, it would appear that Pb does not enter a high-T water-rich fluid (as with Cu), as previously suggested by Stanton (1991) and Beaudoin and Scott (2009). In the presence of an immiscible sulphide liquid, Pb will be strongly partitioned into it, as evidenced from the high DPbSL/melt values that range from 3–48, reported by several authors (Li & Audédat, 2012; Lagos et al., 2008; Wood et al., 2008). Therefore the incompatible behaviour of Pb provides further evidence that the magmas have not reached sulphide saturation.

The concentration of Co decreases with decreasing MgO wt% of the melt (from ~37 ppm at 8.3 wt% MgO to ~2 ppm at 0.3 wt% MgO). Our modelling shows that Co is partitioned into olivine and to lesser extent into clinopyroxene early during magmatic fractionation (as indicated by the high $D_{Co}^{ol/melt}$ of 4.7 – 19.3 over Fo 89 – 79, and $D_{Co}^{cpx/melt}$ values of 0.9 to 2.3 over Mg# 90–82; Fig. 6.8). Co also partitions into magnetite as indicated by $D_{Co}^{mt/melt}$ values of 6 to 18 over a MgO range of 5.3 to 2.3 wt%. As a consequence, the melt is being depleted in cobalt and therefore Co behaves as a compatible element. The fact that we can model the Co evolution trend very well by taking into account its partitioning to the silicate/oxide minerals only (Fig. 6.8) is another argument in support of the lack of sulphide saturation during evolution of these magmas.

The concentration of Sc decreases with decreasing MgO wt% content of the melt (from ~37 ppm at 8.3 wt% MgO to ~8 ppm at 0.3 wt% MgO) (Fig. 6.9). Our modelling shows that this can be explained as a result of Sc partitioning into clinopyroxene, as indicated by the high $D_{Sc}^{cpx/melt}$ of 1.9–12.6 (Mg# 90–75). As magma evolution progresses, Sc also partitions into magnetite as indicated by $D_{Sc}^{mt/melt}$ of 0.6 to 1.6 over a MgO range of 5.3 to 2.3 wt%. The amount of magnetite required to account for the observed Sc partitioning has been estimated to be approximately 6–8%. This is slightly lower than the amount of magnetite calculated from modelling using IgPet and Petrolog (8–11%). Similarly to Zn, the discrepancy between the observed and modelled Zn trends could be due to the calculated $D_{Sc}^{mt/mel}$ values used in the modelling being too high.

In summary, the behaviour of all metals, but copper, can be explained by fractionation of the main silicate minerals and magnetite. The behaviour of copper requires an additional factor that decreases its content in the melt during fractionation. Our data suggest that copper is likely lost to the fluid phase from the onset of degassing, as there is no evidence for sulphide saturation during fractionation of these magmas.

Chapter 7

Identification of the adakite fractionation series

7.1 Introduction

Adakites are often associated with large porphyry-style deposits (e.g. Baldwin & Pearce, 1982; Thiéblemont et al., 1997; Oyarzun et al., 2001; Sun et al 2011) and epithermal gold mineralisation (Sajona & Mauri, 1998; Chiaradia et al., 2004).

Although adakites are linked to subduction-zone magmatism, not all subduction zones seem capable of generating them. Recent adakite formation is very sparse and reduced to a certain number of continental and oceanic arcs, such us the Philippines, Ecuador, Kamchatka, and Hunter Ridge, amongst others (e.g. Sajona & Mauri, 1993; Beate et al., 2001; Bourdon et al., 2002; Yogodzinski et al., 2001; Danyushevsky et al., 2008). Adakites are classified mainly on the basis of trace element abundances, notably high Sr/Y (e.g. Sr/Y >40), high La/Yb (e.g. La/Yb >15) and unradiogenic Sr isotopes ratios ($^{87}Sr/^{86}Sr$ <0.7040) (Kay, 1978; Defant & Drummomnd, 1990; Kelemen et al., 2003b; Martin et al., 2005; Richards & Kerrich. 2007). Distinct petrogenetic models have been proposed to explain the genesis of adakites and, to date, there is little agreement towards their origin and formation. Some authors proposed that adakites represent partial melts generated from subducting oceanic crust under eclogite and/or amphibolite facies conditions (e.g. Drummond et al., 1996 and Martin et al., 2005). Such a model is only thought to be possible where the subducting oceanic lithosphere is hot and young (i.e. <5 Ma) (Peacock, 1996). This has been proposed for the origin of the adakites in the Austral Volcanic Zone in South America, with the subduction of segments of the Chile Ridge beneath the South American Plate close to the Chile Triple Junction (Guivel et al., 2003), and in the Northern Volcanic Zone of South America, with the subduction of the Carnegie Ridge beneath Ecuador (i.e. 'shallow-subduction' of Gutscher et al., 2000). However, more recently it has been recognised that slab-melting could also occur in older, colder crust, for example where subduction occurs into hot mantle associated with a nearby spreading axis (Danyushevsky et al., 2006). This model, called "hot subduction", is used to explain the low-Mg/high-Si adakites found in western Kadavu, Fiji. Another mechanism proposed with a similar result is in the region of a slab-tear, where hot, convecting, asthenospheric mantle is brought into contact with older, cold, oceanic crust leading to partial melting of the slab component (Yogodzinski et al., 2001).

Some adakites contain high Cr and Ni concentrations, which has been attributed to interaction between peridotide and slab-derived melts during their ascent through the asthenosphere (Sen and Dunn, 1994; Martin, 1999). Conversely, a number of researchers have argued that some adakites are not the result of slab melting, but are instead generated either by i) low-pressure assimilation–fractional-crystallization (AFC) processes (Castillo et al., 1999; Chiaradia, 2009; Chiaradia et al., 2009), or ii) reflect high-pressure crystallization of typical subduction-related magmas that formed garnet (Macpherson et al., 2006). Some other workers have even argued that adakites reflect melting

of crustal material in the upper plate overlying a mantle wedge (Atherton and Petford, 1993). Finally, it has been noted that some high-Mg/low-silica adakites possess enrichments in certain incompatible trace elements (e.g. Sr, La). This has been explained in a two-stage process involving partial melting of a mantle wedge previously metasomatised though the addition of slab-derived melts (Stern & Kilian, 1996; Martin et al., 2005). A similar model is invoked in the genesis of the high-Mg/low-Si adakites in the east Kadavu islands, Fiji, with melting of hot mantle wedge previously metasomatised by adakitic slab-derived melts (Danyushevsky et al., 2008).

From the above discussions it is evident that the formation of adakites can be explained by multiple models and to try to come up with a solution to this is beyond the scope of this research. Furthermore, given the possible range in environments that are likely to occur at different subduction zones, many of the above models may be valid on a case-by-case basis.

For the adakites found at the Hunter Ridge, we favour the two-stage model involving partial melting of a mantle wedge initially metasomatised by adakitic melts generated in a 'hot subduction' type setting. Crucially, this does not require any interaction with continental crust.

Our study focuses on whether adakite rock suites are more prospectively attractive for porphyry mineral systems than associated calc-alkaline suites. A link between porphyry deposits and "adakite-like magmas" has been known for some time. Some authors like Baldwin & Pearce (1982) realised that intrusions associated with porphyry deposits in northern Chile have large negative anomalies for Y, Mn, Th, and HREE relative to barren ones, and proposed that these might be the result of high-pressure differentiation of hydrous arc magmas. Similarly, other researchers noted that porphyry-related intrusions from Arizona, northern Chile and northern Argentina display high Sr/Y ratios and depletions in HREE and attributed these effects to magmatic fractionation of amphibole and/or deep-crustal garnet (Cornejo et al., 1997; Ossandón & Zentilli, 1997; Lang & Titley, 1998; Kay et al., 1999; Kay & Mpodozis, 2001; Richards et al., 2001; Richards et al., 2006). Other authors (e.g. Thiéblemont et al., 1997; Sajona & Maury, 1998; Oyarzun et al., 2001) have suggested a direct link between adakite-like rocks and the formation of porphyry deposits but attribute this to the adakites being the product of direct melting of the subducting plate. Sajona & Mauri (1993) attributed adakitic magmatism of the Luzon Central Cordillera and eastern Mindano (Philippines) to subduction of young hot oceanic crust (Philippine Sea plate) beneath eastern Mindanao. More recently, Sajona and Mauri (1998) suggested a direct association between adakites and the porphyry copper-gold, copper-molybdenum, and epithermal gold deposits in the Philippine islands (e.g. Tampakan, Lepanto-Far South East, Baguio district). Similarly, Oyarzun et al. (2001) proposed that shallow subduction of the Farallon Plate beneath the South America Plate during the late Eocene-Early Oligocene led to melting of the subducting slab to form plutonic rocks of adakitic affinity. Subsequently, the same authors argued that the giant porphyry deposits in northern Chile (i.e. Chuquicamata) that formed during the same geological period are a direct result of adakitic magmatism.

The authors that favour slab melting as a direct factor for the fertility of adakitic rocks have cited various explanations including: i) high S contents (Oyarzun et al., 2001), ii) high water content (Sajona and Maury, 1998), and iii) high oxidation state of slab melts from oxidative sea-floor alteration (Mungall, 2002). However, high water contents and high oxidation states are characteristic of most

arc magmas and the factors that control the abundance and speciation of S are also the same for typical calc-alkaline arc magmas with which adakites are often associated.

In the subsequent sections, adakites from the Hunter Ridge are described in terms of major and trace elements and metal contents. These are compared to spatially and temporally associated calc-alkaline rocks. By comparing rocks from these two different magma series we can examine the links between slab melts and the potential for porphyry mineralisation.

7.2 Major elements

Adakitic rocks from the Hunter Ridge cover a range of compositions from basalt to andesite, with MgO contents from 5.2 to 13.2 wt% and SiO_2 contents between 54.3 and 58.0 wt%. Major element data for whole-rock and glass analyses are shown in Figure 7.1 and Table 7.1. SiO_2, TiO_2, Al_2O_3, Na_2O and K_2O display good negative correlations with MgO, whereas CaO and FeO do not show any correlation with MgO. The variation in major element contents can be explained by continuous fractionation of olivine and clinopyroxene. This is confirmed by the absence of plagioclase phenocrysts in the adakitic samples studied, which is a common feature of primitive, high Mg# lavas. It is widely understood that this is caused by relatively high dissolved water contents in the melt (Tatsumi, 1981; Tatsumi and Ishizaka 1982; Hirose, 1997; Carmichael 2002). Supporting evidence comes from the progressive increase in Al_2O_3 contents with decreasing MgO wt% contents, which shows that plagioclase is not entering as a liquidus phase. The magnitude of the Al_2O_3 peak and corresponding SiO_2 contents are indicative of the H_2O content of the parent magma and the pressure of crystallization. For the Hunter Ridge adakites, the amount of dissolved H_2O in the melt led to the suppression of plagioclase crystallisation across the studied MgO range (13.2–5.17 wt%).

Table 7.1. Major element composition (wt%) of the Hunter Ridge adakites (XRF whole-rock geochemistry and glass compositions).

Sample	SiO_2	TiO_2	Al_2O_3	FeO	MnO	MgO	CaO	Na_2O	K_2O	P_2O_5	Total
D15-1	54.43	0.43	11.54	7.23	0.13	13.19	9.40	2.35	1.09	0.20	100
D15-2	54.81	0.48	12.66	7.54	0.14	11.33	9.43	2.43	0.98	0.20	100
D15-3	54.31	0.43	11.59	7.22	0.13	13.19	9.48	2.38	1.06	0.19	100
D15-4	54.69	0.43	12.07	6.99	0.12	12.84	9.14	2.59	0.97	0.17	100
D15-5	54.45	0.45	12.02	7.54	0.13	12.36	9.44	2.52	0.90	0.19	100
D15-6	54.36	0.46	12.21	7.57	0.14	12.18	9.31	2.62	0.95	0.20	100
D15-4*	57.97	0.54	15.69	6.80	0.12	5.17	9.08	3.07	1.32	0.24	100

* = Glass sample.

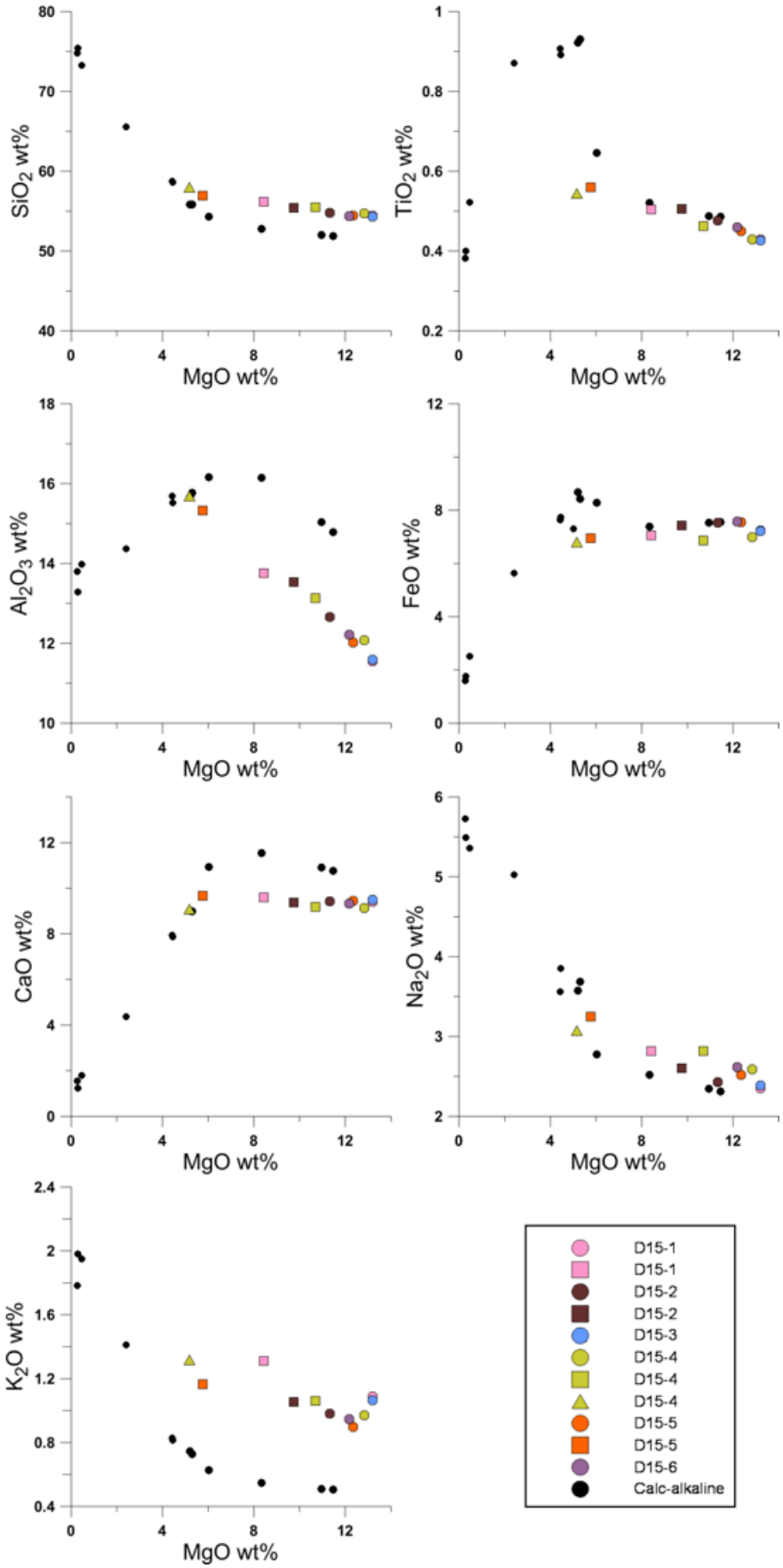

Fig. 7.1. Major element composition of the Hunter Ridge adakitic rocks compared to the Hunter Ridge calc-alkaline samples (black dots). Triangle symbols represent glass compositions, circles represent whole-rock data and square symbols represent calculated groundmass compositions.

7.3 Trace elements

The mantle-normalised trace element patterns for the adakites are shown in Figure 7.2. All of the samples display similar patterns characterised by: i) enrichment in large-ion lithophile elements (LILE), ii) enrichment in mobile elements (Ba, K, Pb and Sr), iii) negative anomalies for Nb and Ta, and iv) enrichment of light rare earth elements (LREE) over heavy rare earth elements (HREE). Additional distinguishing characteristics include: a) La and Yb concentrations from 17–26 ppm and ~1 ppm, respectively, with $(La/Yb)_N$ ratios between 12 and 18, and b) Sr and Y concentrations from 700–1000 ppm and 10–12 ppm, respectively, with $(Sr/Y)_N$ ratios close to 16. Bulk Ni and Cr contents range from 187–250 ppm and 580–757 ppm, respectively (Figs 7.3, 7.4).

High whole-rock Sr/Y ratios are most likely to be an inherited characteristic of the parental melt. This is because crystallisation of olivine and clinopyroxene will not fractionate Sr from Y. Additionally, neither plagioclase (which preferentially partitions Sr) or amphibole (which preferentially partitions Y and HREE) are present in these rocks. Similarly, the strong enrichment in LREE over HREE displayed by these rocks is difficult to explain by fractional crystallisation alone (Fig. 7.2). Although clinopyroxene and hornblende preferentially partition HREE over LREE ($D_{La}^{cpx/melt}$ ~0.02–0.03 and $D_{Yb}^{cpx/melt}$ ~is 0.21–0.91, in basaltic to andesitic melts: this study), this would require the crystallisation of an unrealistic amount of clinopyroxene (~10% observed) or >40% amphibole (none observed in the samples). These samples also possess $(Dy/Yb)_N$ ratios >1.5 (i.e. enrichment in MREE over HREE). Melting in the presence of garnet would produce the observed patterns and enrichment in LREE over HREE and $(Dy/Yb)_N$ ratios >1.5 (Kelemen et al., 2003). It seems most likely, therefore, that the adakitic rocks in the Hunter Ridge were formed from melts generated in the presence of garnet in the source region (i.e. eclogitic rocks), as evidenced by the high Sr/Y, high La/Yb and high Dy/Yb ratios (Fig 7.4).

7.4 Establishing mineral/melt correspondence

Due to the presence of large numbers of microlite crystals it was not possible to directly obtain element concentrations on groundmasses. To overcome this, a mass-balance approach was used to calculate the groundmass composition (see Chapter 5 for more detailed explanation on the methodology). Average mineral composition and proportions are listed in Tables 7.2 (major-element data) and in Table 7.4 (trace-element data).

The compositions of minerals in equilibrium with the glass and/or groundmass were derived using Petrolog v3 (Danyushevsky & Plechov, 2011). These calculations were carried out using the same parameters and models as those described in Section 5.2.2 of Chapter 5. Sample D15-4-groundmass (most primitive melt composition, i.e. 10.7 wt% MgO) has both olivine (Fo ~92) as a liquidus phase and clinopyroxene (Mg# ~93) as pseudo-liquidus phase (Table 7.3). These are in good agreement with the mineral compositions obtained from sample D15-4, in which olivine compositions range from Fo 86–92 and clinopyroxene from Mg# 86–92. For sample D15-1-groundmass (8.4 wt% MgO), melt-liquidus calculations predict olivine (Fo ~89) and clinopyroxene (Mg# ~91) as liquidus

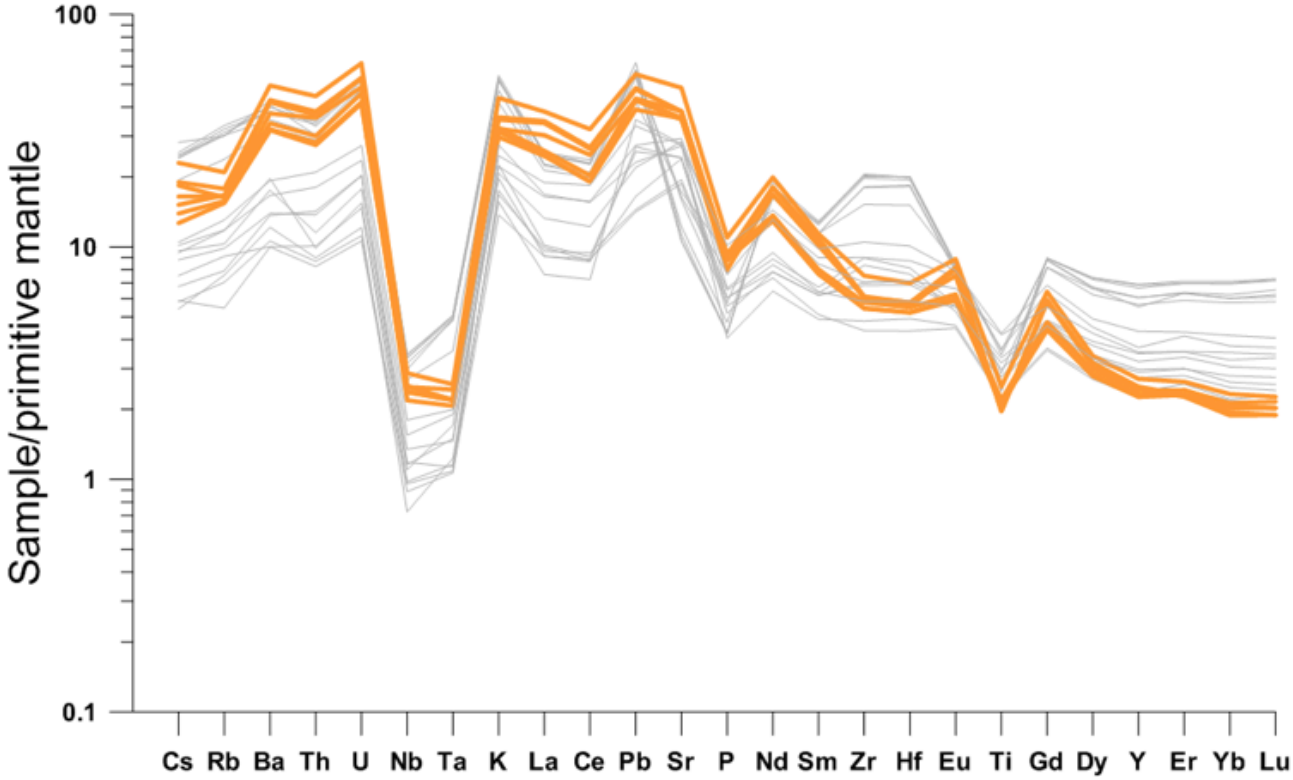

Fig. 7.2. Primitive mantle-normalised trace element patterns for the Hunter Ridge adakites (orange) compared to the Hunter Ridge calc-alkaline rocks.

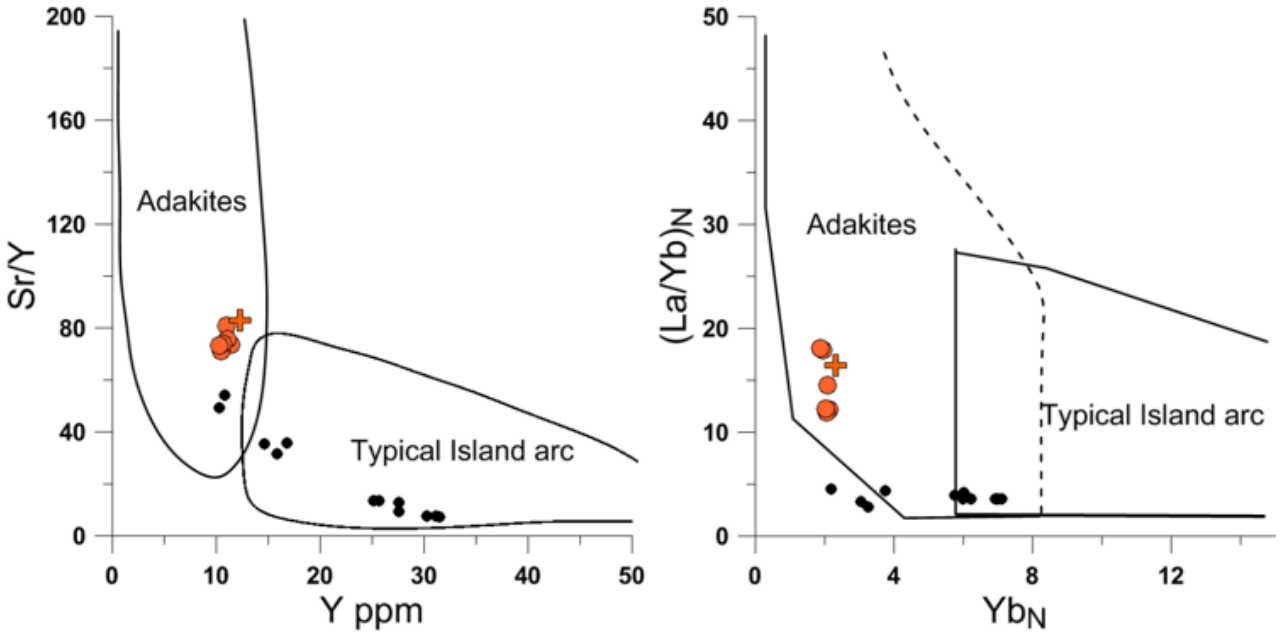

Fig. 7.3. A) Plots of Sr/Y vs Y (modified after Defant and Drummond, 1993), and B) (La/Yb)N vs YbN (modified after Martin et al., 1999), showing fields for adakites and typical island arc lavas. Hunter Ridge adakites are shown as orange dots (rocks) and orange crosses (glass). Calc-alkaline rocks are shown as black dots.

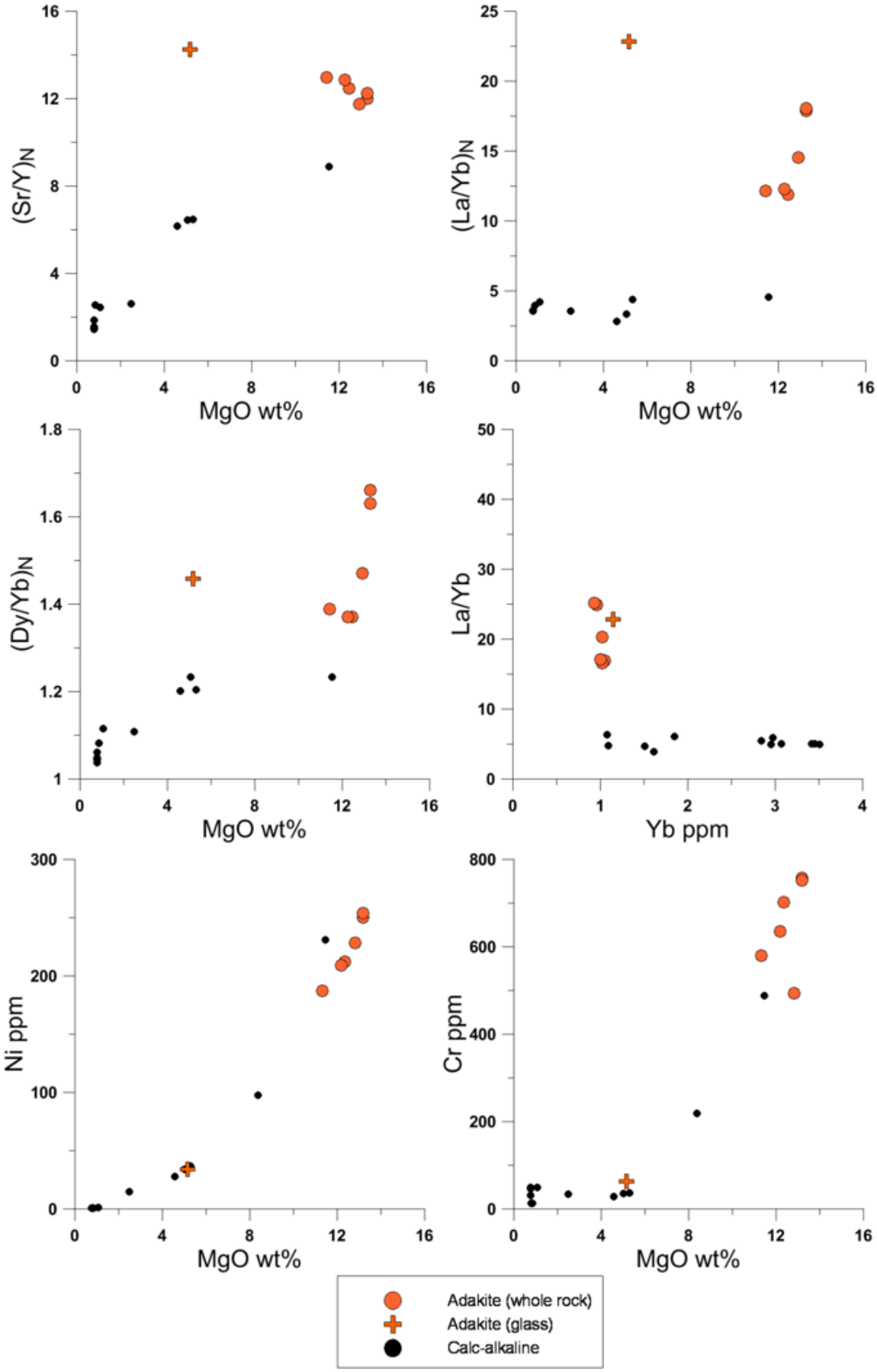

Fig. 7.4. Plots of A) (Sr/Y)N vs MgO wt%, B) (La/Yb)N vs MgO wt%, C) (Dy/Yb)N vs MgO, D) La/Yb vs Y, E) Ni ppm vs MgO wt%, and F) Cr vs MgO wt% for the Hunter Ridge adakites, compared to the Hunter Ridge calc-alkaline samples (black dots).

Table 7.2. Calculated groundmasses and mineral compositions (wt%) and modal proportions of the Hunter Ridge adakitic rocks. g = groundmass.

Sample	SiO_2	TiO_2	Al_2O_3	FeO	MnO	MgO	CaO	Na_2O	K_2O	P_2O_5	Total	%
D15-1-g	56.18	0.50	13.76	7.05	0.12	8.43	9.59	2.82	1.31	0.24	100	0.830
D15-1-ol	40.19	0.00	0.00	10.96	0.21	48.46	0.18	0.00	0.00	0.00	100	0.100
D15-1-cpx	54.03	0.15	1.74	4.06	0.15	19.32	20.32	0.24	0.00	0.00	100	0.070
D15-2-g	55.39	0.51	13.54	7.43	0.14	9.75	9.37	2.60	1.05	0.21	100	0.930
D15-2-ol	40.37	0.00	0.00	12.90	0.24	46.28	0.19	0.01	0.00	0.00	100	0.035
D15-2-cpx	53.73	0.18	2.03	5.03	0.18	18.34	20.29	0.21	0.00	0.00	100	0.035
D15-4-g	55.49	0.46	13.13	6.86	0.12	10.69	9.18	2.82	1.06	0.19	100	0.913
D15-4-ol	40.52	0.00	0.00	10.99	0.22	48.06	0.21	0.00	0.00	0.00	100	0.050
D15-4-cpx	53.98	0.20	2.23	4.69	0.17	18.13	20.23	0.31	0.04	0.01	100	0.037
D15-5-g	56.97	0.56	15.33	6.94	0.11	5.77	9.67	3.24	1.16	0.25	100	0.770
D15-5-ol	40.16	0.00	0.00	12.93	0.25	46.47	0.19	0.00	0.00	0.00	100	0.130
D15-5-cpx	53.68	0.19	2.16	5.17	0.18	18.70	19.70	0.21	0.00	0.00	100	0.100

Table 7.3. Calculated melt-liquidus association for groundmass and glass compositions for the Hunter Ridge adakitic rocks.

Sample	Fo	T (°C)	Mg#	T (°C)
D15-4-groundmass	91.67	1187	92.87	1115
D15-1-groundmass	89.15	1131	90.66	1093
D15-5-groundmass	84.77	1052	86.14	1051
D15-4-glass	83.25	1038	84.48	1039

and pseudo-liquidus phases (Table 7.3). These are a close match to those measured in sample D15-1, in which olivine compositions range from Fo 88-90 and clinopyroxene from Mg# 87–92. For sample D15-5-groundmass (second most evolved melt composition, i.e. 5.8 wt% MgO) the melt-liquidus calculations produce olivine (Fo 85) and clinopyroxene (Mg# 86) as liquidus phases (Table 7.3). These are in good agreement with the mineral compositions obtained by EMP, in which olivine compositions range from Fo 86–89 and clinopyroxene from Mg# 85–90. For sample D15-4-glass (most evolved melt composition, i.e. 5.2 MgO), the melt-liquidus calculations produce olivine (Fo 83) and clinopyroxene (Mg# ~84) as liquidus phases (Table 7.3). No phenocrysts large enough to analyse were found in the sample.

7.5 Metal behaviour during differentiation

In order to study the partitioning of Cu, Zn, Pb, V, Co and Sc during differentiation of the Hunter Ridge adakite magmas, mineral/melt partition coefficients (Ds) were calculated. These were determined directly from LA-ICP-MS analyses of phenocrysts and groundmass/glass equilibrium pairs.
Olivine/melt and clinopyroxene/melt D values were determined for melt MgO contents between 5.2

to 10.7 wt% and mineral compositions across olivine Fo 86–93 and clinopyroxene Mg# 83–90. A comparison of the calculated metal Ds obtained for the adakitic samples with those obtained for the calc-alkaline samples is listed in Table 7.5 and shown in Figures 7.5–7.10.

Table 7.4. Rock, glass, and average mineral trace element compositions (ppm) of the Hunter Ridge adakitic rocks.

Sample	**Sc**	**Ti**	**V**	**Cr**	**Co**	**Ni**	**Cu**	**Zn**	**Rb**	**Sr**
D15-1	30.40	2498.00	174.00	757.00	46.02	250.00	74.00	58.00	11.30	803.00
D15-2	31.30	2772.00	188.00	580.00	44.31	187.00	89.00	60.00	10.60	792.00
D15-3	29.70	2496.00	176.00	752.00	46.96	254.00	75.00	58.00	10.50	788.00
D15-4	27.56	2572.58	182.00	493.00	42.54	228.32	71.10	57.58	10.38	757.82
D15-5	32.90	2655.00	183.00	702.00	45.46	212.00	67.00	55.00	10.00	734.00
D15-6	30.60	2677.00	133.00	635.00	46.23	209.00	83.00	60.00	9.81	715.00
D15-4*	25.18	3263.02	211.52	62.83	25.81	33.86	118.24	51.54	13.31	1020.95
D15-1-cpx	65.19	766.91	95.43	5466.98	37.61	254.54	2.90	23.65	-	60.70
D15-1-ol	4.62	12.06	2.17	204.89	163.51	1598.92	5.24	96.46	-	0.01
D15-4-cpx	88.73	1100.76	188.24	3931.59	39.60	194.44	1.34	18.52	-	31.97
D15-1-ol	4.78	12.95	2.52	243.98	168.56	1750.73	4.62	93.87	-	0.01
Sample	**Y**	**Zr**	**Nb**	**Cs**	**Ba**	**La**	**Ce**	**Nd**	**Sm**	**Eu**
D15-1	11.40	68.60	1.79	0.15	299.00	23.90	47.60	24.50	4.84	1.37
D15-2	11.00	64.70	1.78	0.12	238.00	17.80	36.00	18.50	3.55	1.05
D15-3	11.10	67.40	1.79	0.13	293.00	23.40	46.90	24.30	4.69	1.35
D15-4	10.49	67.94	1.56	0.15	262.04	20.78	44.19	22.75	4.50	1.26
D15-5	10.60	60.80	1.69	0.11	224.00	16.90	33.90	17.60	3.41	1.01
D15-6	10.30	61.20	1.70	0.10	222.00	17.10	33.90	17.50	3.39	0.99
D15-4*	12.32	84.18	2.04	0.18	345.85	26.23	56.95	27.00	5.05	1.49
D15-1-cpx	4.84	3.85	-	-	-	0.91	4.04	4.36	1.34	0.42
D15-1-ol	0.05	0.01	-	-	-	-	-	-	-	-
D15-4-cpx	4.78	3.77	-	-	-	0.21	1.18	1.71	0.69	0.26
D15-1-ol	0.05	0.02	-	-	-	-	-	-	-	-
Sample	**Gd**	**Dy**	**Er**	**Yb**	**Lu**	**Hf**	**Ta**	**Pb**	**Th**	**U**
D15-1	3.52	2.34	1.11	0.96	0.14	1.78	0.09	3.42	3.25	1.12
D15-2	2.83	2.18	1.16	1.05	0.16	1.70	0.10	3.09	2.55	0.96
D15-3	3.45	2.31	1.09	0.93	0.14	1.71	0.09	3.38	3.14	1.12
D15-4	3.52	2.25	1.16	1.02	0.15	1.78	0.08	3.06	3.05	1.02
D15-5	2.73	2.09	1.11	1.02	0.15	1.62	0.09	3.03	2.39	0.88
D15-6	2.62	2.05	1.11	1.00	0.15	1.61	0.09	2.77	2.33	0.87
D15-4*	3.82	2.50	1.26	1.15	0.17	2.16	0.11	3.92	3.79	1.30
D15-1-cpx	1.32	1.00	0.51	0.41	0.06	0.19	-	0.02	-	-
D15-1-ol	-	-	-	0.02	-	-	-	-	-	-
D15-4-cpx	0.90	0.96	0.54	0.42	0.06	0.21	-	0.01	-	-
D15-1-ol	-	-	-	0.02	-	-	-	-	-	-

*glass composition

Table 7.5. Calculated mineral-melt partition coefficients for olivine and clinopyroxene for the Hunter Ridge adakitic and calc-alkaline rocks.

Olivine		**Adakites**			**Calc-alkaline**		
Fo	92	89	86	88	84	81	78
MgO melt wt%	10.69	8.43	5.77	8.35	6.12	5.21	2.41
D Cu	0.04	0.06	0.06	0.04	0.03	0.05	0.20
D Zn	1.19	1.67	2.28	1.40	2.00	2.26	2.12
D V	0.01	0.01	0.01	0.01	0.02	0.03	0.06
D Co	4.26	4.57	7.23	4.70	6.27	9.75	19.39
D Sc	0.09	0.16	0.17	0.12	0.18	0.26	0.39
Clinopyroxene		**Adakites**			**Calc-alkaline**		
Cpx Mg#	91	86	84	90	85	83	75
MgO melt wt%	8.43	5.77	5.17	8.35	6.12	5.21	2.41
D La	0.03	0.05	0.02	0.02	0.05	0.06	0.23
D Ce	0.06	0.10	0.05	0.05	0.11	0.13	0.52
D Nd	0.12	0.24	0.17	0.11	0.26	0.30	1.23
D Sm	0.18	0.41	0.37	0.21	0.48	0.54	1.40
D Eu	0.20	0.44	0.41	0.24	0.48	0.54	1.83
D Gd	0.24	0.53	0.63	0.30	0.65	0.73	2.42
D Dy	0.24	0.55	0.91	0.33	0.75	0.85	2.62
D Er	0.25	0.51	1.03	0.32	0.73	0.81	2.40
D Yb	0.21	0.46	0.91	0.28	0.62	0.71	2.10
D Lu	0.21	0.44	0.93	0.26	0.60	0.70	2.04
D Y	0.23	0.52	0.95	0.33	0.71	0.86	2.57
D Cu	0.03	0.04	0.02	0.01	0.02	0.03	0.04
D Zn	0.34	0.56	0.62	0.30	0.56	0.66	1.67
D V	0.37	0.53	1.08	0.68	0.97	1.45	0.84
D Pb	0.01	0.01	0.01	0.01	0.01	0.01	0.02
D Co	1.06	1.60	1.77	0.94	1.43	2.25	1.95
D Sc	1.64	2.36	3.68	1.93	3.22	4.95	12.55
D Sr	0.07	0.06	0.05	0.05	0.06	0.10	0.09
D Zr	0.03	0.07	0.14	0.05	0.10	0.10	0.21
D Hf	0.05	0.14	0.27	0.10	0.19	0.16	0.37
D Ti	0.19	0.28	0.47	0.28	0.39	0.38	0.31

7.5.1 Copper

As described in Chapter 6.2, copper is found to be incompatible in silicate minerals as indicated by the measured $D_{Cu}^{ol/melt}$ of 0.04–0.06 (Fo 93–86) and $D_{Cu}^{cpx/melt}$ of ~ 0.02–0.03 (Mg# 90–83) indicating that Cu partitioning into silicates is negligible. Cu contents in clinopyroxene range between 2 and 5 ppm and do not display any clear trend with decreasing clinopyroxene Mg# (Fig. 7.5). In olivine, Cu contents vary between 3 and 6 ppm and seem to slightly increase with decreasing olivine Fo content (Fig. 7.5)

In the melt, Cu behaves incompatibly (i.e increasing with decreasing MgO) throughout the entire studied MgO range (i.e. 10.7 – 5.2 wt% MgO). Cu contents increase from ~70 ppm at 10.8 wt% MgO to 118 ppm at 5.2 wt% MgO (Fig. 7.5).

7.5.2 Zinc

Zinc is found to be compatible in olivine as indicated by the measured $D_{Zn}^{ol/melt}$ of 1.19–2.28. $D_{Zn}^{ol/melt}$ increases with decreasing Fo content in olivine within the measured range (Fo 93–86). Zinc contents in olivine increase from 66 ppm at olivine Fo 93 to 125 ppm at olivine Fo 86 (Fig. 7.6). In clinopyroxene, $D_{Zn}^{cpx/melt}$ slightly increases from 0.34 to 0.62 with decreasing Mg# (Mg# 90–83). Zn contents in clinopyroxene vary between 19 ppm and 32 ppm with clinopyroxene Mg# 90 and Mg# 83, respectively (Fig. 7.6).

In the melt, Zn behaves compatibly (i.e decreasing with decreasing MgO) across the entire studied MgO range, from ~52 ppm at 10.7 wt% MgO to 45 ppm at 5.2 wt% MgO. (Fig. 7.6).

7.5.3 Vanadium

Vanadium is incompatible in olivine as indicated by the measured $D_{V}^{ol/melt}$ of ~0.01 within the measured range (Fo 93–86). Vanadium contents in olivine range between 1 and 3 ppm, increasing with decreasing Fo content (Fig. 7.7). Vanadium behaves almost compatibly in clinopyroxene, $D_{V}^{cpx/melt}$ increase from 0.37 to 1.08 with decreasing Mg# (Mg# 90–83) (Fig. 7.7). Vanadium contents in clinopyroxene vary between 74 to 229 ppm, increasing with decreasing Mg# (Fig. 7.7).

In the melt, V behaves incompatibly (i.e increasing with decreasing MgO). V contents increase from 174 ppm at 10.7 wt% MgO to 212 ppm at 5.2 wt% MgO (Fig. 7.7).

7.5.4 Lead

Lead is almost perfectly incompatible in clinopyroxene and olivine. This is indicated by the measured $D_{Pb}^{cpx/melt}$ of 0.007–0.005 (Mg# 90–83), and the extremely low contents of Pb in olivine (which are close to, or below detection ~0.1 ppb) (Fig. 7.8).

In the melt, lead values increase slightly during differentiation from ~3 ppm at 10.7 wt% MgO to ~4 ppm at 8.4 wt% MgO, after which it remains constant (Fig. 7.8).

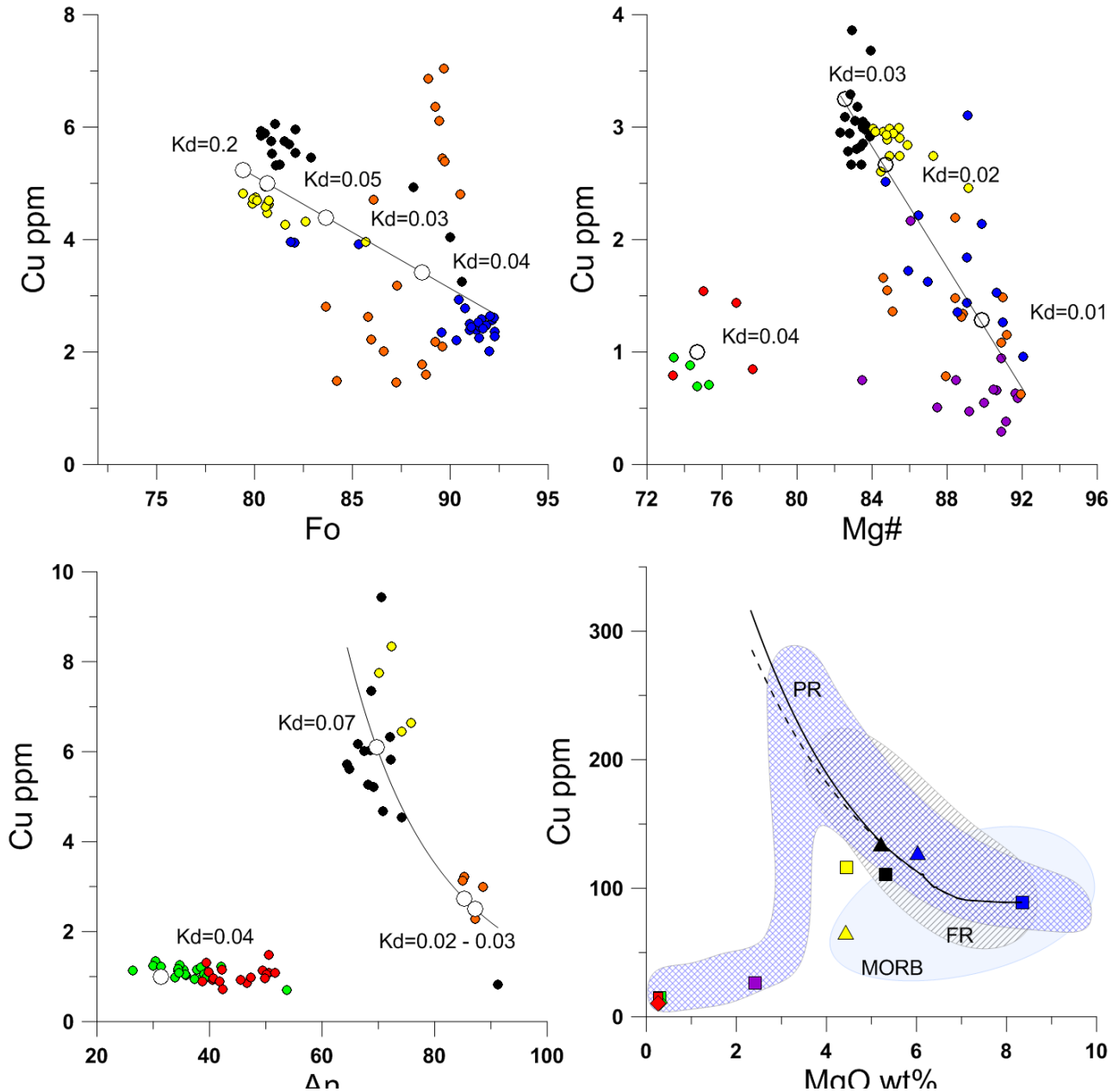

Fig. 7.5. Covariation diagrams showing variations in A) Cu vs Fo, B) Cu vs Mg#, and C) Cu vs MgO wt% for the Hunter Ridge adakites compared to the Hunter Ridge calc-alkaline samples (black dots). Triangle symbols represent glass compositions, square symbols represent calculated groundmasses and circles represent whole-rock compositions. LLD calc-alkaline trend was calculated using D values from this study.

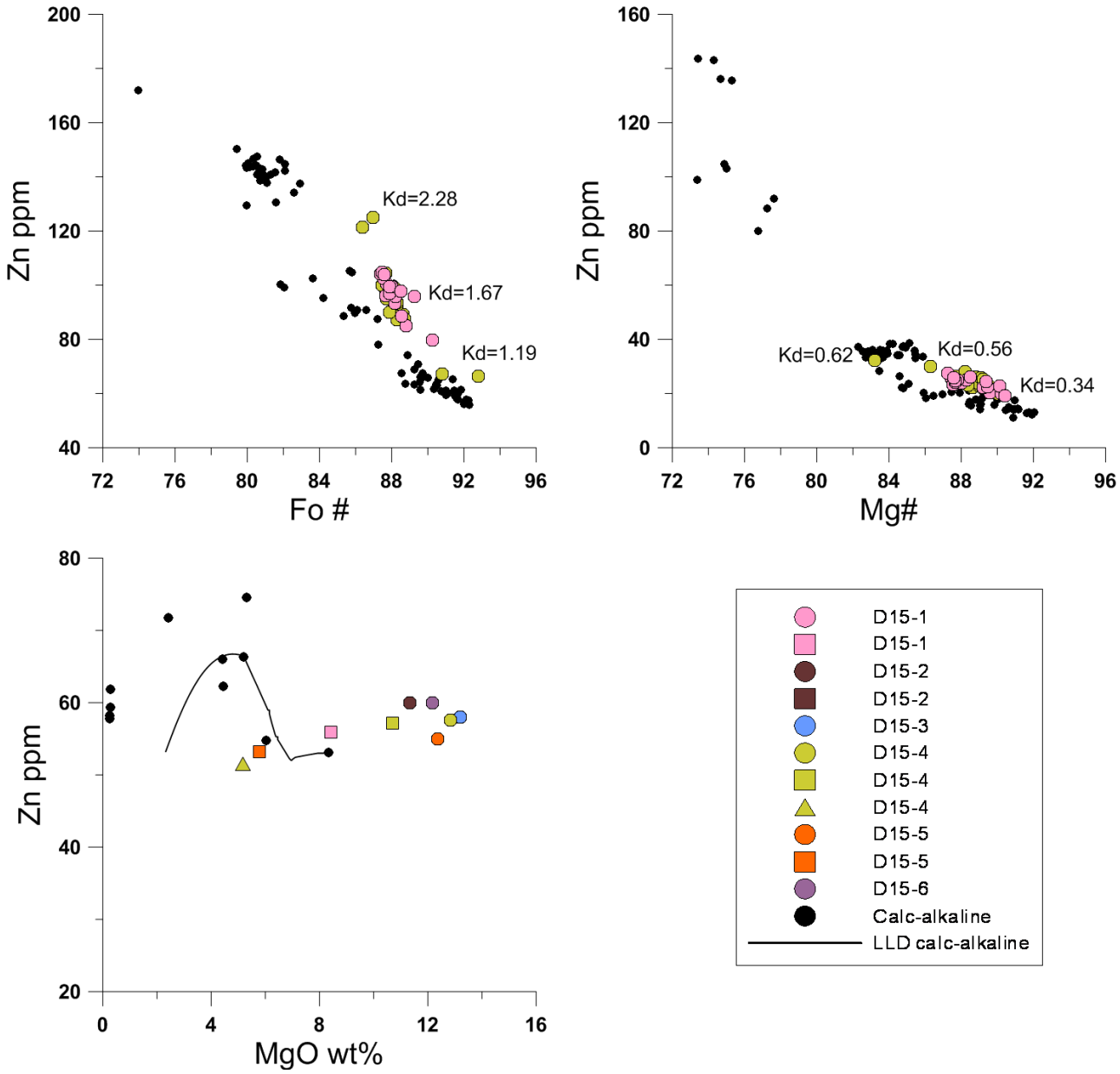

Fig. 7.6. Covariation diagrams showing variations in A) Zn vs Fo, B) Zn vs Mg#, and C) Zn vs MgO wt% for the Hunter Ridge adakites compared to the Hunter Ridge calc-alkaline samples (black dots). Triangle symbols represent glass compositions, square symbols represent calculated groundmasses and circles represent whole-rock compositions. LLD calc-alkaline trend was calculated using D values from this study.

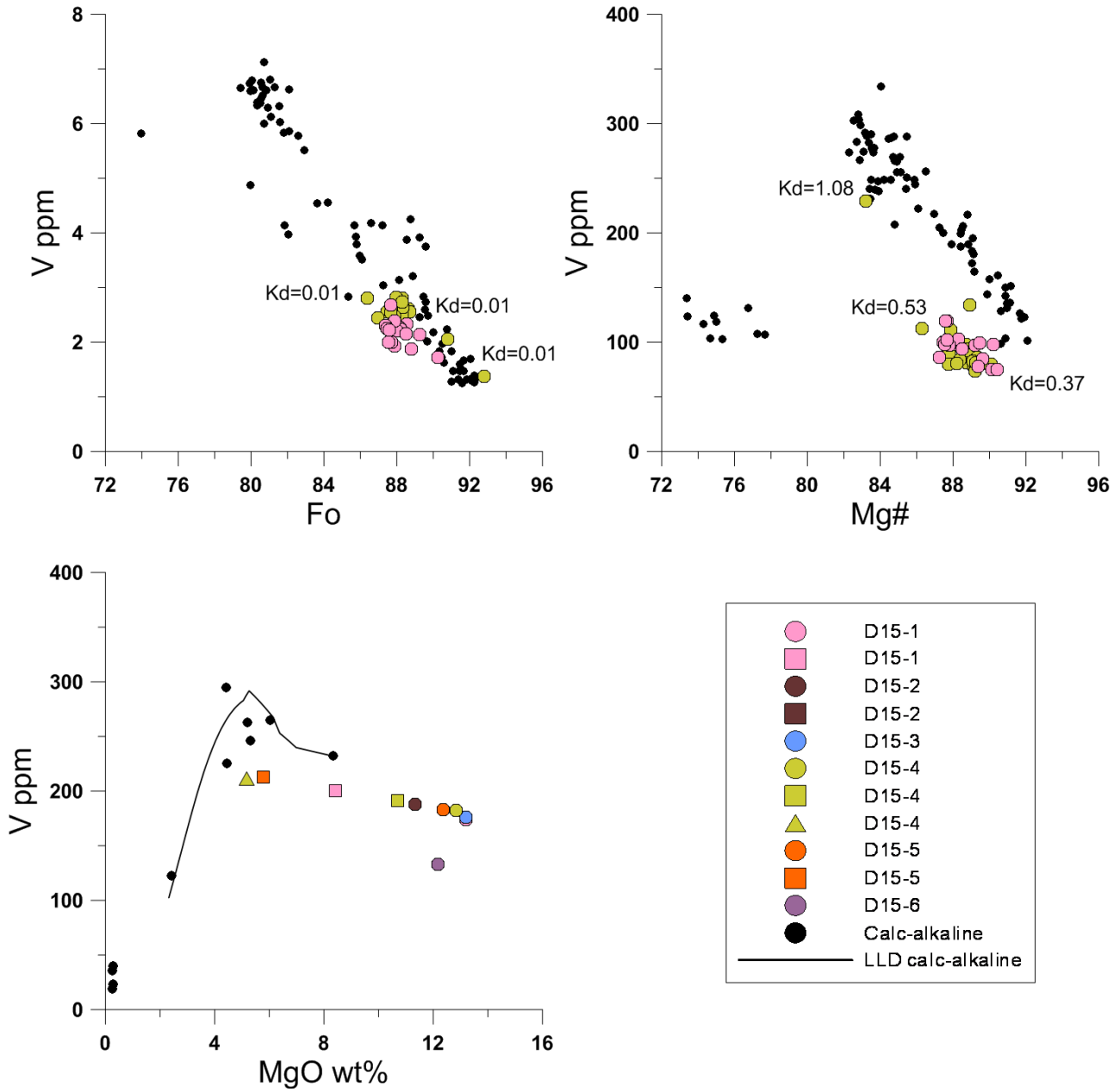

Fig. 7.7. Covariation diagrams showing variations in A) V vs Fo, B) V vs Mg#, and C) V vs MgO wt% for the Hunter Ridge adakites compared to the Hunter Ridge calc-alkaline samples (black dots). Triangle symbols represent glass compositions, square symbols represent calculated groundmasses and circles represent whole-rock compositions. LLD calc-alkaline trend was calculated using D values from this study.

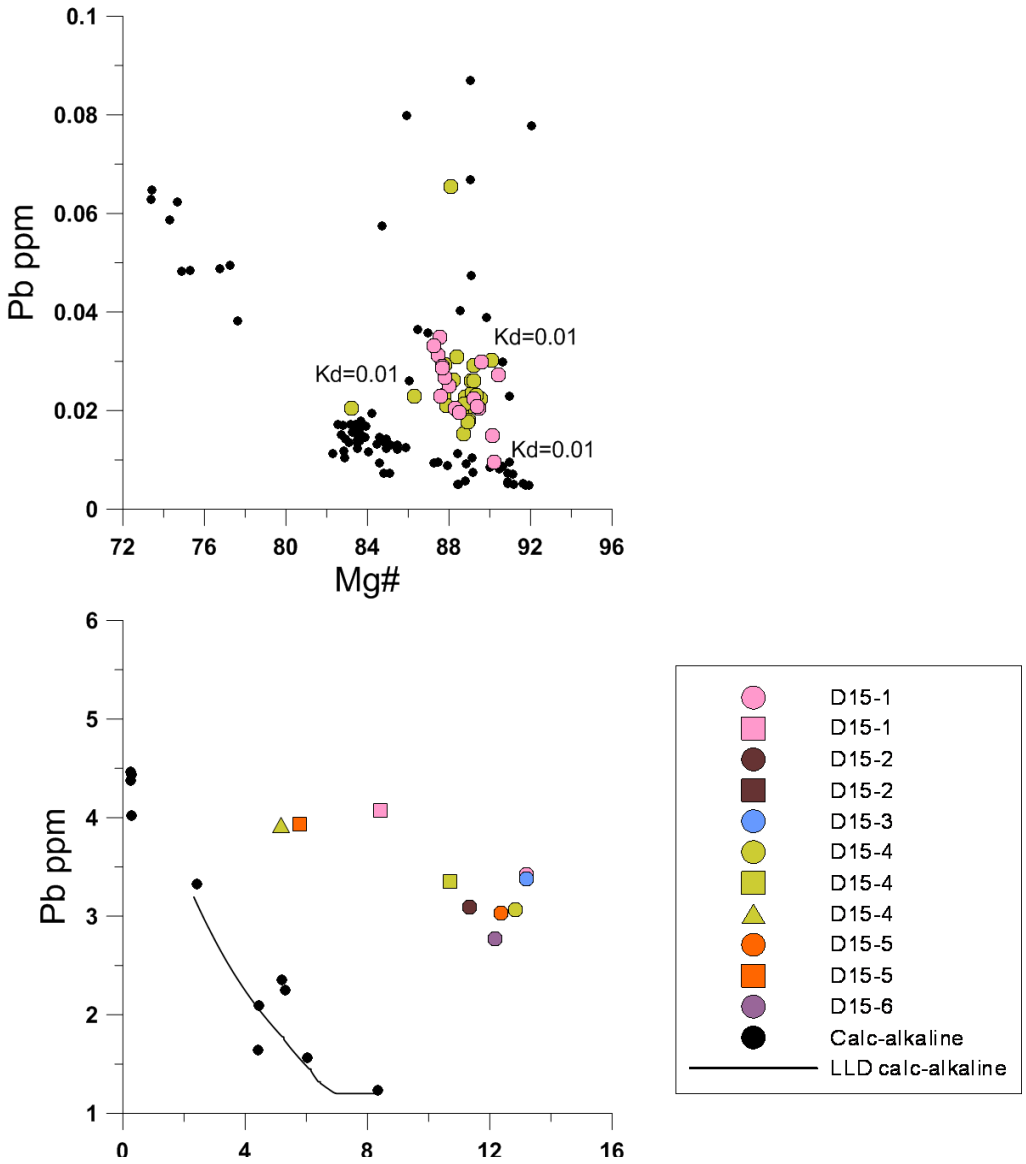

Fig. 7.8. Covariation diagrams showing variations in A) Pb vs Mg#, and B) Pb vs MgO wt% for the Hunter Ridge adakites compared to the Hunter Ridge calc-alkaline samples (black dots). Triangle symbols represent glass compositions, square symbols represent calculated groundmasses and circles represent whole-rock compositions. LLD calc-alkaline trend was calculated using D values from this study.

7.5.5 Cobalt

Cobalt is extremely compatible in olivine as indicated by the measured $D_{Co}^{ol/melt}$ of 4.26 – 7.23. $D_{Co}^{ol/melt}$ increases with decreasing Fo content in olivine within the measured range (Fo 93–86). Co contents in olivine increase from 139 ppm at olivine Fo 93 to 184 ppm at olivine Fo 86 (Fig. 7.9). Cobalt is also compatible in clinopyroxene, $D_{Co}^{cpx/melt}$ increases from 1.06 to 1.77 with decreasing Mg# (Mg# 90–83). Co contents in clinopyroxene slightly increases with decreasing Mg# from 33 ppm at Mg# 90 to 46 ppm at a Mg# 83 (Fig. 7.9).

In the melt, Co behaves compatibly across the entire range in MgO. Co contents decrease from ~32 ppm at 10.7 wt% MgO to a minimum value of ~26 ppm at 5.2 wt% MgO (Fig. 7.9).

7.5.6 Scandium

Scandium is incompatible in olivine as indicated by the measured $D_{Sc}^{ol/melt}$ of 0.09–0.17. $D_{Sc}^{ol/melt}$ increases with decreasing Fo content in olivine within the measured range (Fo 93–86). Sc contents in olivine vary from 3 ppm at Fo 92 to 6 ppm at Fo 86 (Fig. 7.10). Scandium behaves very compatibly in clinopyroxene, $D_{Sc}^{cpx/melt}$ increase from 1.64 to 3.68 with decreasing Mg# (Mg# 83–90). Sc contents in clinopyroxene increase from 51 ppm (Mg# 90) to 83 ppm (Mg# 83) (Fig. 7.10).

In the melt, Sc contents initially increase from 24 ppm at 10.7 wt% MgO to 31 ppm at 8.4 wt% MgO, after which they decrease to values of ~25 ppm at a MgO content of 5.2 wt% (Fig. 7.10).

7.6 Comparison to the Hunter Ridge calc-alkaline magma series

In this section, we compare the compositions of the Hunter Ridge adakitic rocks with those of the Hunter Ridge calc-alkaline lavas (also see Chapter 4) in terms of major and trace element systematics and metal content and behaviour (Figs 7.1-7.10).

7.6.1 Major elements

We examine the differences in major elements between these the adakite and calc-alkaline magma series as a function of MgO wt% contents. The calc-alkaline samples studied range from basalt (SiO_2 ~50 wt%, MgO ~13 wt%) to rhyolite (SiO_2 ~73 wt%, MgO ~0.3 wt%). The adakites range from basalt (SiO_2 ~54 wt%, MgO ~13 wt%) to andesite (SiO_2 ~58 wt%, MgO ~5 wt%) (Fig. 7.1). One of the main differences between these two magma suites is the higher SiO_2 contents of the adakites for a given MgO wt%. For example, the SiO_2 contents for the adakites and the calc-alkaline rocks are 57 and 53 wt%, respectively, at the same MgO content of ~8 wt% (Fig. 7.1). In turn, the high-Mg character of the adakites is reflected in the composition of the crystallising minerals. For example, at ~8 wt% melt MgO, the expected olivine and clinopyroxene compositions for the adakites are Fo 89 and Mg# 91, whereas for the calc-alkaline rocks these are Fo 88 and Mg# 89.

Another significant difference is observed from the trend displayed by Al_2O_3, which increases progressively with decreasing MgO contents. This is opposite to the Hunter Ridge calc-alkaline rocks,

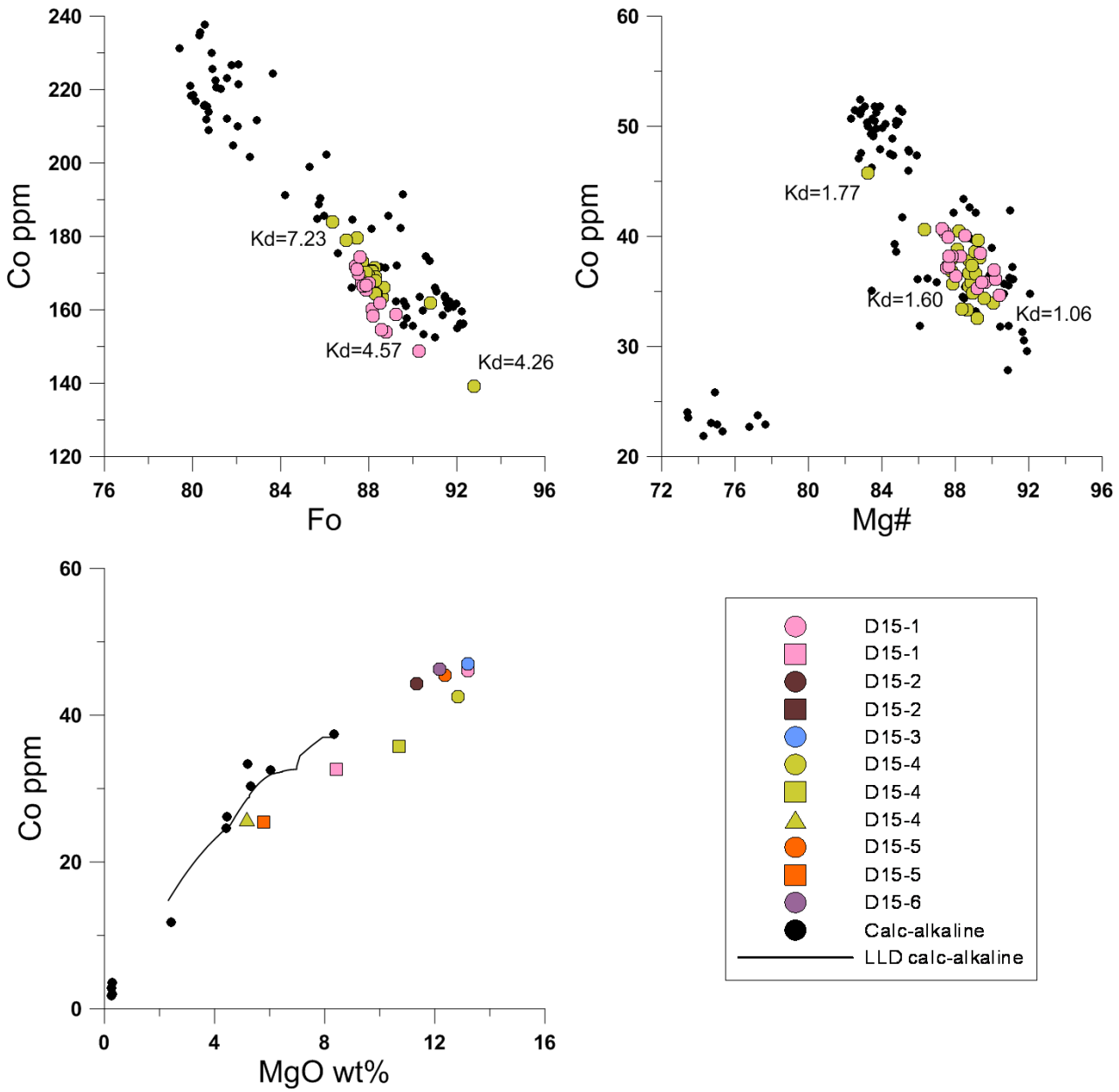

Fig. 7.9. Covariation diagrams showing variations in A) Co vs Fo, B) Co vs Mg#, and C) Co vs MgO wt% for the Hunter Ridge adakites compared to the Hunter Ridge calc-alkaline samples (black dots). Triangle symbols represent glass compositions, square symbols represent calculated groundmasses and circles represent whole-rock compositions. LLD calc-alkaline trend was calculated using D values from this study.

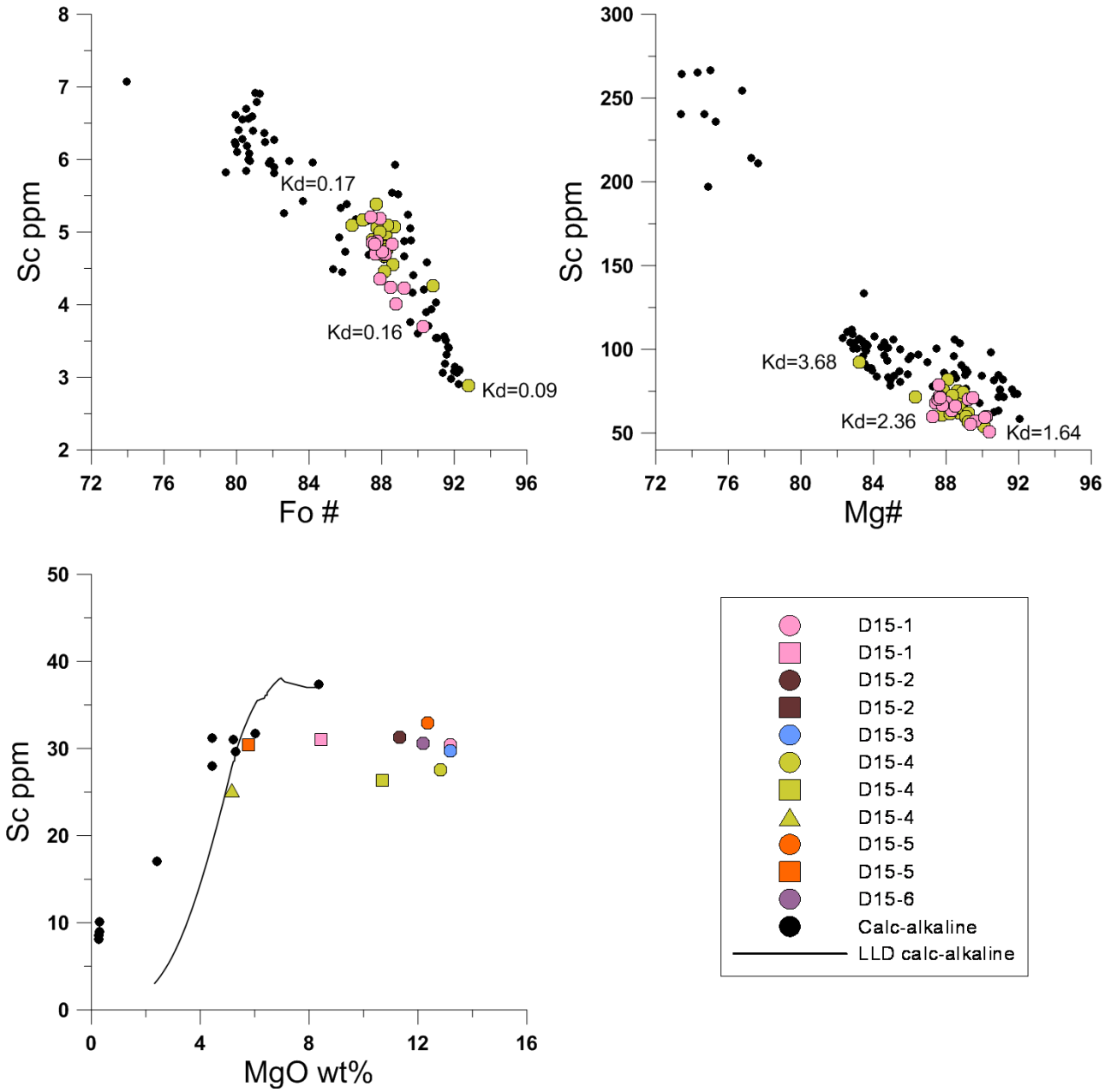

Fig. 7.10. Covariation diagrams showing variations in A) Sc vs Fo, B) Sc vs Mg#, and C) Sc vs MgO wt% for the Hunter Ridge adakites compared to the Hunter Ridge calc-alkaline samples (black dots). Triangle symbols represent glass compositions, square symbols represent calculated groundmasses and circles represent whole-rock compositions. LLD calc-alkaline trend was calculated using D values from this study.

in which Al_2O_3 initially increases (composition range 8.3–6 MgO wt%), then falls dramatically at the onset of plagioclase crystallisation (Fig. 7.1). TiO_2 and CaO contents of adakitic rocks are slightly lower than in the calc-alkaline rocks, FeO and Na_2O contents are similar and K_2O contents are slightly higher (Fig. 7.1).

7.6.2 Trace elements

Calc-alkaline and adakitic rocks share many characteristics in terms of their trace element concentrations. Thus they are enriched in LILE, together with LREE, Pb, K and Sr, and all lavas present Nb-Ta depletions (Fig. 7.2). However, there are also some differences; the middle to heavy REE ratios, La/Yb and Sr/Y ratios are higher in all adakitic rocks. These features are observed globally, even in the most primitive adakitic lavas (Figs 7.2, 7.3, 7.4).

7.6.3 Metal content

The most primitive samples from the Hunter Ridge adakite series (i.e. highest MgO wt%) have Cu, Zn, V, Pb, Co and Sc contents comparable (if not less) than those of the more primitive calc-alkaline samples (Fig. 7.4).

As noted previously, clinopyroxene and olivine crystallising from adakitic melts are predicted to be more magnesium-enriched than those crystallising from calc-alkaline melts at same melt MgO contents (Section 7.5.1). This leads to a small, but noticeable, offset in the metal contents for the same clinopyroxene Mg# and olivine Fo (i.e. the same Mg# and Fo reflect different degrees of melt evolution; Figs 7.5–7.10). In turn, this will affect the D values calculated for metals (i.e. Cu, Zn, V, Pb, Co and Sc) at a given melt MgO content (Table 7.5). This will be insignificant for metals that are incompatible in clinopyroxene and olivine (D values $<<1$; e.g. Cu and Pb), whereas metals that are compatible (D values >1; e.g. Zn in olivine and Sc in clinopyroxene) show subtly different D values for the adakite and calc-alkaline melts at the same melt MgO contents.

Copper contents in the Hunter Ridge adakitic samples increase during fractional crystallisation (i.e. over the range observed from 10.8–5.2 wt% MgO). This is unlike the trends of the calc-alkaline samples, which record an initial increase in Cu with decreasing MgO content (8.3–6.5 MgO wt%) followed by a decrease (6.5–0.5 MgO wt%; Fig. 7.5). As discussed previously, we believe this behaviour reflects the partitioning of Cu into a fluid phase that exsolves from the silicate melt at an MgO wt% of approximately 6.5 (Chapter 6).

Zinc contents in the adakites decrease slightly across the entire range in MgO studied, from ~52 ppm at 10.8 wt% MgO to 45 ppm at 5.2 wt% MgO. This decrease in Zn during fractionation is best explained as a result of partitioning of Zn into olivine, and to lesser extent clinopyroxene. In contrast, V contents in the adakites increase from 174 ppm at 10.8 wt% MgO to 212 ppm at 5.2 wt% MgO. This is most likely caused by its generally incompatible behaviour in the crystallising phases. In the calc-alkaline rocks the Zn and V contents show an initial increase during fractionation (8.3–5.0 wt% MgO) followed by a decrease (5.0–0.5 MgO wt%; Fig. 7.4). The initial increase in Zn and V contents in the melt can be explained as a result of the crystallisation of assemblages comprising olivine-

clinopyroxene-plagioclase. Given that neither of these elements are compatible in plagioclase, its crystallisation will be the dominant factor controlling the Zn and V contents in the melt during the early stages of fractionation. The subsequent decrease in Zn and V contents after 5.0 MgO wt% is the result of the appearance of magnetite on the liquidus as both these elements have high D values in this phase.

In the adakite samples, Sc contents initially increase from 24 ppm at 10.8 wt% MgO to 31 ppm at 8.4 wt% MgO, after which they decrease to reach values of ~25 ppm at a MgO content of 5.2 wt%. The initial increase of Sc in the melt can be attributed to its incompatibility into olivine, which is most likely the principle phase crystallising during the early stages of fractionation. Conversely, in the calc-alkaline samples Sc behaves compatibly over the MgO range studied and progressively decreases during fractionation.

Lead contents in the adakites initially increase slightly from ~3.3 ppm at 10.8 wt% MgO to 4~ ppm at 8.4 wt% MgO, after which they remain constant. In the calc-alkaline rocks, Pb behaves as an incompatible element during the entire studied MgO range.

In both the adakitic and calc-alkaline rocks, Co behaves as a compatible element, leading to progressive decreases in their concentration in the melt during fractionation.

7.7 Discussion

In summary, in the case of the Hunter Ridge adakites it is probably right to state that these rocks are the result of slab melts that interacted with a metasomatised mantle wedge. This is evidenced by two important facts: i) there is no crustal contamination involved in the genesis of these lavas as shown by unradiogenic Sr isotopes compositions ($^{87}Sr/^{86}Sr \sim 0.70289$) and ii) there is no fractionation of “normal” phenocrysts assemblages (hornblende-garnet-titanite) that could also produce adakitic geochemical characteristics such as high La/Yb and Sr/Y ratios.

As shown in the previous section, the most primitive samples from the Hunter Ridge adakite series have Cu, Zn, Pb, Co and V contents comparable (if not less) with those in primitive calc-alkaline samples (Fig. 7.4), demonstrating that slab melts were not enriched in these elements.

The results emphasize that there are major differences in the crystallisation sequences of the calc-alkaline and adakitic magma types. This is due to the fact that the physical conditions under which the Hunter Ridge adakite lavas formed, were distinct from those which created the Hunter Ridge calc-alkaline magmas. Basalts in both magma series are initially saturated with olivine and clinopyroxene, but the absence of plagioclase phenocrysts from the adakitic basaltic andesitic lavas contrasts with that of the plagioclase-phyric basalts and basaltic andesites from the calc-alkaline series.

From the above observations, it is suggested that magmas that crystallise at deeper levels (e.g., Hunter Ridge adakites) will exsolve a hydrothermal fluid containing higher Cu contents, thereby maximizing the efficiency of Cu partitioning into the fluid phase. In the opposite case, when vapour exsolution happens at shallower depths (e.g., Hunter Ridge calc-alkaline rocks) the released fluids will not likely contain enough metal concentrations to form economic Cu deposits. This is in good

agreement with models that favour large porphyry deposit formation by a single-phase fluid (vapour or supercritical) exsolved at deep crustal levels (Sillitoe, 2010; William-Jones & Heinrich, 2005; Cloos, 2001; etc.).

Chapter 8

Summary and conclusions

The behaviour of key ore-forming metals during magmatic differentiation of typical island-arc lava suites from the Hunter Ridge (i.e. calc-alkaline rocks and adakites) has been investigated using the geochemistry of minerals and glass/groundmass, petrographic observations, and quantitative geochemical modelling. Calc-alkaline rocks record a protracted history of magma evolution from the very earliest stages of fractionation (i.e. before volatile loss) to eruption on the sea floor. However, as with most arc magmas, these have been affected to some extent by crystal accumulation and magma mixing. Using groundmass and glass compositions (rather than whole-rock geochemistry data) together with detailed trace-element compositions using LA-ICP-MS, we were able to reproduce the LLD along which the magmas evolved. This is crucial, since the geochemical modelling relies on the rocks being genetically related. We can demonstrate that the minerals and melts in our calc-alkaline series are genetically related, and therefore belong to a single magma fractionation series, and that fractional crystallisation of olivine + clinopyroxene + plagioclase + magnetite ± amphibole is the primary process that operated during the evolution of these rocks. Our study also suggests that mixing processes do not entirely obscure the chemical trends imparted by crystal fractionation, and that detailed petrographic and geochemical studies can be used to identify these processes in order to filter out the most affected samples. Together, these steps allow us to define well-constrained LLD from which information about initial metal contents in the magmas, and metal behaviour during their differentiation, can be extracted.

The main objective of this work is to show how magma ascent, crystallisation and degassing can lead to either enrichment or depletion of key ore-forming metals and other chalcophile elements during arc magma differentiation. To this aim, we calculated mineral/melt partition coefficients (Ds) for Cu, Zn, V, Pb, Co, Sc and a suite of other trace elements using LA-ICP-MS data acquired from phenocryst-groundmass/glass equilibrium pairs. Olivine/melt, clinopyroxene/melt and plagioclase/melt partition coefficients for Cu, Zn, V, Pb, Co and Sc were determined for the following range of phenocrysts compositions: olivine Fo 89–79; clinopyroxene Mg# 90–75 and plagioclase An 87–31, and melt MgO contents between 2.4 wt% and 8.3 wt%. Partition coefficients for Cu, Zn, V, Pb, Co and Sc between magnetite and host magma were calculated from LA-ICP-MS and EMP analyses (magnetite grains and glass) in samples with a MgO range from 0.4 wt% to 2.3 wt%. From this, the D values were extrapolated for magmas up to 5.0 wt% MgO. For comparison, modelling was also conducted (where possible) using D values obtained from the LSM and the parameterisation method of Bédard (2005).

Our data show that although basaltic rocks from the calc-alkaline samples have initial ore metal abundances similar to those in mid-ocean ridge basalts (MORB), the contents of chalcophile elements such as Cu increase early during magma evolution beyond the range found in typical MORB (from 8.3 to 6.5 MgO wt% Cu contents in the melt increase from ~89 ppm to ~128 ppm). This

behaviour can be linked to the presence of higher water contents and higher oxidation states of arc magmas compared to MORB, which suppresses the formation of sulphide liquids that might otherwise scavenge Cu from a silicate magma. Our data also show that plagioclase saturation occurs at a melt MgO wt% of 6.5, which is accompanied by a rapid decrease in Cu contents in the magma. We believe this most likely marks the onset of degassing. These results provide evidence that Cu partitions into a fluid phase at crustal levels before sulphide saturation occurs. This is consistent with a model whereby Cu-enriched hydrous fluids can be generated directly from mafic-intermediate magmas, in addition to other proposed mechanisms such as remobilisation of pre-existing sulphides. Furthermore, our results confirm that arc magmas may exsolve a magmatic-hydrothermal fluid before they are able to segregate an immiscible sulphide liquid, due to their higher oxidation states and volatile contents.

Zinc and V increase during magma evolution (from ~50 ppm and 230 ppm respectively at 8.3 MgO wt%, to a maximum of ~66 ppm and 275 ppm respectively at 5 wt% MgO). Once magnetite enters the liquidus at ~5 wt% MgO, melt contents of Zn and V both decrease within decreasing MgO (falling to ~50 ppm and 20 ppm respectively at MgO <0.5 wt%). Given that, both $D_{Zn}^{mt/mel}$ and $D_{V}^{mt/melt}$ are high at 5.7 and 9.8 respectively (at ~ 5 wt% MgO), their behaviour can be explained by the partitioning of Zn and V into magnetite.

Lead contents increase from ~1 ppm at 8.3 wt% MgO, to 4.5 ppm at 0.3 wt% MgO. Our modelling shows that partitioning of Pb into olivine, clinopyroxene and plagioclase is negligible. In addition, it would appear that Pb does not enter a volatile phase (as with Cu) as previously suggested by Stanton (1991) and Beaudoin and Scott (2009). Lead will be strongly partitioned into any immiscible sulphide liquid present, as shown by the high $D_{Pb}^{SL/melt}$ values that range from 3 to 48 reported by several authors (Li & Audédat, 2012; Lagos et al., 2008; Wood et al., 2008). The apparent incompatible behaviour of Pb, therefore, provides further evidence that the magmas did not reach sulphide saturation before the onset of degassing.

In contrast to the above elements, Co and Sc concentrations decrease with decreasing MgO wt% of the melt (both metals from ~37 ppm at 8.3 wt% MgO, to ~2 ppm and ~8 ppm respectively at 0.3 wt% MgO). This can be explained by the partitioning of Co into olivine and to lesser extent clinopyroxene, and Sc into clinopyroxene (only), during the early stages of magmatic fractionation (as indicated by the high $D_{Co}^{ol/melt}$ of 5.6–22.2, $D_{Co}^{cpx/melt}$ of 1.1, $D_{Sc}^{cpx/melt}$ of 2–14, measured $D_{Sc}^{ol/melt}$ of 0.1–0.4). Co and Sc can also partition into magnetite once it enters the liquidus, as indicated by $D_{Co}^{mt/melt}$ from 6 to 18 and $D_{Sc}^{mt/melt}$ from 0.9 to 2.2 (over a MgO range of 5.3 to 2.3 wt%).

There are some notable differences in the crystallisation sequences of the calc-alkaline and adakitic magmas from the Hunter Ridge. Basalts from both magma series contain olivine and clinopyroxene as early liquidus phases. In the calc-alkaline series, plagioclase enters the liquidus at ~6.5 MgO wt%, whereas in the adakite series plagioclase saturation is suppressed below 5.2 MgO wt%. The adakite magmas are, therefore, consistent with differentiation under higher water and/or volatile contents and at deeper crustal levels than the calc-alkaline magmas. This will have an important effect on the partitioning of metals that have affinity for a volatile phase.

There are also some notable differences in some metallic element behaviour between calc-alkaline and adakitic magmas. The calc-alkaline samples that show an initial increase in Cu with

decreasing MgO from 8.3 and 6.5 MgO wt%, followed by a decrease between 6.5 and 0.5 MgO wt%. This is unlike that of the adakitic samples where Cu contents progressively increase during magma evolution (i.e. from 10.8–5.2 wt% MgO). Zinc and V contents in the calc-alkaline rocks also show an initial increase with decreasing MgO content (between 8.3 and 5.0 wt% MgO) followed by a decrease between 5.0 and 0.5 MgO wt%. Zinc contents in adakites remain fairly constant (~50 ppm) and V contents decrease across the entire studied MgO range (i.e. 10.8–5.2 wt% MgO). Scandium in the calc-alkaline samples behaves compatibly over the MgO range studied, whereas Sc in the adakite samples does not show any significant variation during fractionation. In both calc-alkaline and adakitic rocks, Pb behaves as an incompatible element whereas Co behaves as a compatible element.

Adakites from the Hunter Ridge possess high La/Yb, high Sr/Y and high Dy/Er signatures as a result of interaction between slab-derived melts and metasomatised mantle wedge. However, these slab melts were not enriched in chalcophile elements. This is evidenced by the fact that the most primitive samples from the Hunter Ridge adakites display Cu, Zn, Pb, Co and V contents comparable (if not less) with those in the most primitive calc-alkaline samples.

Even so, adakitic magmas have more potential to generate economically important ore deposits because they are more likely to exsolve a metal-enriched (e.g. Cu) single-phase fluid at deep crustal levels, before sulphide saturation occurs in the magma. This is considered favourable to the formation of large porphyry deposits.

Concluding Remarks

- A critical step in forming magmatic/hydrothermal ore deposits is concentrating and removing metals (i.e. Cu) from a magma before saturation of an immiscible sulphide liquid occurs. As Cu is incompatible in any of the early crystallizing silicates and oxides, it's concentration in the melt will progressively increase and it will be available to partition into an aqueous fluid phase.
- No direct links were found between slab-derived melts and the enrichment in Cu contents of the parental melts.
- It was demonstrated that:
  - Zn and V are strongly controlled by magnetite fractionation.
  - And that Co and Sc partition into olivine and clinopyroxene from the early stages of fractionation, and magnetite once it enters the liquidus. These metals are therefore removed from the system and are not incorporated in a volatile phase.
  - Pb behaves incompatibly and is concentrated in the melt during magmatic differentiation.
- The Hunter Ridge samples used during this study provide a well-constrained, natural sample set that cover a wide range of bulk compositions. Furthermore, mineral/melt partitioning data acquired from high precision laser ablation ICP-MS can be used to model igneous processes in arc-related systems.

References

Arculus, R. J., 2004. Evolution of arc magmas and their volatiles. In: Sparks, R. S. J. & Hawkesworth, C. J. (eds.) The State of the Planet: Frontiers and Challenges in Geophysics. Geophysical Monograph, American Geophysical Union 150, 95^108.

Arculus, R.J. 1994. Aspects of magma genesis in arcs. In: Arculus, R.J., Banno, S., Charvet, J. and Kushiro, I. (eds). Tectonics, metamorphism and magmatism in island arcs. Lithos 33, no.1-3: 189-208.

Arculus, R.J. and Powell, R., 1986. Source component mixing in the regions of arc magma generation. In: Hildreth, W., Grove, T.L. and Dungan, M.A. (prefacers). Special section on open magmatic systems. Journal of Geophysical Research 91, B6: 5913-5926.

Arculus, R.J., 1985. Oxidation status of the mantle: past and present. Annual Reviews Earth Planet Sciences 13, 75-95.

Ariskin, A. A., and Barmina, G. S., 1999. An empirical model for the calculation of spinel-melt equilibria in mafic igneous systems at atmospheric pressure: 2. Fe-Ti oxides. Contributions to Mineralogy and Petrology 134, 251-263.

Ariskin, A. A., Frenkel, M. Y., Barmina, G. S., and Nielsen R., 1993. COMAGMAT: A FORTRAN program to model magma differentiation processes, Comput. Geosci., 19, 1155-1170.

Atherton, M.P., and Petford, N., 1993. Generation of sodium-rich magmas from newly underplated basaltic crust: Nature 362, p. 144-146.

Audétat, A., Pettke, T., Heinrich, C.A., Bodnar, R.J., 2008. The composition of magmatic hydrothermal fluids in barren and mineralized intrusions. Economic Geology 103, 877-908.

Audétat, A., Keppler, H., 2005. Solubility of rutile in subduction zone fluids, as determined by experiments in the hydrothermal diamond anvil cell. Earth and Planetary Science Letters 232, 393-402.

Auzende, J.M., Pelletier, B. & Eissen J.P., 1996. The North Fiji Basin: geology, structure and geodynamic evolution. In: Taylor, B (ed.), Backarc basins: tectonics and magmatism, Plenum Press, New York, 139-175.

Auzende, J., Pelletier, B. and Lafoy, Y., 1994. Twin active spreading ridges in the North Fiji Basin (Southwest Pacific). Geology 22, 1: 63-66.

Auzende, J.-M., Lafoy, Y., and Marsset, B., 1988. Recent geodynamic evolution of the North Fiji Basin (Southwest Pacific): Geology 16, 925-929.

Baldwin, J.A., and Pearce, J.A., 1982. Discrimination of productive and non productive porphyritic intrusions in the Chilean Andes. Economic Geology 77, 664-674.

Ballhaus, C., 1993. Redox states of lithospheric and asthenospheric upper mantle. Contributions to Mineralogy and Petrology 114, 331-348.

Barnes, S.-J., Savard, D., Bédard, L. P. & Maier, W. D., 2009. Selenium and sulfur concentrations in the Bushveld Complex of South Africa and implications for formation of the platinum-group element deposits. Mineralium Deposita 44, 647-663.

Bea, F., Montero, P., & Ortega, M., 2006. A LA–ICP–MS evaluation of Zr reservoirs in common crustal rocks: Implications for Zr and Hf geochemistry, and zircon-forming processes. The Canadian Mineralogist 44, 693-714.

Beate, B., Monzier, M., Spikings, R., Cotten, J., Silva, J., Bourdon, E., and Eissen, J.-P., 2001. Mio-Pliocene adakite generation related to flat subduction in southern Ecuador: the Quimsacocha volcanic center: Earth and Planetary Science Letters 192, 561-570.

Beaudoin, Y., Scott, S.D., 2009. Pb in the Pacmanus Sea-floor hydrothermal system, Eastern Manus Basin: Numerical modelling of a magmatic versus leached origin. Economic Geology 104, 749-758.

Bédard, J.H., 2007. Trace element partitioning coefficients between silicate melts and orthopyroxene: Parameterizations of D variations. Chemical Geology 244, 263-303.

Bédard, J.H., 2005. Partitioning coefficients between olivine and silicate melts. Lithos 83, 394-419.

Blatter, D.L., Carmichael, I.S.E., 1998. Hornblende peridotite xenoliths from central Mexico reveal the highly oxidized nature of subarc upper mantle. Geology 26, 1035-1038.

Blundy, J., Cashman, K.V., Rust, A., Witham, F., 2010. A case for CO2-rich arc magmas. Earth and Planetary Science Letters 290, 289-301.

Blundy J., Dalton J., 2000. Experimental comparison of trace element partitioning between clinopyroxene and melt in carbonate and silicate systems, and implications for mantle metasomatism. Contributions to Mineralogy and Petrology 139, 356-371.

Blundy, J.D., Wood, B.J., 1991. Crystal-chemical controls on the partitioning of Sr and Ba between plagioclase feldspar, silicate melts, and hydrothermal solutions. Geochimica and Cosmochimica Acta 55, 193-209.

Blundy, J.D.,Wood, B.J., 1994. Prediction of crystal-melt partition coefficients from elastic moduli. Nature 372, 452-454.

Blundy J., Wood B., 2003a. Mineral-melt partitioning of uranium, thorium and their daughters. In: Bourdon B. et al. (ed.), Uranium series geochemistry. Reviews in Mineralogy and Geochemistry 52, 39-123

Blundy, J., Wood, B.J., 2003b. Partitioning of trace elements between crystals and melts. Earth and Planetary Science Letters 210, 383-397.

Blundy J.D., Wood B.J., Davies A., 1996. Thermodynamics of rare earth element partitioning between clinopyroxene and melt in the system CaO-MgO-Al2O3-SiO2. Geochimica and Cosmochimica Acta 60, 359-364.

Bourdon, E., Eisse, J.P., Gutscher, M.A., Monzier, M., Samaniego, P., Robin, C., Bollinger, C., Cotten, J., 2002. Slab melting and melt metasomatism in the northern Andean volcanic zone: Adakites and high Mg andesites from Pichincha volcano (Ecuador): Bulletin de la Société géologique de France 173, 195-206.

Botcharnikov, R.E., Linnen, R.L., Holtz, F., 2010. Solubility of Au in Cl- and S-bearing hydrous silicate melts. Geochimica and Cosmochimica Acta 74, 2396-2411.

Brenan, J. M., McDonough, W. F., & Ash, R., 2005. An experimental study of the solubility and partitioning of iridium, osmium and gold between olivine and silicate melt. Earth and Planetary Science Letters 237, 855-872.

Brenan, J. M., McDonough, W. F., & Dalpe, C., 2003. Experimental constraints on the partitioning of rhenium and some platinum-group elements between olivine and silicate melt. Earth and Planetary Science Letters 212, 135-150.

Brandon, A.D., Draper, D.S., 1996. Constraints on the origin of the oxidation state of mantle overlying subduction zones: an example from Simcoe, Washington, USA. Geochimica et Cosmochimica Acta 60, 1739-1749.

Breeding, C.M., Ague, J.J., Bröcker, M., 2004. Fluid–metasedimentary rock interactions in subduction-zone mélange: implications for the chemical composition of arc magmas. Geology 32, 1041-1044.

Brice, J.C., 1975. Some thermodynamic aspects of the growth of strained crystals. J. Crystal Growth 28, 249-253.

Burnham, C.W., 1997. Magmas and hydrothermal fluids, In: Barnes, H.L. (ed.), Geochemistry of Hydrothermal Ore Deposits, 3rd edition. John Wiley and Sons, New York, pp. 63-123.

Campbell, I.H., Naldrett, A.J., 1979. The influence of silicate:sulfide ratios on the geochemistry of magmatic sulfides. Economic Geology 74, 1503-1506.

Candela, P.A., 1989a. Felsic magmas, volatiles, and metallogenesis. In: Whitney, J.A., Naldrett, A.J. (eds.), Ore Deposition Associated with Magmas: Soc. Econ. Geol., Reviews in Economic Geology, 4, pp. 223-233.

Candela, P.A., 1989b. Calculation of magmatic fluid contributions to porphyry-type ore systems: predicting fluid inclusion chemistries. Geochemical Journal 23, 295-305.

Candela, P.A., Holland, H.D., 1986. A mass transfer model for copper and molybdenum in magmatic hydrothermal systems: the origin of porphyry-type ore deposits. Economic Geology 81, 1-19.

Candela, P.A., Holland, H.D., 1984. The partitioning of copper and molybdenum between silicate melts and aqueous fluids. Geochimica et Cosmochimica Acta 48, 373-380

Candela, P.A., Piccoli, P.M., 2005. Magmatic processes in the development of porphyry type ore systems. In: Hedenquist, J.W., Thompson, J.F.H., Goldfarb, R.J., Richards, J.P. (eds.), Economic Geology 100th Anniversary Volume. Society of Economic Geologists, Littleton, CO, pp. 25-37.

Candela, P.A., Piccoli, P.M., 1995. Model ore-metal partitioning from melts into vapor and vapor/brine mixtures. In: Thompson, J.F.H. (ed.), Magmas, Fluids, and Ore Deposits. Short Course Series, 23. Mineralogical Association of Canada, 101-127.

Carmichael I.S.E., 2002. The andesite aqueduct: perspectives on the evolution of intermediate magmatism in west-central (105-99º W) Mexico. Contributions to Mineralogy and Petrology 143, 641-663

Carr, M.J., 2001. IgPet software. Terra Softa Inc.

Carroll, M.R., Rutherford, M.J., 1985. Sulfide and sulfate saturation in hydrous silicate melts. Proceedings of the Fifteenth Lunar and Planetary Science Conference, Part 2: Journal of Geophysical Research 90, C601-C612.

Carroll, M.R., Webster, J.D., 1994. Solubilities of sulfur, noble gases, nitrogen, chlorine, and fluorine in magmas Reviews in Mineralogy and Geochemistry 30, 231-279.

Castillo, P.R., Janney, P.E., and Solidum, R.U., 1999. Petrology and geochemistry of Camiguin Island, southern Philippines: Insights to the source of adakites and other lavas in a complex arc setting: Contributions to Mineralogy and Petrology 134, 33-51.

Chiaradia, M., 2009, Adakite-like magmas from fractional crystallization and melting-assimilation of mafic lower crust (Eocene Macuchi arc, Western Cordillera, Ecuador): Chemical Geology 265, 468-487.

Chiaradia, M., Müntener, O., Beate, B., Fontignie, D., 2009. Adakite-like volcanism of Ecuador: lower crust magmatic evolution and recycling. Contributions to Mineralogy and Petrology 158, 563-588.

Chiaradia, M., Fontboté, L., and Beate, B., 2004. Cenozoic continental arc magmatism and associated mineralization in Ecuador: Mineralium Deposita 39, 204-222.

Cline, J.S., 1995. Genesis of porphyry copper deposits: the behavior ofwater, chloride, and copper in crystallizing melts. In: Pierce, F.W., Bolm, J.G. (eds.), Porphyry Copper Deposits of the American Cordillera: Arizona Geological Society Digest, 20, pp. 69-82.

Cline, J.S., and Bodnar, R.J., 1991. Can Economic Porphyry Copper Mineralisation be generated by a typical calc-alkaline melt. Journal of Geophysical Research-Solid Earth and Planets 96, 8113-8126.

Cloos, M., 2001. Bubbling magma chambers, cupolas, and porphyry copper deposits. International geology review 43, 285-311.

Cornejo, P., Tosdal, R.M., Mpodozis, C., Tomlinson, A.J., Rivera, O., and Fanning, C.M., 1997. El Salvador, Chile porphyry copper deposit revisited: Geologic and geochronologic framework: International Geology Review 39, 22-54.

Coumou, D., Driesner, T., Heinrich, C.A., 2008. Heat transport at boiling, near-critical conditions. Geofluids 8, 208-215.

Crawford A. J., 1989. Boninites. Unwin Hyman, London, 446 pp.

Crawford, A.J., Meffre, S. and Symonds, P.A., 2003. 120-0 Ma tectonic evolution of the southwest pacific and analogous geological evolution of the 600 to 220 Ma Tasman Fold Belt System. Geological Society of Australia Special Publication 22: 377-397.

Czamanske, G. K. & Moore, J. G., 1977. Composition and phase chemistry of sulfide globules in basalts from the Mid-Atlantic-Ridge rift valley near 378N lat. Geological Society of America Bulletin 88, 587-599.

Danyushevsky, L.V., Plechov P., 2011. Petrolog3: Integrated software for modeling crystallization processes. Geochemistry Geophysics Geosystems 12, 7: Q07021.

Danyushevsky, L.V., Falloon, T.J., Crawford, A.J., Tetroeva, S.A., Leslie, R.A.J., Verbeeten, A., 2008. High-Mg adakites from Kadavu Island Group, Fiji, southwest Pacific: Evidence for the mantle origin of adakite parental melts. Geology 36, 6: 499-502.

Danyushevsky, L.V., Falloon, T.J., Crawford, A.J., 2006. Subduction-related magmatism at the southern tip of the North Fiji back-arc basin. AESC2006, Melbourne, Australia.

Danyushevsky, L.V., Leslie, R.A., Crawford, A.J. and Durance, P., 2004. Melt inclusions in primitive olivine phenocrysts: the role of localised reaction processes in the origin of anomalous compositions. Journal of Petrology 45, 2531-2553

Danyushevsky, L. V., Sokolov, S. & Falloon, T. J., 2002c. Melt inclusions in olivine phenocrysts: using diffusive re-equilibration to determine the cooling history of a crystal, with implications for the origin of olivine-phyric volcanic rocks. Journal of Petrology 43, 1651-1671.

Danyushevsky, L. V., Eggins, S. M., Falloon, T. J., & Christie, D. M., 2000. H2O abundance in depleted to moderately enriched mid-ocean ridge magmas; Part I: incompatible behaviour, implications for mantle storage, and origin of regional variations. Journal of Petrology 41, 1329-1364.

Danyushevsky, L.V., Sobolev, A.V. and Falloon, T.J., 1995. North Tongan high-Ca boninite petrogenesis: the role of Samoan plume and subduction-transform fault transition. Journal of Geodynamics, 20, no.3: 219-241.

Danyushevsky L.V., Sobolev, A.V. and Kononkova, N.N., 1992. Methods of studying melt inclusions in minerals during investigations on water-bearing primitive mantle melts (Tonga trench boninites). Geochemical International, 29: 4, 8-62.

Davey, F.J., 1982. The structure of the South Fiji Basin. In. Packham, G.H. (ed.), The evolution of the India-Pacific plate boundaries. Tectonophysics, 87, 1-4: 185-241.

Davidson J.P., Tepley F.J. III, 1997. Recharge in volcanic systems: evidence from isotope profiles of phenocrysts. Science 275, 826-829.

Davidson J.P., Hora J.M., Garrison J.M., Dungan M.A., 2005. Crustal forensics in arc magmas. Journal of Volcanology and Geothermal Research 140, 157-170.

Davidson, P., Kamenetsky, V.S., Cooke, D.R., Frikken, P., Hollings, P., Ryan, C, Van Achterbergh, E., Mernagh, T., Skarmeta, J., Serrano, L., and Vargas, R., 2005. Magmatic precursors of hydrothermal fluids at the Río Blanco Cu-Mo deposit, Chile: Links to silicate magmas and metal transport. Economic Geology 100, 963-978.

Deer, W.A., Howie, R.A. and Zussman, J. 1962a. Rock-forming minerals: Ortho and Ring silicates, 1, London, Longman, 371 pp.

Defant M. J. and Drummond M. S., 1990. Derivation of some modern arc magmas by melting of young subducted lithosphere. Nature 347, 662-665.

Doe, B. R., 1995. Zinc, copper, and lead geochemistry of oceanic igneous rocks-ridges, islands, and arcs. International Geology Review 37, 379-420.

Doe, B. R., 1994. Zinc, copper, and lead in mid-ocean ridge basalts and the source rock control on Zn/Pb in ocean-ridge hydrothermal deposits. Geochimica et Cosmochimica Acta 58, 2215-2223.

Dreyer, B.M., Morris, J.D., Gill, J.B., 2010. Incorporation of subducted slab-derived sediment and fluid in arc magmas: B–Be–10Be–εNd systematics of the Kurile convergent margin, Russia. Journal of Petrology 51, 1761-1782.

Drummond, M.S., Defant, M.J., and Kepezhinskas, P.K., 1996. Petrogenesis of slab-derived trondhjemite-tonalite-dacite/adakite magmas: Geological Society of America, Special Paper 315, 205-215.

Duggen, S., Portnyagin, M., Baker, J., Ulfbeck, D., Hoernle, K., Garbe-Schönberg, D., Grassineau,N., 2007. Drastic shift in lava geochemistry in the volcanic-front to rear-arc region of the Southern Kamchatkan subduction zone: evidence for the transition from slab surface dehydration to sediment melting. Geochimica et Cosmochimica Acta 71, 452-480.

Dungan M.A., Davidson J., 2004. Partial assimilative recycling of the mafic plutonic roots of arc volcanoes: an example from the Chilean Andes. Geology 32, 773-776

Elliott T., Plank T., Zindler A., White W., and Bourdon B., 1997. Element transport from slab to volcanic front at the Mariana Arc. Journal of Geophysical Research 102, 14991-15019.

Falloon, T.J., Danyushevsky, L.V., Crawford, T.J, Maas R., Woodhead, J.D., Eggins, S.M., Bloomer, S.H., Wright, D.J., Zlobin, S.K., Stacey, A.R., 2007. Multiple Mantle Plume Components involved in the Petrogenesis of Subduction related Lavas from the Northern Termination of the Tonga Arc and northern Lau Basin: evidence from the Geochemistry of Arc and Backarc Submarine Volcanics. Geochemistry, Geophysics, Geosystems 8: Q09003.

Falloon, T.J., Danyushevsky, L.V., 2000. Melting of refractory mantle at 1.5, 2 and 2.5 GPa under anhydrous and H2O-undersaturated conditions: implications for high-Ca boninites and the influence of subduction components on mantle melting. Journal of Petrology 41, 257-283.

Falvey, D.A., 1975. Arc reversals, and a tectonic model for the North Fiji Basin. Australian Society of Exploration Geophysicists, Bulletin 6, 2/3, First Southwest Pacific workshop-symposium: 47-49.

Falvey, D.A., 1978. Analysis of palaeomagnetic data from the New Hebrides. Bulletin of Australian Society of Exploration Geophysics 9, 3:117-123.

Foley, S. F., Jackson, S. E., Fryer, B. J., Greenouch, J. D., & Jenner, G. A., 1996. Trace element partition coefficients for clinopyroxene and phlogopite in an alkaline lamprophyre from Newfoundland by LAM-ICP-MS. Geochimica et Cosmochimica Acta 60, 629-638.

Ford, C. E., Russell, D. G., Groven, J. A., Fisk ,M. R,. 1983. Distribution coefficients of Mg^{2+}, Fe^{2+}, Ca^{2+} and Mn^{2+} between olivine and melt. Journal of Petrology 24, 256-265.

Forneris, J.F., and Holloway, J.R., 2003. Phase equilibria in subducting basaltic crust: Implications for H2O release from the slab: Earth and Planetary Science Letters 214, 187-201.

Frikken, P.H., Cooke, D.R., Walshe, J.L., Skarmeta, J., Serrano, L., and Vargas, R., 2005. Sulfur isotope and mineral zonation in the Sur-Sur breccia complex, Río Blanco copper-molybdenum deposit, Chile: Implications for ore genesis: Economic Geology, 100, 935-961.

Gaetani, G.A., and Grove, T.L., 2003. Experimental constraints on melt generation in the mantle wedge: American Geophysical Union Geophysical Monograph 138, 107-134.

Gill, J.B., 1981. Orogenic andesites and Plate tectonics, Springer-Verlag, Berlin.

Gill, J.B., 1976. From island arc to oceanic islands: Fiji, southwestern Pacific. Geology 4: 123-126.

Gill, J.B. and Whelan, P., 1989b. Post subduction ocean island alkali basalts in Fiji. Journal of Geophysical Research. 94: 4579-4588.

Grégoire, D. C., & Sturgeon, R. E., 1999. Analyte transport efficiency with electrothermal vaporization inductively coupled plasma mass spectrometry. Spectrochimica Acta Part B: Atomic Spectroscopy 54, 773-786.

Guillong, M., Meier, D. L., Allan, M. M., Heinrich, C. A., & Yardley, B. W. D., 2008. SILLS: A MATLAB-based program for the reduction of laser ablation ICP-MS data of homogeneous materials and inclusions. Mineralogical Association of Canada Short Course 40, 328-333.

Guillong, M., Latkoczy, C., Seo, J. H., Günther, D., & Heinrich, C. A., 2008. Determination of sulfur in fluid inclusions by laser ablation ICP-MS. Journal of Analytical Atomic Spectrometry 23, 1581-1589.

Guivel, C., Lagabrielle, Y., Bourgois, J., Martin, H., Arnaud, N., Fourcade, S., Cotten, J., Maury, R.C., 2003. Very shallow melting of oceanic crust during spreading ridge subduction: origin of near-trench Quaternary volcanism at the Chile Triple Junction. Journal of Geophysical Research 108, B7: 2345.

Gutscher, M.-A., Maury, R., Eissen, J.-P., Bourdon, E., 2000. Can slab melting be caused by flat subduction? Geology 28, 535-538.

Hamburger, M.W. and Isacks, B.L., 1987. Deep earthquakes in the southwest Pacific: a tectonic interpretation. Journal of Geophysical Research, 92: 13841-13854.

Halter, W.E., Heinrich, C.A., Pettke, T., 2005. Magma evolution and the formation of porphyry Cu–Au ore fluids: evidence from silicate and sulfide melt inclusions. Mineralium Deposita 39, 845-863.

Hanger B. J., 2009. Behaviour of Chalcophile Elements during Magnetite Fractionation in Arc Magmas. Honours Thesis. Australian National University.

Harris, A.C., Kamenetsky, V.S., White, N.C., van Achterbergh, E., Ryan, C.G., 2003. Melt inclusions in veins: linking magmas and porphyry Cu deposits. Science 302, 2109-2111.

Hathway, B. and Colley, H., 1994. Eocene to Miocene geology of southwest Viti Levu, Fiji. In: Stevenson, A.J., Herzer, R.J. and Ballance, P.F. (eds.), Geology and submarine resources of the Tonga-Lau-Fiji region SOPAC Technical Bulletin, 8: 153-169.

Hattori, K.H., 1997. Occurrence and origin of sulfide and sulfate in the 1991 Mount Pinatubo eruption products. In: Newhall, C.G., Punongbayan, R.S. (eds.), Fire and Mud: Eruptions and Lahars of Mount Pinatubo, Philippines. University of Washington Press, Seattle, pp. 807-824.

Hawkesworth, C. J., Powell, M., 1980. Magma genesis in the lesser Antilles island arc. Earth and Planetary Science Letters 51, 297-308.

Hawkins, J.W., 1995. The geology of the Lau basin in Taylor B. (ed.), Backarc basins: Tectonics and magmatism. New York, Plenum Press. 63-138.

Hedenquist, J.W., Lowenstern, J.B., 1994. The role of magmas in the formation of hydrothermal ore deposits. Nature 370, 519-527.

Henley, R.W., McNabb, A., 1978. Magmatic vapor plumes and ground–water interaction in porphyry copper emplacement. Economic Geology 73, 1-20.

Hermann, J., Spandler, C.J., 2008. Sediment melts at sub-arc depths: an experimental study. Journal of Petrology 49, 717-740.

Hill E., Blundy J.D., Wood B.J., 2000. Clinopyroxene-melt trace element partitioning and the development of a predictive model for HFSE and Sc. Contributions to Mineralogy and Petrology 161, 423-438.

Hirose K., 1997. Melting experiments on lherzolite KLB–1 under hydrous conditions and generation of high-magnesian andesitic melts. Geology 25, 42-44.

Ihinger, P. D., Hervig, R. L., McMillan, P. F., 1994. Analytical methodos for volatiles in glasses, in Volatiles in Magmas, Reviews in Mineralogy 30 Carroll, R. and Holloway, J. R. (eds.), Mineralogical Society of America, Washington, D. C.

Jarosewich, E., Nelen, J.A. and Norberg, J.A., 1980. Reference samples for electron microprobe analysis. Geostandards Newsletter 4, 1: 43-47.

Jeffries, T. E., W. T. Perkins, and N. J. G. Pearce., 1995. Measurements of trace elements in basalts and their phenocrysts by laser probe microanalysis inductively coupled plasma mass spectrometry (LPMA-ICP-MS). Chemical Geology 121.1, 131-144.

Jenner, F.E., O'Neill, H. St, C., 2012. Analyses of 60 elements in 616 ocean floor basaltic glasses. Geochemistry Geophysics Geosystems 13, Q02005.

Jenner, F.E., O'Neill, H. St. C., Arculus, R.J., Mavrogenes, J.A., 2010. The magnetite crisis in the evolution of arc-related magmas and the initial concentration of Au, Ag and Cu. Journal of Petrology 51, 2445-2464.

Jochum, K. P., Stoll, B., Herwig, K., & Willbold, M., 2006. Improvement of in situ Pb isotope analysis by LA-ICP-MS using a 193 nm Nd: YAG laser. Journal of Analytical Atomic Spectrometry 21, 666-675.

Jochum, K. P., Stoll, B. I., 2008. Reference materials for elemental and isotopic analyses by LA-(MC)-ICP-MS: successes and outstanding needs. In: Sylvester, P. (ed.). Laser Ablation ICP-MS in the Earth Sciences: Current practices and outstanding issues. Mineralogical Association of Canada. Short Course Volume 40, 147-168.

Johnson, M.C., Plank, T., 1999. Dehydration and melting experiments constrain the fate of subducted sediments. Geochemistry Geophysics Geosystems 1, 1007.

Johnson, M.C., Anderson, A. T. Jr., Rutherford, M. J., 1994. Pre-eruptive volatile contents of magmas. Volatiles in Magmas, Minerological Society of America, Reviews in Mineralogy 30, 281-330.

Jugo, P.J., 2009. Sulfur content at sulfide saturation in oxidized magmas. Geology 37, 415-418.

Jugo, P.J., Candela, P.A., Piccoli, P.M., 1999. Magmatic sulfides and Au:Cu ratios in porphyry deposits: an experimental study of copper and gold partitioning at 850 °C, 100 MPa in a haplogranitic melt–pyrrhotite–intermediate solid solution–gold metal assemblage, at gas saturation. Lithos 46, 573-589.

Kay, R. W., 1984. Elemental abundances relevant to identification of magma sources. Philosophical Transactions of the Royal Society of London A310, 535-547.

Kay, R.W., 1978. Aleutian magnesian andesites: Melts from subducted Pacific Ocean crust: Journal of Volcanology and Geothermal Research 4, 117-132.

Kay, S.M., and Mpodozis, C., 2001. Central Andean ore deposits linked to evolving shallow subduction systems and thickening crust: GSA Today 11, 3: 4-9.

Kay, S.M., Mpodozis, C., and Coira, B., 1999. Neogene magmatism, tectonism, and mineral deposits of the Central Andes (22°-33°S latitude): Society of Economic Geologists Special Publication 7, 27-59.

Keith, J.D., Whitney, J.A., Hattori, K., Ballantyne, G.H., Christiansen, E.H., Barr, D.L., Cannan, T.M., Hook, C.J., 1997. The role of magmatic sulfides and mafic alkaline magmas in the Bingham and Tintic mining districts, Utah. Journal of Petrology 38, 1679-1690.

Kelemen, P.B., Hanghoj, K., and Greene, A.R., 2003. One view of geochemistry of subduction-related magmatic arcs, with an emphasis on primitive andesite and lower crust, in Rudnick, R.L., (ed.), The crust: Oxford, Elsevier-Pergamon, Treatise on Geochemistry 3, 593-650.

Kelemen P. B., Rilling J. L., Parmentier E. M., Mehl L., and Hacker B. R., 2003a. Thermal structure due to solid state flow in the mantle wedge beneath arcs, in Eiler, J., (ed.), Inside the subduction factory: American Geophysical Union Geophysical Monograph 138, 293-311.

Kelemen, P.B., Yogodzinski, G.M., and Scholl, D.W., 2003. Along-strike variation in the Aleutian Island Arc: Genesis of high Mg# andesite and implications for continental crust, in Eiler, J., (ed.), Inside the subduction factory: American Geophysical Union Geophysical Monograph 138, 223-276.

Keller, N.S., Arculus, R.J., Hermann, J. and Richards, S., 2008. Submarine back-arc lava with arc signature: Fonualei Spreading Center, northeast Lau Basin, Tonga. Journal of Geophysical Research 113, 1-28.

Keller, N.S., 2008. Metals and Volatiles in Melts: An Experimental and Field Study. PhD thesis, Australian National University.

Kelley, K.A., Cottrell, E., 2009. Water and the oxidation state of subduction zone magmas. Science 325, 605-607.

Kessel, R., Schmidt, M.W., Ulmer, P., Pettke, P., 2005a. Trace element signature of subduction-zone fluids, melts and supercritical liquids at 120–180 km depth. Nature 437, 724-727.

Klemm, L.M., Pettke, T., Heinrich, C.A., Campos, E., 2007. Hydrothermal evolution of the El Teniente deposit, Chile: porphyry Cu-Mo ore deposit from low-salinity magmatic fluids. Economic Geology 102, 1021-1045.

Kogiso, T., Tatsumi, Y., Nakano, S., 1997. Trace element transport during dehydration processes in the subducted oceanic crust: 1. Experiments and implications for the origin of ocean island basalts. Earth and Planetary Science Letters 148, 193-205.

Kroenke, L.W., 1984. Cenozoic tectonic development of the southeast Pacific. UN, ESCAP, CCOP/SOPAC Technical Bulletin no.6.

Lagos, M., Ballhaus, C., Münker, C., Wohlgemuth-Ueberwasser, C., Berndt, J., Kuzmin, D.V., 2008. The Earth's missing lead may not be in the core. Nature 456, 89-92.

Lang, J.R., and Titley, S.R., 1998. Isotopic and geochemical characteristics of Laramide magmatic systems in Arizona and implications for the genesis of porphyry copper deposits: Economic Geology 93, 138-170.

Launay, J., 1982. Morphology and structure of the New Hebrides island arc in its southern termination, Contribution to the geodynamic study of the Southwest Pacific. Travaux et Documents de l›ORSTOM, 147: 163-178.

Leake, B.E., 1978. Nomenclature of amphiboles. American Mineralogist 63, 1023-1052.

Lee, C.-T. A., Luffi, P., Chin, E. J., Bouchet, R., Dasgupta, R., Morton, D. M., Le Roux, V., Yin, Q.-Z., Jin, D., 2012. Copper Systematics in Arc Magmas and Implications for Crust-Mantle Differentiation. Science 336, 64-68.

Lee, C.-T. A., Luffi, P., Le Roux, V., Dasgupta, R., Albaréde, F., Leeman, W. P., 2010. The redox state of arc mantle using Zn/Fe systematics. Nature 468, 681-685.

Lee, C.-T. A., Leeman, W. P., Canil, D.& Li, Z.-X. A., 2005. Similar V/Sc systematics in MORB and arc basalts: implications for the oxygen fugacities of their mantle source regions. Journal of Petrology 46, 2313-2336.

Lewis, K.C., Lowell, R.P., 2009. Numerical modeling of two-phase flow in the NaCl–H_2O system: 2 examples. Journal of Geophysical Research 114, B8: B08204.

Leslie, R. A. J. 2004. Primitive Shoshonites from Fiji: Mineralogy, Melt Inclusions and Geochemistry. PhD Thesis, University of Tasmania.

Li, Y., Audeéat, A., 2012. Partitioning of V, Mn, Co, Ni, Cu, Zn, As, Mo, Ag, Sn, Sb, W, Au, Pb, and Bi between sulphide phases and hydrous basanite melt at upper mantle conditions. Earth and Planetary Science Letters 355-356, 327-340.

Liu, Y.N., Samaha, N.T., Baker, D.R., 2007. Sulfur concentration at sulfide saturation (SCSS) in magmatic silicate melts. Geochimica and Cosmochimica Acta 71, 1783-1799.

Macdonald R., Hawkesworth C. J., and Heath E. 2000. The Lesser Antilles volcanic chain: a study in arc magmatism. Earth Sci. Rev. 49, 1-76.

Macpherson, C.G., Dreher, S.T., and Thirlwall, M.F., 2006. Adakites without slab melting: High pressure differentiation of island arc magma, Mindanao, the Philippines: Earth and Planetary Science Letters 243, 581-593.

Malahoff, A., Hammond, S.R., Naughton, J.J., Keeling, D.L. and Richmond, R.N., 1982a. Geophysical evidence for post-Miocene rotation of the island of Viti Levu, Fiji, and its relationship to the tectonic development of the North Fiji Basin. Earth and Planetary Science Letters 57, 398-414.

Mc Neill, A. W., 1997. The crystallisation history of N-MORB from the East-Pacific Ocean and implications for primary MORB magma. PhD Thesis, University of Tasmania.

Martin, H., 1999. Adakitic magmas: Modern analogues of Archaean granitoids: Lithos 46, 411-429.

Martin H., Smithies R. H., Rapp R., Moyen J.-F., Champion D., 2005. An overview of adakite, TTG andsanukitoid: Relationships and some implications for crustal evolution. Lithos 79, 1: 1-24.

Mavrogenes, J. A., Jenner, F. E. & Arculus, R. J., 2008. Magnetite fractionation of 'chalcophile' elements, American Geophysical Union, Fall Meeting, San Francisco, CA, USA,V33C-2229.

Métrich, N. & Clocchiatti, R., 1996. Sulfur abundance and its speciation in oxidised alkaline melts. Geochimica et Cosmochimica Acta 60, 4151-4160.

Mungall, J.E., 2002. Roasting the mantle: slab melting and the genesis of major Au and Au-rich Cu deposits. Geology 30, 915-918.

Nadeau, O., Williams-Jones, A.E., Stix, J. 2010. Sulphide magma as a source of metals in arc-related magmatic hydrothermal ore fluids. Nature Geosciences 3, 501-505.

Nielsen, R.L., 1985. A method for the elimination of the compositional dependence of trace element distribution coefficients. Geochimica and Cosmochimica Acta 49, 1775- 1779.

Nielsen, R.L., Forsythe, L.M., Gallahan, W.E., Fisk., M.R., 1994. Major-and trace-element magnetite-melt equilibria. Chemical Geology 117, 167-191.

Nielsen, R.L., Drake, M.J., 1979. Pyroxene-melt equilibria. Geochimica and Cosmochimica Acta 43, 1259-1272.

Norton, D.L., Dutrow, B.L., 2001. Complex behavior of magma–hydrothermal processes: role of supercritical fluid. Geochimica et Cosmochimica Acta 65, 4009-4017.

Onuma, N., Higuchi, H., Wakita, H., Nagasawa, H., 1968. Trace element partitioning between two pyroxenes and the host lava. Earth and Planetary Science Letters 5, 47- 51.

Ossandón, G., and Zentilli, M., 1997. El distrito de Chuquicamata: una concentración de cobre de clase mundial: Universidad Católica del Norte, VIII Congreso Geológico Chileno, 1888-1892.

Oyarzun, R., Márquez, A., Lillo, J., López, I., Rivera, S., 2001. Giant versus small porphyry copper deposits of Cenozoic age in northern Chile: adakitic versus normal calcalkaline magmatism. Mineralium Deposita 36, 794-798.

Packham, G.H., 1973. Aspects of the geological history of the New Hebrides and South Fiji basins. Bulletin-Australian Society of Exploration Geophysicists, 6, no.2-3, First Southwest Pacific workshop-symposium: 50-51.

Parkinson I. J. and Arculus R. J., 1999. The redox state of subduction zones: insights from arc peridotites. Chemical Geology 160, 409-423.

Parman, S.W., Grove, T.L., Kelley, K.A., and Plank, T., 2011. Along-arc variations in the pre-eruptive H2O contents of Mariana arc magmas inferred from fractionation paths: Journal of Petrology 52, 257-278.

Peach, C.L., Mathez, E.A., Keays, R.R., 1990. Sulfide melt–silicate melt distribution coefficients for noble metals and other chalcophile elements as deduced from MORB: implications for partial melting. Geochimica et Cosmochimica Acta 54, 3379-3389.

Peacock, S. M., 1996. Thermal and petrologic structure of subduction zones: American Geophysical Union, Geophysical Monograph 96, 119-133.

Peacock, S. M., Rushmer T., and Thompson A. B., 1994. Partial melting of subducting oceanic crust. Earth and Planetary Science Letters 121, 227-244.

Pearce J. A., 1982. Trace element characteristics of lavas from destructive plate boundaries. In Andesites: Orogenic Andesites and Related Rocks (ed. R. S. Thorpe). Wiley, Chichester, 526-547.

Pelletier, B., Layfoy, Y. and Missegue,F., 1993. Morphostructure and magnetic fabric of the northwestern North Fiji Basin. Geophysics Research Letters, 20:11251-1154.

Petterson, M.G., Neal, C.R., Mahoney, J.J., Kroenke, L.W., Saunders, A.D., Babbs, T.L., Duncan, R.A., Tolia, D. and McGrail, B., 1997. Structure and deformation of north and central Malaita, Solomon Islands; tectonic implications for the Ontong Java Plateau-Solomon arc collision, and for the fate of oceanic plateaus. Tectonophysics, 283, no.1-4: 1-33.

Plank, T., 2005. Constraints from thorium/lanthanum on sediment recycling at subduction zones and the evolution of the continents. Journal of Petrology 46, 921-944.

Poli, S., and Schmidt, M.W., 2002. Petrology of subducted slabs: Annual Reviews of Earth and Planetary Sciences 30, 207-235.

Rapp R. P. and Watson E. B., 1995. Dehydration melting of metabasalt at 8-32 kbar: implications for continental growth and crust–mantle recycling. Journal of Petrology 36, 891-931.

Rapp R. P., Watson E. B., and Miller C. F., 1991. Partial melting of amphibolite/eclogite and the origin of Archean trondhjemites and tonalites. Precambian Research 51, 1-25.

Reubi O., Blundy J.D., 2008. Assimilation of plutonic roots, formation of high-K ‘‘exotic’’ melt inclusions and genesis of andesitic magmas at Volcan de Colima, Mexico. Journal of Petrology 49, 2221-2243

Richards, J.P., 2011. Magmatic to hydrothermal metal fluxes in convergent and collided margins. Ore Geology Reviews 40, 1-26.

Richards, J.P., 2009. Postsubduction porphyry Cu–Au and epithermal Au deposits: products of remelting of subduction-modified lithosphere. Geology 37, 247-250.

Richards, J.P., and Kerrich, R., 2007. Adakite-like rocks: Their diverse origins and questionable role in metallogenesis: Economic Geology 102, 537-576.

Richards, J.P., Ullrich, T., and Kerrich, R., 2006. The late Miocene-Quaternary Antofalla volcanic complex, southern Puna, NW Argentina: Protracted history, diverse petrology, and economic potential: Journal of Volcanology and Geothermal Research 152, 197-239.

Richards, J.P., Boyce, A.J., and Pringle, M.S., 2001. Geological evolution of the Escondida area, northern Chile: A model for spatial and temporal localization of porphyry Cu mineralization: Economic Geology 96, 271-305.

Richards, J.P., Kerrich, R., 1993. The Porgera gold mine, Papua New Guinea: magmatic–hydrothermal to epithermal evolution of an alkalic-type precious metal deposit. Economic Geology 88, 1017-1052.

Ringwood, A.E., 1977. Petrogenesis in island arc systems, in Talwani, M., and Pitman, W.C., (eds.), Island arcs, deep sea trenches, and back arc basins: American Geophysical Union [Maurice Ewing Series I], 311-324.

Robinson P., 2003. XRF analysis of flux-fused discs. Geoanalysis 2003, The 5th International Conference on the Analysis of Geological and Environmental Materials, Abstracts, 90.

Rowe, M.C., Kent, A.J.R., Nielsen, R.L., 2009. Subduction influence on oxygen fugacity and trace and volatile elements in basalts across the Cascade Volcanic Arc. Journal of Petrology 50, 61-91.

Sajona, F.G., and Maury, R.C., 1998. Association of adakites with gold and copper mineralization in the Philippines: Comptes rendus de l'Académie des sciences. Série II, Sciences de la terre et des planètes 326, 27-34.

Sajona, F.G., Maury, R.C., Bellon, H., Cotten, J., Defant, M.J., and Pubellier, M., 1993. Initiation of subduction and the generation of slab melts in western and eastern Mindanao, Philippines: Geology 21, 1007-1010.

Sattari, P., Brenan, J. M., Horn, I., & McDonough, W. F., 2002. Experimental constraints on the sulfide-and chromite-silicate melt partitioning behavior of rhenium and platinum-group elements. Economic Geology 97, 385-398.

Scaillet, B. 2010. Volatile Destruction. Direct evidence for the role of volatiles in magmatic ore formation has been elusive. Magma degassing at Merapi volcano in Indonesia is found to be directly linked to the selective leaching of metals from sulphide melts that ultimately form ore deposits. Nature Geosciences 3, 456-457.

Scaillet, B., Pichavant, M., 2003. Experimental constraints on volatile abundances in arc magmas and their implications for degassing processes. In: Oppenheimer, C., Pyle, D.M., Barclay, J. (eds.), Volcanic Degassing. Geological Society, Special Publications 213, 23-52.

Scaillet, B., Clemente, B., Evans, B.W., Pichavant, M., 1998. Redox control of sulphur degassing in silicic magmas. J. Geophys. Res. 103 (B10), 23,937-23,949.

Schmidt, M.W., and Poli, S., 1998. Experimentally based water budgets for dehydrating slabs and consequences for arc magma generation: Earth and Planetary Science Letters, 163, 361-379.

Sen, C., and Dunn, T., 1994. Dehydration melting of a basaltic composition amphibolite at 1.5 and 2.0 GPa: Implications for the origin of adakites: Contributions to Mineralogy and Petrology 117, 394-409.

Seo, J.H., Guillong, M., Heinrich, C.A., 2009. The role of sulfur in the formation of magmatic–hydrothermal copper–gold deposits. Earth and Planetary Science Letters 282, 323-328.

Sillitoe, R.H., 2010. Porphyry copper systems. Economic Geology 105, 3-41.

Sillitoe, R.H., 1973. The tops and bottoms of porphyry copper deposits. Economic Geology 68, 799-815.

Simon, A. C., & Ripley, E. M., 2011. The role of magmatic sulfur in the formation of ore deposits. Reviews in Mineralogy and Geochemistry 73, 513-578.

Simon, A.C., Pettke, T., Candela, P.A., Piccoli, P.M., Heinrich, C.A., 2006. Copper partitioning in a melt–vapor–brine–magnetite–pyrrhotite assemblage. Geochimica et Cosmochimica Acta 70, 5583-5600.

Skinner, B.J. 1983. Submarine volcanic exhalations that form mineral deposits: An old idea now proven correct. In Hydrothermal Processes at Seafloor Spreading Centres. P.A. Rona, K. Boström, L. Laubier, and K. L. Smith, (eds.), NATO Conference Series IV:12, Plenum Publishing Corp., New York, NY, 557-569.

Stanton, R.L., 1994. Ore elements in arc lavas. Oxford Monograph on Geology and Geophysics 29, 391 pp.

Stix, J., Layne, G.D., 1996. Gas saturation and evolution of volatile and light lithophile elements in the Bandelier magma chamber between two caldera-forming eruptions. Journal of Geophysical Research. 101, 25181-25196

Stavast, W.J.A., Keith, J.D., Christiansen, E.H., Dorais, M.J., Tingey, D., 2006. The fate of magmatic sulfides during intrusion or eruption, Bingham and Tintic districts, Utah. Economic Geology 101, 329-345.

Stern, C.R., and Kilian, R., 1996. Role of the subducted slab, mantle wedge and continental crust in the generation of adakites from the Andean Austral volcanic zone: Contributions to Mineralogy and Petrology 123, 263-281.

Sun, W., Zhang, H., Ling, M.-X., Ding, X., Chung, S.-L., Zhou, J., Yang, X.-Y., and Fan, W., 2011. The genetic association of adakites and Cu-Au ore deposits: International Geology Review 53, 691-703.

Sun, W.D., Arculus, R.J., Kamenetsky, V.S., Binns, R.A., 2004b. Release of gold-bearing fluids in convergent margin magmas prompted by magnetite crystallization. Nature 431, 975-978.

Tatsumi Y., 1981. Melting experiments on a high-magnesian andesite. Earth and Planetary Science Letters 54, 357-365.

Tatsumi, Y., Hamilton, D.L., Nesbitt, R.W., 1986. Chemical characteristics of fluid phase released from a subducted lithosphere and the origin of arc magmas: evidence from high pressure experiments and natural rocks. Journal of Volcanology and Geothermal Research 29, 293-309.

Tatsumi Y., Ishizaka K., 1982. Origin of high-magnesium andesites in the Setouchi volcanic belt, southwest Japan, I. Petrographical and chemical characteristics. Earth and Planetary Science Letters 60, 293-304

Taylor, B., and Martinez, F., 2003, Back-arc basin basalt systematic. Earth and Planetary Science Letters 210, 481-497

Taylor, G.K., Gascoyne, J. and Colley, H., 2000. Rapid rotation of Fiji; paleomagnetic evidence and tectonic implications. Journal of Geophysical Research, B, Solid Earth and Planets, 105, no.3:5771-5781.

Taylor, R.N., Nesbitt, R.W., Vidal, P., Harmon, R.S., Auvray, B., and Croudace, I.W., 1994, Mineralogy, chemistry, and genesis of the boninite series volcanics, Chichijima, Bonin Islands, Japan. Journal of Petrology 35, 577-617.

Thiéblemont, D., Stein, G., and Lescuyer, J.-L., 1997. Gisements épithermaux et porphyriques: la connexion adakite: C.R. Acad. Sci. Paris, Sciences de la terre et des planètes/Earth and Planetary Sciences 325, 103-109.

Thorkelson, D.J., Breitsprecher, K., 2005. Partial melting of slab window margins: genesis of adakitic and non-adakitic magmas. Lithos 79, 25-41.

Tomkins, A.G., Mavrogenes, J.A., 2003. Generation of metal-rich felsic magmas during crustal anatexis. Geology 31, 765-768.

Ulrich, T., Günther, D., Heinrich, C.A., 2001. The evolution of a porphyry Cu–Au deposit, based on LA-ICP-MS analysis of fluid inclusions: Bajo de la Alumbrera, Argentina. Economic Geology 96, 1743-1774.

Verbeeten, A., Crawford, A.J., Eggins, S.M., and Maillet, P., 1995. Petrology, geochemistry and tectonic implications of magmatism in northern Hunter Ridge– Kadavu island group (Fiji), in St. George, J.D., (ed.), Exploring the rim: Proceedings of the 1995 PACRIM Congress: Australasian Institute of Mining and Metallurgy Publication Series 9/95, p. 599-603.

Verbeeten, A.C. 1996. Petrology, geochemistry and tectonic implications of magmatism along the northern Hunter Ridge and Kadavu Island Group, Fiji. Unpublished PhD thesis, lodged at the Geology Department, University of Tasmania.

Wallace, P.J., 2005. Volatiles in subduction zone magmas: concentrations and fluxes based on melt inclusion and volcanic gas data. Journal of Volcanology and Geothermal Research 140, 217-240.

Wallace, P.J., Anderson, A.T., Davis, A.M., 1999. Gradients in H2O, CO2, and exsolved gas in large-volume silicic magma system: interpreting the record preserved in melt inclusions from the Bishop Tuff. Journal of Geophysical Research 104, 20097-20122.

Watson J.S., 1996. Fast, Simple Method of Powder Pellet Preparation for X-Ray Fluorescence Analysis. X-Ray Spectrometry, 25, 173-174.

Webster, J.D., 2004. The exsolution of magmatic hydrosaline chloride liquids. Chemical Geology 210, 33-48.

Webster, J.D., 1992. Water solubility and chlorine partitioning in Cl-rich granitic systems: effects of melt composition at 2 kbar and 800 °C. Geochimica et Cosmochimica Acta 56, 679-687.

Webster, J.D., Sintoni, M.F., De Vivo, B., 2009. The partitioning behavior of Cl, S, and H_2O in aqueous vapor-±saline-liquid saturated phonolitic and trachytic melts at 200 MPa. Chemical Geology 263, 19-36.

Webster, J.D., Sintoni, M.F., De Vivo, B., 2005. The role of sulfur in promoting magmatic degassing and volcanic eruption at Mt. Somma-Vesuvius. In:, Volcanism in the Campania plain: Vesuvius, Campi Flegrei and ignimbrites, De Vivo, B. (ed.). Development in Volcanology 9, 221-236.

Webster, J.D., De Vivo, B., Tappen, C., 2003. Volatiles, magmatic degassing and eruptions of Mt. Somma-Vesuvius: constraints from silicate melt inclusions, Cl and H2O solubility experiments and modeling. In: De Vivo, B., Bodnar, R.J. (eds.), Melt Inclusions in Volcanic Systems methods, applications and problems: Development in Volcanology 5, 207-226.

Webster, J.D., De Vivo, B., 2002. Experimental and modeled solubilities of chlorine in aluminosilicate melts, consequences of magma evolution, and implications for exsolution of hydrous chloride melt at Mt. Somma-Vesuvius. American Mineralogist 87, 1046-1061.

Weissel, J.K. and Watts, A.B., 1975. Tectonic complexities in the South Fiji marginal basin. Earth and Planetary Science Letters, 28, 121-126.

Williams, T.J., Candela, P.A., Piccoli, P.M., 1995. The partitioning of copper between silicate melts and two-phase aqueous fluids: an experimental investigation at 1 kbar, 800 °C and 0.5 kbar, 850 °C. Contributions to Mineralogy and Petrology 121, 388-399.

Williams-Jones, A.E., Heinrich, C.A., 2005. Vapor transport of metals and the formation of magmatic-hydrothermal ore deposits. Economic Geology 100, 1287-1312.

Wood, B.J., Blundy, J.D., 1997. A predictive model for rare earth element partitioning between clinopyroxene and anhydrous silicate melt. Contributions to Mineralogy and Petrology. 129, 166-181.

Wood, B.J., Nielsen, S.G., Rehkämper, M., Halliday, A.N., 2008. The effects of core formation on the Pb- and Tl- isotopic composition of the silicate Earth. Earth and Planetary Science Letters 269, 326-336.

Wood B.J., Blundy J.D., 2001. The effect of cation charge on crystal-melt partitioning of trace elements. Earth and Planetary Sciences Letters 188, 59-71.

Wood B.J., Blundy J.D., 2002. The effect of H2O on crystal-melt partitioning of trace elements. Geochimica and Comsochimica Acta 66, 3647-3656.

Wood B.J., Blundy J.D., 2003. Trace element partitioning. In Treatise on Geochemistry, vol. 2, Carlson R. (ed.) Elsevier-Pergamon, Oxford, 395-424.

Yan, C.Y. and Kroenke, L.W., 1993, A plate tectonic reconstruction of the southwest pacific, 0-100 Ma. Proceedings of the Ocean Drilling Program, Scientific Results 130: 697-707.

Yi, W., Halliday, A. N., Alt, J. C., Lee, D.-C., Rehkämper, M., Garcia, M. O., Langmuir, C. H. & Su, Y., 2003. Cadmium, indium, tin, tellurium, and sulfur in oceanic basalts: Implications for chalcophile element fractionation in the Earth. Journal of Geophysical Research 105, 18927-18948.

Yogodzinski, G.M., Lees, J.M., Churikova, T.G., Dorendorf, F., Wöerner, G., Volynets, .N., 2001. Geochemical evidence for the melting of subducting oceanic lithosphere at plate edges. Nature 409, 500-504.

Zajacz, Z., Seo, J.H., Candela, P.A., Piccoli, P.M., Tossell, J.A., 2011. The solubility of copper in high-temperature magmatic vapors: a quest for the significance of various chloride and sulfide complexes. Geochimica et Cosmochimica Acta 75, 2811-2827.

Zajacz, Z., Halter, W.E., Pettke, T., Guillong, M., 2008. Determination of fluid/melt partition coefficients by LA-ICPMS analysis of co-existing fluid and silicate melt inclusions: controls on element partitioning. Geochimica et Cosmochimica Acta 72, 2169-2197.